Three Dimensional Simulations of Scrape-Off Layer Filaments

Luke Easy

Doctor of Philosophy

University of York
Physics

July 2016

Abstract

In the Scrape-Off Layer (SOL) of magnetic confinement devices, cross-field transport of particles is dominated by the convection of filamentary plasma structures via self-generated $\boldsymbol{E} \times \boldsymbol{B}$ velocity fields. This thesis investigates the dynamics of such *filaments* using three dimensional simulations to further theoretical understanding of SOL transport. A new 3D SOL simulation code called STORM3D has been developed using the BOUT++ framework to implement an isothermal drift-reduced fluid model in a slab geometry. Verification and validation exercises are documented to demonstrate that the code has been implemented correctly and that the physical model adequately reproduces experimental observations.

A comprehensive characterisation of how a filament's initial geometry affects its subsequent dynamics is provided via a series of 3D simulations of isolated filaments. In particular the size of a filament in the plane perpendicular to the magnetic field, $\delta_\perp$, is shown to have a strong influence on its motions, as it determines which currents balance the filament's pressure-driven diamagnetic currents, which in turn determines its $\boldsymbol{E} \times \boldsymbol{B}$ velocity. At small $\delta_\perp$, this balance is predominantly provided by polarisation currents and the filament's radial velocity is observed to increase with $\delta_\perp$. In contrast, at large $\delta_\perp$, parallel currents closing through the target are found to be dominant, and the radial velocity decreases with $\delta_\perp$.

Comparisons are made between 3D simulations and 2D simulations using different parallel closures; namely the sheath dissipation closure, which neglects parallel gradients, and the vorticity advection closure, which neglects the influence of parallel currents. The vorticity advection closure is found not to replicate the 3D perpendicular dynamics well and overestimates the initial radial velocity of all filaments studied. A more satisfactory comparison is obtained with the sheath dissipation closure, even in the presence of significant parallel gradients, where the closure is no longer valid. The vorticity advection closure's poor performance occurs because in the 3D case parallel currents closing through the sheath play an important role in reducing the extent to which polarisation currents are driven. In a conduction-limited or detached SOL regime however, low plasma temperatures and high neutral densities near the divertor will produce significantly higher resistivity values in the region than that used in the aforementioned 3D simulations.

Therefore the effect of increasing the normalised plasma resistivity in the last quarter of the domain nearest the targets is examined using 3D simulations. Whilst small $\delta_\perp$ filaments are observed to be relatively unaffected by this quantity, large $\delta_\perp$ filaments exhibit faster radial velocities at higher resistivity values due to two mechanisms. Firstly, parallel currents are reduced meaning that polarisation currents are necessarily enhanced and secondly, a potential difference forms along the parallel direction so that higher potentials are produced in the region of the filament for the same amount of current to flow into the sheath. This indicates that broader SOL profiles could be produced at higher values of normalised resistivity, and hence at larger reference SOL densities and at colder temperatures.

Contents

List of Figures

List of Tables

Acknowledgements

This thesis would not have been possible without the support I have received over the last four years from a vast number of individuals within the fusion community. Primarily I wish to express my gratitude to my two supervisors, Fulvio Militello and Ben Dudson, for their enthusiasm, guidance, and for always making time for me.

I have also been fortunate enough to work closely with John Omotani and Nick Walkden, who have both been extraordinarily helpful, and have provided many fruitful discussions. Furthermore I would like to acknowledge a number of people who I have collaborated to some degree during the course of my PhD; Patrick Tamain, Anders Nielsen, Jens Madsen, Volker Naulin, Eva Havlíčková, Paolo Ricci, Fabio Riva and Wayne Arter. I would also like to acknowledge my sister, Emma, for her careful proofreading of this thesis.

In addition, I wish to acknowledge the funding I have received from the Engineering and Physical Sciences Research Council [EP/K504178/1] and also the access that I have had to high powered computing facilities. These include the HECToR and ARCHER machines through the Plasma HEC Consortium EPSRC Grant No. EP/L000237/1, and the HELIOS supercomputer system at Computational Simulation Centre of International Fusion Energy Research Centre (IFERC-CSC), Aomori, Japan, under the Broader Approach collaboration between Euratom and Japan, implemented by Fusion for Energy and JAEA.

Lastly I wish to thank my parents, who have always supported and encouraged my education.

Author's Declaration

The work contained in this thesis is original and no part of it has been submitted for any other degree at this or any other institution. I am the sole author. All sources are acknowledged as References.

Parts of this thesis are based upon joint research conducted with collaborators. In particular:

- Patrick Tamain and Eva Havlickova respectively carried out the TOKAM-3X and SOLF1D simulations presented in Section 5.3.
- In Section 5.5 the experimental analysis and GBS simulations were carried out by Fabio Riva. The HESEL simulations were carried out by Anders Nielsen, Jens Madsen, Volker Naulin, Jeppe Olsen and Jens Rasmussen, whilst the TOKAM-3X simulations were carried out by Patrick Tamain, Clothilde Colin-Bellot, Eric Serre and Julian Denis.

Aspects of this work have previously been presented in the following publications:

- Sections 5.2 and 5.3 and Chapter 6 are based on work published in L. Easy et al, "3D Simulations of Plasma Filaments in the Scrape Off Layer: A Comparison with Models of Reduced Dimensionality". *Physics of Plasmas* **21**.12, p. 122515. DOI: 10.1063/1.4904207.
- Section 7.2 is based on work published in L. Easy et al. "Investigation of the effect of resistivity on scrape off layer filaments using three-dimensional simulations". *Physics of Plasmas*, **23**.1, pp. 012512–14. DOI: 10.1063/1.4940330
- Section 5.5 is based on work published in Riva et al. "Blob dynamics in the TORPEX experiment: a multi-code validation". *Plasma Physics and Controlled Fusion* **58**.4, pp. 1–16. DOI: 10.1088/0741-3335/58/4/044005.

Chapter 1

Introduction

1.1 Energy Demand

Global energy consumption is expected to continue to rise dramatically over the course of the next century, with almost a 50% increase from the 2012 level expected by 2040 [1]. As shown in Figure 1.1, this increase is expected to be predominantly driven by nations outside the Organisation for Economic Co-operation and Development (OECD), i.e. developing countries, as their growing populations prosper and attain a standard of living comparable to that found in the developed world.

Currently 86% of the energy consumed globally originates from fossil fuels (coal, oil and natural gas) [2], and it is essential that this fraction is reduced in the future as much as possible for four key reasons.

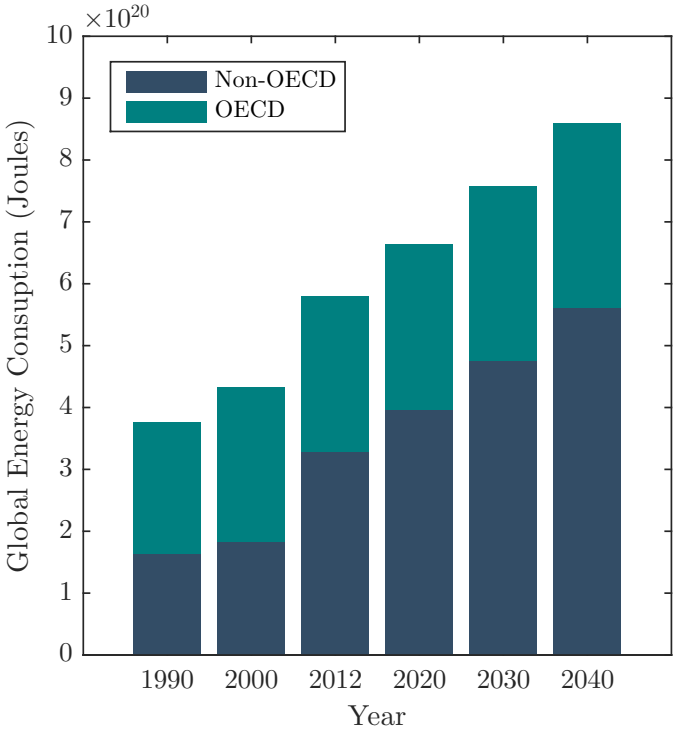

Figure 1.1: Historical and predicted world energy consumption to 2040. OECD refers to the Organisation for Economic Co-operation and Development. Data obtained from Reference [1].

1. To reduce air pollution.
   Burning fossil fuels releases harmful pollutants into the atmosphere, including nitrogen oxides, sulphur oxides and small particulates. Such air pollution causes a variety of serious diseases that reduce standards of living and ultimately lead to loss of life. The World Health Organisation estimates that in 2012 approximately 8 million premature deaths were caused globally due to air pollution. Over half of these were attributed to household or indoor air pollution (as opposed to outdoor). This is in particular a problem in the developing world, where over 3 billion people cook and heat their homes using open fires and basic stoves which burn biomass or coal [3, 4].

2. To reduce climate change.
   Combustion of fossil fuels also releases vast amounts of carbon dioxide into the atmosphere. The overwhelming consensus of the scientific community is that this leads to global warming and climate change through the greenhouse effect [5]. This will have severe consequences for future generations such as land loss due to rising sea levels, drought and famine.

3. To provide energy security.
   Many countries in the world do not possess fossil fuel resources and rely on those who do. It is advantageous for such countries to reduce this dependency, to prevent war and political instability.

4. Fossil fuels are finite resources.
   Despite the continued discovery of new oil and gas reserves and the introduction of new techniques such as fracking to harvest previously unextractable deposits, fossil fuels are not renewable and will eventually become increasingly scarce and prohibitively expensive. British Petroleum estimates that the global proven reserves of natural gas and conventional oil will last for around 50 years at current production levels, whilst coal will last for 110 years [6]. However, these estimates only include known deposits that can be currently extracted economically using existing technology and so if all known resources are included, these estimates extend to around 200 years for oil and gas and 2000 years for coal, according to the International Energy Agency [7].

Shifting the world-wide energy market away from fossil fuels and towards technologies that do not release carbon dioxide into the atmosphere is a difficult global challenge. Indeed, the International Energy Agency's 'New Policies Scenario', which assumes successful implementation of all agreed national policies and announced commitments designed to save energy and reduce the use of fossil fuels, predicts that by 2035 fossil fuel consumption and carbon dioxide production will have risen by 33% and 20% respectively from 2010 values [8].

A wide range of low carbon technologies are being currently developed and used, but there exist few with the genuine potential to fill the void left by (or more importantly compete economically with) fossil fuels. Many renewables such as wind, wave and tidal power are inherently intermittent, and require fossil fuel backup for when they are not operational. Furthermore, these technologies can only generate relatively small quantities of electricity and therefore cannot be used as a base load energy source. Solar power, whilst also suffering from intermittency, does have the potential to generate a significant fraction of the world's energy requirements, but it is currently very expensive and will require drastic technological advances in energy storage for this to happen [9]. Biofuels may reduce carbon emissions, but

their cultivation on a mass scale would significantly increase deforestation and reduce the land available for food production. For reference, the aforementioned energy sources generated only 5.7% of global electricity in 2013 [10]. Nuclear fission is in principle a viable solution, although it does have an extremely high capital cost and does produce long-lived radioactive waste that is difficult to manage. Furthermore, concerns over nuclear proliferation and accidents such as Chernobyl and Fukushima (despite it in reality having an exceptional safety track record [11]) have made it politically unpopular.

It is clear from this brief discussion that there are a number of critical requirements that an energy source must fulfil for it to significantly reduce fossil fuel use. The source must be renewable or sufficiently abundant to avoid future depletion issues. It must have the potential to satisfy a large fraction of global electricity consumption at a price competitive with fossil fuels. It is preferable for the source not to be dependent on inherently intermittent processes or have a large geographical footprint. Lastly, it should not produce any long-lived radioactive or otherwise hazardous waste. Satisfying all these requirements is difficult, but one such energy source which may be able to meet each of these critera is nuclear fusion.

1.2 Nuclear Fusion

In a nuclear fusion reaction two or more atomic nuclei fuse together upon collision to form a heavier nucleus and other by-products. The mass of any nucleus is less than that of its constituent nucleons (protons and neutrons). Through Einstein's equation, $E = mc^2$, this 'loss' of mass can be interpreted as a *binding energy*, so called because this is the energy required to disassemble the nucleus into its constituent parts. For certain fusion reactions, the binding energy of the resulting nucleus is greater than that of the reactants and the excess energy is released as the kinetic energy of the products. From Figure 1.2, which plots the average binding energy per nucleon for a wide variety of nuclei, it can be seen that generally energy is released for fusion reactions involving two nuclei lighter than iron-56 (Fe^{56})*. This mechanism powers the stars and nuclear fusion has enormous potential to be used to generate electricity without producing long-lived radioactive waste. The technology to release a vast amount of fusion energy has existed since the *Ivy Mike* hydrogen bomb test in 1952, but obtaining a net energy gain from fusion reactions in a controlled (and non-devastating) fashion has yet to be achieved.

In order for a fusion reaction to occur, the positively charged nuclei must collide together with sufficient kinetic energy to overcome the Coulomb repulsion and become close enough for the strong nuclear force (which has a very short range) to fuse the nuclei together. The magnitude of this energy barrier is prohibitively high ($\sim$1 MeV), but fortunately quantum tunnelling allows fusion reactions to occur in a small fraction of collisions which have lower energies. The likelihood of this happening can be parametrised using a reaction cross section, σ, which has units of m^2 and is a function of the relative velocity of the colliding nuclei, v. If the reacting particles have distributions of velocities (e.g. Maxwellian distributions), then it is convenient to calculate the average over both distributions of the product σv. This quantity is termed the reactivity and is denoted by $\langle \sigma v \rangle$. The reaction rate per unit volume, $\mathcal{R}$, can then

*Energy can also be released from nuclei heavier than iron-56, through a *fission* reaction where a heavier nuclei splits apart into lighter nuclei. This process is used to generate electricity in conventional nuclear fission power stations.

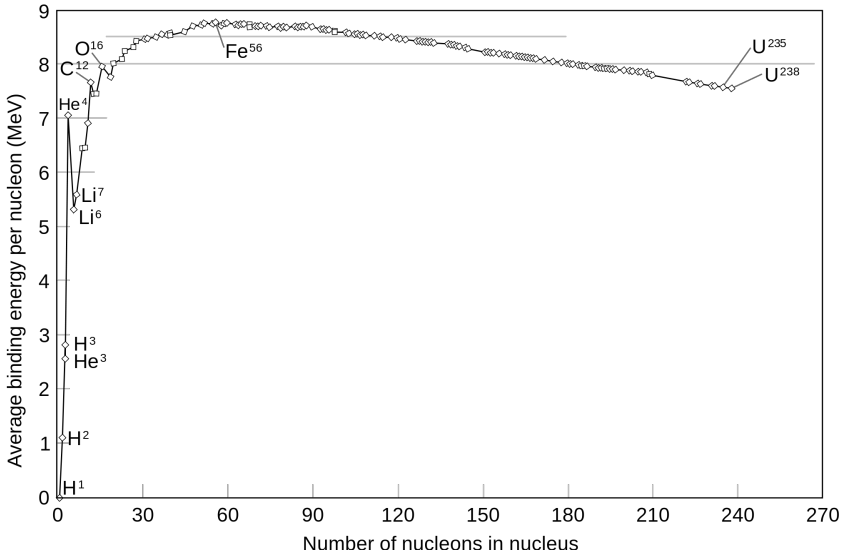

Figure 1.2: Nuclear binding energy curve. Image reproduced from Wikipedia Commons.

be expressed as

$$\mathcal{R} = n_1 n_2 \langle \sigma v \rangle \,, \tag{1.1}$$

where n_1 and n_2 are the number densities of the two reacting particle species.

Listed below are a number of fusion reactions of interest for electricity generation.

$$\begin{aligned}
&\mathrm{D} + \mathrm{D} \rightarrow \mathrm{T} + \mathrm{p} + 4.03 \text{ MeV} \\
&\mathrm{D} + \mathrm{D} \rightarrow \mathrm{He}^3 + \mathrm{n} + 3.27 \text{ MeV} \\
&\mathrm{D} + \mathrm{T} \rightarrow \mathrm{He}^4 + \mathrm{n} + 17.6 \text{ MeV} \\
&\mathrm{D} + \mathrm{He}^3 \rightarrow \mathrm{He}^4 + \mathrm{p} + 18.3 \text{ MeV}
\end{aligned}$$

Here D = H^2 and T=H^3 stand for deuterium and tritium nuclei, which are two isotopes of hydrogen, H. He^3 and He^4 are the nuclei of two isotopes of helium, whist p and n denote protons and neutrons respectively. It is worth noting that the energy gain from these reactions is exceptionally high and approximately one million times higher than that released by the chemical reactions which occur during the combustion of fossil fuels. The reactivity of each of these reactions is plotted as a function of temperature in Figure 1.3 (a combined reactivity is shown for the D-D reactions), and it is clear that the D-T is the most promising reaction in that its reactivity is at least an order of magnitude larger than that of the other reactions except at impractically high temperatures. In addition, the energy yield from D-T fusion is comparable to that produced by D-He^3, and considerably more than that released by each of the D-D reactions. For these reasons, the D-T fusion reaction has by far the most potential to be used for electricity generation.

Whilst deuterium is a stable element and is easily sourced from sea water, tritium has a half-life of 12.3 years, and only small quantities occur on earth as a result of interactions between cosmic rays and nitrogen in the atmosphere, or as a by-product from nuclear fission reactors (in particular CANDU reactors [13]). Fortunately, it can be bred from lithium (Li), using the following two fission reactions:

$$\begin{aligned}
&\mathrm{Li}^6 + \mathrm{n} \rightarrow \mathrm{T} + \mathrm{He}^4 + 4.8 \text{ MeV} \\
&\mathrm{Li}^7 + \mathrm{n} \rightarrow \mathrm{T} + \mathrm{He}^4 + \mathrm{n} - 2.5 \text{ MeV}
\end{aligned}$$

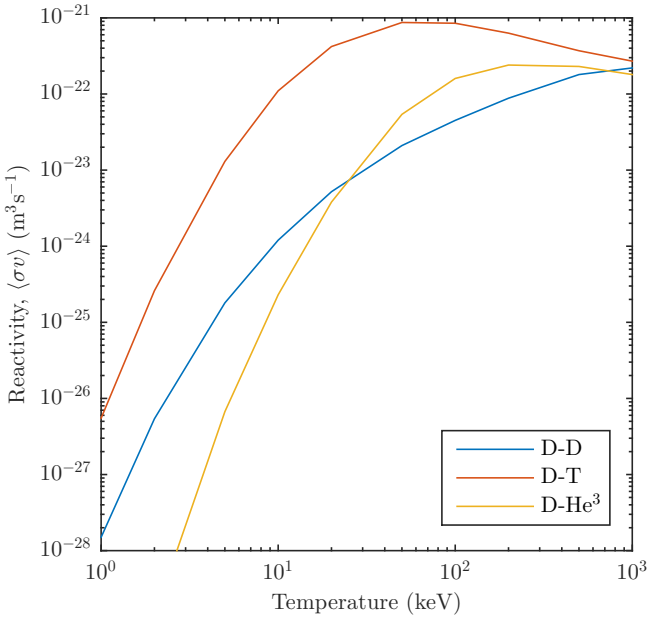

Figure 1.3: Temperature dependence of the reactivity of key fusion reactions. The graph plots the sum of the two D-D reactivity values. Data obtained from Reference [12].

Thus a self-sustaining system can in principle be formed in which the neutron released from a D-T fusion reaction is used to breed tritium for further fusion reactions. Lithium can be obtained from ore deposits in the earth and also from sea water, although the latter option is less economically viable. Nevertheless Table 1.1 shows that both deuterium and lithium are sufficiently abundant to supply the world's electricity needs for thousands, if not millions of years [14].

In order to provide the conditions required for fusion, the deuterium and tritium species need to be held at sufficiently high temperatures and densities for long enough to allow the reactions to occur. In particular, a temperature of the order of 10 keV or 100 million degrees Kelvin is required, which is approximately 10 times hotter than the centre of the sun, and this precludes the use of solid materials to confine the fusion reactants. In stars, this confinement is provided by gravity, but such strong gravitational fields are not achievable on earth. A number of different schemes are currently being researched with the ultimate aim of electricity generation in mind, but arguably the most promising makes use of the fact that at such high temperatures all atoms become ionised (i.e. split into positively charged nuclei and negatively charged electrons), and thus matter exists in its fourth state, plasma. Therefore in the presence of a magnetic field, $\boldsymbol{B}$, and electric field, $\boldsymbol{E}$, the ionised particles within the plasma are subject to the Lorentz force:

$$\boldsymbol{F} = q_s \left[\boldsymbol{E} + (\boldsymbol{v}_s \times \boldsymbol{B}) \right]. \tag{1.2}$$

Here q_s and $\boldsymbol{v}_s$ are respectively the charge and the velocity of the particle. This force means that whilst the ionised particles may move freely parallel to $\boldsymbol{B}$, they are constricted in the perpendicular plane to move in orbits about the magnetic field lines, whose radii are inversely proportional to the magnitude of $\boldsymbol{B}$. Consequently, strong magnetic fields with an appropriate topology can be used to confine a fusion plasma. Such a scheme is referred to as Magnetic Confinement Fusion.

Table 1.1: Estimated reserves of the fuels required for D-T fusion, in terms of the number of years that they would be able to supply the global energy demand. Data reproduced from Reference [14].

Fusion Resource	Years of use to supply global electricity demand (at 1995 levels)
Deuterium	150 billion years
Lithium (in ore deposits)	3000 years
Lithium (in sea water)	60 million years

1.3 Magnetic Confinement Fusion

Two theorems provide constraints on the possible magnetic configurations for confining a fusion plasma. The virial theorem [15] provides a relationship between the total kinetic and potential energies of a system of particles. A consequence of this is that a plasma will always expand in the absence of external forces. Therefore a confining magnetic field cannot be entirely self generated through the dynamics of the ionised particles, and must be in some part produced via external coils. The second theorem, 'the hairy ball' theorem of algebraic topology [16], states that a sphere's surface cannot have a non-vanishing continuous tangent vector field. In layman's terms this means that it is impossible to comb a hairy ball flat without a creating a *cow lick*. This means that all magnetic geometries topologically equivalent to a sphere necessarily have at least one null point through which a plasma would be able to escape and therefore cannot be used for confinement.

One topology which does not suffer this limitation is a torus (it is possible to comb the hair flat on a hairy doughnut) and for this reason the majority of magnetic confinement devices utilise this geometry, with the magnetic field predominantly acting in the toroidal direction. However, a purely toroidal field provides little better confinement than if there were no magnetic field at all. This is because a toroidal magnetic field is necessarily curved and becomes weaker further away from the centre of the torus. These effects cause the centre about which the charged particles undergo their orbits to slowly drift across the magnetic field and thus the particles are not confined. Fortunately this problem can be remedied with the addition of a poloidal magnetic field component. The resultant magnetic field lines follow a helical path around the torus, such that each field line resides on one of a set of nested flux surfaces. As the particles transit along these helical field lines, they drift outwards from the core when they are on the top of the device, but drift inwards when they are on the bottom of the device, so that their net displacement from the core averages to zero.

Whilst the toroidal component of the magnetic field is generally produced by passing currents through a number of external coils that wrap around the plasma, the poloidal component can be generated in two different ways, corresponding to two classes of device. The first, a *stellarator* [17], also generates the poloidal magnetic field externally from the plasma, either through additional poloidal field coils, or as in more recent machines, by producing both components of the magnetic field from one set of coils. A schematic diagram of the latest generation Wendelstein 7-X stellarator design is shown in Figure 1.4. It can be seen that the coils take highly contorted shapes, which make stellarators very difficult to design, manufacture and maintain. They are therefore less common and their state of development is less advanced than that of the second class of device, the *tokamak*.

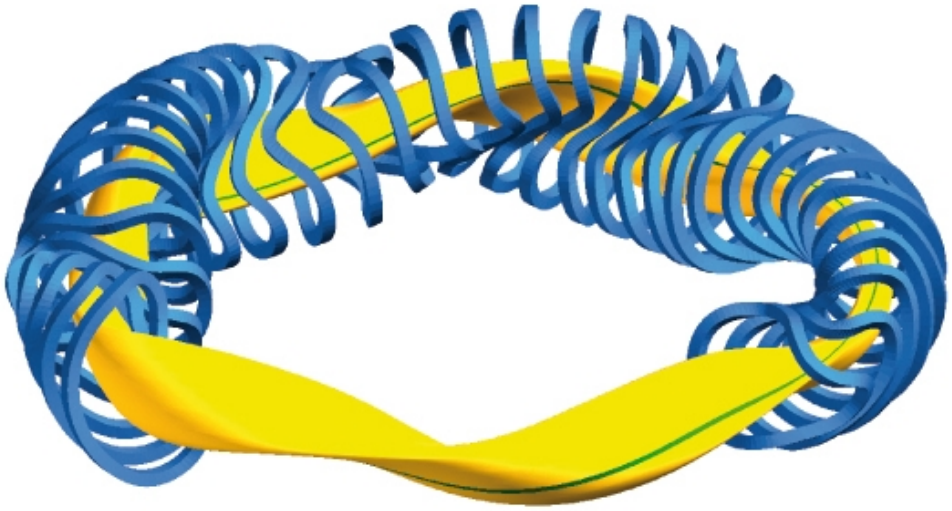

Figure 1.4: Schematic diagram of the Wendelstein 7-X stellarator. The magnetic field coils are shown in blue, whilst the plasma shape is shown in yellow. A green line shows an example magnetic field line. Image produced by Max Planck Institute for Physics [CC BY 3.0 (`http://creativecommons.org/licenses/by/3.0`)], via Wikimedia Commons.

1.4 Tokamaks

In a *tokamak**, the poloidal magnetic field component is generated by a toroidal current driven through the plasma itself via transformer action. A current is ramped up through a central solenoid located in the middle of the device, which acts as the primary winding of the transformer. This generates an increasing magnetic flux through the solenoid and in turn drives the toroidal current in the plasma, which acts as the secondary winding. A schematic diagram of a tokamak's magnetic field coil arrangement and resulting magnetic field is shown in Figure 1.5. It is noted however that the current through the solenoid cannot be increased indefinitely, and therefore tokamaks are inherently pulsed devices.

1.4.1 Plasma Heating

Despite the confining presence of magnetic fields, collisions and so called *anomalous transport* from turbulence ensure that ionised particles and energy will inevitably diffuse outwards towards the walls of the tokamak vessel. Furthermore, energy is also lost through a number of radiative processes. The electrons constantly emit Bremsstrahlung radiation through their collisions with ions and synchrotron radiation as a result of their gyration about magnetic field lines, whilst impurities (heavy, non-hydrogen-like particles originating from the vessel walls or purposefully seeded from outside the device) and neutral deuterium and tritium atoms emit line radiation.

A constant source of heat is thus required to sustain the plasma temperature. This can be provided in part by the Ohmic heating that occurs as a convenient side effect of driving the toroidal plasma current. However, the resistivity of the plasma reduces as the temperature

*The term tokamak originates from the acronym of the Russian phrase 'тороидальная камера с магнитными катушками', which is phonetically pronounced as 'toroidal'naya kamera s magnitnymi katushkami' and translates as 'toroidal chamber with magnetic coils'

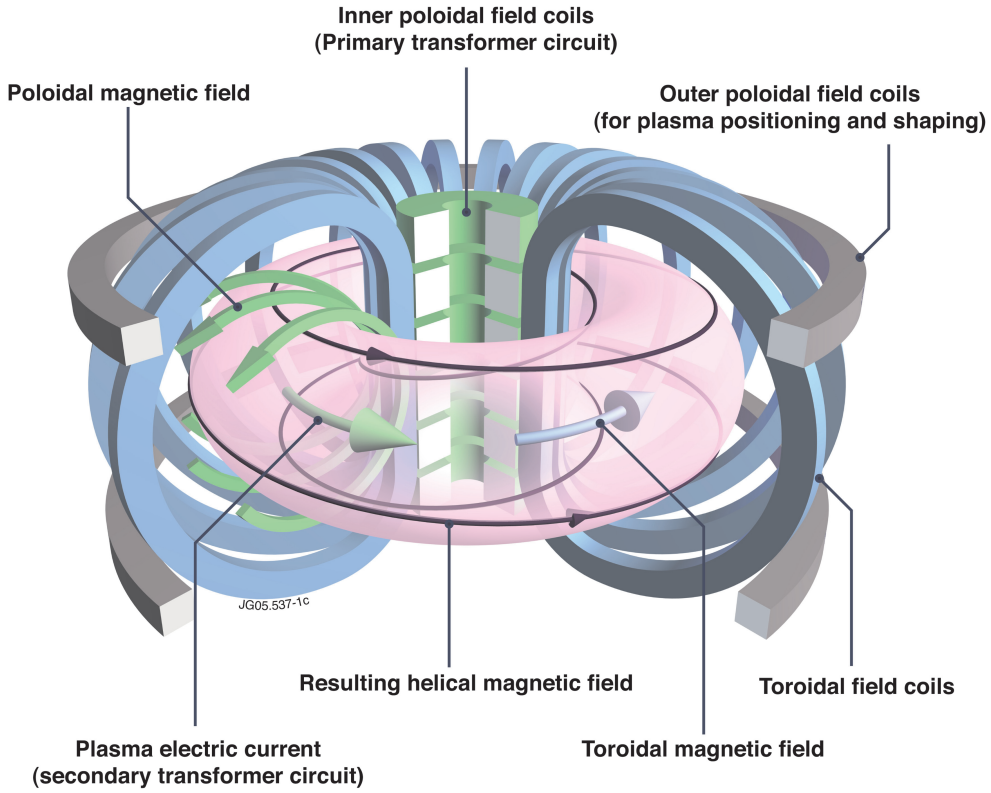

Figure 1.5: Schematic diagram of the arrangement of magnetic coils and the resulting magnetic field in a tokamak. Image courtesy of Eurofusion.

increases and this means that there is a limit to the temperature that can be achieved through this effect alone. Other heating mechanisms are therefore needed to reach the temperatures required for fusion. One method uses microwaves at the resonant frequency of the electron's or ion's gyro-motion to excite the particles and hence heat the plasma (such microwaves are also used to drive a toroidal current in the device to extend the duration of a pulse). Further heating can also be achieved by firing a beam of neutral deuterium atoms at high velocities into the plasma. Through collisions, the neutral deuterium particles rapidly become ionised themselves and transfer their energy to the rest of the plasma.

Provided that sufficiently high temperatures and densities are reached, a final source of heating originates from the fusion reactions themselves. Due to conservation of momentum, the 17.6 MeV of energy released from a D-T reaction is split such that the resultant He^4 ion (or alpha particle) receives 3.5 MeV whilst the neutron receives 14.1 MeV. Neutrons are not confined by magnetic fields, and so will leave the plasma with minimal further interaction. The alpha particles on the other hand are confined, and their 3.5 MeV of energy heats up the plasma through collisions. It is noted that the exit of the 14.1 MeV neutrons is convenient, as in a future power plant they will collide and heat up blankets surrounding the vessel. These blankets will contain lithium so the neutral interactions will breed tritium, whilst the energy deposited in the blanket as heat will be utilised to power a steam turbine to ultimately generate electricity.

1.4.2 Power Balance

With the aim of electricity generation in mind, it is essential that a future power plant produces more fusion power, P_{fusion} than the external heating power put into the plasma, P_{heating} (this excludes the alpha particle heating). The ratio between these two quantities,

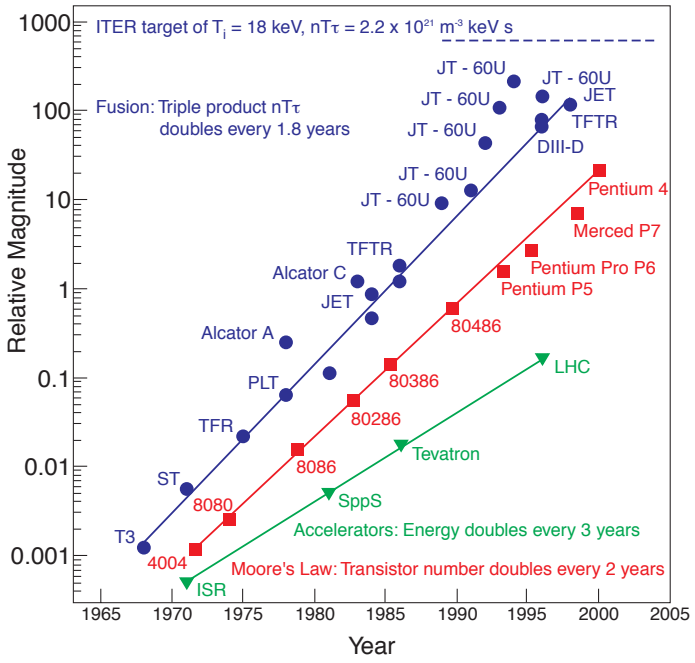

Figure 1.6: Relative progress in fusion research (measured using the fusion triple product), compared against particle accelerators (measured using particle energy) and computer processors (measured using transistor count). Image courtesy of J B Lister, CRPP Lausanne (`crppwww.epfl.ch`) and M Greenwald, MIT (`www.psfc.mit.edu`).

$Q = P_{\text{fusion}}/P_{\text{heating}}$ corresponds to the fusion energy gain factor. It is noted that this factor does not take into account the efficiency of the heating systems themselves, or indeed the power required to run any of the other auxiliary systems required to run a tokamak, such as the magnetic coils, cooling systems and diagnostics. Nevertheless Q provides a representative measure of the efficiency of the plasma physics aspects of a fusion reactor (the quantity is often referred to as the *physics* Q, as opposed to the *engineering* Q), with $Q = 1$ corresponding to *break even*.

As the fusion power output of the plasma increases, the fraction of the heating provided by the alpha particles also increases until eventually it completely balances all the energy loss mechanisms of the plasma. This means that plasma can maintain its temperature solely through nuclear fusion reactions and the external microwave and neutral beam heating mechanisms can be turned off. The point at which this occurs is called *ignition*, by analogy to combustion, and corresponds to $Q = \infty$.

1.4.3 Progress in Tokamak Research

It is recalled that to allow fusion reactions to occur, the plasma has to be held at a high enough temperature and density for a sufficiently long period of time. Therefore a figure of merit of the performance of a fusion reactor is given by the fusion triple product, $n_i T_i \tau_E$. Here n_i and T_i respectively correspond to the peak values of the number density and the temperature of the ions at the centre of the plasma, whilst τ_E is the energy confinement time, a representative measure of the time scale at which energy is lost from the plasma. It can be shown [18] that to achieve ignition, the triple product must satisfy

$$n_i T_i \tau_E > 5 \times 10^{21} \text{ m}^{-3} \text{ s keV}. \tag{1.3}$$

As shown by Figure 1.6, remarkable advancements have been made in tokamak fusion research over the last five decades, with the world record fusion triple product approximately doubling every 1.8 years. The rate of progress exceeds that of particle accelerators and the much vaunted Moore's law for the development of computer processors. This rapid development has in part been driven by a move to larger devices, as this effectively increases the confinement time because the particles and energy have to travel further from the centre of the plasma to become unconfined. However, break even is yet to be attained*, and the current world record fusion energy gain factor is $Q \approx 0.7$. This was achieved in 1997 on the Joint European Torus (JET) [21] in Culham, Oxfordshire and corresponded to 16MW of fusion power being produced, also a world record [22].

1.4.4 ITER and DEMO

ITER [23, 24] (Latin for 'the way'†) is the next generation tokamak fusion reactor that is currently being constructed in Cadarache in the south of France. It will be the largest tokamak built to date, with a major radius of 6.2 m and a plasma volume of 840 m^3 (for comparison, the current largest tokamak, JET, has a major radius of 2.98 m and a plasma volume of 100 m^3). The project is the result of a vast international collaboration involving China, the European Union, India, Japan, South Korea, Russia and the United States. It is estimated that its construction will cost in excess of $14 billion USD, and it is expected to become operational in 2025, with D-T experiments beginning at a later date [25]. The key aim of the ITER project is to achieve $Q = 10$, corresponding to 500 MW of fusion power, for a pulse length of more than 400 seconds. It is also hoped that it will achieve ignition for an albeit shorter period of time. In addition, the machine will be used to test and develop various auxiliary systems that will be required in a future power plant, such as the tritium breeding blankets and remote handling systems [26].

Assuming ITER to be successful, the next stage in fusion research will be to build a demonstration fusion power plant, called DEMO, although the design, scope and timeline of such a device are yet to be agreed. Indeed, it is not clear whether DEMO will be one single machine, or whether each of the major parties involved in ITER will build their own separate machine. In a report produced by the European Fusion Development Agreement [27], outlining a path to the realisation of fusion energy, it was suggested that DEMO may be built and operational by 2050. However this is quite optimistic considering funding would likely have to be secured before ITER achieves its scientific objectives.

As shall become apparent in the following section, interactions between the edge of the plasma and materials surfaces of the device are a key issue for future devices such as ITER and DEMO.

1.5 The Scrape-Off Layer

As previously discussed, collisions and anomalous transport from turbulence ensure that ionised particles will inevitably diffuse outwards towards the walls of the tokamak vessel, despite the

*Conditions have been reached in a solely deuterium plasma in the JT-60 tokamak [19] in Japan that would equate to a $Q = 1.2$ in a deuterium-tritium plasma [20].

†ITER was originally an acronym of International Thermonuclear Experimental Reactor, but this was dropped because it was felt that the word 'thermonuclear' has negative connotations which may reduce public support for the project.

confining presence of magnetic fields. The interactions between the plasma and the vessel walls result in the erosion of the surface, whose particles (non hydrogen ions from the wall materials such as carbon, beryllium or tungsten) can then be transported into the core of the plasma, where they radiate energy strongly. This can reduce the temperature of the plasma, and hence the performance of the tokamak. Evidently it is desirable to reduce the plasma-surface interactions as much as possible.

1.5.1 Limiters

One such method of reducing plasma surface interaction is to add a protruding structure to the wall, called a *limiter*, to produce a *limited plasma*. The schematic poloidal cross section in Figure 1.7 illustrates the distinct regions of plasma created by using a configuration in which a limiter is extruded in the toroidal direction. The dashed concentric circles represent the magnetic flux surfaces, on which the helical magnetic field lines lie. In the core plasma region, the magnetic field lines are termed *closed*, because they do not come into contact with the limiter and close back upon themselves. Further radially out from the core plasma, there is a region in which the magnetic field lines do come into contact with the limiter, and so they are described as *open*.

The particle's motion parallel to the magnetic field is generally collision-less and as such, particles have very fast parallel velocities of the order of the sound speed along magnetic field lines. In contrast, their motion perpendicular to the magnetic field relies on collisions and diffusive action, and is typically many orders of magnitude slower than the parallel velocity. Therefore, once a particle diffuses across the last closed flux surface, it will hit the limiter before it reaches the outer wall. Thus, a thin layer of plasma surrounds the core called the Scrape-Off Layer (SOL) and a rarefied and weakly ionised gas exists further out. This allows the plasma-surface interaction to be predominantly localised at the limiter, rather than the entire surface of the vessel, and results in a cleaner plasma, with fewer impurities (non hydrogen-like ions) from the wall transported to the core. The plasma in the SOL is typically very turbulent due to the presence of steep gradients and a variety of instabilities. Ultimately the width of the SOL is determined by the relative magnitudes of plasma transport perpendicular and parallel to the magnetic field within this turbulence. It is noted that Figure 1.7 shows a toroidal limiter, but a poloidal limiter (consisting of a ring in the poloidal plane) would produce an equivalent effect.

1.5.2 Divertors

Although the use of limiters does improve the performance of tokamaks to an extent, impurities from the limiter-plasma interaction are still sufficient to have a significantly adverse effect. This is because limiters are generally located relatively near to the core of the plasma, and so impurities can still easily diffuse inwards. A more sophisticated configuration is therefore used in advanced tokamaks to produce a *diverted plasma*, in which the plasma surface interaction is located further way from the core of the plasma, in a *divertor* region. Figure 1.8 illustrates how a such a diverted plasma is formed. It is recalled that the plasma carries a toroidal current, which is used to generate the poloidal magnetic field. By passing a second current in the same direction as the plasma current through a coil beneath the core plasma, a null or X-point is formed in the poloidal magnetic field between the two currents. The SOL then extends below and away from the core plasma, where it is directed onto the remote target

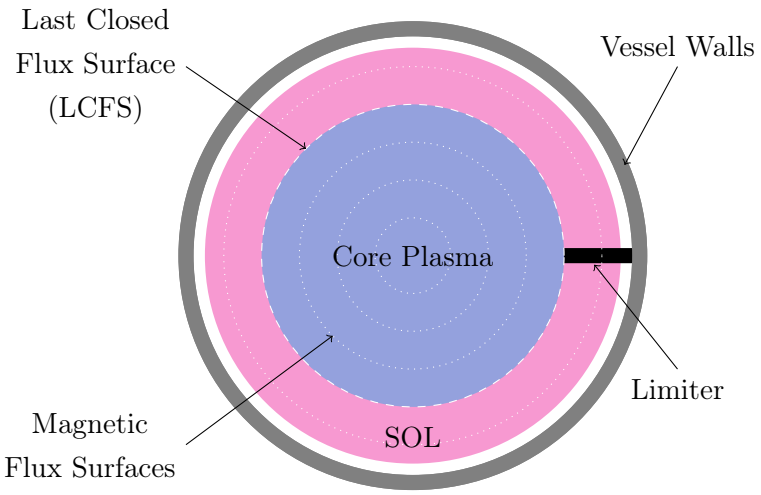

Figure 1.7: Schematic poloidal cross section of a toroidally limited tokamak plasma.

plates. The magnetic flux surface passing through the X-point is termed the *separatrix*, whilst the volume directly below the X-point is referred to as the *private flux region*. In addition, a *double null* configuration can be produced by passing an additional current above the core plasma to produce a second X-point and hence a divertor region at the top of the plasma.

A divertor results in a substantially cleaner core plasma that is relatively free of impurities. Furthermore a lower heating power threshold is required in a diverted configuration (compared to a solely limited tokamak) to achieve a distinct regime of operation in which the confinement becomes significantly enhanced as strongly sheared flows develop in the edge of the core which suppress turbulence in the region [28]. Typically the energy confinement time, τ_E, is increased by a factor or two or larger in this *High confinement mode*, or *H-mode*, compared to the alternative *Low confinement mode* or *L-mode* [29, 30]. This facilitates higher densities and temperatures to be reached in the core of the plasma and hence allows more fusion power to be produced. It is therefore planned that ITER will be operated by default in H-mode to achieve its fusion targets.

1.5.3 SOL Operating Regimes

An important parameter in SOL physics is the SOL electron collisionality,

$$\nu^* = \frac{\ell_\parallel}{\lambda_e}, \tag{1.4}$$

which is defined as the ratio between the parallel length scale of the SOL (typically the mid-plane to target connection length), $\ell_\parallel$, and the electron mean free path, λ_e. This parameter provides an estimate of the number of collisions an electron will experience as it travels from the outboard mid-plane to the divertor or limiter targets. It has a strong effect on the behaviour of the SOL, and three broad operating regimes exist depending on its value [31, 32].

Sheath-Limited Regime

At low collisionality values ($\nu^* < 10$) the SOL is described as being in the *sheath-limited regime*. Heat conduction is very efficient parallel to the magnetic field lines and so the average temperature and density profiles are roughly uniform all along the SOL from target to target.

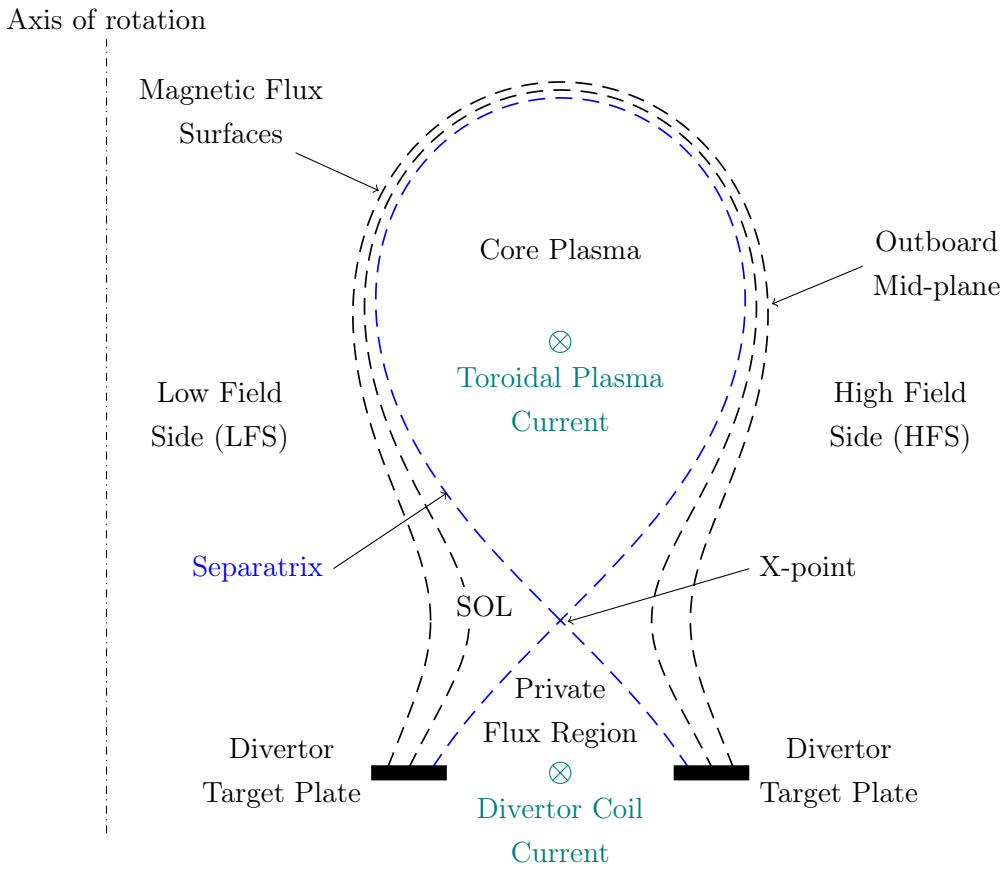

Figure 1.8: Schematic poloidal cross section of a diverted tokamak plasma.

Conduction-Limited Regime

At intermediate collisionality values ($10 < \nu^* < 85$) the SOL lies in the *conduction-limited regime*. The collisionality is sufficient to reduce heat conduction and so temperature gradients form along the SOL, such that the plasma temperature at the target is lower than that further upstream. Once the temperature at the target drops below ~ 10 eV, a positive feedback effect occurs, in that losses from charge exchange processes drastically increase, which acts to reduce the temperature at the target further. This reduction in temperature from the mid-plane to the target is compensated by an increase in the density, so that the pressure remains approximately constant along field lines.

Detached Regime

At high collisionality values ($\nu^* > 85$), the SOL enters a *detached regime* [33]. Here, the collisionality of the SOL is large enough that the plasma temperature at the target drops below ~ 5 eV. At such temperatures volume recombination becomes strong and a cloud of neutrals forms in front of the target surfaces, forming a protective shield from the plasma. Unlike the other operating regimes, the plasma pressure is not constant along field lines, as both the plasma temperature and density decrease near to the target. This phenomenon is referred to as *detachment*.

1.5.4 The Heat Exhaust Problem

Although a divertor configuration improves the performance of the core plasma by allowing access to H-mode, it also introduces a new problem in that the thin width of the SOL

corresponds to extremely high heat and particle fluxes along the magnetic field lines and thus onto the divertor surfaces. The parallel heat flux onto the divertor is an area of particular concern for future reactors such as ITER and DEMO because as the fusion power of a device increases, the power deposited into the SOL also increases, leading to higher parallel heat fluxes in the SOL. This is exacerbated because the SOL heat flux width, λ_q, appears to be invariant to the major radius of the machine and decreases as the toroidal magnetic field increases [34]. Therefore as these future machines become larger and possess stronger magnetic fields to produce more fusion power, λ_q is expected to decrease, which will increase the parallel heat fluxes even further. For reference, present day machines have a λ_q between 1 and 10 mm and steady state parallel heat fluxes at the outboard mid-plane (see Figure 1.8) can reach 500 MWm^{-2}, while pessimistic estimates for these quantities in ITER are $\lambda_q \approx$ 1mm and $\sim$1 GWm^{-2} [34, 35]. In addition to this SOL loading, the divertor region will also be subject to a high energy neutron flux from fusion reactions in the core.

The current heat flux engineering limits on actively cooled structures are approximately 10 MWm^{-2} perpendicular to the surface in steady state or up to 20 MWm^{-2} during transient events [36]. Divertor damage is unacceptable for ITER and future power plants because the radioactivity within such machines will prevent human access for maintenance, and also simply because replacing a divertor will prove to be very expensive. Furthermore future power plants will need to be continuously operational for as long as possible to be economically viable. Therefore strategies must be employed to reduce the parallel heat flux before it reaches the divertor surfaces to prevent them from melting. In current devices, the divertor heat fluxes are lowered by increasing the surface area of the divertor targets onto which the heat is deposited. This is accomplished by expanding the magnetic flux in the region of the divertor targets and inclining the divertor surfaces to be at a small angle to the impinging magnetic field. Such schemes will also be employed in ITER, but will be insufficient on their own to reduce divertor heat loading to within the engineering limits.

One means to further protect the divertor is to force the SOL to be in the detached regime by increasing ν^*. Since ν^* is proportional to the SOL density, this can be achieved in practice by raising the line-averaged density of the plasma through increased fuelling levels. In addition, impurities can be seeded into the divertor to enhance radiative cooling and thus lower the plasma temperature at the divertor target plates such that detachment occurs [31]. Essentially, divertor detachment reduces the heat fluxes to the divertor surfaces by forcing the plasma to emit radiation upstream of the target, which deposits the energy over a wider surface area, whilst also reducing the plasma density, temperature and thus the heat load at the target [18]. Unfortunately, when detachment occurs completely, a large amount of neutrals can reach the core and ultimately cause violent plasma disruptions. Therefore the operating scenario for ITER is a *partially detached* plasma regime, which is expected to provide adequate protection for the divertor [36] without endangering the overall stability of the plasma.

However, even a fully detached plasma will be insufficient to handle the divertor heat loads anticipated for DEMO and future power plants, which will be approximately five times larger than in ITER. As concluded in an EFDA report outlining a path to fusion energy, "A reliable solution to the problem of heat exhaust is probably the main challenge towards the realisation of magnetic confinement fusion" [27].

1.5.5 Other SOL Issues

In addition to the heat exhaust problem, high particle fluxes to plasma-facing components are another area of concern for future devices. Due to the presence of a very thin electric field called a *sheath* at the interface between a plasma and a solid surface, ions are accelerated into material surfaces at high velocities. The subsequent cascade of collisions can result in sputtering of the material surface, i.e. the material's atoms are ejected from the surface into the plasma. In the presence of high particle fluxes, significant erosion of the plasma-facing components can occur through this process, whilst the sputtered atoms will act as impurities and degrade the performance of the core. Furthermore, the incoming ions can also become embedded within the material surface, which is an issue because ITER will only be licensed to contain 1 kg of tritium within the vessel for safety reasons [37]. Therefore it is important to prevent a significant proportion of this allowance being taken up by tritium being retained within the plasma-facing components.

High particle fluxes are primarily an issue for the divertor, again due to the thin width of the SOL. However, the SOL's density width, λ_n, is generally wider than its heat flux width, and under certain operating conditions the perpendicular density transport in the SOL can increase to significantly broaden this width [38, 39]. This means that plasma interactions with the main vessel wall (also known as the first wall) and any attached antennae may become a critical issue in future devices. Despite initial concern when such broadening was first discovered [36], this issue is not expected to limit the operational lifetime of ITER, although concerns persist for power plant scale devices such as DEMO.

1.5.6 SOL Filaments

As discussed previously, the width of the SOL in terms of density or heat flux is ultimately determined by the balance between parallel and perpendicular transport in the turbulence of the SOL. A clear understanding of SOL transport is therefore required to make accurate predictions of the fluxes to plasma-facing components in future power plant scale reactor designs.

In recent years, it has become clear that perpendicular transport of particles [40] (and to a lesser extent, heat [41]) in the SOL is dominated by the radial outwards motion of coherent plasma structures that are significantly more dense and hot than their surrounding plasma, with peak fluctuations typically of the order of the background [42]. These structures are aligned to the equilibrium magnetic field, are strongly localised in the drift-plane perpendicular to it and hence are referred to as *filaments* (or *blobs* due to their appearance in the perpendicular plane). Filaments are a universal phenomenon of open field line regions of magnetic confinement devices; aside from tokamaks they have been observed in stellerators, reversed field pinches and linear devices [43–45]. A 3D visualisation of the field-aligned nature of filaments in the Mega Ampere Spherical Tokamak (MAST) is provided by Figure 1.9.

Such filaments are the subject of this thesis, with particular emphasis placed on the mechanism of their propagation, which has been studied theoretically and using three dimensional simulations to further the understanding of SOL transport.

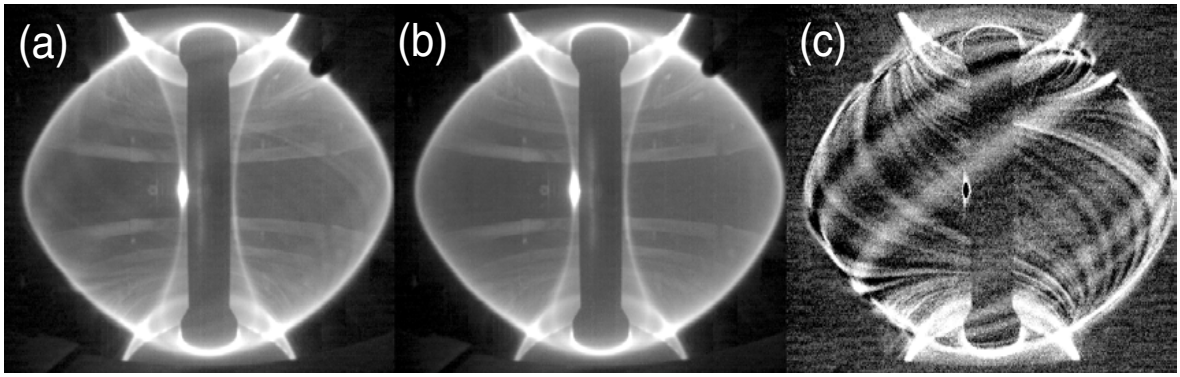

Figure 1.9: Visualisation of filaments in MAST by background subtraction of D_α emission camera data. Shown from left to right are the (a) original D_α emission image, (b) calculated background and (c) image with the background subtracted. Image reproduced with permission from Reference [46].

1.6 Thesis Outline

The remainder of this thesis is organised as follows. Chapter 2 provides a thorough review of experimental measurements of SOL filaments and of existing theoretical and computational studies into their dynamics. Chapter 3 provides a derivation of the 3D simulation model utilised in this work and also of a number of 2D models which are commonly used in the literature. Chapter 4 then documents the numerical implementation of these models in the STORM simulation code, which has been developed to carry out the research presented in the subsequent chapters. However, verifying that a simulation code has been implemented correctly and to the expected order of accuracy is not trivial, whilst validating that the model itself provides an adequate representation of what is observed in experiments is also challenging. Chapter 5 thus presents a number of verification and validation exercises which have been completed to provide confidence in the STORM simulation code and model, with respect to these issues. In particular the code has been tested using the method of manufactured solutions and compared against experimental results from TORPEX device. Chapter 6 then provides a series of 3D STORM simulations using MAST relevant parameters, which provide a comprehensive characterisation of how a filament's initial geometry affects its subsequent motions. In addition, comparisons are also made between 3D and 2D simulations, to clearly demonstrate the different dynamics produced. As shall be established, currents travelling parallel to the magnetic field in the SOL play an important role in filament propagation. The effect of plasma resistivity is therefore examined in Chapter 7. This chapter also investigates the influence of key input parameters to the simulation model, such as the reference temperature, density and magnetic field of the SOL. Lastly, Chapter 8 summarises the main conclusions of this work and identifies opportunities for future research.

Chapter 2

Literature Review

2.1 Introduction

Filaments are coherent plasma structures that are observed in edge turbulence in a wide variety of magnetic confinement devices, including tokamaks, stellarators, reversed field pinches and linear plasma devices [43, 44]. A number of recent works have provided reviews of the experimental evidence for filaments [42] and of the current state of theory and simulation of their dynamics and contribution to SOL transport [47, 48]. The most comprehensive review on the subject however is provided by Reference [45], which presents and compares both aspects. In this thesis, a filament is defined as a coherent plasma structure which satisfies the following three properties:

1. It has a monopole (single-peaked) density distribution with a peak value much higher than the surrounding root mean squared fluctuations of the background plasma (typically greater than 2 times higher).

2. It is aligned parallel to the magnetic field, $\boldsymbol{B}$, and its variation along $\boldsymbol{B}$ is much weaker than in the transverse direction.

3. It has a dominant $\boldsymbol{E} \times \boldsymbol{B}$ velocity component in the direction of a charge polarising force and associated electrostatic potential and vorticity fields, which each can be decomposed to have components which take the form of dipole structures in the direction transverse to its propagation.

This definition is a slightly relaxed version of that given in Reference [45] and is sufficiently broad to encompass the objects that are found in experiments, theory and simulations. A number of alternative terms to *filaments* have also been used to describe such objects in the literature, the most common of which being *blobs*, due to their density structure in the plane perpendicular to the magnetic field. In this work however, the term filament will be used throughout. Accompanying the concept of a filament is that of a *hole*, corresponding to a coherent field-aligned structure with a lower density than its surrounding background plasma. A 3D visualisation of the field-aligned nature of filaments in MAST is provided by Figure 1.9, whilst Figure 2.1 shows the structure of filaments in the plane perpendicular to the magnetic field in NSTX.

In tokamaks and stellarators, filaments are most likely generated in the edge of the core as a result of non-linear saturation of turbulence and dominant edge instabilities [42, 45]. This saturation process is not well understood by the community and as such, a detailed discussion

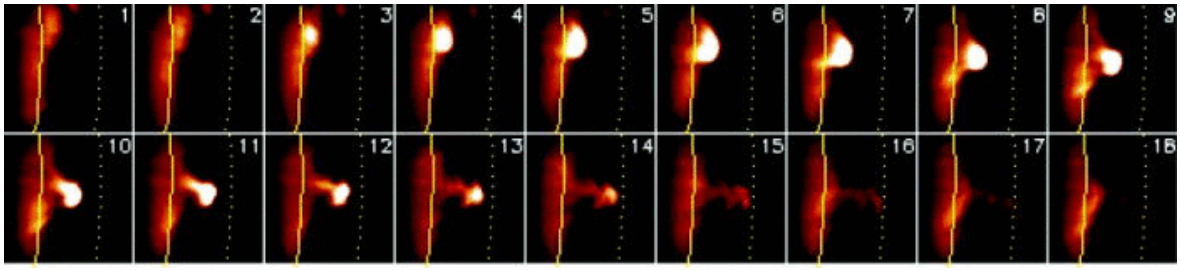

Figure 2.1: Filament creation and propagation in NSTX, visualised through a Gas Puff Imaging (GPI) diagnostic. The images show a 25cm×25cm region near the separatrix (shown using a yellow line) at the outboard mid-plane. The time between frames is 7.5μs. Image reproduced with permission from Reference [54]. Copyright (2011), Elsevier.

of which is beyond the scope of this review. Nevertheless it is pertinent to note that filaments have been found to be produced preferentially at the outboard mid-plane [49, 50], which is consistent with the theoretical prediction that curvature driven modes are most unstable on the Low Field Side (LFS) where the curvature is most unfavourable (the locations of the outboard mid-lane and LFS are shown in Figure 1.8). Once born, filaments are observed to travel across magnetic field lines radially outwards from the core plasma towards the main chamber walls.

Whilst evidence of filaments was present in early plasma confinement experiments in that Langmuir probe measurements of edge turbulence displayed then unexplained intermittent high-amplitude fluctuations, the first clear experimental observations of filaments as coherent structures were made over 30 years ago using high speed cameras [51] and a few years later using 2D probe arrays [52]. However, the important role that filaments play in edge transport was not realised by the magnetic confinement community for some years, and an incorrect consensus held that perpendicular particle transport in the edge could be adequately modelled as a diffusive process, as it is in the core or in many neutral fluid turbulent flows.

A reassessment of this view was prompted just before the turn of the century by the discovery of the "main chamber recycling regime" [38] in Alcator C-Mod, which occurs when the line averaged density is sufficiently high. In this regime, it was demonstrated that the majority of the particles entering the SOL from the core interacted with the main chamber walls, rather the divertor plates, contradicting the classical SOL picture of parallel transport to the divertor dominating over radial transport to the main chamber walls. This challenged the diffusive transport paradigm because an unphysically large effective diffusion coefficient, D_{eff}, far in excess of that given by Bohm diffusion (which characterises large and violent magneto-hydrodynamical events) and that strongly increased with radial position, would be required to overcome the fast parallel transport along field lines. The results also caused significant concern for the ITER design, which had assumed negligible plasma interactions with the main chamber wall. In the same publication, it was suggested that filaments may be the cause of this non-diffusive transport, by hypothesising 'a rapid transport of unstable flux tubes towards the wall surfaces'. This idea was more explicitly expressed in a review article on edge physics issues published in the same year [53], which proposed that 'plasma filaments (strips, with extension along magnetic field less than $q\pi R$) moving in a vacuum are not confined at outer side of torus and quickly propagate all the way to the wall'.

The basic mechanism by which filaments move radially outwards was proposed a few years later by Krasheninnikov [55]. Assuming filaments to be produced in the SOL by turbulent

processes around the Last Closed Flux Surface (LCFS), it was suggested that curvature and ∇B drifts on the LFS of toroidal machines lead to a polarisation of charge and thus the formation of an electric field in the bi-normal direction (perpendicular to both the magnetic field and radial direction), within a filament. Through $\boldsymbol{E} \times \boldsymbol{B}$ motions, this electric field corresponds to the filament possessing a radial velocity that transports it outwards towards the main chamber walls. An analytical solution was derived using a simplified model of a filament density perturbation propagating in vacuum, which showed that filaments could travel as coherent structures with velocities of the order of 100-1000 ms^{-1} (corresponding to a Mach number of ~ 0.02), which was in rough agreement with then available experimental measurements. A follow-up paper [56] extended the model to include the transport of heat and vorticity, and explicitly demonstrated that the motions of relatively isolated filaments travelling in the far SOL could explain experimental measurements of relatively flat SOL density profiles and increasing D_{eff} with radial position [38, 39, 41].

Considering filaments, propelled as proposed by Krasheninnikov, to be the basic entity for cross-field particle transport in the SOL, provides an explanation for a number of other important experimental observations in addition to those outlined above. It naturally incorporates the intermittent and non-Gaussian statistical nature of probe measurements of SOL and edge turbulence, which are described in Section 2.2. It also provides a mechanism for the transport of impurities towards the core, by considering the propagation of holes, whose charge polarisation and hence direction of motion will be in the opposite direction to that of filaments [57]. Furthermore, it offers a possible explanation for the two-scale structure found in many experimental density SOL profiles, where an exponential decay is found near the LCFS, followed by an outer *shoulder* region in which the profiles are relatively flat. Whilst the flat profiles in the far SOL are caused by the motions of intermittent isolated filaments, the turbulence around the LCFS is characterised by smaller amplitude fluctuations with respect to the effective background plasma, which may be the origin of the exponential decay as the region can be more closely approximated as a diffusive process. [47].

Prompted by the C-Mod results, an extensive body of experimental and theoretical research has been carried out over the last fifteen years or so to further the understanding of edge turbulence and transport. Probe diagnostics have clarified and characterised the intermittent and filament-like structure of turbulence in the SOL and the dominant role that filaments play in particle transport in the region has been explicitly demonstrated, with measurements indicating that they can account for significant fractions (35-75%) of the perpendicular particle flux in the scrape-off layers of a variety of different machines including DIII-D [40, 58], TEXTOR [59], HL-2A [60] and MAST [61]. In addition the structure and motions of individual filaments have also been measured using 2D probe arrays and high speed cameras (Figures 1.9 and 2.1). Simultaneously, the theory of propagation of isolated filaments has been developed by expanding the original Krasheninnikov model with additional physics. 2D and, more recently, 3D simulations have been used both to verify analytical results and to provide detailed representations of the evolution of filaments using different models. In addition, 2D turbulence simulations that generate filamentary transport have had much success in reproducing the statistical behaviour observed in experiments.

This introduction has focused on the role that filaments play in perpendicular particle transport in the SOL because it is the reason that filaments first became of significant interest to the fusion community, and the evidence for their large contribution is comprehensive. Determining the cross-field SOL particle flux is an important issue, as plasma-material

interactions with main chamber walls and antennae are undesirable in future devices such as ITER. Such interactions may limit the lifetime of devices due to significant erosion of the first wall through sputtering, or because tritium retention by the wall may cause the machine to exceed its tritium inventory limit. However there is also evidence that filaments can transport heat in addition to particles [40, 58, 62–64], and may to some extent advantageously spread the heat load on the divertor, which is another concern for future generation fusion devices. Studies have also indicated that increased convective heat transport near the LCFS may be correlated with the density limit in some tokamaks [41, 65, 66]. The transfer of momentum by filaments can also have important consequences, with theory and simulations suggesting it can affect the edge velocity shear layer and thus core confinement, in that it provides a means by which the edge plasma can spin up without external influence [67, 68].

A final reason why filament studies may be of interest to the community is that the saturated non-linear phase of Edge Localised Modes (ELMS) [69] produces filaments which also travel into the far SOL. Whilst ELM filaments differ from L-mode and inter-ELM H-mode filaments in that they are hotter, more dense, have a larger perpendicular size and can carry significantly more parallel current [70, 71], their structure is similar and they share a common propagation mechanism into the far SOL. Therefore insight into ELMs can be gained from an increased understanding of filamentary dynamics.

The remainder of this chapter seeks to provide an overview of the advances made in the understanding of filament physics over recent years, with particular emphasis on theoretical and computational studies of the propagation of non-ELM filaments, as this is most relevant to the research presented in this thesis. Section 2.2 begins by presenting experimental measurements of filaments to provide a detailed characterisation of their properties and behaviours. Next, Section 2.3 describes in detail the basic mechanism by which filaments propagate, and outlines the progress that has been made in the theory and simulation of filament dynamics. A brief review of the comparisons that have been made between theoretical predictions and experimental measurements is then given in Section 2.4, before Section 2.5 discusses why further filament studies are necessary and summarises the chapter as a whole.

2.2 Experimental Measurements of Filaments

The ubiquitous nature of filaments within edge and SOL turbulence in magnetic confinement devices is illustrated by Tables I and II of Reference [45], which list approximately 100 publications from 40 devices on which explicit measurements of filaments have been made. These references cover key tokamaks such as JET [72–76], D-IIID [40, 58, 62–64, 77], ASDEX-U [78–81], NSTX [54, 82–87], MAST [46, 61, 70, 88–91], TCV [92–96] and C-Mod [49, 97–102], stellarators such as LHD [103–105] and W7-AS [106, 107], reversed field pinches such as RFX [108–111], linear machines such as LAPD [112] and Vineta [113], and basic toroidal devices such as TORPEX [114–124]. This section will review filament measurement techniques and the common properties of filaments observed in these experiments, and will provide a thorough characterisation of their structure and behaviour.

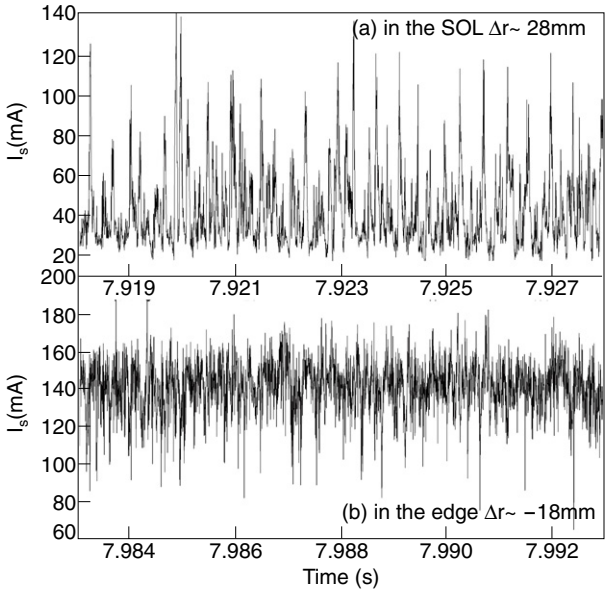

Figure 2.2: Example raw Langmuir probe signals of ion saturation current, I_s, from JET in the SOL (top plot) and edge of the core (bottom plot). Positive fluctuations with respect to the mean predominate in the SOL, whilst negative fluctuations predominate in the edge of the core. Image reproduced with permission from Reference [75]. Copyright (2009), IAEA.

2.2.1 Langmuir Probe Measurements

Statistical Evidence

A Langmuir probe is a diagnostic device that can be used to measure the density, temperature and electrostatic potential of a plasma. It consists of one or more electrodes which are inserted directly into the plasma. In one operating regime, the probes are biased to a sufficiently negative potential, such that all electrons (or negative ions) are repelled from the probe. The current the probe draws from the plasma is then solely due to the ions, and is referred to as the *ion saturation current*, I_s. It can be shown that

$$I_s \propto n_e \sqrt{T_e + T_i}, \tag{2.1}$$

where n_e is the electron number density, T_e is the electron temperature and T_i is the ion temperature. The ion saturation current thus acts as a good proxy for density and temperature fluctuations in the plasma [31]. An example Langmuir probe time trace of I_s from the SOL of JET is shown in the top plot of Figure 2.2. The signal is clearly highly intermittent, with significantly more positive fluctuations (with respect to the mean) than negative. This is caused by the presence of filaments in the SOL, which have a significantly higher density (and in some cases temperature) than the effective background plasma, and so cause positive perturbations to the signal. In the bottom plot of the same figure, an equivalent time trace from the edge of the core in JET (∼18 mm inside the separatrix) is shown, which displays the opposite behaviour in that negative fluctuations dominate, due to the presence of holes moving inwards towards the core.

A greater understanding of the intermittent nature of filaments can be gained by constructing the Probability Distribution Functions (PDFs) of probe signals, as shown in Figure 2.3 for various positions in JET. In the shear layer in which filaments and holes are believed to be born, the PDF is approximately symmetric about the mean, indicating that positive and negative fluctuations were equally present in the signal. Furthermore, the distribution

closely resembles a Gaussian distribution, as shown by the best fit to the data plotted in red. In the near and far SOL however, the PDFs are clearly non-Gaussian, in that they are not symmetric and are skewed towards positive values, reflecting the dominance of positive fluctuations in the SOL, as shown in Figure 2.2. In contrast, the edge PDF is skewed towards negative fluctuations. Furthermore, in the far SOL it can be seen that the positive tail of the distribution does not fall away as quickly as in the near SOL or in the Gaussian-distributed shear layer. This indicates that a greater number of large, extreme fluctuations are present in the SOL, which is consistent with the picture of filaments of high density moving into the far SOL which has a relatively low effective background density.

A quantitative description of the shape of a PDF is given by the third and fourth central moments of the data series, respectively called the skewness, S and kurtosis, K. These quantities are defined as

$$S = \frac{1}{N}\sum_{i=1}^{N}\frac{\left(X_i - \bar{X}\right)^3}{\sigma_X^3}, \tag{2.2}$$

$$K = \frac{1}{N}\sum_{i=1}^{N}\frac{\left(X_i - \bar{X}\right)^4}{\sigma_X^4}, \tag{2.3}$$

where N is the number of points in the time series of the variable X (here the ion saturation current, I_s), $\bar{X}$ is the mean of X and σ_X is its standard deviation. The skewness measures the asymmetry of the PDF with respect to the mean, whilst the kurtosis measures the "tailedness" or flatness of the distribution, with a large K corresponding to one or both of the tails being relatively long and a high prevalence of extreme events. The skewness and kurtosis of each of the PDFs in Figure 2.3 is given in each plot and for reference, a Gaussian distribution has $S = 0$ and $K = 3$. Positively skewed probe signal PDFs with a large kurtosis compared to a Gaussian distribution (>3) appear to be a universal feature or SOL turbulence, as they have been found in a wide range variety of magnetic confinement devices, including tokamaks, stellarators and linear devices [43, 44, 125]. This commonality is displayed in Figure 2.4, which plots the PDFs of probe signals from the SOLs of MAST, Tore Supra and C-Mod tokamaks, as well as from the PISCES linear device.

A number of works have also been dedicated to further characterising the statistical behaviour of turbulence in the SOL. A Gamma distribution was found to effectively parametrise the density perturbations in the SOL of TCV during L-mode [92]. However, since a Gamma distribution does not allow for negative values of skewness, a subsequent work instead found the Beta distribution to produce a good fit for TORPEX probe data [116]. In both of these references however, the same approximate parabolic relationship was found between S and K,

$$K \approx 1.5S^2 + 3. \tag{2.4}$$

Similar parabolic relationships were also observed across a number of tokamaks operating in both L-mode and H-mode, as well as reversed field pinches [126], with the fitted quadratic coefficient remaining close to, but slightly different from 1.5 for each machine and operating regime. However as discussed in Reference [127], the existence of such a parabolic relationship can be expected for many systems and is not likely to provide relevant information on the underlying filament dynamics.

Conditionally Averaged Measurements

Insight can be gained into the density structure of individual filaments by conditionally averaging Langmuir probe density signals. This involves selecting perturbations greater than

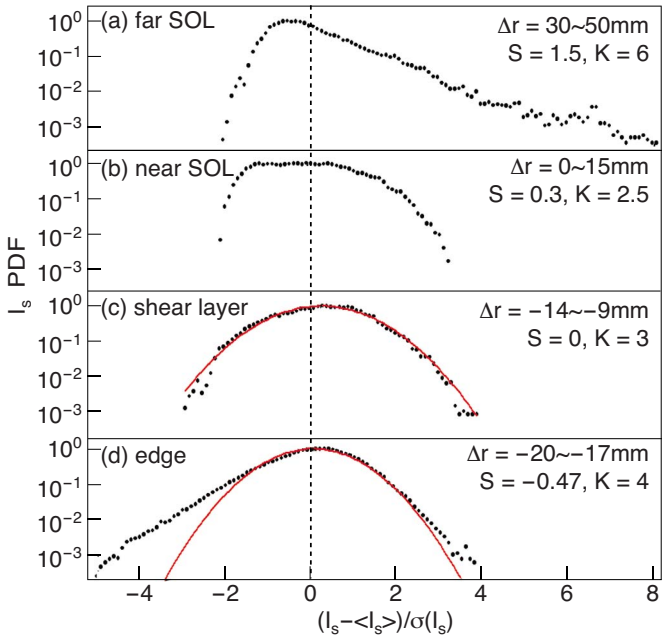

Figure 2.3: Probability Distribution Functions (PDFs) of ion saturation current signals, I_s, from JET measured in (a) the far SOL, (b) the near SOL, (c) the shear layer and (d) the edge of the core. The distance from the LCFS, Δr, is labelled on each plot, alongside the Skewness (S) and Kurtosis (K). Image reproduced from Reference [76] with the permission of AIP Publishing.

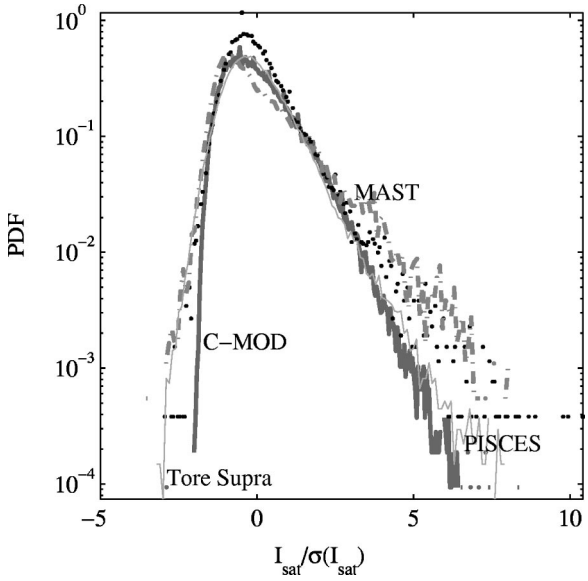

Figure 2.4: Probability Distribution Functions (PDFs) of ion saturation current signals, I_s, from MAST, Tore Supra, C-Mod and PISCES. The ion saturation current is normalised to its standard deviation and the integral of each PDF is equal to 1. Image reproduced from Reference [44], with the permission of AIP Publishing.

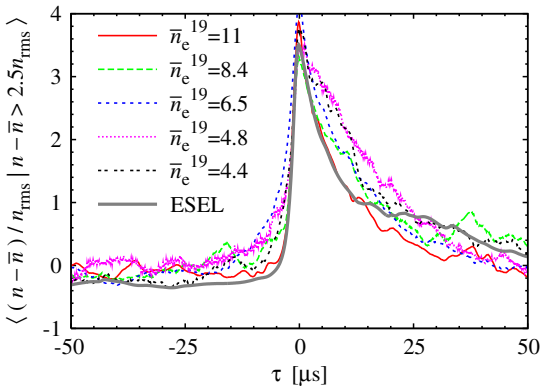

Figure 2.5: Conditional averages of filament density pulse shapes in time at the wall radius in TCV, for different line averaged densities $\bar{n}_e$, which are given in 10^{19} m^{-3}. An amplitude threshold of $n - \bar{n} > 2.5 n_{\mathrm{rms}}$ was been applied to select fluctuations for the averages, where $\bar{n}$ and n_{rms} are respectively the mean and root mean squared values of the density signal at the wall. An equivalent data series from the 2D simulation code ESEL is also shown for comparison. Image reproduced with permission from Reference [94]. Copyright (2009), IAEA.

a certain threshold, synchronising the peaks of the perturbation time traces to a common time and ensemble averaging. This process removes much of the noise from the raw data, and results in an average filament pulse shape in time. Example filament density pulse shapes from TCV obtained using such a technique are shown in Figure 2.5. The pulse shape, which displays a steep rise followed by a more gentle decay, is typical of filament perturbations in most machines. In MAST however, more symmetric conditional averages are observed, possibly due to greater collisional dissipation [128].

Equivalent conditional averages can also be used to yield information on the radial velocity of filaments, by assessing the filament's local poloidal electric field from the floating potentials of two nearby probe heads and calculating the radial velocity as $\boldsymbol{v}_r = \boldsymbol{E}_{\mathrm{pol}} \times \boldsymbol{B}/B^2$ (here the poloidal direction is assumed to be approximately normal to both the magnetic field and the radial direction). This measurement technique relies on the assumption that electron temperature fluctuations do not significantly alter the filament's motion and that the probes themselves do not have a perturbing effect. Combined with probe density measurements, the radial velocities obtained in this way have been used to estimate that filaments can account for around 50% of the radial particle flux in the SOLs of a number of different machines [40, 58–61].

An alternative conditional averaging technique to obtain filament profiles and velocities uses one probe in ion saturation current mode in a fixed position to detect the presence of a filament and then measures the signal on another probe for varying delay times after the detection by the first probe. If the second probe can be moved, 1D or 2D profiles perpendicular to the magnetic field of filament quantities can be mapped out versus time through appropriate cross-averages. Example density and floating potential profiles of propagating filaments and holes obtained through this procedure are shown in 2.6. The filaments and holes can be seen to have a broadly monopolar density structure, whilst their potential structures are dipolar, which through $\boldsymbol{E} \times \boldsymbol{B}$ motions correspond to a pair of counter-rotating vortices. These features are typical of SOL filaments and holes and have been observed in multiple machines including DIII-D [58], TEXTOR [59], JET [75], C-Mod [99], and TORPEX [123].

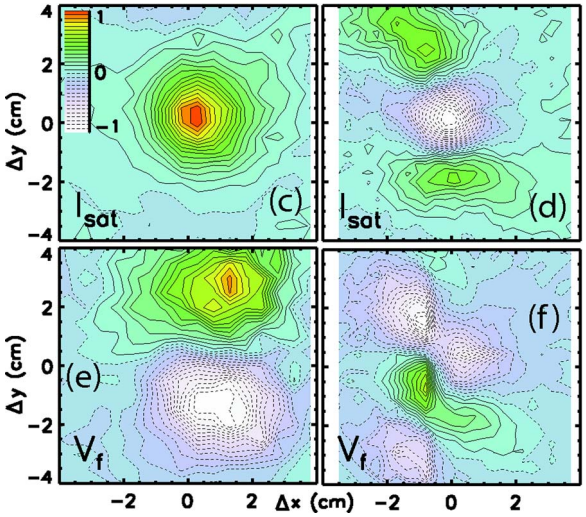

Figure 2.6: 2D cross-conditional average profiles in the perpendicular plane of the ion saturation current, I_s, and floating potential, V_f, associated with filaments (left column) and holes (right column) in LAPD. All cross-conditional averages are normalised to the maximum of the absolute value of the average and the colour bar in (c) applies to all plots. Image reproduced from Reference [112], with the permission of AIP Publishing.

2D Probe Arrays

A limitation of averaged measurements is that they assume that filaments reliably take similar trajectories in space and time. By using a 2D array of probes, instantaneous filament profile measurements have been taken on devices such as TORPEX [115, 122–124] and VTF [129]. Example measurements from the latter device are shown in Figure 2.7, and the mushroomed density shape is significant because this is predicted by theory and simulations. However, such 2D probe arrays can only be used in relatively simple plasma devices, as the probes are typically suspended by thin wire frames to minimise the perturbing effect the diagnostic has on the plasma. In more fusion-relevant plasma devices, these frames would be destroyed by the high heat and particle fluxes, and moreover, less space is available for edge diagnostics.

2.2.2 Optical Imaging

Filament profiles and velocities can be obtained in tokamaks and stellarators by recording the light emission (typically Lithium, Helium, or D_α wavelengths) associated with filaments as they interact with any neutrals using fast optical cameras. These measurements inherently provide instantaneous 2D profile representations, but it can be difficult to interpret the light intensities in terms of relevant quantities such as density or temperature, as the emissivity is a complex function of local plasma conditions, whose measurements from other diagnostics will have large uncertainties.

Optical imaging of filaments can be achieved either passively by relying on the naturally occurring background neutrals in the SOL, or by Gas Puff Imaging (GPI) in which a localised puff of neutral gas is injected into a specific area to enhance light emission. Passive imaging yields information about the global structure of filaments along field lines and has been used in MAST [46, 70, 88, 89, 130, 131] and NSTX [87]. In particular, the MAST imaging results used a novel background subtraction technique, as shown in Figure 1.9, and demonstrated that filaments exist both in L-mode and inter-ELM H-mode [46, 88]. On the other hand

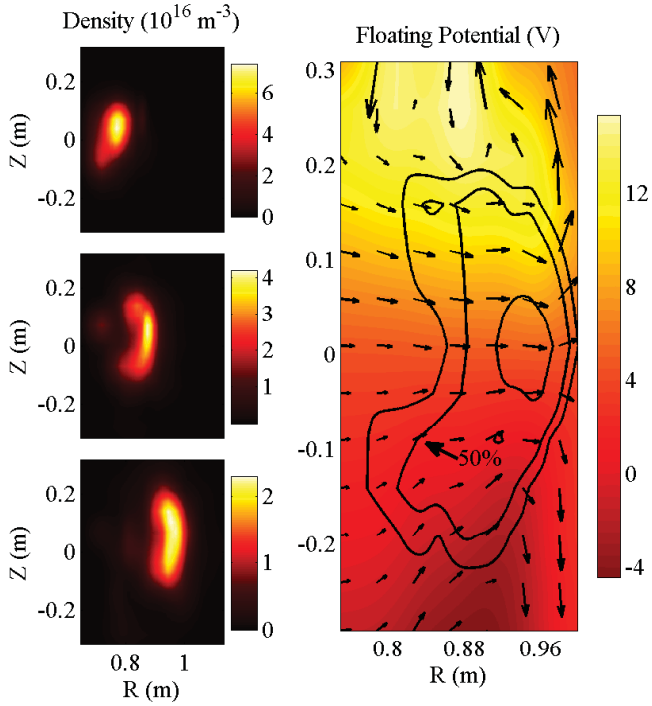

Figure 2.7: Instantaneous density and floating potential measurements of a filament propagating in the basic toroidal device VTF, from a 2D probe array. In the floating potential plot, the corresponding $\boldsymbol{E} \times \boldsymbol{B}$ velocity is overlaid using arrows. Image reproduced with permission from Reference [129]. Copyright (2008) by the American Physical Society.

GPI can give highly resolved images of a filament's perpendicular structure and motions, and such measurements have been taken on NSTX [54, 82–84, 86, 87] and C-Mod [49, 83, 97, 99, 101, 102]. Example GPI imaging of the propagation of a filament in NSTX is shown in Figure 2.1. One of the most important conclusions from optical imaging measurements is that they have confirmed that filaments are highly aligned to the magnetic field [46, 82, 88, 99]. Furthermore, they have shown that whilst filaments at the mid-plane are broadly circular in shape perpendicular to the magnetic field, in the divertor region of tokamaks they are much more elongated and stretched due to the magnetic shear and flux expansion present around the X-point [87, 101, 130], as predicted by Reference [132].

2.2.3 Characterisation of Filaments

To provide a characterisation of SOL filaments, it is useful to differentiate between L-mode filaments, inter-ELM H-mode filaments and ELM filaments, as whilst they all have much in common, they each have distinguishing behaviours and properties.

A key feature of all types of filaments in tokamaks is that they generally have a higher ion temperature, T_i, than electron temperature, T_e [133–135]. This property is largely true of the SOL in general because the conduction of heat to the targets is far greater for electrons [31], although it is noted that the difference between T_e and T_i becomes less pronounced at high collisionalities. This is of particular importance because, as will be discussed later, the majority of theoretical non-ELM filament models unjustifiably assume cold ions for simplicity.

As mentioned previously, ELM filaments exhibit significant differences from L-mode and inter-ELM H-mode filaments. They typically have a larger perpendicular size, can carry greater parallel currents to the target, and are significantly hotter and more dense [70, 71]. Non-ELM filaments thus have a much lower plasma beta ($\beta = n_e T_e/(B^2/2\mu_0)$, where μ_0 is the magnetic

Table 2.1: Key filament parameters across different tokamaks.

Machine	Perpendicular Size (cm)	Density fluctuation, $\delta n/n_{bg}$	Radial Velocity (km s^{-1})	Lifetime (μs)	References
MAST	0.5-10	0.1-4	0.5-2.0	40-60	[89, 137]
NSTX	3-5	n/a	0.2-1.4	60-70	[84, 85]
ASDEX-U	0.2-10	n/a	0.1-3.5	n/a	[81]
C-Mod	0.65-1.5	n/a	0.15-1.5	1-50	[97, 99, 100, 102]
DIII-D	0.5-3.9	0.05 - 1	0.33-2.6	15-20	[58, 77]
JET	0.5-2	0.3-1.5	0.2-1.5	20-130	[74, 75]
TORPEX	1.3-2.5	0.6-0.85	0.2-1.85	n/a	[120, 124]

permeability in a classical vacuum) than ELM filaments and it is typically low enough for electro-static models to be justified. Electro-magnetic effects should be maintained for ELM models however.

Comparing L-mode and inter-ELM H-mode filaments, it is well established that the latter are less frequent (consistent with the suppression of edge turbulence in H-mode). A study in MAST found that inter-ELM H-mode filaments tend to have a lower density than L-mode filaments, but that L-mode filaments tend to have shorter lifetimes than both inter-ELM H-mode and ELM filaments. Similar radial velocities were found for L-mode and H-mode filaments and crucially, neither type were observed to accelerate in the radial direction, unlike ELM filaments [46].

Table 2.1 provides a comparison of the perpendicular size, density fluctuation amplitude ($\delta n/n_{bg}$), radial velocity and lifetime of non-ELM filaments in different tokamaks as measured via different diagnostics. These parameters are of particular interest because they each have an influence on the resultant radial particle flux associated with filaments, and, as discussed later, they are relevant parameters from a theoretical perspective. The majority of the data in the table were originally compiled in Reference [136], and have been supplemented with additional measurements here. Whilst there is clearly some variation in these measurements, they do show that filaments across a variety of machines and operating conditions have a perpendicular size of 0.5-10 centimetres (around 1-100 ion Larmor radii), have fluctuation amplitudes of the order of or greater than the effective background density, exist for tens of μs and travel in the radial direction at velocities of up to a few kilometres per second or around 1 to 10% of the sound speed, c_s. In particular, larger fluctuation amplitudes are found in the far SOL compared to the near SOL, as the effective background density is lower further away from the core.

2.3 Theory and Simulation

2.3.1 Propagation Mechanism

The fundamental mechanism by which filaments propagate can be understood by examining the effect of a net species-summed force per unit volume, $\boldsymbol{F}$, on a filament density perturbation that is broadly circular in the perpendicular plane. The $\boldsymbol{F} \times \boldsymbol{B}$ fluid drifts cause electrons and ions to travel in opposite directions in the perpendicular plane. A current density thus flows

perpendicular to the magnetic field, given (in SI units) by

$$\boldsymbol{j}_F = \frac{\boldsymbol{F} \times \hat{\boldsymbol{b}}}{B}, \tag{2.5}$$

where $B = |\boldsymbol{B}|$ and $\hat{\boldsymbol{b}} = \boldsymbol{B}/B$. Examples of forces which can lead to such perpendicular currents include the pressure force, which produces the diamagnetic current density,

$$\boldsymbol{j}_{\text{dia}} = \frac{\hat{\boldsymbol{b}} \times \nabla p}{B}, \tag{2.6}$$

and the 'fictitious' inertial force, which yields the ion polarisation current density,

$$\boldsymbol{j}_{\text{pol}} = \frac{d}{dt}\left(\frac{n_e m_i}{B^2}\nabla_\perp \varphi\right). \tag{2.7}$$

Here p is the plasma pressure, m_i is the ion mass, φ is the electrostatic potential, and d/dt is the total derivative of the ions given by

$$\frac{d}{dt} = \frac{\partial}{\partial t} + \boldsymbol{v}_i \cdot \nabla, \tag{2.8}$$

where $\boldsymbol{v}_i$ is the ion velocity. A detailed derivation of $\boldsymbol{j}_{\text{dia}}$ and $\boldsymbol{j}_{\text{pol}}$ is provided in Chapter 3. For explanatory purposes, in the following discussion $\boldsymbol{j}_F$ will be used to represent all perpendicular currents except for $\boldsymbol{j}_{\text{pol}}$. The total current density can thus be written as $\boldsymbol{j} = \boldsymbol{j}_{\text{pol}} + \boldsymbol{j}_F + \hat{\boldsymbol{b}} j_\parallel$, where $j_\parallel$ is the magnitude of the parallel current density, $\boldsymbol{j}_\parallel$. Consideration of current continuity, $\nabla \cdot \boldsymbol{j} = 0$, then yields

$$\nabla_\perp \cdot \frac{d}{dt}\left(\frac{n_e m_i}{B^2}\nabla_\perp \varphi\right) = \nabla_\parallel j_\parallel + \nabla_\perp \cdot \left(\frac{\boldsymbol{F} \times \hat{\boldsymbol{b}}}{B}\right). \tag{2.9}$$

Therefore it can be seen that if $\boldsymbol{j}_F$ is compressible (meaning that the currents do not all close back on themselves, i.e. $\nabla \cdot \boldsymbol{j}_F \neq 0$), then some combination of polarisation currents in the perpendicular plane and parallel currents that close elsewhere along the field line must flow to ensure current continuity. The polarisation currents forced in this way lead to the filament perturbation developing a broadly dipolar electrostatic potential field, which through $\boldsymbol{E} \times \boldsymbol{B}$ motions correspond to a pair of counter-rotating vortices that propel the filament across field lines in the direction perpendicular to the alignment of the potential poles.

In tokamaks and other toroidal machines, the dominant effective force that drives the filament motion is in fact that which arises from pressure gradients (which filaments possess by definition) because magnetic curvature and ∇B effects mean that $\boldsymbol{j}_{\text{dia}}$ is compressible. However other effects can also cause filaments to propagate, such as divertor plate tilt [138], parallel shear of the $\boldsymbol{E} \times \boldsymbol{B}$ velocity [139, 140] and perpendicular temperature gradients at the plasma sheath [139–141]. In linear machines, the drive can be provided by a "neutral wind" frictional force [142], or through the centrifugal force if the plasma column is spinning on its axis [47].

Whilst it was Krashennikov who first proposed this mechanism for filamentary motion [55], the process shares many similarities with the dynamics of plasma clouds formed after the ablation of injected fuel pellets into confinement devices [143]. Furthermore, it also has much in common with the Rosenbluth-Longmire description of the interchange instability [144]. It is for this reason that in much of the literature on filament theory, the force which drives the polarisation is written in the form $\boldsymbol{F} = nm_i\boldsymbol{g}$ where $\boldsymbol{g}$ is an effective single particle gravitational acceleration.

Specifically, it is common to simplify realistic geometries by approximating them as a simplified local slab geometry with a uniform magnetic field, $\boldsymbol{B} = B\hat{\boldsymbol{z}}$. In such a geometry the magnetic curvature and ∇B effects of a toroidal device disappear, but can be reintroduced by using a $\boldsymbol{g}$ acting in the effective radial direction, with magnitude $g = 2c_s^2/R$, where $c_s = \sqrt{T_e/m_i}$, T_e is the electron temperature and R is the major radius of the machine. If x and y are respectively the local radial and poloidal coordinates, Equation (2.9) can then be simplified as

$$\frac{m_i}{B^2}\nabla_\perp \cdot \left(n_e \frac{d}{dt}\nabla_\perp \varphi\right) = \nabla_\parallel j_\parallel - \frac{eg}{\Omega_i}\frac{\partial n_e}{\partial y}, \tag{2.10}$$

where $\Omega_i = eB/m_i$ is the ion gyro-frequency and e is the elementary charge. A negligible ion temperature, $T_i \ll T_e$ and an isothermal electron temperature* have been assumed to derive this equation, which are common assumptions used in filament theory and simulation. It is noted the cold ion assumption in particular is poorly justified at low collisionality in the SOL, as $T_i \gtrsim T_e$ is predicted theoretically [31] and has been observed in experiments [133–135]. The influence of this assumption is addressed later in Section 2.3.5. With alternative definitions of g, Equation (2.10) can also describe all the mechanisms listed above except for the parallel shear of the $\boldsymbol{E} \times \boldsymbol{B}$ velocity and perpendicular temperature gradients at the plasma sheath, whose dynamics are different and more complicated [47]. Nevertheless, since magnetic geometry effects dominate the drive of filaments in toroidal devices, the subsequent review of filament theory and simulation will focus on this equation, and the final term on its Right Hand Side (RHS) will be referred to as the diamagnetic current drive.

For computational and analytical ease, the majority of filament models used to date make the *Boussinesq approximation* to simplify the ion polarisation current term in Equation (2.10) as

$$\frac{m_i}{B^2}\nabla_\perp \cdot \left(n_e \frac{d}{dt}\nabla_\perp \varphi\right) \approx \frac{n_e m_i}{B^2}\frac{d}{dt}\nabla_\perp^2 \varphi. \tag{2.11}$$

This approximation is commonly used in studies of neutral fluid turbulence† and is valid for small density perturbations, $\delta n_e/n_e \ll 1$. Since order unity filament perturbations are commonplace in the SOL, its use is not rigorously justified, but qualitative insight into filament dynamics can still be gained from models employing it. Having made the above approximation, Equation (2.10) can then be written as an evolution equation for the vorticity $\omega = (\nabla_\perp^2 \varphi)/B$:

$$\frac{m_i}{B}\left(\frac{\partial}{\partial t} + \boldsymbol{v}_E \cdot \nabla + v_{\parallel i}\nabla_\parallel\right)\frac{\nabla_\perp^2 \varphi}{B} = \frac{1}{n_e}\nabla_\parallel j_\parallel - \frac{eg}{n_e \Omega_i}\frac{\partial n_e}{\partial y}. \tag{2.12}$$

In obtaining the above equation, the gyro-viscous cancellation [145–148] has been employed to write the ion velocity as $\boldsymbol{v}_i = \boldsymbol{v}_E + \boldsymbol{v}_{\parallel i}$ where $\boldsymbol{v}_E$ is the $\boldsymbol{E} \times \boldsymbol{B}$ drift velocity and $\boldsymbol{v}_{\parallel i} = \hat{\boldsymbol{b}} v_{\parallel i}$ is the parallel ion velocity. A detailed discussion of the influence of the Boussinesq simplification on the detailed motions of filaments is also provided later in Section 2.3.5, but in general, solving the full polarisation current term leads to more coherent filament propagation and hence greater net cross-field transport [149–152].

Thus far, the discussion has neglected the influence of parallel currents, but they play an important role because if the diamagnetic currents in a perpendicular drift-plane drive parallel

*The isothermal electron temperature assumption is not essential and can be easily relaxed by replacing n_e with $n_e T_e$ in the last term on the RHS of Equation (2.10).

†In neutral fluid dynamics, the Boussinesq approximation removes the acoustic wave from the system. In a magnetised plasma (such as the SOL), the analogous ion acoustic wave can only propagate parallel to the magnetic field. Such waves are not removed from the system by making the Boussinesq approximation given by Equation (2.11), because it only neglects perpendicular density gradients.

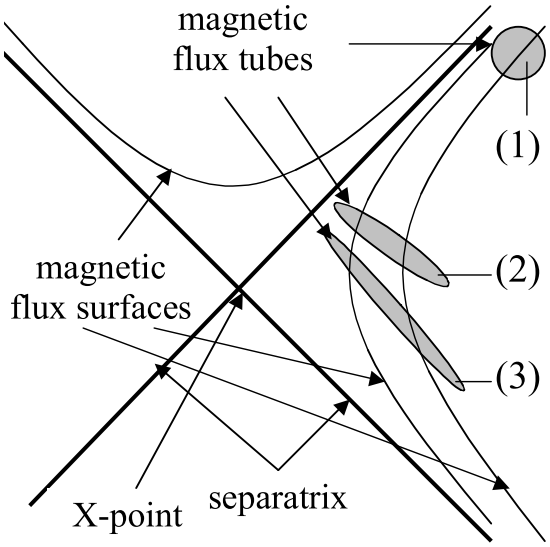

Figure 2.8: Schematic diagram of the elliptical distortion of a flux tube that is circular at the mid-plane as it passes close to an X-point. The numbered points each correspond to different toroidal locations. Image reproduced from Reference [153], with permission from the Japan Society of Plasma Science and Nuclear Fusion Research (JSPF).

currents, this necessarily means that the polarisation currents in the same drift-plane will be smaller in magnitude than if no parallel currents are driven at all. The parallel currents therefore can be said to *limit* the polarisation currents and thus the motion of the filament. However, parallel currents can only flow if they form a closed circuit in the perpendicular direction somewhere else along the field line. As proposed in Krasheninnikov's original paper, one way in which this can happen is for parallel currents to travel all the way through the plasma and sheath to close through the target material itself.

Alternatively, parallel currents can close in a different drift-plane to that from which they originated if polarisation currents can flow more easily in a different drift-plane due to the magnetic geometry of the SOL. One location in particular where this can happen is in the vicinity of an X-point, where the local magnetic shear is large and the poloidal magnetic field becomes small. This means that a magnetic flux tube (and hence filament) that is circular in the perpendicular plane at the outboard mid-plane (as filaments are observed to be in experiments), is a thin elliptical *fan* at the X-point [132], as shown in Figure 2.8. Intuitively, polarisation currents can flow more easily across the thin fan in this region than across the circular cross-section further upstream. Furthermore, if filaments are sufficiently stretched at the X-point, then the electrostatic potential field in the region will vary on a scale much smaller than the ion Larmor radius. In this case, the ions' $\boldsymbol{E} \times \boldsymbol{B}$ velocity will not be equal to that of the electrons and this provides an additional current path in the region [47, 153, 154].

The exact balance of currents that close the compressible diamagnetic currents can be modelled to be dependent on the effective *resistivity-length** of each current path. This is illustrated by Figure 2.9, which shows a schematic circuit diagram of the currents paths discussed. The repeated sub-circuits between the top and bottom rails represent the continuum of individual drift-planes. Only half the SOL is shown, with the left sub-circuit representing the drift-plane located midway between the two targets. In each drift-plane, the compressible

*The relationship between a resistivity-length and a current density is analogous to that between a resistance and a current. A full discussion of this quantity is discussed in Section 7.1.

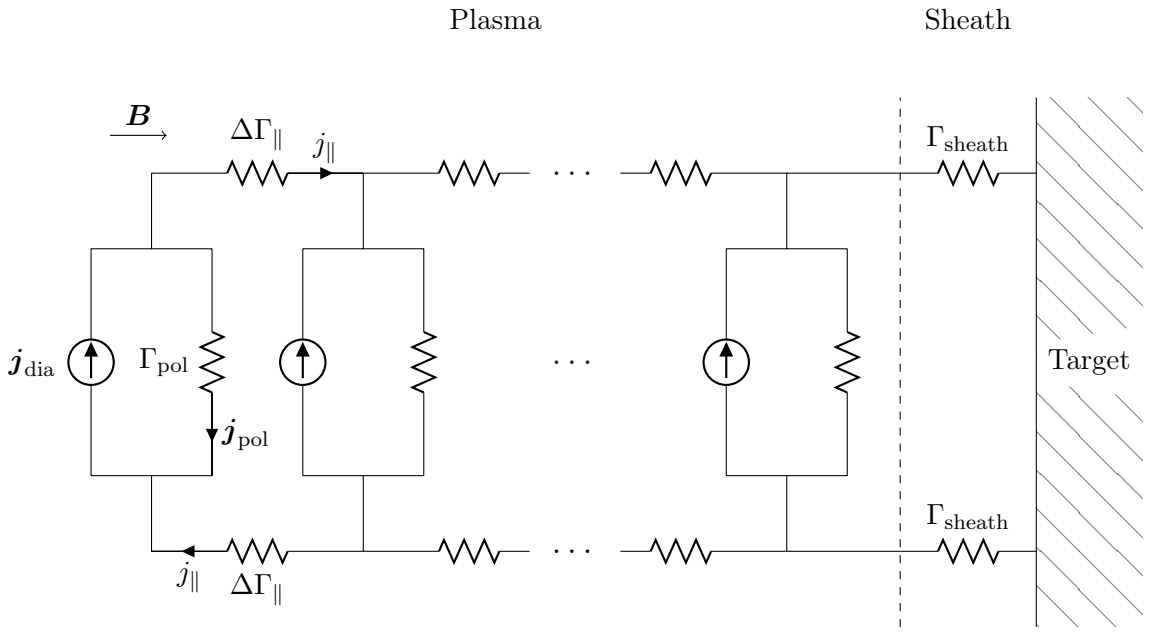

Figure 2.9: Schematic diagram of the current paths in a filament. The pressure driven diamagnetic current density $\boldsymbol{j}_{\text{dia}}$ is represented as an ideal current source, whilst each of the other current paths have an effective resistivity-length.

component of the diamagnetic current is modelled as an ideal current source, whilst the polarisation current density has an associated resistivity-length Γ_{pol}*. It is noted that the possible $\boldsymbol{E}\times\boldsymbol{B}$ current path near to an X-point region is not shown. Along the top and bottom rails parallel currents can flow between different drift-planes, with the resistivity length of the path between two adjacent drift-planes separated by a distance Δz given by $\Delta\Gamma_{\parallel}$. Finally, the resistivity-length of the path that currents take through the sheath to the target is denoted Γ_{sheath}.

In addition to the evolution of currents, a description of density evolution is also required to construct a model of filamentary motions. Such a description is provided by the electron density continuity equation:

$$\frac{\partial n_e}{\partial t} + \nabla\cdot(n_e\boldsymbol{v}_e) = s_n. \tag{2.13}$$

Here s_n is a source or sink of particles through ionisation or recombination processes, whilst $\boldsymbol{v}_e$ is the electron velocity which can be written as the sum of its parallel component $\boldsymbol{v}_{\parallel e} = \hat{\boldsymbol{b}}v_{\parallel e}$, and its $\boldsymbol{E}\times\boldsymbol{B}$ and diamagnetic drift velocities, $\boldsymbol{v}_E$ and $\boldsymbol{v}_D$:

$$\boldsymbol{v}_e = \boldsymbol{v}_E + \boldsymbol{v}_D + \boldsymbol{v}_{\parallel e}. \tag{2.14}$$

The electron polarisation drift velocity has been neglected through drift ordering considerations [145]. Equations (2.9) and (2.13) thus form the starting basis for any fluid model of filamentary motion. In principle, to make the continuity equation compatible with Equation (2.10) and specifically its slab geometry, the influence of magnetic curvature and gradients in a toroidal device on the divergences of particle fluxes must be included appropriately by writing

$$\nabla\cdot(n_e\boldsymbol{v}_E) = \boldsymbol{v}_E\cdot\nabla n_e - \frac{gn_e}{c_s^2 B}\frac{\partial\varphi}{\partial y} \tag{2.15}$$

*It is remarked that Γ_{pol} best represents the advective component $(\boldsymbol{v}_i\cdot\nabla)$ of the polarisation current, whilst the $\partial/\partial t$ component may be better represented by a capacitor. Nevertheless, the advective component is found to be dominant in all but the earliest stages of filament simulations.

and

$$\nabla \cdot (n_e \boldsymbol{v}_D) = \frac{g}{\Omega_i} \frac{\partial n_e}{\partial y}, \tag{2.16}$$

so that Equation (2.13) becomes

$$\left(\frac{\partial}{\partial t} + \boldsymbol{v}_E \cdot \nabla \right) n_e = -\nabla_\parallel \left(n_e v_{\parallel e} \right) + \frac{g n_e}{c_s^2 B} \frac{\partial \varphi}{\partial y} - \frac{g}{\Omega_i} \frac{\partial n_e}{\partial y} + s_n. \tag{2.17}$$

The terms proportional to g in Equation (2.17) are often neglected in many theoretical and numerical filament studies, because they are not as important to the filament's motion as the diamagnetic drive in Equation (2.10). However such simplifications do mean that particle conservation is no longer ensured.

Before discussing individual models in detail, it is helpful to highlight that theoretical and computational studies of filaments tend to consider either isolated filaments or fully saturated turbulence containing many filaments. Turbulence studies naturally provide a more complete description of filamentary transport, in that they can provide insight into the formation of filaments, as well as their subsequent propagation. However, they are computationally more expensive and offer no direct control is over the size or amplitude of filaments generated. Isolated filament studies on the other hand are considered to be more valid for filaments in the far SOL than in the near SOL because interactions between multiple filaments are likely to be more common nearer to the separatrix. Nevertheless, such simulations are valuable as they allow for the propagation mechanism to be studied in detail. Filaments are typically initialised as Gaussian density perturbations in the perpendicular plane onto a uniform background, meaning that the effect of filament geometry (size, amplitude) can be directly investigated. For these reasons, and because the research presented in the later chapters of this thesis uses such an approach, the review of existing 2D and 3D models in Sections 2.3.3 and 2.3.4 will focus on isolated filament studies, although some relevant turbulence studies will also be discussed.

2.3.2 Filament Formation

In contrast to the process of filament propagation, little understanding has been gained analytically into filament generation [45]. Nevertheless analysis of turbulence simulations suggests that the formation of filaments is strongly influenced by the presence of mean sheared flows that satisfy $\partial v_y / \partial r \neq 0$, where r is the minor radial direction, and v_y is the velocity in the direction perpendicular to both $\boldsymbol{B}$ and r (hereafter referred to as the bi-normal direction) [45]. In the absence of such shear flows, coherent plasma structures form which are extended in the radial direction, rather than being blob-like or a mono-polar in the perpendicular plane [155]. When relatively weak sheared flows are present, these streamers are broken apart into filament structures that are more blob-like in the perpendicular plane [156]. However, a sufficiently strong sheared flow will suppress turbulence locally by reducing the linear growth rate of instabilities and tearing apart coherent structures, so that fewer filaments are formed [157]. These simulation based results are consistent with experimental observations of strong shear flows in the edge region of H-mode plasma [28] and the corresponding suppression of turbulence and number of filaments in the SOL compared to L-mode plasmas, which have weaker shear flows.

2.3.3 2D Models

The fact that filaments are observed to be field-aligned means that to some extent the filaments motions are similar between different drift-planes. Therefore insight can be gained using 2D

models that represent dynamics in the perpendicular plane, which are easier to analyse and to solve numerically. To construct such models however, closures are required to describe the parallel dynamics of the system. This sub-section will discuss common closures used in the literature, with particular focus on how they affect the dynamics of filaments.

Sheath Dissipation Closure

One of the most commonly used 2D closures is obtained by assuming that negligible gradients of density and potential exist along the parallel direction of a filament. Then by using the standard sheath boundary conditions for the parallel ion and electron velocities [31, 158],

$$v_{\parallel i}\big|_{z=\pm\ell_\parallel} = \pm c_s, \tag{2.18a}$$

$$v_{\parallel e}\big|_{z=\pm\ell_\parallel} = \pm c_s \exp\left(-\frac{e\varphi}{T_e}\right), \tag{2.18b}$$

Equations (2.17) and (2.12) can be integrated and averaged along the field line between the targets located at $z = \pm\ell_\parallel$ to produce

$$\left(\frac{\partial}{\partial t} + \boldsymbol{v}_E \cdot \nabla\right) n_e = -\frac{n_e}{\ell_\parallel} \exp\left(-\frac{e\varphi}{T_e}\right) + \frac{g n_e}{c_s^2 B}\frac{\partial \varphi}{\partial y} - \frac{g}{\Omega_i}\frac{\partial n_e}{\partial y}, \tag{2.19}$$

$$\frac{m_i}{B}\left(\frac{\partial}{\partial t} + \boldsymbol{v}_E \cdot \nabla\right)\frac{\nabla_\perp^2 \varphi}{B} = \frac{e c_s}{\ell_\parallel}\left(1 - \exp\left(-\frac{e\varphi}{T_e}\right)\right) - \frac{eg}{n_e \Omega_i}\frac{\partial n_e}{\partial y}. \tag{2.20}$$

It is noted that Equation (2.18b) has been derived by defining the potential of the target wall to be

$$\varphi_w = -\frac{T_e}{e}\ln\left[\left(\frac{m_i}{2\pi m_e}\right)^{1/2}\right], \tag{2.21}$$

where m_e is the mass of an electron, and that s_n was neglected in deriving Equation (2.19). The first term on the RHS of Equation (2.20), which arises from the $\nabla_\parallel j_\parallel$ term in Equation (2.12), is of particular importance. It essentially models all parallel currents to close through the target and to only experience resistance when travelling through the sheath. The sheath therefore determines the magnitude of the parallel currents in the system. Such a model for the parallel currents is often described as a *sheath dissipation* closure, as the sheath currents ultimately act to reduce the polarisation currents and hence the radial velocity of the filament, whilst more generally the term can be shown to dissipate the kinetic energy in a system [159]. In many works the term is linearised so that Equation (2.20) becomes

$$\frac{m_i}{B}\left(\frac{\partial}{\partial t} + \boldsymbol{v}_E \cdot \nabla\right)\frac{\nabla_\perp^2 \varphi}{B} = \frac{e c_s}{\ell_\parallel}\left(\frac{e\varphi}{T_e}\right) - \frac{eg}{n \Omega_i}\frac{\partial n_e}{\partial y}. \tag{2.22}$$

The first instance of the sheath dissipation model in the literature was in Krashenninikov's seminal paper [55]. In this work, the entire RHS of Equation (2.19) and Left Hand Side (LHS) of Equation (2.22) were neglected, and the filament was assumed to be in a vacuum. Whilst neglecting the influence of polarisation currents was not strictly self-consistent and in experiments filaments are observed to propagate on a background plasma, these simplifications allowed for an analytical solution in which the filament propagated stably at a velocity in agreement with experimental measurements.

A number of subsequent works have thoroughly investigated the dynamics of isolated filaments under sheath dissipation using analytic theory and simulations [56, 57, 122, 149–151, 159–169]. Importantly, the use of simulations has allowed filament propagation solutions to

be obtained with the effects of polarisation currents and finite plasma backgrounds included. Across these works, it has been demonstrated that the perpendicular length scale of the filament's pressure perturbation, $\delta_\perp$, plays a large role in determining the radial velocity of a filament and the stability of its propagation [57, 160, 161, 166]. Following the scaling arguments in References [122] and [168], it can be shown that for an order unity filament perturbation with respect to the background, the polarisation current and sheath dissipation terms in Equation (2.22) will be approximately the same order when $\delta_\perp \sim \delta_*$. In which case the filament will have a radial velocity, v_r, of the order v_*, where

$$\delta_* = \rho_s \left(\frac{g \ell_\parallel^2}{2 \rho_s c_s^2} \right)^{1/5} \tag{2.23}$$

and

$$v_* = c_s \left(\frac{\rho_s^2 g^3 \ell_\parallel}{c_s^6} \right)^{1/5} . \tag{2.24}$$

Here, $\rho_s = c_s/\Omega_i$ is the combined species Larmor radius, and it is emphasised that these are only order of magnitude estimates. For $\delta_\perp \ll \delta_*$, the polarisation current is dominant in closing the diamagnetic current drive, and the radial velocity of the filament is predicted to scale like $v_r \propto \sqrt{\delta_\perp}$, whilst for $\delta_\perp \gg \delta_*$, the sheath dissipation term dominates and $v_r \propto \delta_\perp^{-2}$ is predicted. In the literature, the $\delta_\perp \ll \delta_*$ case is often described as the *inertial* or *resistive ballooning* regime, whilst the $\delta_\perp \gg \delta_*$ case is referred to as the *sheath current limited* or *sheath connected interchange* regime. These analytical scaling predictions have been confirmed by 2D simulations [167]. Recently, more general scaling estimates which include the effects of filament ellipticity (i.e. the filament having a different size in the local radial and poloidal directions) and filament amplitude with respect to the background have been derived and have again been confirmed through simulations [169].

Simulations have also allowed the extent to which filaments propagate coherently using a sheath dissipation model to be investigated [57, 160–162, 166, 168]. It has been found that at low collisional dissipation, filaments in the inertial regime quickly evolve into *mushroom-like* structures through the Rayleigh-Taylor-like interchange instability, and subsequently develop Kelvin-Helmholtz instabilities, with both stages causing the filament to lose its coherence. In the sheath current limited regime on the other hand, the interchange instability causes the filaments to develop *finger-like* structures and so again the filaments do not retain their monopolar structure. In between these two regimes however, at filament sizes around δ_*, these two effects to some extent cancel out and filaments are observed to propagate relatively coherently. These contrasting behaviours are illustrated in Figure 2.10.

The sheath dissipation closure has also been utilised in simulations in which the electron temperature was evolved in addition to density and vorticity. It was found that hot filaments (i.e. those which have a broadly mono-polar temperature perturbation, in addition to their density perturbation) are found to spin in the perpendicular plane. This occurs because the sheath boundary condition induces the higher temperature filament to float at a greater potential with respect to the wall than the lower temperature surrounding background plasma, which corresponds, through the $\boldsymbol{E} \times \boldsymbol{B}$ velocity, to a rotation of the filament. This spinning was found to increase filaments' coherence and suppress the growth of finger-like structures [165], although it can also lead to rotational instabilities [164]. 2D simulations of saturated SOL turbulence have also used sheath dissipation, where filaments were generated self-consistently [68, 170–176]. Where comparisons have been made, reasonable agreement has been found with

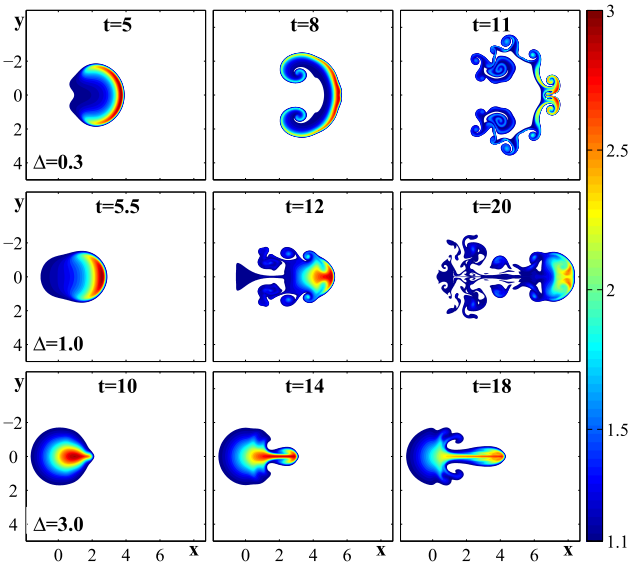

Figure 2.10: Comparison of the dynamics of isolated filaments with different perpendicular sizes, $\delta_\perp$ in 2D sheath dissipation simulations. Here $\Delta = \delta_\perp/\delta_*$, whilst the spatial coordinates and time have been normalised to $\delta_\perp$ and $\sqrt{\delta_\perp/g}$ respectively. Image reproduced from Reference [168], with the permission of AIP Publishing.

experimental measurements of SOL profiles and radial fluxes, as well as PDFs of filament sizes and velocities.

The sheath dissipation closure has two principle limitations. The first comes directly from the assumptions used to derive it; that density and potential are constant along field lines. These assumptions are not generally true for toroidal devices, as experimental measurements indicate that filaments are localised around the outboard mid-plane, meaning that parallel gradients in density may exist [49]. Furthermore, if high electron collisionalities are present in the SOL, this can lead to variations of parameters such as potential along the field line and prevent parallel currents from flowing to the sheath. For example, in a conduction-limited regime, much lower temperatures and higher densities are found in the divertor region than further upstream near the mid-plane, which will mean that a high electron-ion collisionality is present near to the target. The second limitation is that the model does not account for the possibility that diamagnetic currents in one drift-plane can be closed through a combination of parallel currents and polarisation currents in a different drift-plane, for example, in the region of an X-point.

Vorticity Advection Closure

One alternative model, which seeks to address the first limitation of sheath dissipation closure, assumes that the plasma in the SOL has a high enough resistivity to prevent parallel currents from reaching the target, and so neglects these currents instead of parallel gradients. Rather than averaging along the field line, it considers only the drift-plane at the outboard mid-plane, estimating the parallel velocities to be approximately half the sound speed for the majority of the domain (in line with experimental measurements [177]), and the parallel length scale of variation of quantities along the field line to be of order $\ell_\parallel$. This allows the parallel advection terms to be approximated as

$$v_{\parallel i}\nabla_\parallel \approx v_{\parallel e}\nabla_\parallel \approx \frac{c_s}{2\ell_\parallel}. \tag{2.25}$$

Under these assumptions, Equations (2.17) and (2.12) reduce to

$$\left(\frac{\partial}{\partial t} + \boldsymbol{v}_E \cdot \nabla\right) n_e = -\frac{c_s n_e}{2\ell} + \frac{g n_e}{c_s^2 B}\frac{\partial \varphi}{\partial y} - \frac{g}{\Omega_i}\frac{\partial n_e}{\partial y}, \tag{2.26}$$

$$\frac{m_i}{B}\left(\frac{\partial}{\partial t} + \boldsymbol{v}_E \cdot \nabla\right)\frac{\nabla_\perp^2 \varphi}{B} = -\frac{c_s}{2\ell_\parallel}\frac{\nabla_\perp^2 \varphi}{B} - \frac{eg}{n\Omega_i}\frac{\partial n_e}{\partial y}. \tag{2.27}$$

The first term on the RHS of Equation (2.27) models the parallel advection of vorticity in the system, and so hereafter, the above equations will be described as using the *vorticity advection* closure. This term is approximately smaller than the sheath dissipation closure term by an factor of $\rho_s/\delta_\perp$ (typically $\delta_\perp$ is of the order of $10\rho_s$) [47] and so potential is dissipated much less rapidly in this model. It does however act on all scale lengths of potential equally, whereas the sheath dissipation closure term preferentially damps larger scale lengths [178]. Whilst no explicit study of isolated filaments using this closure has been published, the above equations have been used (alongside an additional equation for the electron temperature evolution) in SOL turbulence simulations using the ESEL (Edge-SOL ELectrostatic) code [93–95, 128, 177–182], and good agreement has been found with experimental profiles, SOL decay lengths, fluxes and turbulence statistics from a variety of machines [93–95, 128, 177]. For example a conditionally averaged density pulse shape from a TCV simulation is plotted alongside experimental results in Figure 2.5. However, the fact that both the sheath dissipation and vorticity advection closures have had success in replicating experimental measurements makes it unclear which is most appropriate. It can be argued that since agreement is found with two different models, the experimental features such as the profiles and fluxes are dependent more on the common features between the two models rather than the different terms that are found in their respective vorticity equations.

X-Point Closure

The effect of parallel currents closing through enhanced cross-field currents in an X-point region rather than at the sheath has been investigated heuristically by considering a Wentzel-Kramers-Brillouin (WKB) limit and approximating

$$\nabla_\parallel j_\parallel \approx \frac{\left(\sigma_\parallel \sigma_\perp\right)^{1/2}}{\ell_\parallel \delta_\perp}\varphi, \tag{2.28}$$

where $\sigma_\parallel = 1/\eta_\parallel$ is the parallel conductivity and $\sigma_\perp$ is the perpendicular conductivity [153, 154]. By estimating the remaining terms in Equation (2.12) similarly to how they were for the sheath dissipation velocity scaling predictions and approximating the $\sigma_\perp$ associated with polarisation currents to be $\sigma_\perp \propto \varphi/\delta_\perp^2$, the velocities of filaments whose diamagnetic currents are ultimately closed in the X point region can be estimated scale like $v_r \sim g^{2/3}/\delta_\perp^{1/3}$ for the polarisation current path [47, 183] and like $v_r \sim g/\delta_\perp$ for the unbalanced electron $\boldsymbol{E} \times \boldsymbol{B}$ current path [47, 153].

Whilst this estimate allows insight into how filament velocities will scale if parallel currents close through the X-point, isolated filament simulations have not been performed using Equation (2.28) as it is an order of magnitude estimate of the term, rather than a rigorous closure (for example, it involves $\delta_\perp$ directly). Furthermore, this estimate gives no information as to under what circumstances parallel currents will transition from closing through the target to closing through the X-point.

Two Region Model

This last issue motivated the development of a two region model [184], which is a pseudo-3D model in that reduced forms of the the density and vorticity equations are evolved in two 2D domains, which each represent the average dynamics along a portion of the field line. These domains correspond to the outboard mid-plane and X-point regions, and parallel currents are allowed to flow between them. The diamagnetic current drive term is included only in the mid-plane region for convenience, with the justification being that this is where the curvature and ∇B effects are strongest (although not by a significant amount). By using the postulated *blob correspondence principle*, which proposes that filament velocity scalings can be obtained from the linear instability growth rates of a system, four different filament propagation regimes were identified. The regimes are dependent on three normalised parameters. The first,

$$\Lambda = \frac{\nu_{ei}\ell_{\parallel}}{\Omega_e \rho_s} = \frac{\nu^*}{\sqrt{m_e/m_i}}, \tag{2.29}$$

is a measure of the SOL electron collisionality, $\nu^* = \ell_{\parallel}/\lambda_e$. In these definitions ν_{ei} is the electron-ion collision frequency, Ω_e is the electron gyro-frequency and λ_e is the electron mean free path. The second parameter,

$$\Theta = \hat{\delta}^{5/2} = \left(\frac{\delta_{\perp}}{\delta_*}\right)^{5/2} \tag{2.30}$$

represents the size of the filament, whilst the final parameter ε_x describes the elliptical distortion of flux tubes between the mid-plane and X-point regions. No distortion corresponds to $\varepsilon_x = 1$ and ε_x goes to zero as the distortion is increased. In these definitions ν_{ei} is the electron-ion collision frequency and Ω_e is the electron gyro-frequency. In addition, the work also expresses the filament velocity scalings in terms of a normalised velocity, $\hat{v} = v_r/v_*$, and normalised filament size, $\hat{\delta} = \delta_{\perp}/\delta_*$. The four regimes are:

i *Sheath Connected Interchange Regime* ($\mathrm{C_s}$)
This regime is the equivalent to the sheath current limited regime discussed for the sheath dissipation model and occurs for large filaments at low collisionality. The diamagnetic current drive at the mid-plane is closed through parallel currents closing at the target, producing velocities scaling like $\hat{v} \propto \hat{\delta}^{-2}$.

ii *Ideal Interchange Regime* ($\mathrm{C_i}$)
At low collisionality and for sufficiently small filaments, the compressible diamagnetic currents at the mid-plane are predominantly closed through enhanced polarisation currents in the X-point region, producing a velocity scaling like $\hat{v} \propto \varepsilon_x \hat{\delta}^{1/2}$.

iii *Resistive X-point Regime* (RX)
In this regime the relatively high collisionality and large filament size are such that the compressible diamagnetic currents are predominantly closed by parallel currents closing through the sheath. The resistivity causes a potential difference to form between the mid-plane and X-point such that the velocity of filaments scales like $\hat{v} \propto \Lambda \hat{\delta}^{-2}$.

iv *Resistive Ballooning Regime* (RB)
This regime corresponds to the inertial regime and occurs at small $\delta_{\perp}$ and at high collisionality. The compressible diamagnetic currents are closed through polarisation currents at the mid-plane region and filament velocities scaling like $\hat{v} \propto \hat{\delta}^{1/2}$ are predicted.

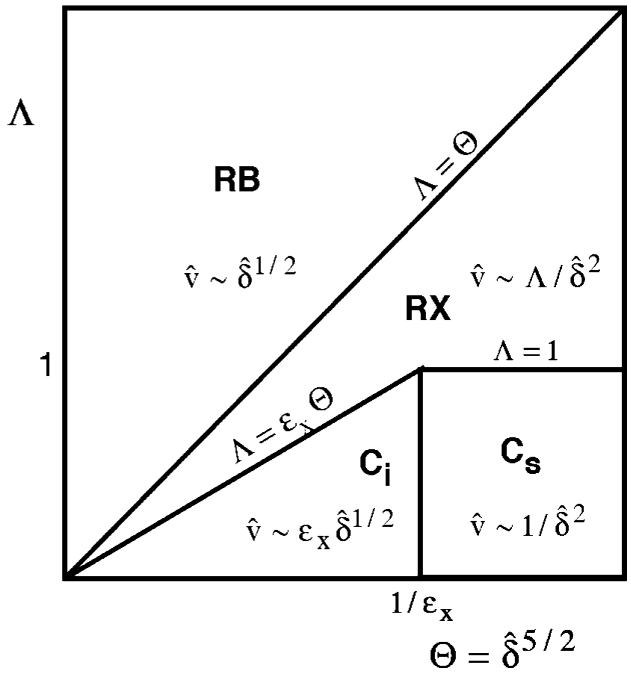

Figure 2.11: Two region model regime diagram in the space of normalised collisionality Λ, and perpendicular scale size, $\Theta = \hat{\delta}^{5/2}$. The dependence of the normalised velocity, $\hat{v}$ on normalised size, $\hat{\delta}$ is given for each regime. Image reproduced from Reference [184], with permission from AIP Publishing.

A diagram illustrating the extent of these regimes in $\Theta - \Lambda$ space is shown in Figure 2.11, in which the transition boundaries between each regime are also given. The key predictions from this model therefore, are that increased collisionality will lead to an increase in filament velocities and hence turbulence transport, whilst increased magnetic field line fanning and shear has the opposite effect. These predictions have been confirmed through simulations of isolated filaments [184] and of saturated turbulence [155] using the two region model equations.

Other Closures

In addition to those described in detail above, a number of alternative parallel closures have been used in the literature to study SOL filaments. A model for filamentary motion in a dusty plasma is derived and simulated in Reference [185], whilst a variation on the sheath dissipation closure is used in [186]. Furthermore, the vorticity equation, Equation (2.12), should in principle have an additional term $+\mu_i \nabla_\perp^4 \varphi$ on its RHS to include the effect of viscosity, where μ_i is the kinematic viscosity of the ion fluid. The influence of this term balancing the compressible diamagnetic currents, in addition to the inclusion of particle diffusion in the density continuity equation has been investigated numerically [159, 187]. A final closure concerns the limit where filaments have a sufficiently high plasma beta such that electromagnetic effects become important. In particular, field line bending can occur and filament dynamics at the mid-plane can become independent of conditions further downstream. This case is relevant for ELM filaments and has also been investigated using the blob correspondence principle [183] and through 2D simulations [149].

2.3.4 3D Models

Advances in computational power and methods over the last decade has meant that 3D simulations of SOL filaments, whilst still expensive compared to 2D, are routinely possible. The original BOUT turbulence code [188] was used to conduct the earliest 3D simulations of filaments [57, 89, 189, 190]. These studies were of saturated turbulence, rather than of isolated structures and included a vast array of effects including full magnetic geometry and electromagnetic terms in addition to the parallel dynamics of ions and electrons. Whilst such a comprehensive description is desirable in the long term, no rigorous interpretation of the underlying dynamics of the filaments was provided as it was difficult to disentangle the various effects. Furthermore, the community now views these simulations with caution because the BOUT code was not rigorously verified and it is suspected that the results may have been under-resolved.

A few years after these works, the first rigorous 3D studies of isolated filaments were conducted in a slab geometry [168, 191, 192] using the newly developed BOUT++ framework [193, 194]. These works essentially solved Equations (2.10) and (2.17) by assuming the parallel ion velocity to be negligible and using collisional Ohm's law to model the parallel current as

$$j_{\parallel} = \sigma_{\parallel}\left(\frac{T_e}{en_e}\nabla_{\parallel}n - \nabla_{\parallel}\varphi\right) \tag{2.31}$$

where $\sigma_{\parallel} = ne^2\nu_{ei}/0.51m_e$ is the parallel conductivity and ν_{ei} is the electron-ion collision frequency.

A simplified local linear analysis of the equations identified that filaments may develop unstable resistive *drift waves*. Such waves are an inherently 3D phenomena and do not exist in 2D filament models because they involve parallel electron dynamics. The physical mechanism of a drift wave can be understood by considering a magnetised plasma with a perpendicular density gradient, which undergoes a small sinusoidal density perturbation, δn, that has structure in the directions perpendicular and parallel to $\boldsymbol{B}$. The perpendicular plane of such a situation is shown in Figure 2.12. Through Equation (2.31) the density perturbation drives electrons to move along the field line to align the electrostatic potential perturbation, $\delta\varphi$, with δn so that a parallel electric field forms to establishes force balance with the parallel pressure gradient. The alignment between n and φ also corresponds to the formation of a perpendicular electric field and thus an $\boldsymbol{E}\times\boldsymbol{B}$ velocity perturbation that is a quarter of a period out of phase with the density perturbation. The perturbations therefore collectively constitute a wave, which propagates perpendicular to ∇n and B. The wave remains stable, so long as the density and $\boldsymbol{E}\times\boldsymbol{B}$ velocity perturbations remain a quarter of a period out of phase. However, if the electrons cannot provide force balance along the field line instantaneously, due to say non-zero resistivity or Landau damping, then a phase shift will develop between the density and $\boldsymbol{E}\times\boldsymbol{B}$ velocity perturbations and the amplitude of the perturbations will grow, i.e. the wave becomes unstable.

Such instabilities were indeed found in the simulations, and led to filaments breaking down into turbulence and losing their coherence much faster than equivalent 2D filaments, as illustrated by Figure 2.13. The inclusion of parallel electron dynamics thus was found to reduce cross-field transport. The linear analysis predicted the maximum growth rate of the instability to scale like $\sim 1/\delta_{\perp}$. In agreement with this, smaller filaments were found to be most unstable in the simulations

In addition, References [168] and [192] investigated the effect of filaments possessing

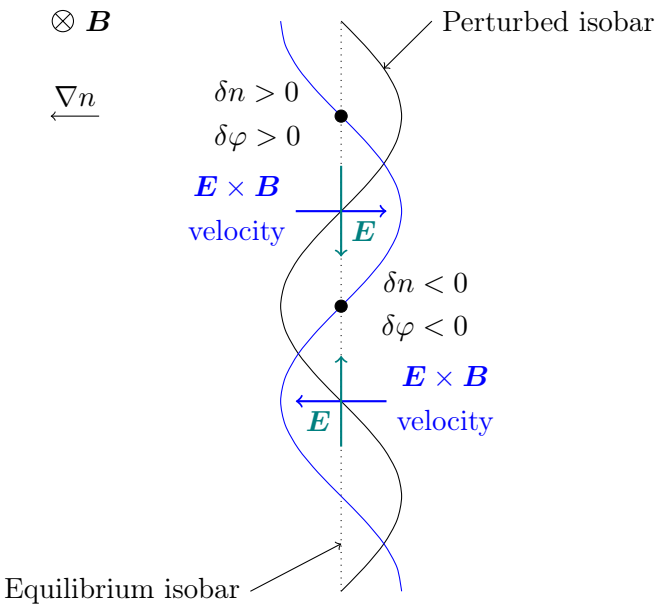

Figure 2.12: Schematic diagram of a drift wave.

macroscopic (i.e with a scale length $\sim \ell_{\parallel}$) parallel density gradients, which may arise in experiments due to sheath losses or because turbulence in the SOL has been observed to be localised about the outboard mid-plane [49]. It was again found that parallel gradients in density drove the potential to also have parallel gradients through Equation (2.31). This alignment of φ and n_e, referred to as a Boltzmann potential response, induced the filaments to spin in the perpendicular plane through $\boldsymbol{E} \times \boldsymbol{B}$ motions. This *Boltzmann spinning* was observed to enhance the coherence of the filament to some extent, in that the onset of drift-waves turbulence was delayed, and fingering effects were reduced in large $\delta_{\perp}$ filaments. It also reduced the radial velocity of the filament slightly and induced the filament to move in the poloidal direction.

Using effectively the same 3D model as in References [168, 191] and [192], filament studies were independently carried out using a realistic MAST SOL flux tube geometry, in which the collisionality of the SOL was varied through the input (isothermal) electron temperature [195]. It was found that at both high and low collisionality, the high magnetic flux expansion and local magnetic shear around the X-point induced filaments to develop parallel density gradients. One mechanism for this across all collisionalities was that the strong shearing of the filament in the divertor region caused the filament's density profile to be dissipated through diffusion more rapidly than further upstream. In addition, at high collisionalities the filaments exhibited strong ballooning motions and hence parallel gradients, because compared to at the mid-plane, the polarisation currents at the X-point could flow more easily, producing a weaker potential dipole and hence slower radial velocity. This latter mechanism was not present at low collisionalities because parallel currents allowed for the mid-plane's diamagnetic currents to be closed through the X-point as well. Unstable resistive drift waves were also found in these simulations, although the filaments were observed to propagate for longer and further before they took effect than in the previously discussed 3D simulations [168, 191, 192]. Boltzmann spinning effects were also reproduced at low collisionality. The filaments dynamics at the mid-plane were found to be independent of the sheath boundary condition regardless of collisionality and thus the high and low collisionality cases can be interpreted as analogous to the resistive ballooning and ideal interchange regimes respectively in the two region model

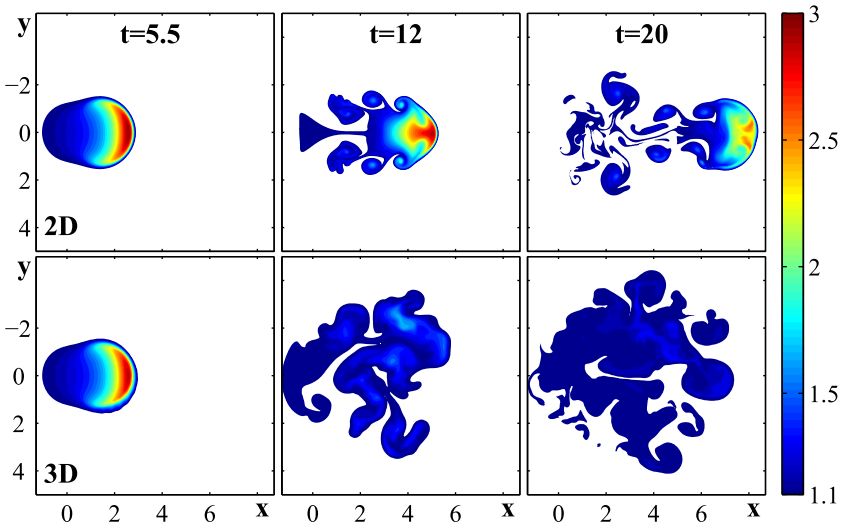

Figure 2.13: Comparison of the density evolution of a filament using 2D and 3D models. Unstable drift-waves can be observed to destroy the coherence of the filament in 3D. The initial perpendicular size of both filaments was $\delta_\perp = \delta_*$, whilst the spatial coordinates and time have been normalised to $\delta_\perp$ and $\sqrt{\delta_\perp/g}$ respectively. Image reproduced with permission from Reference [191]. Copyright (2012) by the American Physical Society.

discussed previously [184]. This classification was further demonstrated in a follow-up paper [196] that used the same model to investigate the dependence of filament velocities at the mid-plane on $\delta_\perp$ and input T_e. The poloidal velocity was found to scale linearly with T_e, whilst the radial velocity was found to increase with both temperature and $\delta_\perp$. These results are also discussed in more detail in Reference [136].

3D simulations of isolated filaments have also been carried out using the GBS (Global Braginskii Solver) code [197], which unlike previous models includes the evolution of the parallel ion velocity and electron temperature, although the influence of T_e was not discussed. Furthermore, in this study all fields were separated into their background and fluctuating components, with only the latter evolved. Filaments were simulated using the magnetic geometry of TORPEX (TORoidal Plasma EXperiment), which is a simple magnetic torus, and the dependence of the filament velocity on its perpendicular size was investigated. The simulations in general found good agreement with the 2D sheath dissipation model in that the predicted inertial and sheath current limited regime velocity scalings were obtained for small and large $\delta_\perp$. Whilst no direct comparison between 2D and 3D simulations was shown, it was commented that faster radial velocities were produced compared to previous 2D works. This was attributed to the fact that the sheath dissipation term in Equation (2.22) overestimates the strength of sheath currents as it does not account for the density drop between the mid-plane and the target that was found to develop in the 3D simulations due to sheath losses. It is noted that the resistive X point and ideal interchange regimes of the two region model are not present in Torpex as it does not have an X-point and because it has a relatively short parallel connection length and low plasma density, respectively. Boltzmann spinning effects were again observed in the presence of density gradients, but the filaments appeared to be stable to drift-waves, possibly due to the presence of additional perpendicular diffusion terms that were included for numerical stability.

A very recent study has also investigated electromagnetic effects using 3D simulations [198]. It was demonstrated that for high beta filaments, the sheath boundary condition has

a reduced influence at the mid-plane due to the reduced Alfvén speed and so faster radial velocities were produced. Furthermore, in the presence of varying diamagnetic drive along the field line (for example peaked at the mid-plane), the high beta filaments were observed to exhibit both ballooning and field line bending. Finally, high beta filaments were found to be more stable to resistive drift-waves.

2.3.5 Limitations

In the majority of models considered so far, cold ions have been assumed and the Boussinesq approximation has been employed. Since typically in experiments $T_i \gtrsim T_e$ [133–135] and filaments have order unity density perturbations, neither of these simplifications are generally justified. A number of works have specifically addressed the influence of these assumptions, to understand the limitations they have on results obtained using them. This subsection will discuss these studies, before addressing more general limitations of fluid based modelling in the SOL. Finally, the limitations of existing 3D models will be discussed to highlight areas for improvements in the field and to motivate some of the results presented in later chapters.

The Boussinesq Approximation

A number of works have conducted 2D simulations using the sheath dissipation model, both with and without the Boussinesq approximation to assess the impact of the ill-justified simplification on the dynamics of isolated filaments [149–151]. Those with a small perpendicular size ($\delta_\perp < \delta_*$) have been found to be more stable when the full polarisation current term is solved, in that mushrooming motions are suppressed so that they remain coherent for longer. This means that net cross-field transport is increased for these filaments. In contrast, for very large filaments ($\delta_\perp \gg \delta_*$) the approximation makes little difference because the polarisation current term is negligibly small. The most stable filament size was found be slightly smaller when the approximation was not made (but still $\sim \delta_*$), as fingering effects were observed to occur at comparatively smaller filament sizes. It has been supposed that this was due to the suppression of mushrooming motions, which are thought to cancel out the finger-like motions to produce coherent filament propagation for sizes around δ_* [149].

It has also been shown that the approximation leads to an incorrect filament velocity scaling with perturbation amplitude [151], and for this reason Reference [169] used the full polarisation current term when investigating the effect of amplitude. Furthermore, it is noted that these conclusions on the influence of the Boussinesq assumption on isolated filaments in a drift fluid model are in agreement with a study into the effect of the corresponding simplification in a 2D gyro-fluid model [152]. Reference [150] also investigated this issue using 3D simulations, and concluded that destruction of the filament structure due to unstable drift-waves meant that the net cross-field transport of filaments was virtually the same regardless of whether the approximation was employed.

More generally, the Boussinesq approximation breaks energy conservation within a model [199, 200] and therefore limits its applicability for turbulence studies.

The Cold Ion Assumption

The effect of hot ions on isolated filaments has been investigated numerically using a 2D isothermal gyro-fluid models [152, 201], because they naturally incorporate Finite Larmor Radius (FLR) effects whilst maintaining a simple form compared to drift-fluid models that

include FLR corrections [152]. It was found that relinquishing the assumption of cold ions caused the poloidal up-down symmetry of the particle density to break, in that a filament would develop a velocity with a non-negligible component in the effective poloidal direction. Furthermore, the FLR effects were found to reduce mixing, stretching and generation of small spatial scales in the density field, resulting in more coherent and stable filament motion. These two effects are illustrated by Figure 2.14 from Reference [201], which compares the density evolution of filaments with $T_i = 0$ (top row) and $T_i = 3T_e$ (bottom row). Both cases undergo mushrooming motions, but in the hot ions case the filament's density is preferentially *swept up* into the lower lobe of the mushroom. The rotation of this lobe in the perpendicular plane causes the density to remain significantly more coherent than in the cold ions case, which mushrooms symmetrically.

The influence of hot ions has also been studied using 2D drift-fluid simulations [131, 186], which corroborated the poloidal symmetry breaking observed in gyro-fluid simulations but found similar levels of coherence and stability with and without hot ions. However, there are mitigating factors in each study which are attributed here to explain this apparent inconsistency with the gyro-fluid simulations. In Reference [186], instabilities were found regardless of whether or not hot ions were included due to the use of a non-standard closure for the parallel current, whilst the relatively high diffusion and viscosity parameters used in Reference [131] acted to suppress the mushrooming motions that would have otherwise occurred in the cold ions case. Since these parameters were MAST relevant, these results indicate that the influence of hot ions on the stability of filaments in MAST may be negligible, though it is noted that their radial velocities were 60-100% faster in the hot ions case due to the enhanced pressure drive. In a different work, also utilising a drift-fluid model, it was shown that evolving the ion temperature (but maintaining an isothermal electron temperature) leads to an elongation of filaments in the poloidal direction and slower radial velocities [202].

Radial filament velocity scaling estimates have also been derived for the case of hot ions using a drift-interchange-Alfvén fluid model [203]. The inclusion of hot ions increases the diamagnetic currents which drive filamentary motion and also provides additional contributions to the polarisation currents, due to the ion diamagnetic drift. Magnetic geometry effects were not included, but collisionality effects were considered, and so the results can be compared directly to the two region model regimes in the reduced case where $\varepsilon_x = 1$ and the ideal interchange regime is not present. Each of the remaining regimes was reproduced for the hot ion case, with identical scalings of the radial velocity with perpendicular size obtained, although the estimated constants for each scaling contained corrections. In addition a new *Ion pressure dominated Resistive Ballooning* regime (iRB) was found for the smallest filaments in which the filament velocity scales like $v_r \sim \delta_\perp^2$. These scalings have been compared against filaments produced within 3D turbulence simulations in Reference [204].

Fluid Models

All of the drift-fluid models discussed have ultimately been derived using a Braginskii collisional treatment [205], which amongst other conditions, requires $\nu^* \gg 1$. However, low values of collisionality ($\nu^* < 10$) are often found in experiments, and under such conditions fluid closures are not strictly justified. In particular, parallel heat transport is a non-local process in non-collisional plasmas because it is dominated by fast electrons and therefore it is poorly described by fluid models. This limitation means that fluid models are unsuitable for the study of ELM filaments, because the high temperatures within these structures generally always ensures

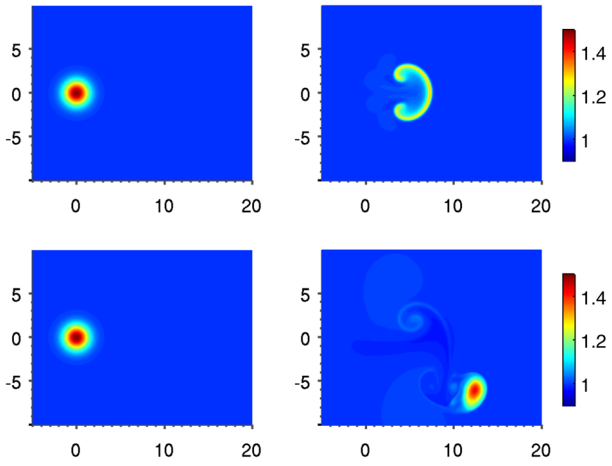

Figure 2.14: Density evolution of isolated filaments from 2D gyro-fluid simulations for $T_i = 0$ (top row) and $T_i = 3T_e$ (bottom row). The left column shows the initial filament profiles at $t = 0$, whilst the right column corresponds to $t = 1250\Omega_i^{-1}$. The initial width of the filaments was $\delta_\perp = 5\rho_s$, and the axes has been normalised to $\delta_\perp$. Image reproduced from Reference [201], with permission from AIP Publishing.

that they are non-collisional and furthermore, because parallel heat transport in ELMs is of particular interest. It is noted that a basic 3D Particle In Cell (PIC) simulation of a filament has been completed to investigate kinetic effects such as non-local parallel heat transport [206], but in general computational cost and memory restraints prevent such simulations being used for detailed filament or SOL turbulence simulations.

Another limitation on the use of fluid models is that they assume that the characteristic perpendicular length scale, $l_\perp$, is much larger than the ion Larmor radius (i.e. $\rho_i \ll l_\perp$) and that they only include higher order FLR effects through the gyro-viscous tensor [205]. This is problematic because the perpendicular length scale of filaments can often approach the ion Larmor radius, particularly in the highly sheared magnetic field region around an X-point. To address this issue, gyro-fluid models have been used for SOL plasmas [152, 201, 204, 207, 208], but either assume small perturbations (delta-F models), or neglect some FLR effects [152]. Furthermore, gyro-fluid models also suffer the same limitations as fluid models regarding collisionality.

From this brief discussion, it is evident that there are significant limitations in using fluid models for SOL or filament studies. However, in the absence of any clearly superior alternatives, they remain a valuable tool for gaining insight into L-mode and inter ELM H-mode filament dynamics in the SOL.

Gaps in Existing 3D Simulations

With respect to the 3D simulations discussed above, no work to date has investigated filament dynamics with the parallel ion velocity treated self-consistently, as the GBS simulations [197] evolved only fluctuating quantities, rather than the full fields. This is an area for future development and is particularly important with the consideration that ultimately it is desirable to move from studying isolated filaments to studying saturated SOL turbulence, where the density profiles produced will be highly dependent on parallel ion dynamics. It is also not clear how the inclusion of electron temperature dynamics will affect filamentary transport in a 3D model. Finally, no study has provided a thorough comparison between 3D and 2D simulations

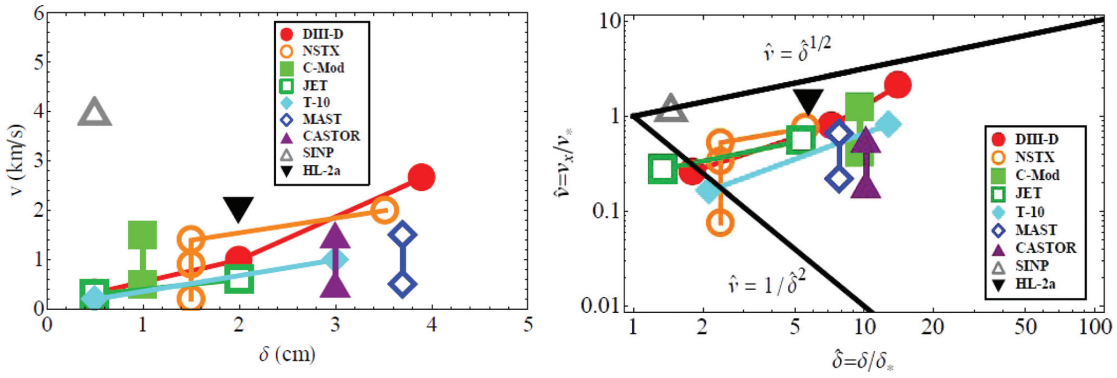

Figure 2.15: Radial velocity plotted against perpendicular size for filaments across a number of different devices. The left hand plot is in dimensional units, whilst the right hand plot is in terms of the normalised quantities. Images reproduced from Reference [45], with permission from AIP Publishing.

of isolated filaments using different parallel closures. Indeed, the dynamics of isolated filaments using the vorticity advection closure have not been explicitly investigated in the literature.

2.4 Comparison between Theory and Experiment

Inspired by the theoretical results discussed in the preceding section, experimental studies have investigated the relationship between the perpendicular size of filaments and their radial velocities. Measurements from a number of different machines were collated in Reference [45] and are plotted in Figure 2.15 in both dimensional and normalised form. There does not appear to be a clear relationship between the filament size and radial velocity, although this may be due to the different diagnostics, filament definitions and analysis techniques that were used in each machine, or indeed because a third parameter, such as the fluctuation amplitude of the filaments, has had an effect on the results.

Specific studies into this issue have also been carried out using GPI on NSTX [67] and Langmuir probes on TORPEX [122], with the distributions of observed filaments in the parameter space of normalised perpendicular size and radial velocity shown in Figure 2.16. With respect to the notation used in the TORPEX plot, $\tilde{a} = \hat{\delta}$ and $\tilde{v}_{\text{blob}} = \hat{v}$ to within constant factors of order unity. Also plotted on both figures are the theoretical scaling predictions of the inertial ($\hat{v} \propto \hat{\delta}^{1/2}$) and sheath current limited regimes ($\hat{v} \propto \hat{\delta}^{-2}$). In the NSTX case, the filament velocities appear to be bounded between these two scalings, whereas in TORPEX, the scalings predictions appear to be an upper bound. This seeming discrepancy between the two devices has been attributed to the relatively high collisionality found in NSTX, meaning that the filaments are predicted to lie in the Resistive X-point regime of the two region model. This regime is in-between the inertial and sheath current regimes and estimates velocities to scale like $\hat{v} \propto \Lambda\hat{\delta}^{-}2$, where Λ is a normalised collisionality parameter. It can be understood therefore that the results from these two machines are consistent with each other, and that reasonable agreement is found with theoretical scaling predictions, which act as bounds on the experimental results. A further study [204] tested the hot ion scaling predictions [203] against experimental measurements from ASDEX-U, finding similar levels of agreement.

A recent work has also claimed to have experimentally validated the two-region model's prediction that large $\hat{\delta}$ filaments change from having velocities scaling like $\hat{v} \sim \hat{\delta}^{-2}$ to $\hat{v} \sim \hat{\delta}^{1/2}$ as the collisionality is increased [81]. Whilst the model may yet be appropriate, this validation

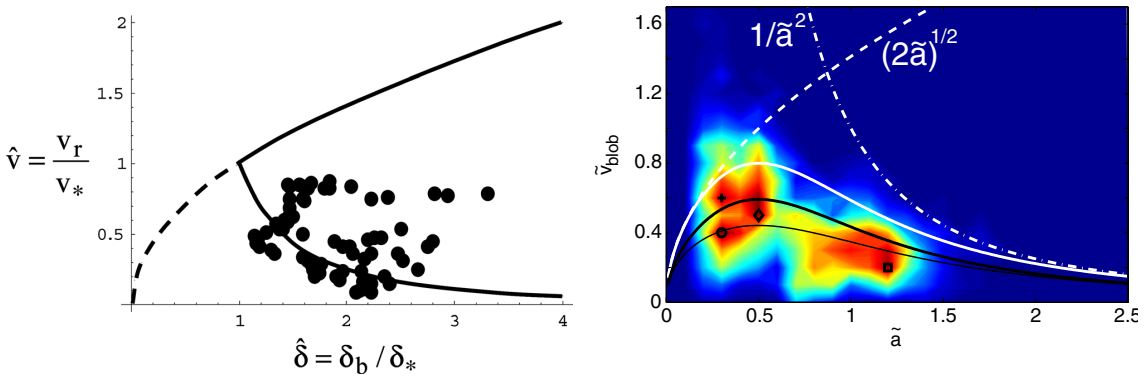

Figure 2.16: Radial velocity, $\hat{v}$, plotted against perpendicular size, $\hat{\delta}$, for filaments from NSTX (left) and TORPEX (right), in normalised units. In the TORPEX plot, $\tilde{a} = \hat{\delta}$ and $\tilde{v}_{\text{blob}} = \hat{v}$ to within constant factors of order unity. The analytic scaling predictions of the inertial and sheath current limited regimes are plotted for comparison, with a dot-dash line used for the TORPEX plot. The additional solid lines in the TORPEX are analytical results for the filament velocity for no background density (white), order unity background (thick black) and neutral damping effects. Left hand figure reproduced with permission from Reference [67]. Copyright (2007) by IAEA. Right hand figure reproduced with permission from Reference [122]. Copyright (2009) by the American Physical Society.

is not entirely convincing, as there are very few data points in the low collisionality regime and more importantly the results appear to indicate a trend towards filament velocities decreasing with enhanced collisionality, which actually contradicts the model's predictions.

2.5 Discussion and Summary

A critically important feature of transport caused by filaments is that it is highly intermittent, as this prevents simplified models providing an adequate description. For example, like the diffusive characterisation, attempts made to capture the convective nature of filaments by parametrising the experimental measurements of turbulent particle fluxes using an effective convective velocity, V_{eff} again yielded the unphysical situation of transport coefficients increasing with radial position [209–211]. It is worth emphasising here that whilst the instantaneous transport by filaments is by definition convective, convective models of turbulent transport operate using mean profiles, and therefore do not provide an adequate description. Nevertheless it remains commonplace today to describe the particle flux simply as the linear combination of effective diffusion and convection terms for analytical and transport code modelling of SOL plasmas [212–214]. Such an approach has been shown to be ill-founded by an analysis of probe measurements from TCV [95] and by an equivalent analysis of 2D SOL turbulence simulations [215]. As reference [215] states, 'Formally it remains possible to calculate effective diffusion coefficients or convective velocities, at every time or on average. These numbers have little meaning beyond stating the average gradient and average flux of the system'. Therefore, whilst models or simulations that use such a diffusive-convective description of the perpendicular transport have utility for applications such as post hoc analysis of experimental shots or in engineering simulations for divertor design, the perpendicular transport should be an input, rather than an output of these models or simulations. In particular, such a description does not have the ability to predict perpendicular transport in future machines such as ITER or DEMO. This lack of predictive capability strongly motivates further investigations of SOL

transport based on first principles physics and in particular, of filamentary dynamics.

To conclude, in this chapter the concept of SOL filaments has been introduced and their importance to SOL transport has been demonstrated. Experimental techniques used to measure filament quantities have been described, and measurements of key parameters have been collated from a number of different machines. From this characterisation, it has been shown that filaments typically have density perturbations of the order of the background plasma, have a perpendicular size in the range of 0.5-10 centimetres (or 1-100 ρ_s), propagate in the radial direction of toroidal machines at speeds of up to 3.5 kilometres a second (or up to 10 % of the sound speed). It has been explained that filament propagation arises in toroidal machines due to the presence of magnetic curvature and gradients, which drive compressible diamagnetic currents and in turn polarisation currents. These cause the filament to possess a broadly dipolar potential field, which through the $\boldsymbol{E} \times \boldsymbol{B}$ velocity, propagates the filament radially. A review of the existing literature on the theory and simulation of filaments has been made, with particular emphasis on studies of the propagation of isolated filaments, and limitations of existing 3D models and simulations have been discussed. In addition it has been shown that the theoretical predictions for the relationship between perpendicular filament size and radial velocity are in reasonable agreement with experimental measurements. Finally, it has been emphasised that simple turbulence models do not adequately describe SOL transport, and that this motivates further theoretical and computational studies of filaments to aid the development of predictive models and simulations.

Chapter 3

Physical Model

3.1 Introduction

In this chapter the governing equations of the physical models that are used within the simulations presented in this thesis are derived from the Braginskii equations. In particular, 3D drift-fluid equations will be derived and appropriate parallel boundary conditions for the plasma sheath at the targets will be stated. Following this, the Bohm normalisation used within the simulation code and throughout the rest of this thesis is introduced. Finally the sheath dissipation and vorticity advection closures will be applied to obtain 2D models also used for simulations in later chapters.

3.2 3D Model

3.2.1 Magnetic Curvature and Gradients in Slab Geometry

For simplicity, in this work the SOL is modelled using a local slab (Cartesian) geometry, where x and y represent the effective radial and bi-normal (perpendicular to both the magnetic field and radial direction) coordinate directions and a uniform magnetic field, $\boldsymbol{B} = B\hat{\boldsymbol{z}}$, is assumed. However, as discussed in Section 2.3.1, magnetic curvature and gradients in toroidal machines lead to the propagation of filaments, and so this influence must be retained. In deriving the final evolution equations of the model, a number of terms of the form

$$\nabla \cdot \left(\frac{\hat{\boldsymbol{b}} \times \nabla f}{B} \right) \tag{3.1}$$

will arise, where f is an arbitrary field. Using standard vector calculus identities, this can be expressed as

$$\nabla \cdot \left(\frac{\hat{\boldsymbol{b}} \times \nabla f}{B} \right) = \nabla \left(\frac{1}{B} \right) \cdot \left(\hat{\boldsymbol{b}} \times \nabla f \right) + \frac{1}{B} \left(\nabla \times \hat{\boldsymbol{b}} \right) \cdot \nabla f. \tag{3.2}$$

The first term on the right hand side represents the contribution of magnetic gradients, whilst the second term can be understood to primarily represent the influence of magnetic curvature, $\boldsymbol{\kappa} = (\hat{\boldsymbol{b}} \cdot \nabla)\hat{\boldsymbol{b}}$, since

$$\nabla \times \hat{\boldsymbol{b}} = \hat{\boldsymbol{b}} \times \boldsymbol{\kappa} + \left(\left(\nabla \times \hat{\boldsymbol{b}} \right) \cdot \hat{\boldsymbol{b}} \right) \hat{\boldsymbol{b}}. \tag{3.3}$$

In a toroidal device, the magnetic field strength, B, is roughly proportional to $1/R$, where R is the major radius. Therefore in local slab geometry, where x corresponds to the radial

direction, the magnetic field can be written as

$$\boldsymbol{B} \approx B_0 \left(1 + \frac{x}{R_0}\right)^{-1} \hat{\boldsymbol{z}} \tag{3.4}$$

where $x = R - R_0$, R_0 is the reference major radius location at which the geometry system is defined about, and B_0 is the magnetic field strength at R_0. Inserting this expression into Equation (3.2) leads to

$$\nabla \cdot \left(\frac{\hat{\boldsymbol{b}} \times \nabla f}{B}\right) \approx -\frac{1}{R_0 B_0} \frac{\partial f}{\partial y}. \tag{3.5}$$

However, this expression arises solely due to the magnetic gradients, and does not include the effect of magnetic curvature. However if instead a cylindrical coordinate system, (R, Φ, Z), is considered, where Φ is the azimuthal coordinate, Z is the vertical coordinate and

$$\boldsymbol{B} = \frac{B_0 R_0}{R} \hat{\boldsymbol{\Phi}}, \tag{3.6}$$

the magnetic gradient and curvature terms both contribute equally to produce

$$\nabla \cdot \left(\frac{\hat{\boldsymbol{b}} \times \nabla f}{B}\right) \approx -\frac{2}{R_0 B_0} \frac{\partial f}{\partial Z}, \tag{3.7}$$

and so the magnitude of the term is doubled. Therefore, to artificially include the influence of both magnetic curvature and magnetic gradients in the slab geometry, the following relation will be used throughout the following derivations.

$$\nabla \cdot \left(\frac{\hat{\boldsymbol{b}} \times \nabla f}{B}\right) = -\frac{2}{R_0 B_0} \frac{\partial f}{\partial y}. \tag{3.8}$$

The influence of magnetic gradients and curvature in any other terms that are not in the form of the LHS of Equation (3.8) will be neglected. This approach is equivalent to assuming $\boldsymbol{B}$ to be straight and uniform self-consistently in all terms, but including additional force terms within the momentum equations.

3.2.2 Isothermal Braginskii Equations

The model used in this thesis is derived directly from the Braginskii fluid equations [205], which describe collisional magnetised plasmas. Whilst in principle the Braginskii model can describe plasmas consisting of multiple ion species and neutrals, in this work only the reduced case of a fully ionised plasma consisting of electrons and singly charged ions will be considered. Introducing $l_\parallel$, $l_\perp$ and ω_c as the characteristic parallel length scale, perpendicular length scale and frequency of the system respectively, the Braginskii closure is valid for such plasmas that satisfy

$$\begin{gathered} \frac{\nu_{ei}}{\Omega_e} \ll 1, \quad \frac{\nu_{ii}}{\Omega_i} \ll 1, \quad \omega_c \ll \nu_{ei}, \quad \omega_c \ll \nu_{ii}, \\ l_\parallel \gg \lambda_e, \quad l_\parallel \gg \lambda_i, \quad l_\perp \gg \rho_i, \quad l_\perp \gg \sqrt{\lambda_e \rho_e}, \quad l_\perp \gg \sqrt{\lambda_i \rho_i}. \end{gathered} \tag{3.9}$$

Here the subscripts e and i correspond to electron and ion quantities, and for a species j, $\rho_j = v_{th,j}/\Omega_j$ is the gyro-radius, $v_{th,j} = \sqrt{T_j/m_j}$ is the thermal velocity, $\Omega_j = eB/m_j$ is the gyro-frequency, $\lambda_j = v_{th,j}/\nu_{ji}$ is the mean free path, e is the elementary charge, T_j is the temperature and m_j is the mass of a single particle. In addition

$$\nu_{ei} = \frac{n_e Z_i^2 e^4 \ln \Lambda}{3\varepsilon_0^2 m_e^{1/2} (2\pi T_e)^{3/2}} \tag{3.10}$$

is the electron-ion collision frequency and

$$\nu_{ii} = \frac{n_e Z_i^4 e^4 \ln\Lambda}{12\varepsilon_0^2 m_i^{1/2} (\pi T_i)^{3/2}} \tag{3.11}$$

is the ion-ion collision frequency, where ε_0 is the permittivity of free space, n_e is the electron density, and Z_i is the charge state of the ions. Finally $\ln\Lambda$ is the Coulomb logarithm, which can be approximated in tokamak relevant conditions to be

$$\ln\Lambda \approx 18.0 - \ln\left[\left(\frac{n_e}{10^{19}}\right)^{1/2}\left(\frac{T_e}{10^3 e}\right)^{-3/2}\right], \tag{3.12}$$

where n_e is in m^{-3} and T_e is in Joules [216]. Whilst most of the relations in Equation (3.9) are generally true for SOL plasmas, it is acknowledged that the $l_\parallel \gg \lambda_e$ condition may not be satisfied in all cases.

Throughout the work contained in this thesis, an isothermal plasma is assumed. In this limit, the Braginskii equations can be written in the form

$$\frac{\partial n_e}{\partial t} + \nabla\cdot(n_e \boldsymbol{v}_e) = s_n, \tag{3.13}$$

$$\frac{\partial n_i}{\partial t} + \nabla\cdot(n_i \boldsymbol{v}_i) = s_n, \tag{3.14}$$

$$m_e\left(\frac{\partial}{\partial t} + (\boldsymbol{v_e}\cdot\nabla)\right)(n_e\boldsymbol{v}_e) + \nabla p_e + \nabla\cdot\boldsymbol{\pi}_e + e n_e(\boldsymbol{E} + \boldsymbol{v}_e\times\boldsymbol{B}) = \boldsymbol{F}_{ei}, \tag{3.15}$$

$$m_i\left(\frac{\partial}{\partial t} + (\boldsymbol{v_i}\cdot\nabla)\right)(n_i\boldsymbol{v}_i) + \nabla p_i + \nabla\cdot\boldsymbol{\pi}_i - e n_i(\boldsymbol{E} + \boldsymbol{v}_i\times\boldsymbol{B}) = -\boldsymbol{F}_{ei}. \tag{3.16}$$

Here for a species j, n_j is the particle density, $\boldsymbol{v}_j$ is the fluid velocity, p_j is the isotropic pressure and $\boldsymbol{\pi}_j$ is the viscous stress tensor. Furthermore s_n is a source or sink of particles from ionisation or recombination processes and $\boldsymbol{E}$ is the electric field. In addition $\boldsymbol{F}_{ei}$ is the effective frictional force between electrons and ions due to collisions, given by

$$\boldsymbol{F_{ei}} = e n_e\left(\frac{\boldsymbol{j}_\parallel}{\sigma_\parallel} + \frac{\boldsymbol{j}_\perp}{\sigma_\perp}\right), \tag{3.17}$$

where $\boldsymbol{j}_\parallel$ and $\sigma_\parallel$ are respectively the current density and conductivity in the parallel direction, whilst $\boldsymbol{j}_\perp$ and $\sigma_\perp$ are the corresponding quantities in the perpendicular direction. The conductivities are defined as

$$\sigma_\parallel = \frac{n_e e^2}{0.51 m_e \nu_{ei}} \tag{3.18}$$

and

$$\sigma_\perp = 0.51\sigma_\parallel. \tag{3.19}$$

Definitions of the Braginskii electron and ion viscosity tensors can be found in Reference [205] directly. It is noted that since the plasma is by definition quasi-neutral, $n_e = n_i$, and so hereafter n_e will be used in place of n_i.

In deriving the model used within this thesis from these isothermal Braginskii equations, the first reduction made is to assume cold ions. This is a common simplification in existing filament models, despite it not being generally justified as often $T_i \gtrsim T_e$ in the SOL [31, 133–135]. A discussion of existing studies into the influence of this assumption can be found in Section 2.3.5. Using $T_i = 0$ greatly simplifies the equations, as it removes the complicated gyro-viscous components of the ion viscous stress tensor and the pressure gradient term in the ion momentum equation (which otherwise would lead to an ion diamagnetic drift velocity),

since $p_i = n_i T_i$. Strictly, under the Braginskii closure, the perpendicular components of the ion viscous stress tensor become infinite at $T_i = 0$, and so finite T_i is retained within these terms to allow the model to include viscous effects. In this cold ion limit, Equations (3.15) and (3.16) in non-conservative form become:

$$m_e n_e \left(\frac{\partial}{\partial t} + \boldsymbol{v_e} \cdot \nabla \right) \boldsymbol{v}_e + T_e \nabla n_e + \nabla \cdot \boldsymbol{\pi}_e + e n_e \left(\boldsymbol{E} + \boldsymbol{v}_e \times \boldsymbol{B} \right) = \boldsymbol{F}_{ei} - m_e s_n \boldsymbol{v}_e, \tag{3.20}$$

$$m_i n_e \left(\frac{\partial}{\partial t} + \boldsymbol{v_i} \cdot \nabla \right) \boldsymbol{v}_i + \nabla \cdot \boldsymbol{\pi}_i - e n_e \left(\boldsymbol{E} + \boldsymbol{v}_i \times \boldsymbol{B} \right) = -\boldsymbol{F}_{ei} - m_i s_n \boldsymbol{v}_i. \tag{3.21}$$

3.2.3 Drift-Fluid Reduction

The velocity of a species j in the perpendicular direction is defined as

$$\boldsymbol{v_{\perp j}} = \frac{\hat{\boldsymbol{b}} \times (\boldsymbol{v_j} \times \boldsymbol{B})}{B}. \tag{3.22}$$

Therefore by manipulation of Equations (3.20) and (3.21), expressions for the electron and ion perpendicular velocities can be obtained:

$$\boldsymbol{v}_{\perp e} = \boldsymbol{v}_E + \boldsymbol{v}_D + \boldsymbol{v}_{Pe} + \boldsymbol{v}_{\pi e} + \boldsymbol{v}_F + \boldsymbol{v}_{Se}, \tag{3.23}$$

$$\boldsymbol{v}_{\perp i} = \boldsymbol{v}_E + \boldsymbol{v}_{Pi} + \boldsymbol{v}_{\pi i} + \boldsymbol{v}_F + \boldsymbol{v}_{Si}. \tag{3.24}$$

Here

$$\boldsymbol{v}_E = \frac{\boldsymbol{E} \times \hat{\boldsymbol{b}}}{B} = \frac{\hat{\boldsymbol{b}} \times \nabla \varphi}{B} \tag{3.25}$$

is the $\boldsymbol{E} \times \boldsymbol{B}$ velocity,

$$\boldsymbol{v}_D = -\frac{\hat{\boldsymbol{b}} \times \nabla p_e}{e n_e B} \tag{3.26}$$

is the electron diamagnetic velocity,

$$\boldsymbol{v}_{Pe} = -\frac{m_e}{eB} \hat{\boldsymbol{b}} \times \left(\frac{\partial}{\partial t} + \boldsymbol{v}_e \cdot \nabla \right) \boldsymbol{v}_e \tag{3.27}$$

and

$$\boldsymbol{v}_{Pi} = \frac{m_i}{eB} \hat{\boldsymbol{b}} \times \left(\frac{\partial}{\partial t} + \boldsymbol{v}_i \cdot \nabla \right) \boldsymbol{v}_i \tag{3.28}$$

are the electron and ion polarisation velocities,

$$\boldsymbol{v}_{\pi e} = -\frac{\hat{\boldsymbol{b}} \times \nabla \cdot \boldsymbol{\pi}_e}{e n_e B} \tag{3.29}$$

and

$$\boldsymbol{v}_{\pi i} = \frac{\hat{\boldsymbol{b}} \times \nabla \cdot \boldsymbol{\pi}_i}{e n_e B} \tag{3.30}$$

are the electron and ion drift velocities due to viscous forces,

$$\boldsymbol{v}_F = \frac{\hat{\boldsymbol{b}} \times \boldsymbol{F}_{ei}}{e n_e B} \tag{3.31}$$

is the drift velocity induced due to friction between electrons and ions and

$$\boldsymbol{v}_{Se} = \frac{m_e s_n}{e n_e B} \hat{\boldsymbol{b}} \times \boldsymbol{v}_e \tag{3.32}$$

and

$$\boldsymbol{v}_{Si} = -\frac{m_i s_n}{e n_e B} \hat{\boldsymbol{b}} \times \boldsymbol{v}_i \tag{3.33}$$

are the electron and ion drift velocities due to the sources or sinks of particles in the system. It is noted that in other works the drifts due to viscous forces are often included within the polarisation drifts, but have been kept separate here to highlight the effect of viscosity.

Following the drift-ordering arguments in References [217] and [218], the parameters $\delta_e = \rho_e/l_\perp$ and $\delta_i = \rho_i/l_\perp$ are introduced, which given the Braginskii assumption of a collisional magnetised plasma, are both small:

$$\delta_e \ll 1, \quad \delta_i \ll 1. \tag{3.34}$$

In addition, the characteristic inverse time scale of interest in the plasma, ω_c, is assumed to be of order

$$\omega_c \sim \delta_i^2 \Omega_i. \tag{3.35}$$

The magnitudes of each of the constituent perpendicular velocities can then be approximated as follows

$$\boldsymbol{v}_E \sim \boldsymbol{v}_D \sim \frac{T_e}{eBl_\perp} \tag{3.36}$$

$$\boldsymbol{v}_{Pi} \sim \boldsymbol{v}_{\pi i} \sim \boldsymbol{v}_F \sim \boldsymbol{v}_{S_i} \sim \delta_i^2 \frac{T_e}{eBl_\perp} \tag{3.37}$$

$$\boldsymbol{v}_{Pe} \sim \boldsymbol{v}_{\pi e} \sim \boldsymbol{v}_{S_e} \sim \frac{m_e}{m_i}\delta_i^2 \frac{T_e}{eBl_\perp}. \tag{3.38}$$

It can be seen therefore that the $\boldsymbol{E} \times \boldsymbol{B}$ and electron diamagnetic velocities are the leading order perpendicular velocities. To reduce the complexity of the model, the remaining consistent velocities can be neglected with the exception of $\boldsymbol{v}_{Pi}$, which is required to determine the perpendicular electric field, and $\boldsymbol{v}_{\pi i}$, which is kept to retain the effect of viscous terms. Under this drift-reduction, Equations (3.23) and (3.24) become

$$\boldsymbol{v}_{\perp e} = \boldsymbol{v}_E + \boldsymbol{v}_{De}, \tag{3.39}$$

$$\boldsymbol{v}_{\perp i} = \boldsymbol{v}_E + \boldsymbol{v}_{Pi} + \boldsymbol{v}_{\pi i}. \tag{3.40}$$

where $\boldsymbol{v}_{Pi}$ is now defined as

$$\boldsymbol{v}_{Pi} = \frac{m_i}{eB}\hat{\boldsymbol{b}} \times \left(\frac{\partial}{\partial t} + \boldsymbol{v}_E \cdot \nabla\right) \boldsymbol{v}_E \tag{3.41}$$

Furthermore, in the following the influence of ion viscosity is simplified by writing $\nabla \cdot \boldsymbol{\pi}_i = -m_i n_e \nu_i \nabla_\perp^2 \boldsymbol{v}_E$, where ν_i is the effective cross field kinematic viscosity of the ions. This simplification essentially neglects parallel viscosity and all viscous terms involving cross-derivatives with the parallel direction (the gyro-viscous components have already been neglected through the cold ion assumption). It is noted that strictly the Braginskii closure specifies the parallel terms of the viscous tensor to be larger than the perpendicular terms. However the parallel viscosity terms can be shown to be small compared to the isotropic pressure terms (which are of the same form) for a sufficiently collisional plasma, whilst the justification for ignoring terms involving cross-derivatives with the parallel direction is that the gradients in the parallel direction are negligible compared to those in the perpendicular direction ($l_\parallel \gg l_\perp$). Under this simplification, $\boldsymbol{v}_{\pi i}$ becomes

$$\boldsymbol{v}_{\pi i} = \frac{m_i \nu_i \nabla_\perp \nabla_\perp^2 \varphi}{eB^2.} \tag{3.42}$$

3.2.4 Model Equations

The total current density in the drift-reduced system, $\boldsymbol{j}$ can be conveniently expressed as

$$\boldsymbol{j} = \boldsymbol{j}_{\text{pol}} + \boldsymbol{j}_{\text{dia}} + \boldsymbol{j}_{\text{visc}} + \hat{\boldsymbol{b}} j_{\parallel}, \tag{3.43}$$

where $\boldsymbol{j}_{\text{pol}} = en_e\boldsymbol{v}_{Pi}$ is the ion polarisation current density, $\boldsymbol{j}_{\text{dia}} = -en_e\boldsymbol{v}_D$ is the electron diamagnetic current density, $\boldsymbol{j}_{\text{visc}} = en_e\boldsymbol{v}_{\pi i}$ is the perpendicular current density arising due to ion viscosity, and $j_{\parallel}$ is the parallel current density. In the local slab geometry described in Section 3.2.1, consideration of current continuity, $\nabla \cdot \boldsymbol{j} = 0$, leads to

$$\frac{m_i}{B^2}\nabla_{\perp} \cdot \left(n_e \frac{d}{dt}\nabla_{\perp}\varphi \right) = \nabla_{\parallel} j_{\parallel} + T_e \nabla \cdot \left(\frac{\hat{\boldsymbol{b}} \times \nabla n_e}{B} \right) + \nabla_{\perp} \cdot \left(\frac{n_e m_i \nu_i \nabla_{\perp} \nabla_{\perp}^2 \varphi}{B^2} \right), \tag{3.44}$$

where $d/dt = \partial/\partial t + \boldsymbol{v}_E \cdot \nabla_{\perp} + v_{\parallel i}\nabla_{\parallel}$ is the total derivative of the ion fluid. By employing the Boussinesq approximation,

$$\nabla_{\perp} \cdot \left(n_e \frac{d}{dt}\nabla_{\perp}\varphi \right) \approx n_e \frac{d}{dt}\nabla_{\perp}^2 \varphi, \tag{3.45}$$

to simplify the polarisation current term, and Equation (3.8) to express the diamagnetic current term, Equation (3.44) can be written as

$$\frac{m_i n_e}{B}\frac{d\omega}{dt} = \nabla_{\parallel} j_{\parallel} - \frac{eg}{\Omega_i}\frac{\partial n_e}{\partial y} + \frac{m_i n_e \nu_i}{B}\nabla_{\perp}^2 \omega. \tag{3.46}$$

Here $\omega = \nabla_{\perp}^2 \varphi / B$ can be understood to be the plasma vorticity based upon the $\boldsymbol{E} \times \boldsymbol{B}$ velocity, $g = 2c_s^2/R$ is an effective gravitational acceleration that captures the influence of magnetic gradients and curvature and R is the characteristic major radius location of the SOL, typically taken at the outboard mid-plane. The Boussinesq approximation is valid for small density perturbations with respect to the effective background, $\delta n_e / n_{e,bg} \ll 1$, and so is not strictly valid in the SOL where order unity perturbations are commonplace. A discussion of the influence of this approximation on filament simulations is provided in Section 2.3.5. In addition, in handling the viscous current term, gradients in the quantity $n_e\nu_i$ have been neglected. The electrostatic potential field can therefore be obtained by integrating (inverting) the vorticity field, whose evolution is given by Equation (3.46).

The density evolution in this drift reduced system is found by using Equations (3.39) and (3.8) within Equation (3.13) to produce

$$\frac{\partial n_e}{\partial t} + \boldsymbol{v}_E \cdot \nabla_{\perp} n_e + \nabla_{\parallel}\left(n_e v_{\parallel e} \right) = \frac{g n_e}{B c_s^2}\frac{\partial \varphi}{\partial y} - \frac{g}{\Omega_i}\frac{\partial n_e}{\partial y} + D\nabla_{\perp}^2 n_e + s_n. \tag{3.47}$$

It can be seen that the diamagnetic velocity does not contribute to particle advection. Similar cancellations occur within the momentum equations and other higher order moments of the kinetic equations [145–148] which are known collectively in some works as the *diamagnetic cancellation*. In addition, a collisional particle diffusion term, $D\nabla_{\perp}^2 n_e$, has also been included on the LHS, where D is the effective particle diffusivity. In principle a term of this form can be derived from the $\boldsymbol{v}_F$ drift velocity [219].

The final equations of the closed system are obtained by isolating the parallel components of Equations (3.20) and (3.21), which produces

$$m_e n_e \left(\frac{\partial}{\partial t} + \boldsymbol{v}_E \cdot \nabla_{\perp} + v_{\parallel e}\nabla_{\parallel} \right) v_{\parallel e} = en_e \nabla_{\parallel}\varphi - T_e \nabla_{\parallel} n_e + en_e \eta_{\parallel} j_{\parallel} - m_e s_n v_{\parallel e}, \tag{3.48}$$

$$m_i n_e \left(\frac{\partial}{\partial t} + \boldsymbol{v}_E \cdot \nabla_{\perp} + v_{\parallel i}\nabla_{\parallel} \right) v_{\parallel i} = -en_e \nabla_{\parallel}\varphi - en_e \eta_{\parallel} j_{\parallel} - m_i s_n v_{\parallel i}, \tag{3.49}$$

where by definition $j_\parallel = en_e\left(v_{\parallel i} - v_{\parallel e}\right)$ and $\eta_\parallel = 1/\sigma_\parallel$ is the parallel resistivity of the plasma. In these equations the diamagnetic cancellation has occurred between the diamagnetic velocity advection terms and the gyro-viscous components of the viscous tensors [145–148]. The remaining viscous terms have been neglected. Equations (3.46) to (3.49), alongside $\omega = \nabla_\perp^2\varphi/B$ thus constitute the physical model used for all 3D simulations in this thesis.

3.2.5 Dissipative Parameter Definitions

In this work, the dissipative parameters are defined as

$$D = \left(1 + 1.3q_{95}^2\right)\left(1 + \frac{T_i}{T_e}\right)\rho_e^2\nu_{ei}, \tag{3.50}$$

$$\nu_i = \frac{3}{4}\left(1 + 1.6q_{95}^2\right)\rho_i^2\nu_{ii}. \tag{3.51}$$

Here q_{95} is the value of the safety factor, q, at the flux surface that encloses 95% of the toroidal magnetic flux. For circular large aspect ratio tokamaks, q is given by

$$q = \frac{rB_\Phi}{RB_\theta}, \tag{3.52}$$

where r is the minor radius and B_Φ and B_θ are the strength of the toroidal and poloidal components of the magnetic field. These expressions for D and ν_i are derived in Reference [177]. They seek to include neoclassical corrections to the classical Braginskii [205] definitions for these quantities, which in turn can be recovered by setting $q_{95} = 0$. It is noted that under the above definition, $\nu_{ii} \to \infty$ and $\rho_i \to 0$ as $T_i \to 0$. Therefore, whilst cold ions are assumed elsewhere in the model equations, non-zero values of T_i will be used within these dissipative parameters. Typically T_i will be set such that $T_i = T_e$.

3.2.6 Sheath Boundary Conditions

In the slab geometry used in this work, the sheath boundaries are defined to be located at $z = \pm\ell_\parallel$. From standard sheath theory [31, 158], the velocities at the entrances to the sheaths must satisfy

$$v_{\parallel i}\big|_{z=+\ell_\parallel} \geq +c_s, \tag{3.53}$$

$$v_{\parallel i}\big|_{z=-\ell_\parallel} \leq -c_s, \tag{3.54}$$

$$v_{\parallel e}\big|_{z=+\ell_\parallel} = +\left(\frac{T_e}{2\pi m_e}\right)^{1/2}\exp\left(\frac{e}{T_e}\left(\varphi_w - \varphi|_{z=+\ell_\parallel}\right)\right), \tag{3.55}$$

$$v_{\parallel e}\big|_{z=-\ell_\parallel} = -\left(\frac{T_e}{2\pi m_e}\right)^{1/2}\exp\left(\frac{e}{T_e}\left(\varphi_w - \varphi|_{z=-\ell_\parallel}\right)\right), \tag{3.56}$$

where φ_w is the electrostatic potential of the walls of the target. However, as shown in Appendix A, in a steady state system that is uniform in the perpendicular directions and assuming $s_n \geq 0$ throughout, a solution to the governing equations of the model, Equations (3.46) to (3.49), does not exist unless

$$v_{\parallel i} \leq \sqrt{\frac{T_e}{m_i + m_e}}. \tag{3.57}$$

Recalling that c_s is defined here to be $\sqrt{T_e/m_i}$, the quantity $\sqrt{T_e/(m_i + m_e)}$ can be understood to be the sound speed of the plasma corrected to include the effect of electron inertia. It can

be seen therefore that this specific condition (3.57) is incompatible with Equations (3.53) and (3.54). This discrepancy occurs because electron inertia is neglected in various aspects of the derivation of Equations (3.53) to (3.56), but has been retained in Equations (3.46) to (3.49). Whilst no derivation of the sheath boundary conditions that includes electron inertia could be found, numerical studies have shown that such an effect will act to lower the minimum speed at which ions must enter the sheath [220]. Therefore in this work the following modified boundary conditions will be enforced at the sheath instead of Equations (3.53) to (3.56) to ensure Equation (3.57) is satisfied:

$$v_{\parallel i}\big|_{z=+\ell_\parallel} \geq +\sqrt{\frac{T_e}{m_i + m_e}}, \tag{3.58}$$

$$v_{\parallel i}\big|_{z=-\ell_\parallel} \leq -\sqrt{\frac{T_e}{m_i + m_e}}, \tag{3.59}$$

$$v_{\parallel e}\big|_{z=+\ell_\parallel} = +\left(\frac{T_e}{2\pi m_e \left(1 + m_e/m_i\right)}\right)^{1/2} \exp\left(\frac{e}{T_e}\left(\varphi_w - \varphi|_{z=+\ell_\parallel}\right)\right), \tag{3.60}$$

$$v_{\parallel e}\big|_{z=-\ell_\parallel} = -\left(\frac{T_e}{2\pi m_e \left(1 + m_e/m_i\right)}\right)^{1/2} \exp\left(\frac{e}{T_e}\left(\varphi_w - \varphi|_{z=-\ell_\parallel}\right)\right). \tag{3.61}$$

In Equations (3.58) and (3.59), the relations $\geq$ and $\leq$ are used instead of simple equalities to allow for the possibility of supersonic flows in systems in which any of the conditions on Equation (3.57) are relaxed (i.e. non-steady state, variation in perpendicular direction, $S_n < 0$), as in such cases supersonic flow remains possible [221]. A description of how the $\geq$ and $\leq$ operators are implemented within the simulations presented in this work is provided in Section 4.3.5.

It is convenient to specify the potential of the target walls to be equal to

$$\varphi_w = -\frac{T_e}{e} \ln\left[\left(\frac{m_i}{2\pi m_e}\right)^{1/2}\right], \tag{3.62}$$

so that Equations (3.60) and (3.61) simplify to

$$v_{\parallel e}\big|_{z=+\ell_\parallel} = +\sqrt{\frac{T_e}{m_i + m_e}} \exp\left(\frac{-e\,\varphi|_{z=+\ell_\parallel}}{T_e}\right), \tag{3.63}$$

$$v_{\parallel e}\big|_{z=-\ell_\parallel} = -\sqrt{\frac{T_e}{m_i + m_e}} \exp\left(\frac{-e\,\varphi|_{z=-\ell_\parallel}}{T_e}\right). \tag{3.64}$$

It can be seen therefore that by specifying the wall potential to be given by Equation (3.62), zero net current will enter the sheath when the potential at the entrance to the sheath is zero.

To prevent the system from being over-constrained, no boundary condition is enforced on any of the remaining fields at the sheath boundaries, which hereafter will be described as having *free* boundary conditions. The conditions specified on the perpendicular boundaries of the domain are given in Section 4.3.5.

3.3 Normalisation

The Buckingham π theorem [222] states that the number of parameters of a system of equations is necessarily reduced by normalisation. Furthermore when performing simulations it is convenient for all of the evolving fields to have approximately the same magnitude so that

the the same error tolerances can be used for each field. In this work therefore the following Bohm normalisation is used:

$$\begin{gathered}\frac{\boldsymbol{x}}{\rho_s} \to \boldsymbol{x}, \quad \Omega_i t \to t, \quad \frac{n_e}{n_{e,0}} = n, \quad \frac{e\varphi}{T_e} = \phi, \quad \frac{v_{\parallel e}}{c_s} = V, \quad \frac{v_{\parallel i}}{c_s} = U, \quad \frac{\omega}{\Omega_i} = \Omega, \\ \frac{s_n}{n_{e,0}\Omega_i} = S_n, \quad \frac{j_\parallel}{e n_{e,0} c_s} = J_\parallel, \quad \frac{0.51\nu_{ei}}{\Omega_i} = \nu_\parallel, \quad \frac{m_i}{m_e} = \mu, \quad \frac{\ell_\parallel}{\rho_s} = L_\parallel \\ \frac{g}{\rho_s \Omega_i^2} = \hat{g} = \frac{2\rho_s}{R} \quad \frac{\eta_\parallel}{B/\left(e n_{e,0}\right)} = \hat{\eta}_\parallel = \frac{\nu_\parallel}{\mu n}, \quad \frac{D}{D_{\text{Bohm}}} = D_n, \quad \frac{\nu_i}{D_{\text{Bohm}}} = D_\Omega.\end{gathered} \tag{3.65}$$

Here $n_{e,0}$ is a characteristic particle density of the SOL, and $D_{\text{Bohm}} = \rho_s^2 \Omega_i$ is the Bohm diffusion coefficient. Under this normalisation, Equations (3.46) to (3.49) can be written as

$$\frac{\partial \Omega}{\partial t} = -\left(\hat{\boldsymbol{b}} \times \nabla\phi\right) \cdot \nabla\Omega - U\nabla_\parallel \Omega + \frac{1}{n}\nabla_\parallel J_\parallel - \frac{\hat{g}}{n}\frac{\partial n}{\partial y} + D_\Omega \nabla_\perp^2 \Omega, \tag{3.66}$$

$$\frac{\partial n}{\partial t} = -\left(\hat{\boldsymbol{b}} \times \nabla\phi\right) \cdot \nabla n - \nabla_\parallel (nV) + n\hat{g}\frac{\partial \phi}{\partial y} - \hat{g}\frac{\partial n}{\partial y} + D_n \nabla_\perp^2 n + S_n, \tag{3.67}$$

$$\frac{dV}{dt} = -\left(\hat{\boldsymbol{b}} \times \nabla\phi\right) \cdot \nabla V - V\nabla_\parallel V + \mu\left(\nabla_\parallel \phi - \frac{1}{n}\nabla_\parallel n + \hat{\eta}_\parallel J_\parallel\right) - \frac{S_n V}{n}, \tag{3.68}$$

$$\frac{\partial U}{\partial t} = -\left(\hat{\boldsymbol{b}} \times \nabla\phi\right) \cdot \nabla U - U\nabla_\parallel U - \nabla_\parallel \phi - \frac{\hat{\eta}_\parallel}{\mu} J_\parallel - \frac{S_n U}{n}, \tag{3.69}$$

whilst the sheath boundary conditions, Equations (3.58), (3.59), (3.63), and (3.64) become

$$U|_{z=+L_\parallel} \geq \frac{1}{\sqrt{1+1/\mu}}, \tag{3.70}$$

$$U|_{z=-L_\parallel} \leq \frac{-1}{\sqrt{1+1/\mu}}. \tag{3.71}$$

$$V|_{z=+L_\parallel} = \frac{1}{\sqrt{1+1/\mu}} \exp\left(-\phi|_{z=+L_\parallel}\right), \tag{3.72}$$

$$V|_{z=-L_\parallel} = \frac{-1}{\sqrt{1+1/\mu}} \exp\left(-\phi|_{z=-L_\parallel}\right). \tag{3.73}$$

3.4 2D Closures

In this work, 2D simulations utilising the sheath dissipation and vorticity advection closures described in Sections 2.3.3 will also be performed in Chapter 6 so that direct comparisons can be made between 2D and 3D models.

3.4.1 Sheath Dissipation Closure

The sheath dissipation closure assumes the density and electrostatic potential to be uniform along the parallel direction so that the equations can be analytically integrated and averaged along field lines. Applying this closure to Equations (3.66) and (3.67) and linearising the terms which arise from the application of the sheath boundary conditions (given by Equations (3.53) to (3.56)) yields

$$\frac{\partial \Omega}{\partial t} = -\left(\hat{\boldsymbol{b}} \times \nabla\phi\right) \cdot \nabla\Omega + \frac{\phi}{L_\parallel} - \frac{\hat{g}}{n}\frac{\partial n}{\partial y} + D_\Omega \nabla_\perp^2 \Omega, \tag{3.74}$$

$$\frac{\partial n}{\partial t} = -\left(\hat{\boldsymbol{b}} \times \nabla\phi\right) \cdot \nabla n + \frac{n\phi}{L_\parallel} - \frac{(n-n_0)}{L_\parallel} + n\hat{g}\frac{\partial \phi}{\partial y} - \hat{g}\frac{\partial n}{\partial y} + D_n \nabla_\perp^2 n. \tag{3.75}$$

Here n_0 is the background density value and it has been assumed that

$$\int_{-L_\parallel}^{L_\parallel} S_n \, dz = 2n_0. \tag{3.76}$$

3.4.2 Vorticity Advection Closure

The vorticity advection closure considers only the drift-plane at the outboard mid-plane, neglects parallel currents and approximates the the parallel advection terms as

$$U\nabla_\parallel \approx V\nabla_\parallel \approx \frac{1}{2L_\parallel}. \tag{3.77}$$

Applying this closure to Equations (3.66) and (3.67) produces

$$\frac{\partial \Omega}{\partial t} = -\left(\hat{\boldsymbol{b}} \times \nabla\phi\right) \cdot \nabla\Omega - \frac{\Omega}{2L_\parallel} - \frac{\hat{g}}{n}\frac{\partial n}{\partial y} + D_\Omega \nabla_\perp^2 \Omega, \tag{3.78}$$

$$\frac{\partial n}{\partial t} = -\left(\hat{\boldsymbol{b}} \times \nabla\phi\right) \cdot \nabla n - \frac{(n - n_0)}{2L_\parallel} + n\hat{g}\frac{\partial \phi}{\partial y} - \hat{g}\frac{\partial n}{\partial y} + D_n \nabla_\perp^2 n. \tag{3.79}$$

Chapter 4

Numerical Implementation

4.1 Introduction

To simulate the physical models outlined in Chapter 3, a collection of simulation codes called STORM has been developed using the BOUT++ framework. In this chapter, this numerical implementation is outlined, beginning first with a brief outline of BOUT++. A description of the numerics of the STORM codes is then provided, before finally the initialisation of the filament simulations presented in the latter chapters of this thesis is detailed.

4.2 BOUT++

BOUT++ (BOUndary Turbulence) [193, 194] is a framework for highly parallel non-linear plasma fluid simulations using finite difference methods. It is primarily developed by Dr Ben Dudson at the University of York and is publicly available at `https://github.com/boutproject/BOUT-dev`. The simulation code itself is written entirely in C++, but there are also a large number of pre and post processing tools written in a variety of higher level languages such as Python, IDL, Matlab and Mathematica. Its foremost application is for studies of the edge region of tokamak plasmas, and for this reason is utilises a general curvilinear geometry system. This can be used to produce a wide range of magnetic configurations such as simple slab, linear device, simple magnetised torus, limited tokamak and diverted tokamak.

To explain what BOUT++ actually consists of, it is first emphasised that there is no such thing as *the* BOUT++ model and instead the user must specify which equations to solve. What BOUT++ provides is a collection of routines, solvers and interfaces to libraries that allow for simulation codes to be written much more quickly, easily and robustly. For example, if a new fluid simulation code is developed from scratch, it will require routines for memory management, communication between processors, spatial differentiation and time integration, amongst many others. Writing and debugging these new routines will be very time consuming and will only be a duplication of what lies in existing codes. By providing a flexible framework that includes all these fundamental components, BOUT++ spares this effort and the development time can be drastically decreased. Since BOUT++ has a relatively wide user base of over one hundred users, the routines have been well tested and are considerably less likely to contain errors than a newly written code. Furthermore, BOUT++ provides a variety of different numerical methods for time integration, spatial differentiation and solving elliptic differential equations, which can be easily selected through an input file or at the command line. This means that the best numerical methods for a given problem can be investigated

quickly and with no change to the source code of the simulation. Finally, it is exceptionally simple to implement evolution equations using BOUT++ as functions have been written for all common terms that arise in fluid plasma models. For example, the normalised density continuity equation, Equation (3.67) can be implemented in BOUT++ as follows

```
ddt(n) = - bracket(phi, n) - n*Grad_par(V) - Vpar_Grad_par(V,n) + D_n*
    Delp2(n) - g*n*DDZ(phi) + g*DDZ(n)+ S ;
```

Here the $\boldsymbol{E} \times \boldsymbol{B}$ term is implemented through the `bracket()` operator (as the term can be written in the form of a Poisson bracket), whilst the substitution $y \rightarrow -z$ has been used to implement the Equations in BOUT++'s coordinate system (See Section 4.2.4). As can be seen, the resulting code is very readable and it is trivial to add new physics through additional terms or equations.

In the remainder of this section, no attempt is made to outline the structure of the BOUT++ code as this topic is thoroughly covered either in References [193] and [194], or in the BOUT++ Developer and User Manuals [223, 224]. To aid the reader's understanding of how BOUT++ operates however, an example is provided of a BOUT++ *Physics Module*, which is the collection of files in which the user's simulation model is coded. This is followed by a concise review of how BOUT++ evolves fluid equations in time and of the various time solvers supported. The implementations of standard boundary conditions in BOUT++ are then outlined, as the author has made some contribution to this aspect. Lastly a brief description of the constraints of the BOUT++ coordinate system is provided.

4.2.1 Structure of a Physics Module

A minimal working example of a BOUT++ physics module will consist of three files. The first is a C++ file, which in the example below is called wave.cxx. This file must contain a `physics_init` function, in which the initialisation of the simulation is prescribed, and a `physics_run` function that calculates the time derivatives of the evolving variables and is called with every iteration of the time solver. The second file is an input file, that by default is called BOUT.inp and is located in a directory called /data, where incidentally the simulation output data and log files are saved. In this input file, the parameters of the simulation can be specified, such as the output time-step and number of outputs, the spatial mesh, input parameters specific to the model, initial conditions and boundary conditions of evolving fields, the numerical methods used for spatial differentiation and the choice of time solver. The final file is a makefile, which specifies how the physics module is to be compiled. As an example, the simple 1D system

$$\frac{\partial f}{\partial t} = \frac{\partial g}{\partial x}, \quad \frac{\partial g}{\partial t} = \frac{\partial f}{\partial x}, \tag{4.1}$$

is implemented in Listings 4.1 and 4.2 below. These listings consist of less than 50 lines of code and illustrate how easy it is to develop simulations using BOUT++. For reference, a typical physics module consists of 100-1000 lines of code, whilst the core BOUT++ code contains approximately 30000 lines of code.

Listing 4.1: wave.cxx

```
#include <boutmain.hxx>
#include <derivs.hxx>
#include <interpolation.hxx>
```

```
// Declare evolving field variables
Field3D f, g ;
int physics_init(bool restart) {
  // Stagger g relative to f
  g.setLocation(CELL_XLOW) ;
  // Specify evolving fields to time solver
  SOLVE_FOR2(f,g) ;
  return 0 ;
}

int physics_run(BoutReal time) {
  // Evaluate ddx(g) on an un-staggered grid
  ddt(f) = DDX(g, CELL_CENTRE) ;
  // Evaluate ddx(g) on a staggered grid
  ddt(g) = DDX(f, CELL_XLOW) ;
  return 0 ;
}
```

Listing 4.2: BOUT.inp

```
nout = 20           # Number of output timesteps
timestep = 0.1      # Time between outputs
MZ = 1              # Number of points in z
MYG = 0             # Number of x guard cells
MXG = 2             # Number of y guard cells
StaggerGrids = true # Enable staggered grids

[mesh]
nx = 68             # Number of x points, including 4 guard cells
dx = 0.1            # x spacing
ny = 1              # Number of y points

[ddx]
first = C2          # Use second order central differencing

[f]
scale = 1.0
function = sin(3*(2*pi*x))     # Specify f initial condition
bndry_xin = dirichlet_o3(0)    # Specify f boundary conditions
bndry_xout = dirichlet_o3(0)

[g]
scale = 1.0
function = cos(2*(2*pi*x))
bndry_xin = neumann_o2(0)
bndry_xout = neumann_o2(0)
```

4.2.2 Time Integration

The Method of Lines

Fluid-like models typically consist of a system of Partial Differential Equations (PDEs) of the form

$$\frac{\partial \boldsymbol{f}}{\partial t} = \boldsymbol{F}\left(x, y, z, t, \boldsymbol{f}, \frac{\partial \boldsymbol{f}}{\partial x}, \frac{\partial \boldsymbol{f}}{\partial y}, \frac{\partial \boldsymbol{f}}{\partial z}, \frac{\partial^2 \boldsymbol{f}}{\partial x^2}, \frac{\partial^2 \boldsymbol{f}}{\partial y^2}, \frac{\partial^2 \boldsymbol{f}}{\partial z^2}, \frac{\partial^2 \boldsymbol{f}}{\partial x \partial y}, \frac{\partial^2 \boldsymbol{f}}{\partial x \partial z}, \frac{\partial^2 \boldsymbol{f}}{\partial y \partial z}, ...\right) \tag{4.2}$$

where $\boldsymbol{f}$ is a vector containing each of the fields which are evolved by the model and $\boldsymbol{F}$ is a general non-linear function. For example, in STORM3D, $\boldsymbol{f} = (n, \Omega, U, V)$, whilst $\boldsymbol{F}$ would correspond to the RHS of Equations (3.66) to (3.69). To solve such a system numerically, BOUT++ uses the Method of Lines [225], which consists of discretising the spatial domain and replacing all spatial derivatives with finite difference approximations. This allows the system of PDEs given by Equation (4.2) to be approximated as a system of Ordinary Differential Equations (ODEs) that can be written as

$$\frac{\partial \boldsymbol{g}}{\partial t} = \boldsymbol{G}\left(\boldsymbol{g}\right). \tag{4.3}$$

Here $\boldsymbol{g}$ is a vector whose elements correspond to the values of each of the fields in $\boldsymbol{f}$ at each grid point in the spatial domain. In the case of the STORM3D equations solved on a spatial domain of $N_x \times N_y \times N_z$ (where N_j is the number of grid points in the j coordinate direction), g would be a vector of length $4N_xN_yN_z$. The advantage of the Method of Lines is that it allows PDEs to be solved using one of the many well established numerical methods for ODEs.

Explicit Methods

One method of numerically solving Equation (4.3), is to discretise the time domain and to use the following first order forward finite difference approximation for the time derivative

$$\frac{\partial \boldsymbol{g}_n}{\partial t} \approx \frac{\boldsymbol{g}_{n+1} - \boldsymbol{g}_n}{\Delta t}. \tag{4.4}$$

Here Δt is the time step, whilst $\boldsymbol{g}_n$ and $\boldsymbol{g}_{n+1}$ are the values of $\boldsymbol{g}$ at $t = t_n$ and $t = t_n + \Delta t$ respectively. Equation (4.3) can then be rearranged to produce

$$\boldsymbol{g}_{n+1} = \boldsymbol{g}_n + \Delta t \boldsymbol{G}\left(\boldsymbol{g}_n\right). \tag{4.5}$$

This method is known as the Forward Euler method. It is referred to as an *explicit* method, as $\boldsymbol{g}_{n+1}$ is obtained using only values of $\boldsymbol{g}$ from previous time steps. Explicit methods are generally easy to implement, but the size of the time step used is constrained by the Courant–Friedrichs–Lewy (CFL) condition [226], which states that the method will not be stable (i.e the solution will not converge) if

$$\Delta t > \frac{h_x h_y h_z}{\mathcal{U}_x h_y h_z + \mathcal{U}_y h_x h_z + \mathcal{U}_z h_x h_y}. \tag{4.6}$$

The condition given here is for a system with three spatial dimensions, with h_j and $\mathcal{U}_j$ corresponding to the mesh spacing and the velocity of the system's fastest wave along the j coordinate direction. This condition means that explicit methods are unsuitable for *stiff* systems, i.e. those which contain time scales much faster than those of interest, because small time steps are required. Thus solving a stiff system with explicit methods can be computationally expensive. Unfortunately, plasma physics models are typically stiff [194].

Implicit methods

The alternative class of numerical integration methods to explicit methods are *implicit* methods. These methods provide an expression for the state of the system at a future time-step that implicitly depends on its state at that future time-step. Whilst implicit methods are generally much more complicated to implement and require more calculations for each time-step, they are not subject to the CFL condition and thus are more stable than explicit methods*. Therefore for stiff systems, an implicit method will be able to take significantly larger time steps than an explicit method and thus can be computationally less expensive overall, despite performing more calculations on each time step.

An example of an implicit method can be obtained by approximating the time derivative in Equation (4.3) with the following first order backwards finite difference approximation (as opposed to the forwards difference approximation used in Equation (4.4)):

$$\frac{\partial \boldsymbol{g}_n}{\partial t} \approx \frac{\boldsymbol{g}_n - \boldsymbol{g}_{n-1}}{\Delta t}. \tag{4.7}$$

Substituting this expression into Equation (4.3) and making the replacements $n \to n+1$, $n-1 \to n$, yields

$$\boldsymbol{g}_{n+1} = \boldsymbol{g}_n + \Delta t \boldsymbol{G}\left(\boldsymbol{g}_{n+1}\right). \tag{4.8}$$

This is referred to as the Backwards Euler method, and it can be seen that the expression for $\boldsymbol{g}_{n+1}$ is implicit because of the term $\boldsymbol{G}(\boldsymbol{g}_{n+1})$. This non-linear problem can be solved via a Newton iteration process by first writing

$$\boldsymbol{H}\left(\boldsymbol{g}_{n+1}\right) = \boldsymbol{g}_{n+1} - \boldsymbol{g}_n - \Delta t \boldsymbol{G}\left(\boldsymbol{g}_{n+1}\right) = 0. \tag{4.9}$$

An initial guess, $\boldsymbol{g}_{n+1}^m$, is then made for $\boldsymbol{g}_{n+1}$. A Taylor series expansion of $\boldsymbol{H}\left(\boldsymbol{g}_{n+1}\right)$ about this point gives

$$\boldsymbol{H}\left(\boldsymbol{g}_{n+1}\right) \approx \boldsymbol{H}\left(\boldsymbol{g}_{n+1}^m\right) + \left.\frac{\partial \boldsymbol{H}}{\partial \boldsymbol{g}_{n+1}}\right|_{\boldsymbol{g}_{n+1}=\boldsymbol{g}_{n+1}^m} \left(\boldsymbol{g}_{n+1} - \boldsymbol{g}_{n+1}^m\right). \tag{4.10}$$

The term $\partial \boldsymbol{H}/\partial \boldsymbol{g}_{n+1}$ can be calculated to be

$$\frac{\partial \boldsymbol{H}}{\partial \boldsymbol{g}_{n+1}} = \mathbb{I} - \Delta t \mathbb{J}, \tag{4.11}$$

where $\mathbb{I}$ is the identity matrix and $\mathbb{J}$ is the Jacobian matrix, given by

$$\mathbb{J} = \begin{pmatrix} \frac{\partial G_1}{\partial g_1} & \frac{\partial G_1}{\partial g_2} & \cdots \\ \frac{\partial G_2}{\partial g_1} & \frac{\partial G_2}{\partial g_2} & \cdots \\ \vdots & \vdots & \ddots \end{pmatrix}. \tag{4.12}$$

An improved guess, $\boldsymbol{g}_{n+1}^{m+1}$, for the value of $\boldsymbol{g}_{n+1}$ that satisfies $\boldsymbol{H}\left(\boldsymbol{g}_{n+1}\right) = 0$ can then be found by setting the LHS of (4.10) to zero, making the replacement $\boldsymbol{g}_{n+1} \to \boldsymbol{g}_{n+1}^{m+1}$ and rearranging:

$$\boldsymbol{g}_{n+1}^{m+1} = \boldsymbol{g}_{n+1}^m - \left(\mathbb{I} - \Delta t \mathbb{J}\big|_{\boldsymbol{g}_{n+1}=\boldsymbol{g}_{n+1}^m}\right)^{-1} \boldsymbol{H}\left(\boldsymbol{g}_{n+1}^m\right). \tag{4.13}$$

This expression can then be iterated until $\boldsymbol{H}\left(\boldsymbol{g}_{n+1}^m\right) = 0$ to within a specified tolerance.

By comparing this implicit Backwards Euler method with the explicit Forward Euler method of Equation (4.5), the increased computational cost of implicit schemes is apparent in

*Many implicit schemes are in fact unconditionally stable

that the implicit scheme requires a Jacobian matrix to be calculated and stored, and a matrix inversion problem to be solved at every iteration of every time step. It is emphasised that the size of these matrices scale linearly with the total number of spatial grid points in the domain and so these calculations can become prohibitively expensive.

One way to reduce this computational cost is to construct the method such that the Jacobian is only ever used as a matrix-vector product of the form $\mathbb{J}\boldsymbol{u}$. This can then be approximated as

$$\mathbb{J}\boldsymbol{u} \approx \frac{\boldsymbol{G}\left(\boldsymbol{g}_{n+1} + \epsilon\boldsymbol{u}\right) - \boldsymbol{G}\left(\boldsymbol{g}_{n+1}\right)}{\epsilon}, \tag{4.14}$$

where ϵ is a small perturbation [227]. By using this approximation, or an equivalent one of higher order, there is no need to compute and store the Jacobian at every iteration of every time step. A review of such *Jacobian-free* methods can be found in Reference [227]. It is noted however that these methods remain relatively computationally costly as they still require a matrix inversion problem to be solved every iteration.

Time Solvers in BOUT++

BOUT++ has a variety of time integration methods that can be selected at runtime. The explicit methods include the Forwards Euler method, the Karniadakis method [228], the 4th order Runge-Kutta method [229] and the 3rd order Runge-Kutta Strong Stability Preserving method [230].

The default implicit method is provided through the PVODE solver [231], which is distributed as part of BOUT++. PVODE implements a Backwards Difference Formula (BDF), which is conceptually similar to the Backwards Euler Method described previously, but using more previous time points to achieve higher accuracy. The order and time step of the integration is dynamically varied to attempt to obtain a solution with the minimum number of steps but that also meets the specified error tolerances [231]. As in the Backwards Euler method, a Newton iteration is required on each time step, in which a problem similar to the form of Equation (4.13) is solved, but with Δt multiplied by a constant that depends on the order being used. PVODE formulates this problem in a Jacobian-free form and then obtains the solution iteratively via the Scaled Preconditioned GMRES method [232], which is a Krylov subspace method [227].

BOUT++ is also compatible with a number of other external implicit solvers. These include CVODE and IDA from the SUNDIALS suite [233], as well as the time solvers provided in the PETSc suite [234].

4.2.3 Implementation of Boundary Conditions

In BOUT++, boundary conditions are enforced in the x and y boundaries through additional *guard* or ghost points on either side of the domain, as shown in Figure 4.1. It can be seen that for un-staggered grids, the boundary is defined to be located half-way between grid points, whilst for staggered grids, the boundaries is located on grid points exactly. The three standard boundary conditions used in this work are:

i *Dirichlet*

This boundary condition type specifies that a field, f, must have the specified values g on the boundary, i.e.

$$f|_b = g,$$

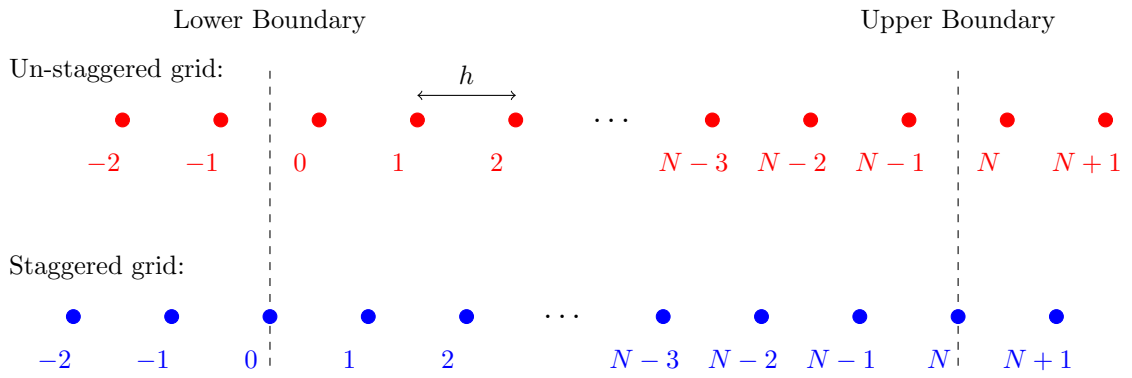

Figure 4.1: Structure of un-staggered and staggered grids at the x and y boundaries in BOUT++.

where $|_b$ denotes the boundary value.

ii *Neumann*
This boundary condition type specifies the gradient of the field f to have specific values on the boundary, i.e for an x boundary, this condition enforces

$$\left.\frac{\partial f}{\partial x}\right|_b = g.$$

iii *Free*
This boundary condition sets no constraint on the field at the boundary at all.

The grid points through which the boundary conditions are implemented (following Figure 4.1's notation, on an un-staggered grid these are indices -2, -1, N and $N+1$, whilst on a staggered grid, these are indices -2, -1, 0, N and $N+1$) are only used when evaluating spatial derivatives near to the boundary, which involve division by h for first derivatives and by h^2 for second derivatives. Therefore to implement an $\mathcal{O}\left(h^2\right)$ boundary condition (i.e. one that allows global $\mathcal{O}\left(h^2\right)$ convergence to be obtained), the boundary grid points must be specified to $\mathcal{O}\left(h^3\right)$ if first order spatial derivatives are present. It has been observed that $\mathcal{O}\left(h^3\right)$ boundary grid points are also sufficient if second derivatives are present and it is speculated that this is because the diffusive nature of second derivatives act to dissipate the expected $\mathcal{O}\left(h\right)$ error. This is fortunate because specifying the boundary grid points to $\mathcal{O}\left(h^4\right)$ has been found to cause numerical stability issues.

In BOUT++, Dirichlet, Neumann and Free boundary conditions can be specified to a variety of orders of accuracy in terms of the mesh spacing, h, up to 4th order, $\mathcal{O}\left(h^4\right)$. The implementations used by the STORM physics modules are documented in Tables 4.1 to 4.3. These are all $\mathcal{O}\left(h^2\right)$ implementations and are selected in the input file using the descriptions `dirichlet_o3(g)`, `neumann_o2(g)` and `free_o3`, where `g` is the value or expression to which boundary conditions are set to*.

4.2.4 A Note on the BOUT++ Coordinate System

The differential operators in BOUT++ have all been written with the implicit assumption that the magnetic field is aligned to the y coordinate, whilst the z direction is always periodic.

*The meaning of the numbers in each of these descriptions are not consistent. It is emphasised that all three boundary conditions are $\mathcal{O}\left(h^2\right)$ boundary conditions. In `dirichlet_o3(g)` and `free_o3`, the `3` refers to the order to which the boundary grid points have been specified to, whilst in `neumann_o2(g)` the `2` refers to the order of the boundary condition itself.

Table 4.1: Implementation of the Dirichlet boundary condition, $f|_b = g$ to order $\mathcal{O}\left(h^3\right)$ in BOUT++. Here the subscripts refer to the grid point index as labelled in Figure 4.1.

Boundary	Grid	Implementation
Lower	Un-staggered	$f_{-1} = (8g - 6f_0 + f_1)/3$ $f_{-2} = 3f_{-1} - 3f_0 + f_1$
Lower	Staggered	$f_0 = g$ $f_{-1} = 3f_0 - 3f_1 + f_2$ $f_{-2} = 3f_{-1} - 3f_0 + f_1$
Upper	Un-staggered	$f_N = (8g - 6f_{N-1} + f_{N-2})/3$ $f_{N+1} = 3f_N - 3f_{N-1} + f_{N-2}$
Upper	Staggered	$f_N = g$ $f_{N+1} = 3f_N - 3f_{N-1} + f_{N-2}$

Table 4.2: Implementation of the Neumann boundary condition, $(\partial f/\partial x)|_b = g$ to order $\mathcal{O}\left(h^3\right)$ in BOUT++. Here the subscripts refer to the grid point index as labelled in Figure 4.1.

Boundary	Grid	Implementation
Lower	Un-staggered	$f_{-1} = f_0 - gh$ $f_{-2} = f_1 - 3gh$
Lower	Staggered	$f_0 = (4f_1 - f_2 - 2gh)/3$ $f_{-1} = f_1 - 2gh$ $f_{-2} = f_2 - 4gh$
Upper	Un-staggered	$f_N = f_{N-1} + gh$ $f_{N+1} = f_{N-2} + 3gh$
Upper	Staggered	$f_N = (4f_{N-1} - f_{N-2} + 2gh)/3$ $f_{N+1} = f_{N-1} + 2gh$

Table 4.3: Implementation of the free boundary condition, to order $\mathcal{O}\left(h^3\right)$ in BOUT++. Here the subscripts refer to the grid point index as labelled in Figure 4.1.

Boundary	Grid	Implementation
Lower	Un-staggered	$f_{-1} = 3f_0 - 3f_1 + f_2$ $f_{-2} = 3f_{-1} - 3f_0 + f_1$
Lower	Staggered	$f_0 = 3f_1 - 3f_2 + f_3$ $f_{-1} = 3f_0 - 3f_1 + f_2$ $f_{-2} = 3f_{-1} - 3f_0 + f_1$
Upper	Un-staggered	$f_N = 3f_{N-1} - 3f_{N-2} + f_{N-3}$ $f_{N+1} = 3f_N - 3f_{N-1} + f_{N-2}$
Upper	Staggered	$f_N = 3f_{N-1} - 3f_{N-2} + f_{N-3}$ $f_{N+1} = 3f_N - 3f_{N-1} + f_{N-2}$

However, the governing equations in Chapter 3 have all been written with the magnetic field aligned to z, as is standard in the literature. Therefore, to implement these equations in BOUT++, the following transformations were made

$$y \to z, \quad z \to -y. \tag{4.15}$$

Throughout the remainder of this chapter and thesis however, the notation used will be consistent with the coordinate system used in Chapter 3 (i.e. the magnetic field will be described as being in the z direction and the simulation domain will be described as periodic in the y direction).

4.3 STORM Physics Modules

Both the 3D and 2D models presented in Chapter 3 have been implemented in a pair of BOUT++ physics modules, which have been collectively named *STORM* (Scrape-off layer TuRbulence Models). In particular, the 3D model comprising of Equations (3.66) to (3.69) have been implemented in the *STORM3D* physics module, whilst the sheath dissipation model and vorticity advection models both have been implemented in the *STORM2D* physics module, with input options controlling which parallel closure is used. In this section the specific details of these implementations are provided. Only the default configuration will be considered and where alternative numerical methods have been used in Chapters 5 to 7, this will noted as appropriate.

4.3.1 Time Integration

Time integration in the STORM physics modules is carried out using the PVODE solver. It has been noted that the 4th order Runge-Kutta method often produces a reduced computational cost for STORM3D simulations if the largest stable time step is used. However, since this time-step size is simulation dependent and generally unknown, the implicit PVODE solver is preferred because the increased computational cost is not significant and the simulations are more robustly stable.

4.3.2 Spatial Differentiation

All of the spatial derivatives are calculated using second order accurate schemes and thus the STORM codes themselves are second order accurate. This accuracy has been verified for STORM3D in Section 5.4. More specifically, parallel advection terms (i.e. $U\nabla_\parallel$, $V\nabla_\parallel$) are calculated using an upwind scheme, an Arakawa scheme [235] is used for the perpendicular $\boldsymbol{E} \times \boldsymbol{B}$ advection terms and all other derivatives are calculated using central difference formulations.

4.3.3 Laplacian Inversion

To obtain the electrostatic potential, a Laplacian Inversion must be performed on the vorticity, since

$$\Omega = \nabla_\perp^2 \phi. \tag{4.16}$$

In the STORM simulations, this inversion problem is effectively a series of N_z decoupled problems, where N_z is the number of grid points along the parallel direction. The inversion

procedure is carried out using Fourier transforms as follows. Since the y direction is periodic, Equation (4.16) can be Fourier transformed in this direction to produce

$$\frac{\partial^2 \hat{\phi}_{k_y}}{\partial x^2} + {k_y}^2 \hat{\phi}_{k_y} = \hat{\Omega}_{k_y}, \tag{4.17}$$

where $\hat{f}_{k_y}$ denotes the k_y^{th} Fourier mode of field f. This Fourier transform further decomposes the system into $N_y N_z/2$ decoupled sub-problems, where N_y is the number of grid points in y. The second derivative in Equation (4.17) is then written using a central difference scheme, meaning that each sub problem becomes a tri-diagonal matrix inversion problem of size N_x, where N_x is the number of grid points in x. These individual tri-diagonal matrix problems are then easily solved using a Thomas-like algorithm [236], before the solutions are Fourier transformed back to real space. This Fourier method is used because it is significantly less computationally expensive than inverting N_z fully populated matrices of size $N_x N_y$. To be precise, the FFT algorithm on an array of length N has a number of operations of order $\mathcal{O}(N \ln N)$, whilst the Thomas algorithm to invert a tri-diagonal matrix of size N requires $\mathcal{O}(N)$ operations. In contrast, the most efficient algorithm for inverting a fully populated matrix scales like $\mathcal{O}\left(N^{2.37}\right)$ [237]. Therefore, the Fourier Laplacian inversion method has a complexity of $\mathcal{O}(N_x N_z N_y \ln N_y)$, compared to a complexity of $\mathcal{O}\left(N_y \left(N_x N_z\right)^{2.37}\right)$ that would otherwise be required.

It is noted that this Fourier method can only be used by virtue of having made the Boussinesq approximation, which is the primary reason why non-Boussinesq simulations are so much more computationally expensive to perform, and therefore why the approximation has been made here*.

4.3.4 Staggered Grids

For numerical stability, the parallel velocity fields, U and V, are staggered in the parallel direction relative to the other fields in STORM3D, as shown in Figure 4.1. Without this staggered approach, a chequerboard-like instability[239] arises due to the $\nabla_\parallel n$ and $\nabla_\parallel \phi$ terms in Equations (3.68) and (3.69). The parallel velocities were chosen to be staggered rather than the other fields because it is more convenient to enforce their Dirchlet-type parallel boundary conditions on a staggered grid as their boundaries then lie exactly on grid points.

4.3.5 Boundary Conditions

In all of the 3D filament simulations presented in this work, the parallel direction of the SOL is assumed to be symmetric about $z = 0$, where a stagnation point in the parallel velocities occurs. Therefore for computational efficiency only half the parallel length of the SOL is simulated from $z = 0$ to $z = L_\parallel$. To implement this, the following symmetry boundary conditions were enforced at $z = 0$, which hereafter will be referred to as the *mid-plane* position:

$$\left.\frac{\partial \Omega}{\partial z}\right|_{z=0} = 0, \quad \left.\frac{\partial n}{\partial z}\right|_{z=0} = 0, \quad \left.\frac{\partial \phi}{\partial z}\right|_{z=0} = 0, \quad U|_{z=0} = 0, \quad V|_{z=0} = 0. \tag{4.18}$$

*By using multi-grid methods, the additional computational cost associated with non-Boussinesq simulations can be significantly reduced[238].

At $z = L_\parallel$, the boundary conditions given by Equations (3.70) and (3.72) are enforced:

$$U|_{z=L_\parallel} \geq \frac{1}{\sqrt{1+1/\mu}}, \tag{4.19}$$

$$V|_{z=L_\parallel} = \frac{1}{\sqrt{1+1/\mu}} \exp\left(-\phi|_{z=L_\parallel}\right). \tag{4.20}$$

Since both of these boundary conditions are non-standard Dirichlet conditions, they are implemented within the STORM3D physics module. In particular, the $\geq$ operator in Equation (3.70) is implemented by first calculating the value of $U|_{z=L_\parallel}$ that would be produced by extrapolating it from the inner domain grid points (as in a free boundary condition). If it is $\geq 1/\sqrt{1+1/\mu}$, the boundary grid point is set to this extrapolated value, otherwise the boundary grid point is set to $1/\sqrt{1+1/\mu}$. Free boundary conditions were used for the remaining fields at $z = L_\parallel$ so that the system was not over constrained. It is noted that STORM3D also offers the option to represent the entire length of the SOL from $z = -L_\parallel$ to $z = L_\parallel$ by enforcing Equations (3.71) and (3.73) at the lower z boundaries, although such functionality was not used in this work.

Regarding the perpendicular boundaries, the y direction was periodic as necessitated by the use of the BOUT++ framework, whilst at the x boundaries of the domain located at $x = 0$ and $x = L_x$, conditions were enforced such that steady state and perpendicularly uniform equilibrium fields with variation only in the parallel direction could be obtained. These specified zero gradients in the x direction at both boundaries for all fields but ϕ, which was set to its equilibrium profile $\phi_{eq}(z)$:

$$\left.\frac{\partial \Omega}{\partial x}\right|_{x=0,L_x} = 0, \ \left.\frac{\partial n}{\partial x}\right|_{x=0,L_x} = 0, \ \left.\frac{\partial V}{\partial x}\right|_{x=0,L_x} = 0, \ \left.\frac{\partial U}{\partial x}\right|_{x=0,L_x} = 0, \ \phi|_{x=0,L_x} = \phi_{eq}. \tag{4.21}$$

However, since ϕ_{eq} cannot be determined *a priori*, it had to be obtained using the iterative procedure described in Section 4.4.1. It is noted that zero gradient Neumann conditions could not be used on the x boundaries of ϕ because this would mean that the Laplacian inversion problem of Equation (4.16) would not have a unique solution for ϕ.

In STORM2D, identical boundary conditions were set on the perpendicular boundaries of n, and Ω, whilst the x boundaries of ϕ were fixed to zero:

$$\phi|_{x=0,L_x} = 0. \tag{4.22}$$

4.3.6 1D Potential Solver

As shown in Appendix A, in a system with no variation in the perpendicular directions, the parallel current is necessarily zero, $J_\parallel = 0$, and the electrostatic potential exhibits an exact Boltzmann response, meaning that the the parallel gradient of the electrostatic potential can be expressed as

$$\nabla_\parallel \phi = \frac{\mu}{\mu+1} \nabla_\parallel \ln n. \tag{4.23}$$

Parallel potential gradient terms are only present in Equations (3.68) and (3.69). As discussed previously, the V and U fields are staggered in the parallel direction relative to ϕ and a second order accurate central differencing scheme is used for $\nabla_\parallel$ terms. This means that $\nabla_\parallel \phi$ is always evaluated in the STORM3D code as

$$\left(\nabla_\parallel \phi\right)_i = \frac{\phi_i - \phi_{i-1}}{h_y}. \tag{4.24}$$

Here $\left(\nabla_\parallel \phi\right)_i$ is located on a staggered grid, h_y is the grid spacing in the parallel direction and the subscripts denote the grid point index as labelled in Figure 4.1. Therefore, if the density field is known in a 1D system, the electrostatic potential can be numerically integrated using

$$\phi_{i+1} = \phi_i + \frac{\mu}{\mu+1}\left(\nabla_\parallel \ln n\right)_{i+1} h_y \tag{4.25}$$

and the boundary condition

$$\phi|_{y=\pm L_\parallel} = 0, \tag{4.26}$$

which ensures that no current enters the sheath, consistent with $J_\parallel = 0$. This method for obtaining ϕ, hereafter referred to as the *1D Potential Solver*, is very useful as it allows the STORM3D physics module to operate effectively as a 1D code that describes the dynamics only along the field line. In particular this solver has been used to reduce the computational cost of obtaining 1D equilibrium fields as outlined in 4.4.1. Furthermore it has also been used in the verification of parallel dynamics detailed in Section 5.3.

4.4 Filament Simulation Initialisation

4.4.1 Generating Equilibria

To investigate the dynamics of individual filaments, steady state equilibrium fields with variation only in the parallel direction were required onto which filament perturbations could be seeded. Furthermore, it was preferable to have minimal parallel velocities and gradients in the parallel direction for as much of the domain as possible so that the equilibrium did not drastically influence the dynamics of filaments. This was achieved by using the density source of the form

$$S_n = \alpha \frac{10\exp\left(10z/L_\parallel\right)}{L_\parallel\left(\exp\left(10\right)-1\right)}. \tag{4.27}$$

This source is primarily localised in the last 10% of the domain nearest the target and, as documented in Section 5.2, produces an equilibrium of the desired form. The parameter α linearly scales the resulting equilibrium density field. Physically, this represents a localised ionisation source in the proximity of the target, given for example by recycling from the targets.

To obtain the equilibrium fields, an iterative procedure was required because, as described in Section 4.3.5, the x boundaries of ϕ must be set to $\phi_{eq}\left(z\right)$ to obtain uniform fields in the perpendicular direction. This iterative procedure consisted of evolving a simulation for a considerable time, to say $t = 1000\Omega_i$, with an initial guess for ϕ_{eq}. The x boundaries of ϕ were then updated to the parallel profile of the steady state ϕ profile at $x = L_x/2$, and the simulation was then restarted and evolved again. This procedure was then repeated until steady state equilibrium fields were obtained which were uniform in the perpendicular direction. This procedure can be sped up by utilising only 1 grid point in the x and y directions and employing the 1D potential solver described in Section 4.3.6. The equilibria produced via this method have been verified against analytic results in Section 5.2.

4.4.2 Filament Initialisation

Defining the density perturbation associated with a filament to be $n_f = n - n_{eq}$, the 3D filament simulations in this work were initialised such that

$$n_f|_{t=0} = \frac{A\ n_{eq}|_{z=0}}{2}\exp\left(-\frac{\left(x-x_0\right)^2+\left(y-y_0\right)^2}{\hat{\delta}_\perp^2}\right)\left(1-\tanh\left(\frac{z-L_f}{\hat{\delta}_\parallel}\right)\right). \tag{4.28}$$

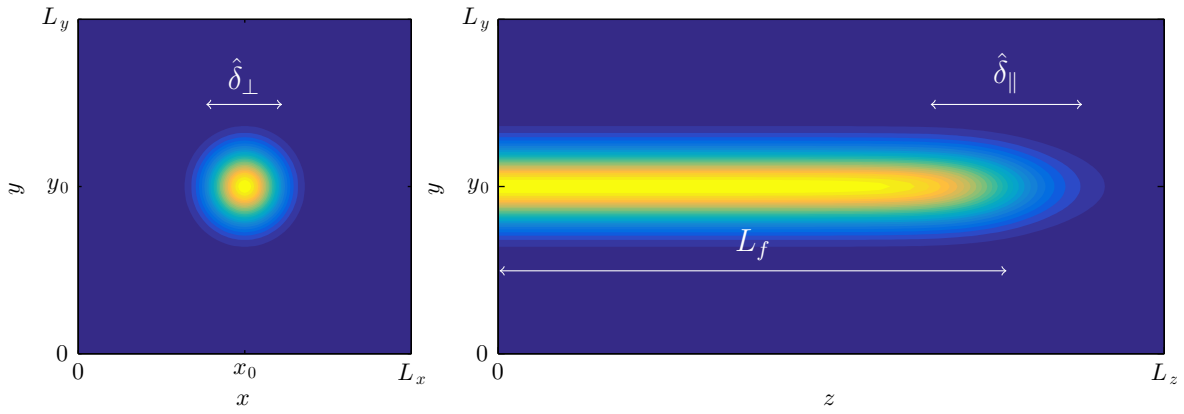

Figure 4.2: Schematic diagram of the geometry of the initialised filament density perturbation. The peak density in the figure is $A\, n_{eq}|_{z=0}$.

Hence the filaments were seeded with Gaussian profiles in the perpendicular plane centred at (x_0, y_0), with normalised perpendicular length scale $\hat{\delta}_\perp = \delta_\perp/\rho_s$ and peak amplitude $A\, n_{eq}|_{z=0}$. In the parallel direction, they are initialised to extend broadly from $z = 0$ to $z = L_f$, where $L_f = \ell_f/\rho_s$. The steepness of the filament front in the parallel direction is controlled through the normalised parameter $\hat{\delta}_\parallel = \delta_\parallel/\rho_s$, with $\hat{\delta}_\parallel = 0$ corresponding to a step function, and $\hat{\delta}_\parallel = \infty$ corresponding to the filament being uniform perturbation in the parallel direction with peak amplitude of $A\, n_{eq}|_{z=0}\,/2$. A schematic diagram of this filament geometry is shown in Figure 4.2.

In the STORM2D simulations, the equilibrium fields were simply specified to be $n_{eq} = 0$, $\Omega_{eq} = 0$ and $\phi_{eq} = 0$, whilst the filaments were initialised as

$$n_f|_{t=0} = A \exp\left(-\frac{(x - x_0)^2 + (y - y_0)^2}{\hat{\delta}_\perp^2}\right). \tag{4.29}$$

Chapter 5

Code Verification and Validation

5.1 Introduction

In the context of computational physics, code verification and validation is the procedure of ensuring that a code reliably simulates the particular physical processes it is designed to represent. This process can be split into two key tasks. The first is to ensure that the model equations are being solved correctly, consistently and to the order of accuracy that is expected. This is *code verification*, and essentially it is the process of ascertaining that there are no errors or *bugs* in the code. The second task, *code validation*, is to check that the model equations being used are valid and represent physical reality. The process of code verification and validation can be thus be summarised as two questions:

1. Are the model equations being solved correctly? (Verification)

2. Do the model equations represent physical reality? (Validation)

The difficulty of code verification lies in finding something against which the code's results can be compared, because unless obviously spurious or unphysical results are produced, it is difficult to tell that there is a problem. Benchmarks can be made against other simulation codes, but there is no guarantee that the comparison codes are error free. Moreover, there are a large number of potential differences between two codes that could cause disagreements. For example, discrepancies could be caused by differences in the equations being solved, the numerical methods utilised or the discretisation used. Therefore it is difficult to determine whether a disagreement is caused by one of these legitimate differences or due to an error in one of the codes. Furthermore, if the legitimate differences can be ruled out, determining which code contains the error can also be quite a challenge (especially if both codes contain errors!).

The use of analytical results for purposes for verification is therefore preferable where possible, as this allows for convergence to be reliably tested and the order of accuracy of the numerical methods to be assessed. Unfortunately simulation codes are typically used for problems that do not have analytical solutions (if a problem has an analytic solution, why bother solving it numerically?). Therefore analytical results can generally only be used to test simplified cases and hence cannot fully verify all aspects of a simulation code. This limitation can be overcome by using the Method of Manufactured Solutions [240] (MMS), which is a methodology that has been used previously within the field of computational fluid dynamics and has more recently been used to verify the SOL simulation code GBS [241].

For code validation, obtaining experimental measurements to compare against is also a challenge. This is particularly the case in plasma physics, where error bars to within a factor of two are commonplace. For the specific case of SOL filaments, which are the subject of this thesis, there are few devices in which key properties of the filaments, such as their perpendicular size and velocities, can be measured at all. One machine that is able to provide such measurements and thus has been used to validate the STORM physics modules is the TORPEX device, which is a Simple Magnetised Torus (SMT).

This chapter details the verification and validation that has been completed for the STORM physics modules. In Section 5.2, the equilibrium fields used throughout this thesis are verified against both analytic results and against other existing SOL codes. Section 5.3 describes the verification of the shock tube problem, which consists of the propagation of a shock wave and an expansion wave along the parallel direction, again by comparison against analytic theory and other SOL codes. The last and most rigorous verification carried out uses the MMS to test the convergence and order of accuracy of the code. Section 5.4 provides a description of the method and the various issues that were encountered in testing, before presenting the verification results. Finally, the results of a validation exercise against experimental measurements from the TORPEX device are presented in Section 5.5.

5.2 Verification of Equilibrium

In this section the equilibrium fields used throughout this thesis are verified against analytical solutions. These equilibrium fields, which are uniform in both perpendicular directions, were obtained using a particle source which varied only in the parallel direction, i.e. $S_n = S_n(z)$. A description of how these equilibrium fields were obtained in the simulations and in particular how the appropriate Dirichlet boundary condition on the x boundary of the ϕ field was determined, is provided in Section 4.4.1.

5.2.1 Analytical Solution

Assuming uniformity in the perpendicular direction and given that $S_n = S_n(z)$, it is shown analytically in Appendix A that the steady state equilibrium solution to the governing equations of the 3D model, Equations (3.66) to (3.69) is given by:

$$\Omega_{eq} = 0, \tag{5.1}$$

$$n_{eq} = \frac{\sqrt{1+\frac{1}{\mu}}\int_0^z S_n\left(z'\right)\mathrm{d}z'}{\alpha - \sqrt{\alpha^2-1}}, \tag{5.2}$$

$$U_{eq} = V_{eq} = \frac{\alpha - \sqrt{\alpha^2-1}}{\sqrt{1+1/\mu}}, \tag{5.3}$$

$$\phi_{eq} = -\frac{\mu}{1+\mu}\ln\left(\alpha^2 - \alpha\sqrt{\alpha^2-1.}\right), \tag{5.4}$$

where the subscript eq denotes the equilibrium of the quantity and

$$\alpha = \frac{\int_0^{L_\parallel} S_n\left(z'\right)\mathrm{d}z'}{\int_0^z S_n\left(z'\right)\mathrm{d}z'}. \tag{5.5}$$

5.2.2 Error Measurements

In order to verify the equilibriums produced by the simulation code against the preceding analytical solutions, a quantitative measure of the error produced by the code is required. One useful measure of the error on a field, f, is given by the norm or root-mean-square of the difference between the numerical solution and the analytical solution, f^a. This is defined as

$$\epsilon_{rms} = \|f - f^a\|, \tag{5.6}$$

where

$$\|f\| = \sqrt{\frac{1}{N}\sum_{i=1}^{N} {f_i}^2}, \tag{5.7}$$

the subscript denotes the index of the grid point and N is the total number of grid points in the variable f. Another useful measure is given by the maximum absolute value of the difference between the numerical solution and analytical solution.

$$\epsilon_{max} = \max\left(|f - f^a|\right) \tag{5.8}$$

Both error measures should converge at the order to which the numerical schemes have been implemented. In STORM3D this is second order, unless a first order upwinding scheme is used. All simulation points within the domain of interest (including points on, but not beyond the boundary) should be included in these measures.

5.2.3 Calculation of the Convergence Order

The error produced by a numerical method can be written as:

$$\epsilon = Ch^P + \mathcal{O}(h^{P+1}), \tag{5.9}$$

where C is a constant, h is the (temporal or spatial) mesh spacing and P is the convergence order of the method. Assuming simulations are performed with sufficient resolution such that the asymptotic limit is reached, the $\mathcal{O}(h^{P+1})$ term will tend to zero and ϵ will be dominated by the Ch^P term. Taking the logarithm of Equation (5.9) in this regime produces:

$$\log(\epsilon) = \log(C) + P\log(h) \tag{5.10}$$

Therefore by performing two simulations in this asymptotic limit with different mesh spacings h_1 and h_2 which produce errors ϵ_1 and ϵ_2 respectively, the convergence order exhibited by the code can be evaluated as:

$$P = \frac{\log\left(\epsilon_1/\epsilon_2\right)}{\log\left(h_1/h_2\right)}. \tag{5.11}$$

Typically in practice convergence is assessed by plotting $\log(h)$ against $\log(\epsilon)$ for successively smaller mesh resolutions until straight lines are produced, indicating that the asymptotic regime has been found.

5.2.4 Results

The verification of the equilibrium fields has been completed on a parallel domain of length $L_\parallel = 5500$ with $\mu = 3646$. These parameters are representative of the values used in the

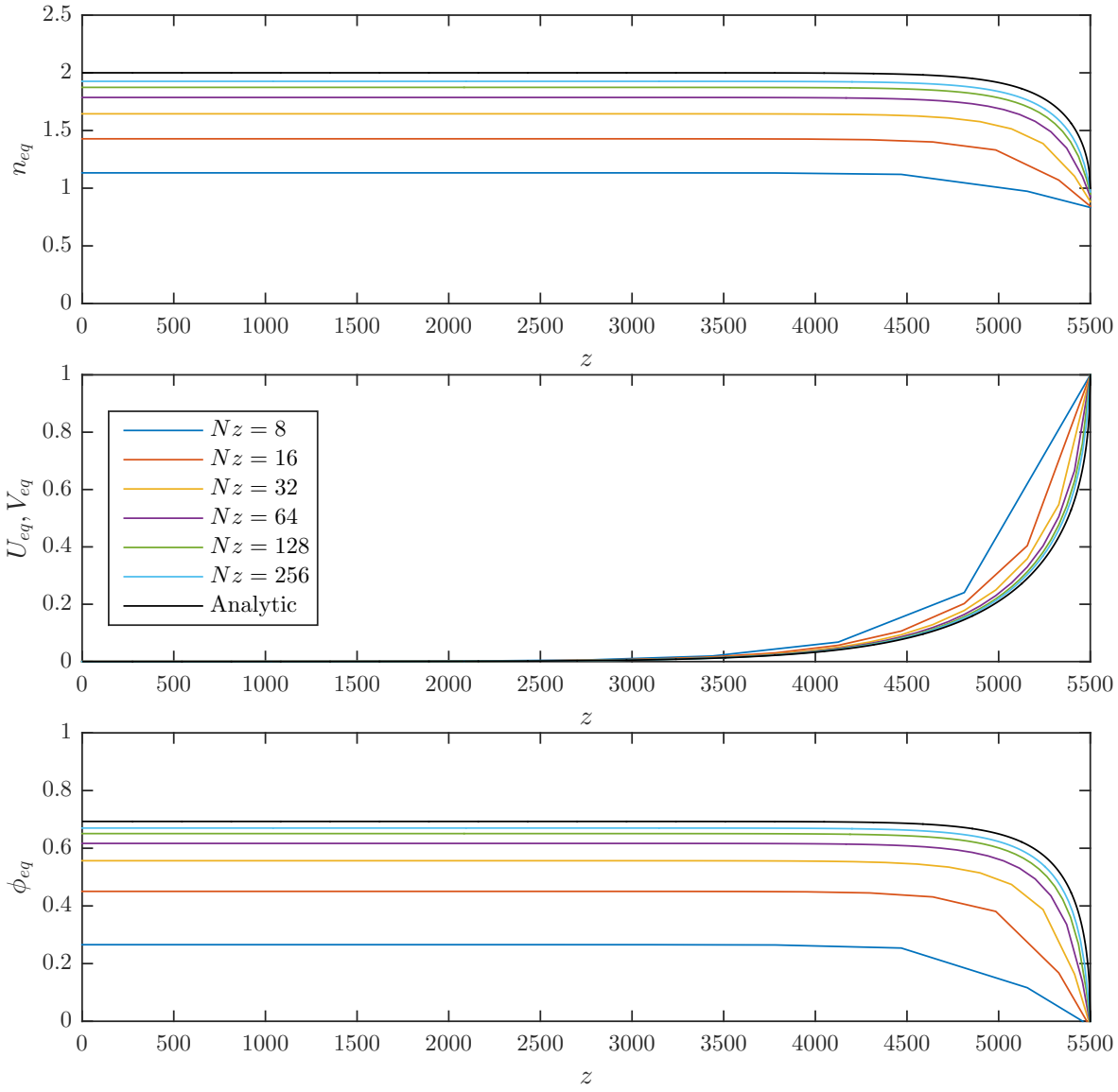

Figure 5.1: Equilibrium fields produced using various parallel resolutions, N_z, alongside analytical solutions.

filament dynamics simulations presented in Chapters 6 and 7, and are relevant to MAST. In addition, the same particle source, given by

$$S_n = \frac{\exp\left(10z/L_\parallel\right)}{L_\parallel\left(\exp\left(10\right) - 1\right)}, \tag{5.12}$$

has been used here as in the later filament simulation results. The remaining parameters of the model, such as $\hat{\eta}_\parallel$, $\hat{g}$ and the perpendicular domain size have not been listed here, as they do not have any influence on the equilibrium fields produced. The exact method by which the equilibrium fields were generated, and in particular how the boundary condition on the x boundaries of the ϕ field was obtained, is described in Section 4.4.1. A second order upwind scheme was used for advective derivatives of the form $U\nabla_\parallel$, $V\nabla_\parallel$, whilst second order central differences were used for all other derivatives.

Figure 5.1 plots the equilibrium fields for n, U, V and ϕ produced using parallel resolutions ranging from $N_z = 8$ to $N_z = 256$, increasing by factors of two. In addition, the analytical solutions given by Equations (5.2) to (5.4) are also plotted in black. It is clear that as the resolution is increased, the numerical equilibrium fields converge to their analytic solutions.

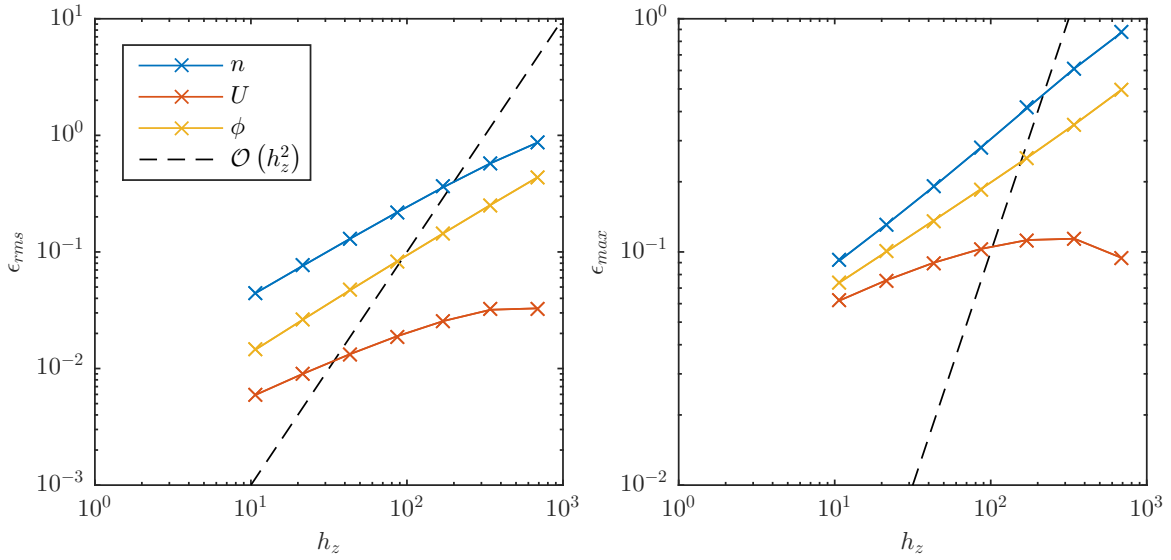

Figure 5.2: Magnitude of the root mean square error (left), ϵ_{rms}, and maximum error (right), ϵ_{max}, of the equilibrium solution plotted against the parallel mesh spacing, h_z. By comparison with the black dashed lines demonstrating $\mathcal{O}\left(h_z^2\right)$ convergence, it can be seen that no field obtains second order convergence.

This convergence towards the analytic solution is explicitly demonstrated in Figure 5.2, which plots ϵ_{max} and ϵ_{rms} against the grid spacing along the parallel direction, $h_z = L_\parallel/N_z$ for values of N_z up to 512. It is evident that as the grid spacing is reduced, both error measures for all fields become smaller and thus the results are converging to the analytical solution. Also plotted for comparison in each sub-plot of the figure is a dashed black line displaying $\mathcal{O}\left(h_z^2\right)$ scaling, which is the order to which the numerical schemes used have been implemented. Neither error measure of any of the fields converges at second order, which on first glance could be interpreted as an indication that there is a problem in the implementation of the code.

However, it is shown analytically in Appendix A that $\nabla_\parallel U$ will diverge when $U = 1/\sqrt{1+1/\mu}$ and that U must satisfy $U < 1/\sqrt{1+1/\mu}$ everywhere in the domain for the gradient to remain finite. Since $U = 1/\sqrt{1+1/\mu}$ is actually imposed as a sheath boundary condition, this means that the analytical solution of U has an infinite gradient at that boundary, as can be seen in Figure 5.1. It is believed that this singularity in the gradient of U prevents the finite difference approximations used (to calculate the parallel derivatives) from converging at their theoretical order of accuracy. This hypothesis is supported by a convergence study carried out in which the boundary conditions

$$U|_{z=L_\parallel} = \frac{1}{2}, \tag{5.13a}$$

$$V|_{z=L_\parallel} = \frac{1}{2}\exp\left(-\phi|_{z=L_\parallel}\right), \tag{5.13b}$$

were imposed instead of Equations (3.70) and (3.72), so that $\nabla_\parallel U$ remained finite within the simulation domain. In this case the expected second order convergence was recovered for each of the equilibrium fields, as demonstrated in Figure 5.3.

Additional simulations have been performed with $\mathcal{O}\left(h^3\right)$ boundary conditions enforced at the sheath, which produced effectively the same convergence as that shown in Figure 5.2 (which was obtained using $\mathcal{O}\left(h^2\right)$ boundary conditions). The problem therefore cannot be solved by using higher order boundary conditions.

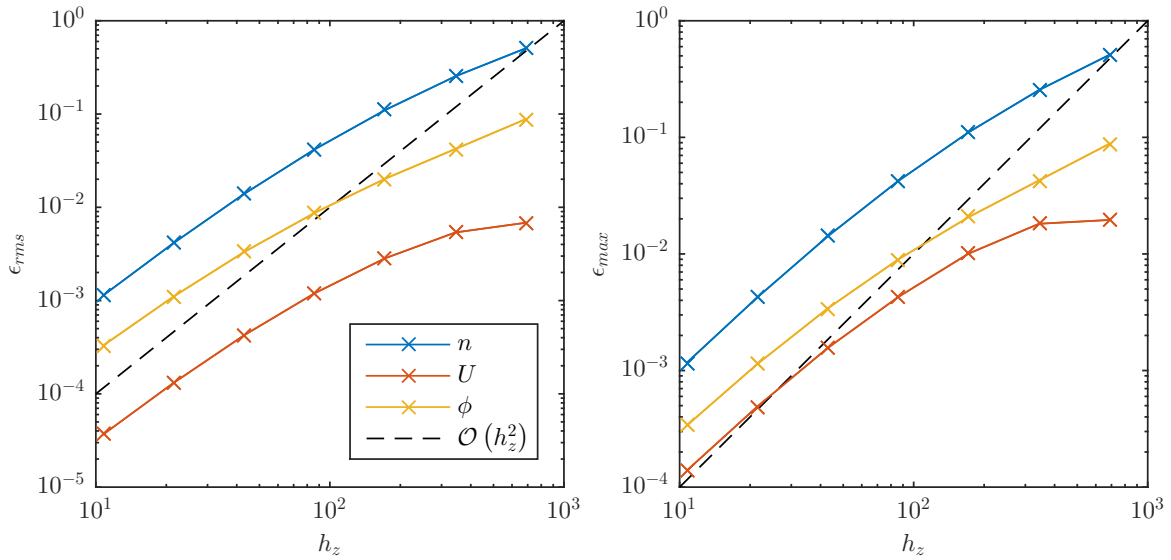

Figure 5.3: Magnitude of the root mean square error (left), ϵ_{rms}, and maximum error (right), ϵ_{max}, of the equilibrium solution plotted against the parallel mesh spacing, h_z, for the case in which the boundary conditions given by Equation (5.13) were imposed. By comparison with the black dashed lines demonstrating $\mathcal{O}\left(h_z^2\right)$ convergence, it can be seen that second order convergence is obtained by all fields.

It is concluded that whilst the simulation code does converge to the analytic equilibrium solution, it does not do so at the order to which the numerical methods have been implemented. Whilst this is clearly not ideal, it is not a disastrous result. As demonstrated in Figure 5.1, the key features of the analytical equilibrium fields are reproduced by the code; namely that they are all uniform throughout the majority of the domain except for in the locality of the sheath boundary where steep gradients exist. Without a solution to this convergence problem, which appears to be inherent to the physics of the SOL, the equilibriums produced by the code are considered sufficient to be used for the filament simulations presented in Chapters 6 and 7.

5.3 Verification of Parallel Dynamics

In the absence of perpendicular dynamics, the governing equations of the model, Equations (3.66) to (3.69), reduce to become identical in form to the 1D Navier Stokes equations for a neutral gas. In this section therefore, a verification problem commonly used in neutral fluid codes, known as the shock tube problem, is used to ensure that STORM3D's parallel dynamics terms have been correctly implemented. The results from the code are verified against an analytical solution to the problem, and also against other SOL simulation codes.

5.3.1 The Shock Tube Problem

A shock tube is a long tube in which a thin diaphragm separates two gases which are uniform and at rest. One of the gases is pumped up to a higher pressure, and then the diaphragm is burst. This produces both a shock wave and an expansion wave moving in opposite directions down the tube. From a SOL plasma perspective, this situation can be considered equivalent to the parallel propagation of an idealised filament perturbation (consisting of a top hat function in the parallel direction) that suddenly appears on top of a uniform SOL background, in the absence of perpendicular dynamics.

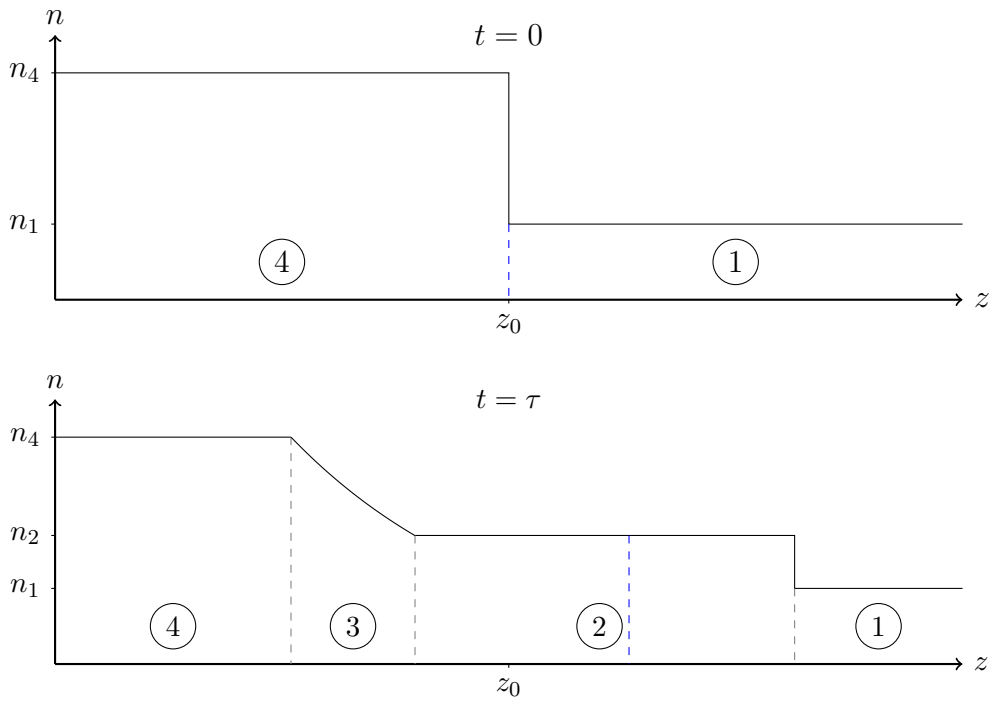

Figure 5.4: Schematic diagrams of the density profile of the analytical solution to the shock tube problem, with distinct regions labelled. Top: The initial density profile, showing two distinct regions. Bottom: The density profile at a later time $t = \tau$.

The top plot of Figure 5.4 schematically shows the shock tube set up at $t = 0$, just as the diaphragm is burst. The interface between two uniform plasma regions is located at $z = z_0$, where the diaphragm was present and is plotted using a dashed blue line. To the left of the interface is region 4, where the density level is $n = n_4$, whilst to the right is region 1, where the density level is $n = n_1$. In both regions the plasma is at rest. An analytical solution to the governing equations of the STORM3D plasma model for this shock tube problem is derived in Appendix B, following the derivation for the neutral fluid case given in Reference [242]. This solution is given by

$$U = \begin{cases} 0 & \dfrac{z-z_0}{at} \leq -1 \\ a + \dfrac{z-z_0}{t} & -1 \leq \dfrac{z-z_0}{at} \leq \sqrt{\dfrac{n_2}{n_1}} - \sqrt{\dfrac{n_1}{n_2}} - 1 \\ a\sqrt{\dfrac{n_2}{n_1}} - a\sqrt{\dfrac{n_1}{n_2}} & \sqrt{\dfrac{n_2}{n_1}} - \sqrt{\dfrac{n_1}{n_2}} - 1 \leq \dfrac{z-z_0}{at} \leq \sqrt{\dfrac{n_2}{n_1}} \\ 0 & \sqrt{\dfrac{n_2}{n_1}} \leq \dfrac{z-z_0}{at} \end{cases}, \tag{5.14a}$$

$$n = \begin{cases} n_4 & \dfrac{z-z_0}{at} \leq -1 \\ n_4 \exp\left(-\dfrac{z-z_0}{at} - 1\right) & -1 \leq \dfrac{z-z_0}{at} \leq \sqrt{\dfrac{n_2}{n_1}} - \sqrt{\dfrac{n_1}{n_2}} - 1 \\ n_2 & \sqrt{\dfrac{n_2}{n_1}} - \sqrt{\dfrac{n_1}{n_2}} - 1 \leq \dfrac{z-z_0}{at} \leq \sqrt{\dfrac{n_2}{n_1}} \\ n_1 & \sqrt{\dfrac{n_2}{n_1}} \leq \dfrac{z-z_0}{at} \end{cases}, \tag{5.14b}$$

where n_2 can be obtained by numerically solving the following implicit equation

$$\ln n_4 - \ln n_2 = \sqrt{\frac{n_2}{n_1}} - \sqrt{\frac{n_1}{n_2}}. \tag{5.15}$$

A schematic diagram of each of the different regions present in this solution after the diaphragm is burst is provided in the bottom plot of 5.4. The interface between the two plasmas has moved in the positive z direction, producing a shock wave moving into the low density side, and an expansion wave moving into the high density side which is region 3. In between each of these waves a uniform region is formed, region 2, which has a density level $n = n_2$.

5.3.2 Results

The analytic solution given by Equation (5.14) has been used to verify that the code provides a satisfactory representation of parallel dynamics and in particular of expansion waves and shock waves. The shock tube problem has been implemented in the code using a parallel domain length of $L_\parallel = 100$. As this is a 1D problem, only one grid point was used in the x and y directions and Ω was set to zero throughout. A value of $\mu = 3650$ was used, corresponding to deuterium, alongside $\hat{\eta}_\parallel = 6.88 \times 10^{-6}$, although the resistivity had no impact on the results. Instead of the standard STORM3D boundary conditions at the parallel boundaries, $z = 0$, $z = L_\parallel$, Dirichlet boundary conditions were enforced on each of the parallel velocities U and V, fixing them to zero. This meant that no density source was required to maintain a background, so S_n was set to zero. Neumann boundary conditions enforcing zero gradients were used at $z = 0$ for both n and ϕ, whilst free boundary conditions were utilised on these fields at $z = L_\parallel$. The ϕ field was obtained using the method described in Section 4.3.6. The system was initialised with $U = V = 0$, and

$$n = \begin{cases} 3 & z \leq 50 \\ 1 & z > 50 \end{cases}, \tag{5.16}$$

so that with reference to Equation (5.14) $n_1 = 1$, $n_4 = 3$ and $z_0 = 50$. Thus by numerically solving Equation (5.15), $n_2 = 1.72$ to 3 significant figures.

Simulations were performed using three different numerical schemes for the parallel upwinding derivative terms (terms of the form $U\nabla_\parallel f$ and $V\nabla_\parallel f$). These schemes were first order upwinding, second order upwinding, and second order central difference. Figure 5.5 plots the profiles of n and U produced using each of these schemes using 256 points in the parallel direction as well as the analytical solution, at the example time of $t = 25$.

It is clear from this figure that the central differencing scheme produces unphysical behaviour around the shock front, and therefore should not be used if discontinuities are present. On the other hand both the upwinding schemes broadly agree well with the analytical solution, reproducing both the shock and expansion wave dynamics and also the intermediate density level n_2. Comparing the two upwinding schemes directly, the first order scheme, being more dissipative, smooths out the discontinuities in the parallel gradients of the expansion wave part of the solution more than the second order scheme. However, the second order scheme does produce an unphysical wiggle in the solution just to the right of the expansion wave. Moreover, it has been observed that numerical instabilities can develop when using the second order scheme when simulating 3D filaments that have steep parallel gradients. Therefore it has been concluded that the first order scheme provides the most accurate and robust representation of parallel dynamics when shock fronts are present.

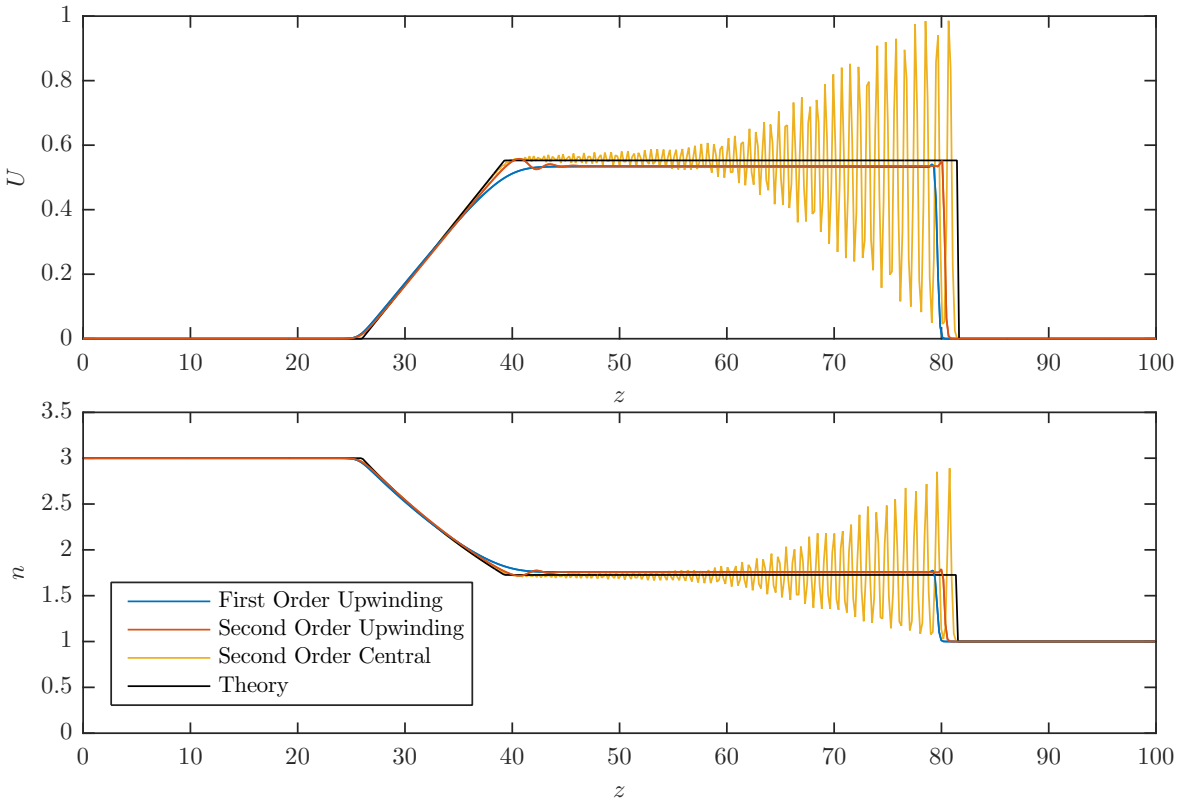

Figure 5.5: Comparison of n and U profiles produced for the shock tube problem using different discretisation schemes for the parallel advective derivatives, at the example output time of $t = 25$. The analytical solution is also plotted for comparison.

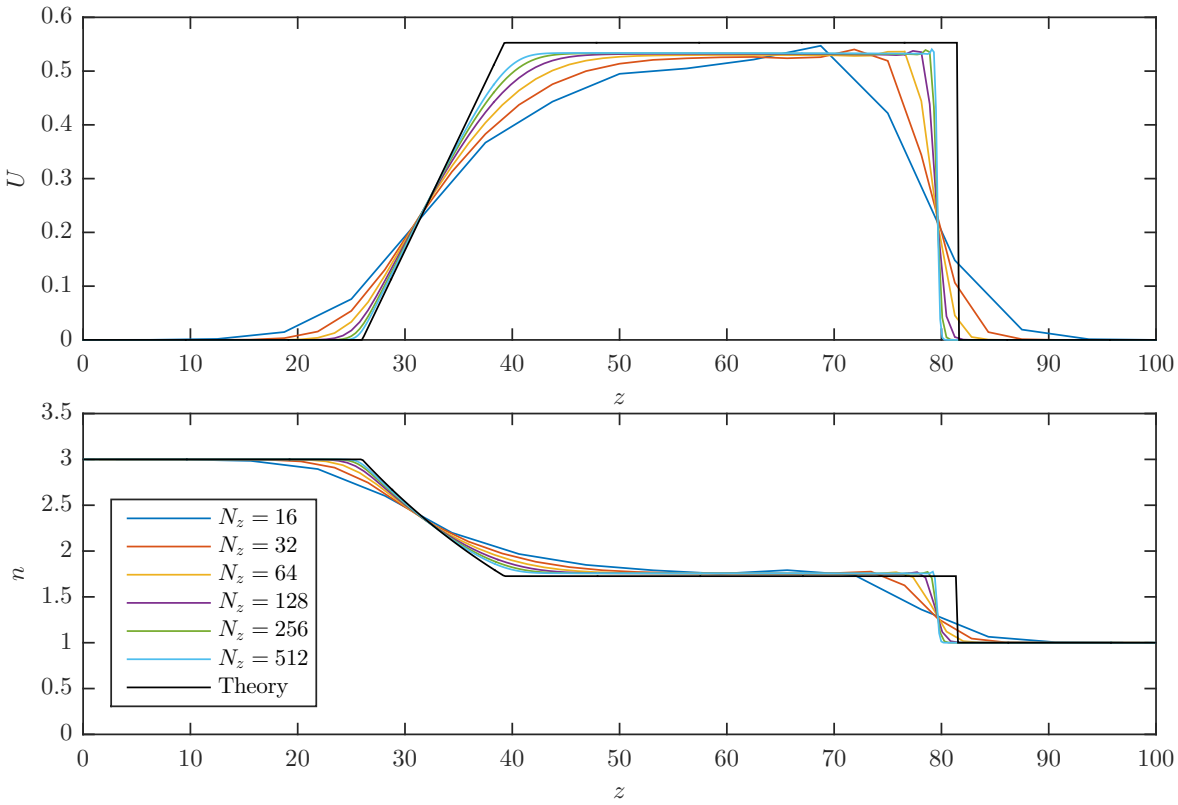

Figure 5.6: Comparison of n and U profiles produced for the shock tube problem using different parallel resolutions, at the example output time of $t = 25$. The analytical solution is also plotted for comparison.

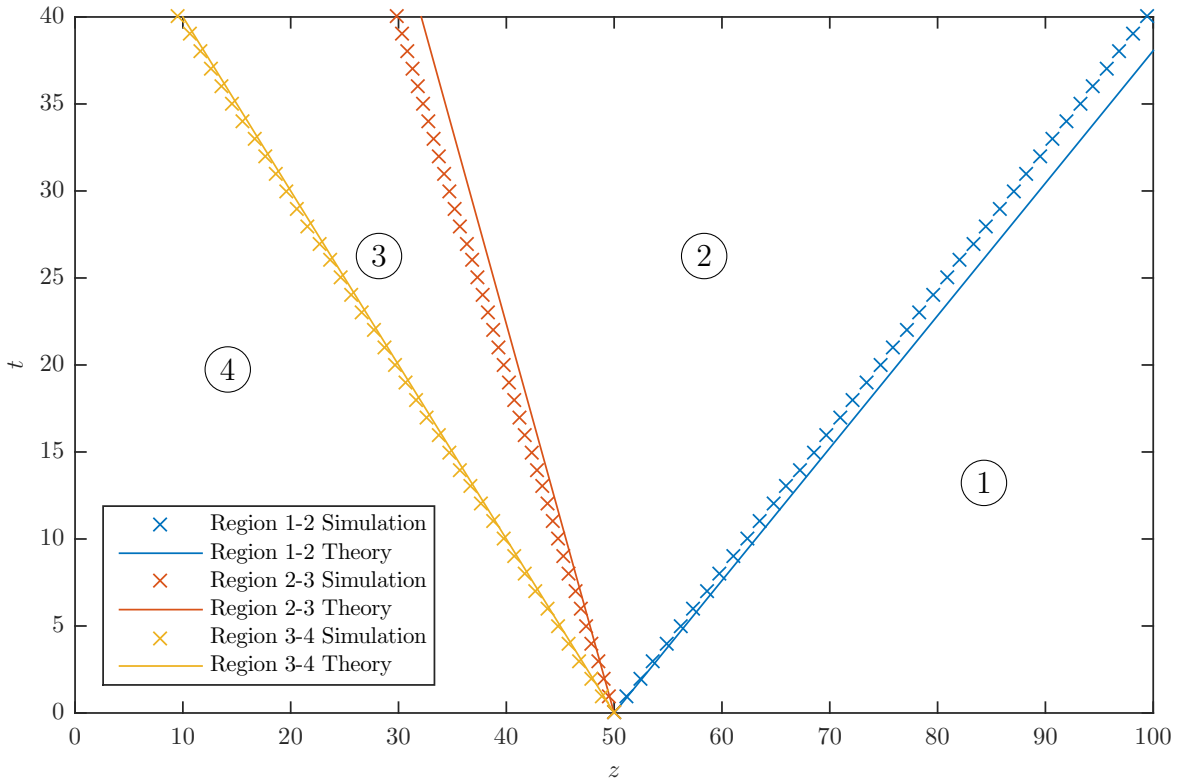

Figure 5.7: A $z - t$ diagram displaying the location of the interfaces between each of the regions labelled in Figure 5.4, for the first order upwinding, $N_z = 256$ simulation as well as the analytical solution.

Figure 5.6 displays the convergence of the first order upwinding simulation with increasing parallel resolution. At low resolutions, the discontinuities and sharp corners of the analytic solution are very much smoothed out, but are better represented as the resolution is increased. However, the simulation code converges to produce a value of $n_2 = 1.75$ at $N_z = 256$, which is slightly larger than the analytical value. The value of U that the code converges to in the same region is correspondingly lower than that specified by the analytical solution. Moreover, the location of the shock front in the code is somewhat behind that of the analytic solution, as it has propagated more slowly. This is explicitly demonstrated in Figure 5.7, which plots on an $x - t$ diagram the locations of the interfaces between each of the regions labelled in Figure 5.4, for the analytic solution and for the $N_z = 256$, first order upwinding simulation. The simulation's interface between regions 1 and 2, corresponding to the shock front, can be seen to consistently travel more slowly than that of the analytic solution. In addition, the simulation's interface between regions 2 and 3 can be observed to travel more quickly in the negative z direction than the analytic solution's interface. It is emphasised however that these discrepancies are relatively minor, and that overall good agreement is found between the simulation and analytic solution.

The shock tube problem has also been used to conduct a cross-code benchmark between the STORM3D code and two other fluid codes commonly used for SOL problems; TOKAM-3X [243, 244] and SOLF1D [245]. TOKAM-3X is a 3D code, whose model is discussed later in Section 5.5, whilst SOLF1D is a 1D code that models only parallel dynamics. For this cross-code benchmark, the standard sheath boundary conditions given by Equations (3.70) and (3.72) were enforced at $z = L_\parallel$ on U and V, which meant that a density source was required to produce a constant equilibrium. The source given by Equation (5.12) was therefore

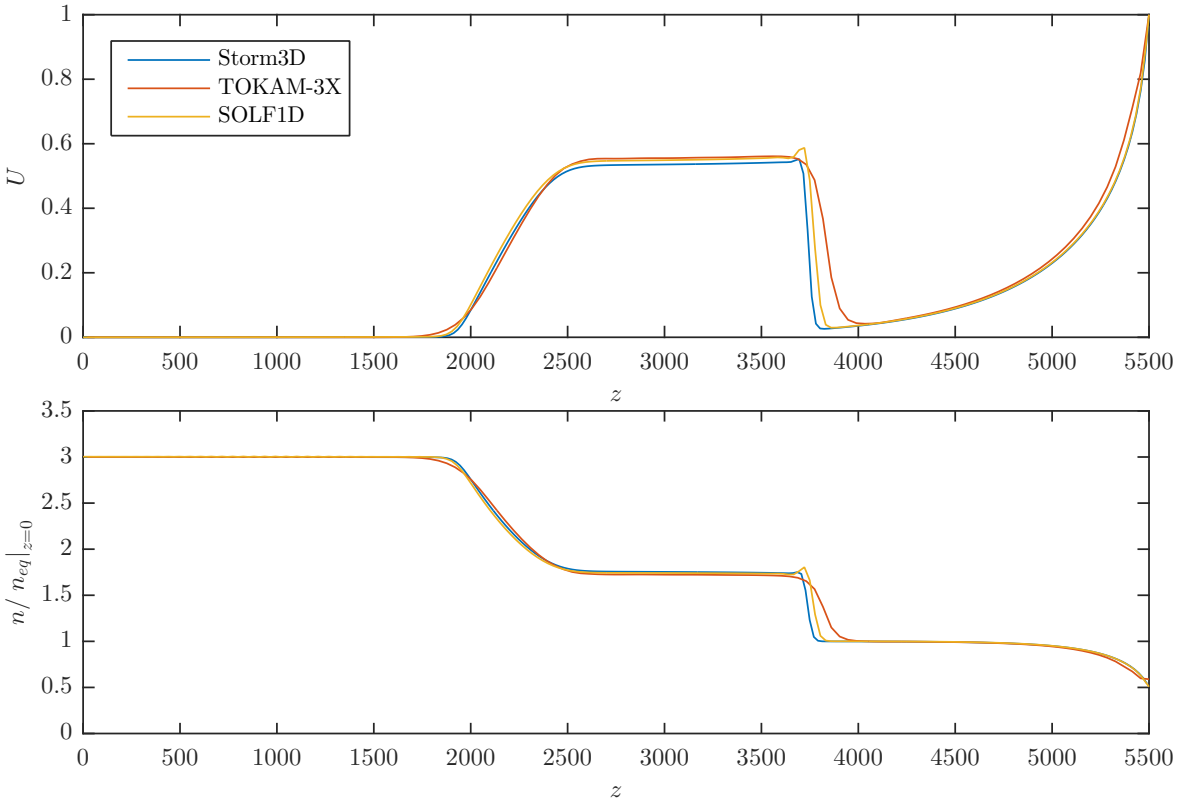

Figure 5.8: Comparison of the n and U parallel profiles produced by the STORM3D, TOKAM-3X and SOLF-1D codes for the shock tube problem using a source driven background, at the example output time of $t = 800$.

used, as this produces an equilibrium consisting of a relatively uniform plasma that is at rest throughout the majority of the domain, as shown in Figure 5.1. Moreover, since the source is effectively zero throughout the domain, except for approximately the last 10% nearest the sheath, the analytical shock tube solution should be comparable in the first 90% of the domain. A density perturbation n_f, given by

$$n_f = \begin{cases} 3\, n_{eq}|_{z=0} & z < L_\parallel/2 \\ 0 & z > L_\parallel/2 \end{cases} \tag{5.17}$$

was then seeded on top of the equilibrium density field. All the other fields were initialised to their equilibrium values. The perturbation was scaled by $n_{eq}|_{z=0}$ because each code produces an equilibrium with a slightly different density level in the uniform region, due to their use of different numerical schemes and grid resolutions. Since Equation (5.15) can be written in terms of n_2/n_1 and n_4/n_2, the dynamics of the shock tube problem is determined by the ratio n_4/n_1. Therefore by scaling the perturbation by $n_{eq}|_{z=0}$, $n_4/n_1 = 3$ across all three codes. A longer parallel domain of $L_\parallel = 5500$ was employed for this cross-code comparison, and as before parameters of $\mu = 3650$ and $\hat{\eta}_\parallel = 6.88 \times 10^{-6}$ were used. Moreover, in the STORM3D code, the ϕ field was again obtained using the method described in Section 4.3.6. Both the STORM3D and TOKAM-3X results were produced using a parallel resolution of $N_z = 128$, whilst 100 points were used in the parallel direction in SOLF1D.

A comparison of the n and U profiles produced by each of these codes at the example output time of $t = 800$ is provided by Figure 5.8, with the density fields for each code divided by $n_{eq}|_{z=0}$ to allow for direct comparison. Generally, excellent agreement is found between

the three codes. It is noted however that the TOKAM-3X results do not exhibit the minor overshoots that are found just behind the shock fronts of the other two codes and furthermore that the TOKAM-3X shock front also propagates faster. These observations are attributed to the use of a Total Variation Diminishing (TVD) scheme [246] that is used in TOKAM-3X, which is a scheme that is designed to capture sharp shock features without oscillations or overshoots. Whilst the STORM3D code does provide a satisfactory representation of the parallel dynamics for present purposes, it is clear that the implementation of such a TVD scheme would be a desirable future development.

5.4 Verification using the Method of Manufactured Solutions

As discussed in the introduction of this chapter, verification against simplified analytic results only tests that certain aspects of the simulation code are error free, and does not truly verify a code in its entirety. For example, the verification of the equilibrium fields and of the shock tube problem in Sections 5.2 and 5.3 demonstrate that the parallel dynamics of the code work correctly, but do not provide any verification of the perpendicular dynamics at all. On first glance, an analytic solution to the full set of equations being solved would be required to rigorously verify all aspects of the simulation code.

5.4.1 The Method of Manufactured Solutions

One testing procedure commonly used in the field of computational fluid dynamics to fully verify a simulation code that solves a problem without an analytic solution is the Method of Manufactured Solutions [240]. In this method, solutions are prescribed or *manufactured* to the equations being solved and additional source terms are included within the equations to ensure that they remain satisfied. For example, a set of partial differential equations can be written in the form

$$\frac{\partial \boldsymbol{f}}{\partial t} = F(\boldsymbol{f}). \tag{5.18}$$

For the equations being solved in the STORM3D physics module, $\boldsymbol{f} = (n, U, V, \Omega, \phi)$. For a manufactured solution $\boldsymbol{f_M}$, the source terms required to satisfy the equation can be calculated analytically:

$$\boldsymbol{S} = \frac{\partial \boldsymbol{f^M}}{\partial t} - F(\boldsymbol{f^M}). \tag{5.19}$$

The code must then be adjusted to add these source terms so that the equations solved are:

$$\frac{\partial \boldsymbol{f}}{\partial t} = F(\boldsymbol{f}) + \boldsymbol{S}. \tag{5.20}$$

The simulation is initialised at $t = 0$ such that $\boldsymbol{f}\,(t = 0) = \boldsymbol{f^M}\,(t = 0)$ and evolved to a later time $t = \Delta t$. At this point, various measures of the error between the numerical and manufactured solutions ϵ, can be calculated as described in Section 5.2.2. Since $\boldsymbol{S}$ is specified analytically, it can be evaluated to numerical precision within the code and so therefore does not impact upon ϵ, which will be dominated by errors from coding mistakes or from discretisation errors. The error should converge to zero (or at least to machine precision) as the spatial and temporal resolution is increased.

More importantly, the error should reduce at the rate expected for the methods being used. For example, if a method is second order accurate, then the error should reduce by a factor of four if the mesh spacing is halved. Temporally and spatially dependent partial differential

equations require both the time step and grid spacing to be refined to achieve convergence at the correct order.

In order to enable MMS testing to be carried out as routinely as possible and to minimise the possibility of introducing additional errors through an incorrect implementation of the method itself, BOUT++ has a number of MMS features that automate as much of the method as possible. A description of how to use these features is provided in Appendix C. A number of core components of BOUT++, such as commonly used boundary conditions, time solvers and spatial derivative terms have been already tested [247], and a number of MMS test cases can be found in the directory BOUT-dev/examples/MMS/. However, it is important to also test complete physics modules, as not every combination of individual components may have been tested. Moreover, physics modules may use non-standard numerical methods or boundary conditions which are coded within the physics module itself.

5.4.2 Guidelines for Constructing Manufactured Solutions

A number of guidelines for the construction of manufactured solutions can be found in Reference [240]. Those relevant for manufacturing solutions to verify the STORM3D physics module are listed below.

1. Manufactured solutions should consist of smooth analytic functions such as polynomial, trigonometric, or exponential functions. This allows for the source terms to be easily calculated, and for both the solution and the source to be computed easily within the code. The solution is required to be smooth to ensure that the theoretical order of accuracy can be obtained.

2. The solutions should exercise or stress every term in the equations being solved.

3. The solutions should have a sufficient number of non-trivial derivatives for the equations being solved such that none of the derivatives in the equations become zero throughout the whole simulation.

4. Solutions should not vary strongly as a function of space or time to ensure that the asymptotic order of accuracy convergence can be attained using practical mesh sizes.

5. The solution should not stop the code from running to completion. For example, if the code is written in such a way that the solution is assumed to be positive, or throws errors if the solution is negative, ensure that the manufactured solution is positive.

5.4.3 Testing Coupled Boundary Conditions

Many physical models use boundary conditions that specify the behaviour of one variable, as a function of another:

$$f_1|_b = g\left(f_2\right). \tag{5.21}$$

Here, f_1 and f_2 are independent variables in the physical model, g is an arbitrary function and $|_b$ denotes the boundary location. In the case of the STORM3D module, Equations (3.72) and (3.73) are examples of such a condition. Reproduced here for convenience it enforces

$$V|_{z=\pm L_\parallel} = \pm\frac{1}{\sqrt{1+1/\mu}}\exp\left(-\phi|_{z=\pm L_\parallel}\right). \tag{5.22}$$

In order to verify the parts of the code which implement such a boundary condition an additional source term must be added on the RHS of the boundary condition itself:

$$f_1|_b = g\left(f_2\right) + S_{BC} \tag{5.23}$$

where

$$S_{BC} = f_1^M|_b - g\left(f_2^M\right). \tag{5.24}$$

Returning to the example of the electron parallel velocity sheath boundary condition, to verify its implementation using MMS, it must be adjusted in the code so that the boundary is set to:

$$V|_{z=\pm L_\parallel} = \frac{\pm\exp\left(-\phi|_{z=\pm L_\parallel}\right) \mp \exp\left(-\phi^M|_{z=\pm L_\parallel}\right)}{\sqrt{1+1/\mu}} + V^M|_{z=\pm L_\parallel}. \tag{5.25}$$

5.4.4 Results

The STORM3D physics module has been verified to ensure that the equations have been correctly implemented so that the code displays second order convergence when using second order accurate discretisation schemes for all spatial derivatives. The results presented here were obtained using a second order Arakawa scheme for the perpendicular $\boldsymbol{E}\times\boldsymbol{B}$ advection terms, a second order upwind scheme for the parallel advection derivatives, and second order central finite difference schemes for all other spatial derivatives. The time integration was carried out using a variable time-step, variable order, fully implicit Newton-Krylov backwards difference formula solver from the PVODE library, which is assumed to converge correctly. The time solver tolerances were therefore set sufficiently small (absolute tolerance $= 10^{-12}$, relative tolerance $= 10^{-8}$) so that the errors in the simulation were dominated by spatial, rather than temporal, discretisation errors. These tolerances were specified under the section `[SOLVER]` in the input file as follows:

```
[solver]
...
ATOL = 1.0e-12
RTOL = 1.0e-8
```

The simulations were conducted on a domain consisting of $L_x \times L_y \times L_z = 1 \times 2\pi \times 2\pi$, whilst the parameters μ, $\hat{\eta}_\parallel$, D_n, D_Ω and $\hat{g}$ were each set to unity. The manufactured solutions used were

$$n^M = \left[3.5 + \sin\left(y\right) + \cos\left(2y\right)\cos\left(t\right) + \sin\left(x\right)\sin\left(3z+t\right)\right]/4, \tag{5.26a}$$

$$\Omega^M = \sin\left(y\right) + \cos\left(2y+t\right) + \cos\left(x\right)\sin\left(z+t\right), \tag{5.26b}$$

$$U^M = \sin\left(y\right) + \cos\left(y+t\right) + \cos\left(2x+z+3t\right), \tag{5.26c}$$

$$V^M = \cos\left(y\right)\cos\left(t\right) + \sin\left(y+t\right) + \cos\left(z+x-t\right), \tag{5.26d}$$

$$\phi^M = \cos\left(y\right)\cos\left(2t\right) + \sin\left(2z\right) + \cos\left(2x+2t\right). \tag{5.26e}$$

This combination of manufactured solutions and parameters was designed such that each term in each of the equations was of approximately equal magnitude, so that the error associated with any particular term did not dominate the others.

The boundary conditions were set such that the types of boundary conditions used by the model (described in Section 4.3.5) were imposed on each field and boundary as appropriate. The equations were evolved to $t = 0.15$, which produced a sufficient number of RHS iterations

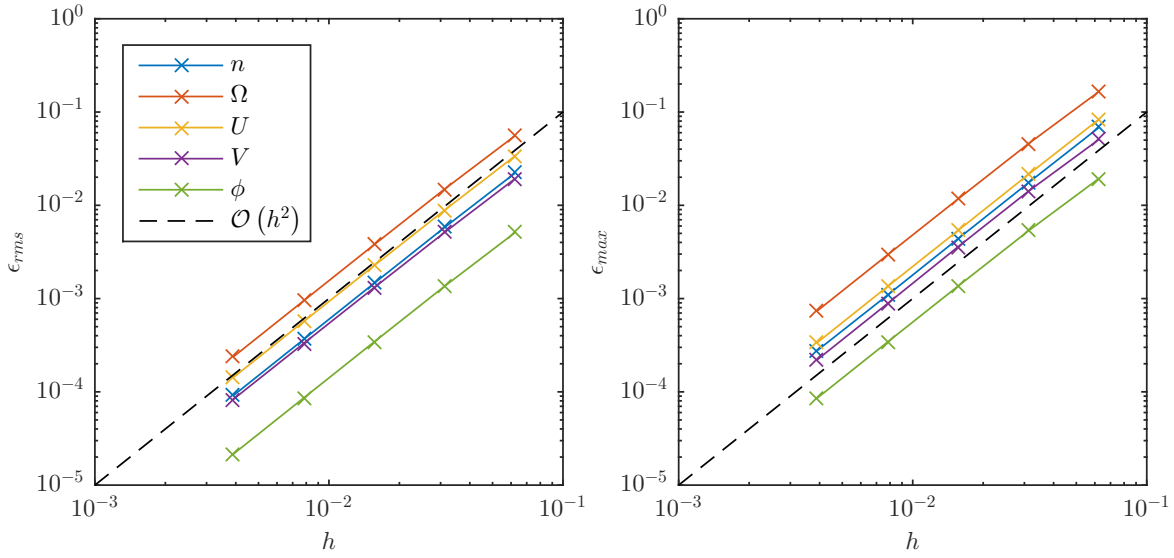

Figure 5.9: Demonstration of STORM3D's convergence order obtained using the method of manufactured solutions.

Table 5.1: STORM3D error convergence orders, obtained using the method of manufactured solutions between the $N_x \times N_y \times N_z = 128 \times 128 \times 128$ and $N_x \times N_y \times N_z = 256 \times 256 \times 256$ simulations at $t = 0.15$.

Field	ϵ_{rms} order	ϵ_{max} order
n	2.001	1.979
Ω	1.999	1.999
U	1.996	2.000
V	1.993	2.004
ϕ	1.999	1.998

for any errors to propagate throughout the entire domain (> 6000), but without running so long such that the errors from the time solver accumulate to dominate over the spatial discretisation errors. Convergence was tested by repeatedly doubling the spatial mesh resolution, $N_x \times N_y \times N_z$, from $16 \times 16 \times 16$ to $256 \times 256 \times 256$.

The error measures, ϵ_{rms} and ϵ_{max} are plotted against a characteristic mesh spacing, h, at $t = 0.15$ in Figure 5.9. Here h has been defined such that $h = \mathrm{d}x = \mathrm{d}y/2\pi = \mathrm{d}z/2\pi$. It is clear from these figures that the simulations are in the asymptotic regime, and that the errors in the simulations are correctly converging at second order. The dependence of the convergence orders as measured between the $N_x \times N_y \times N_z = 128 \times 128 \times 128$ and $N_x \times N_y \times N_z = 256 \times 256 \times 256$ simulations on the time that the simulations were evolved to, t, is shown in Figure 5.10. The ϵ_{rms} convergence order can be seen to remain very close to 2 for the duration of the simulations. The ϵ_{max} convergence orders display more variation, as may be expected, but also remain close to 2 throughout. This demonstrates that the convergence is not dependent on the duration of the simulation. For reference, the calculated convergence orders for each field between $N_x \times N_y \times N_z = 128 \times 128 \times 128$ and $N_x \times N_y \times N_z = 256 \times 256 \times 256$ at $t = 0.15$ are listed in Table 5.1.

During the MMS verification process, it was found that if the errors on the ϕ field were significantly larger than the errors on the V field (by say, an order of magnitude), then this would cause the ϵ_{max} convergence orders for n and Ω to reduce to ~ 1.5, even if the errors

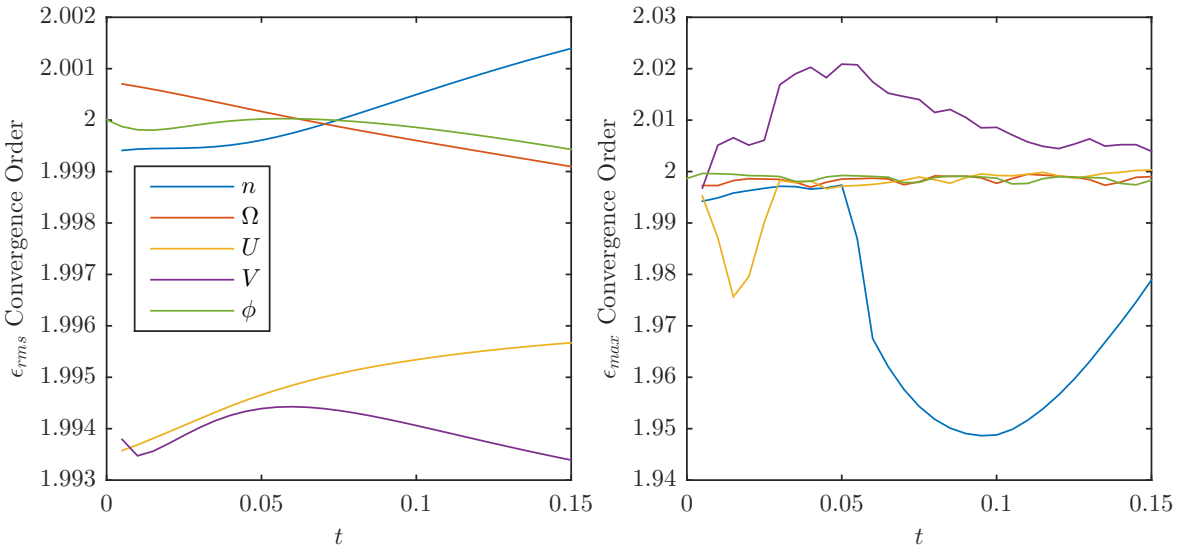

Figure 5.10: Demonstration that the convergence order obtained using the method of manufactured solutions between the two highest resolution simulations ($N_x \times N_y \times N_z = 128 \times 128 \times 128$ and $N_x \times N_y \times N_z = 256 \times 256 \times 256$) is not dependent on evolution time of the simulation.

on ϕ and V were converging correctly at second order. This problem was identified to be related to the V sheath boundary condition, because if it was replaced with simply $V = V^M$ at the sheath boundary, correct convergence was recovered. The problem appeared in the n and Ω fields as their evolution equations contain parallel gradient terms which uses V sheath boundary points. It is supposed that this problem was the result of the fact that a large $\mathcal{O}\left(h^2\right)$ error from ϕ was transmitted to the V field's sheath boundary every time the RHS of the time solver was evaluated, and that the magnitude of this error remained large compared to the other spatial discretisation errors throughout the simulation. Ultimately, this problem was addressed by reducing the perpendicular size of the domain, which reduced the magnitude of the ϕ error field so that it was small compared to the magnitude of the V error field. This issue has been outlined here in case the reader encounters a similar problem, as it was not trivial to diagnose.

5.5 Validation against TORPEX Experiment

This section presents the validation exercise carried out in which filament simulations performed using STORM2D and STORM3D were compared against experimental measurements from the TORPEX device and other SOL simulation codes which each represent different physics in their respective models. A more detailed description of this exercise can be found in Reference [248].

5.5.1 The TORPEX Device

TORPEX (TORoidal Plasma EXperiment) is a toroidal machine with major radius $R = 1$m and minor radius $a = 0.2$m. It is a Simple Magnetised Torus (SMT), meaning that its magnetic field consists of a dominant toroidal component ($B_\Phi = 76$mT on axis) and a smaller vertical magnetic field ($B_Z = 1.6$mT), which results in helical field lines that wind around the device. A schematic diagram of TORPEX is shown in Figure 5.11, which also illustrates the coordinate system used. The coordinate x denotes the radial direction, z is the parallel direction, whilst

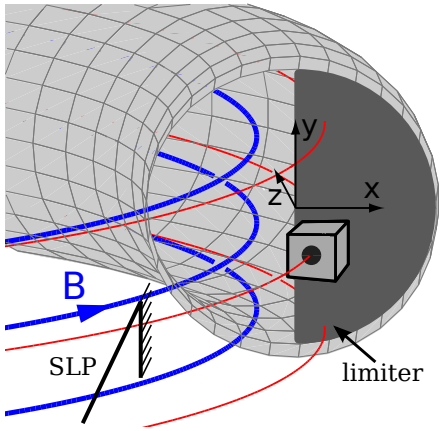

Figure 5.11: Schematic representation of the TORPEX experiment, showing the limiter located in the low field region and the probes used to perform the conditional filament sampling.

y is the bi-normal direction, which is approximately the vertical direction. The coordinates are defined such that $x = 0$, $y = 0$ corresponds to the axis in the middle of the poloidal plane. A poloidal steel limiter is located at one toroidal position that covers the entire low field side ($x > 0$) of the cross-section. Field lines in the low field side of the device therefore intercept this limiter with a near perpendicular incidence, and have a nearly constant connection length $\ell_{\parallel} = 2\pi R$. The field lines on the high field side ($x < 0$) on the other hand intercept the top and inner walls of the device. Plasma is produced and sustained in the device by microwaves in the electron cyclotron range of frequencies. Turbulence is driven in the high field side of the device by ideal interchange modes, which results in filaments that dominate the radial transport in the low field side. Typical plasma parameters in TORPEX are $n_e \sim 10^{16}\text{m}^{-3}$ and $T_e \sim 5$ eV.

5.5.2 Experimental Filament Measurements

The experimental measurements used for this validation exercise were obtained using two diagnostics. The first is a vertically oriented linear array of Langmuir probes with 1.8 cm distance between tips, which hereafter will be referred to as the SLP (Slow Langmuir Probes). This diagnostic was located at $x = 7$ cm and was toroidally positioned 180° from the limiter. The second diagnostic was a single sided Langmuir probe, which was located approximately 3 cm away from the limiter plate, with its collecting plate orientated perpendicular to the magnetic field lines. The time-averaged (hereafter referred to as background) profiles of the density, $n_{e,bg}$, and the electron temperature, $T_{e,bg}$, measured using this diagnostic are shown in Figure 5.12.

Time-dependent measurements of the filament profiles in the perpendicular drift-plane were also obtained using a conditional sampling technique. The SLP probe array, located in a fixed position in the low field region, was biased at -40 V, and operated in ion saturation current mode. The probes of the SLP array were used as reference probes, with a positive burst in a probe signal interpreted as a filament moving past the probe. The single sided probe was operated in swept mode. When a signal within a certain interval was detected by one of the reference probes, a voltage V was applied to the swept probe and the corresponding current I was measured. The ensemble average over many filament detection events produced an $I - V$ characteristic, from which the plasma parameters associated with a conditionally averaged filament event could be obtained. The plasma was assumed to be uniform in the

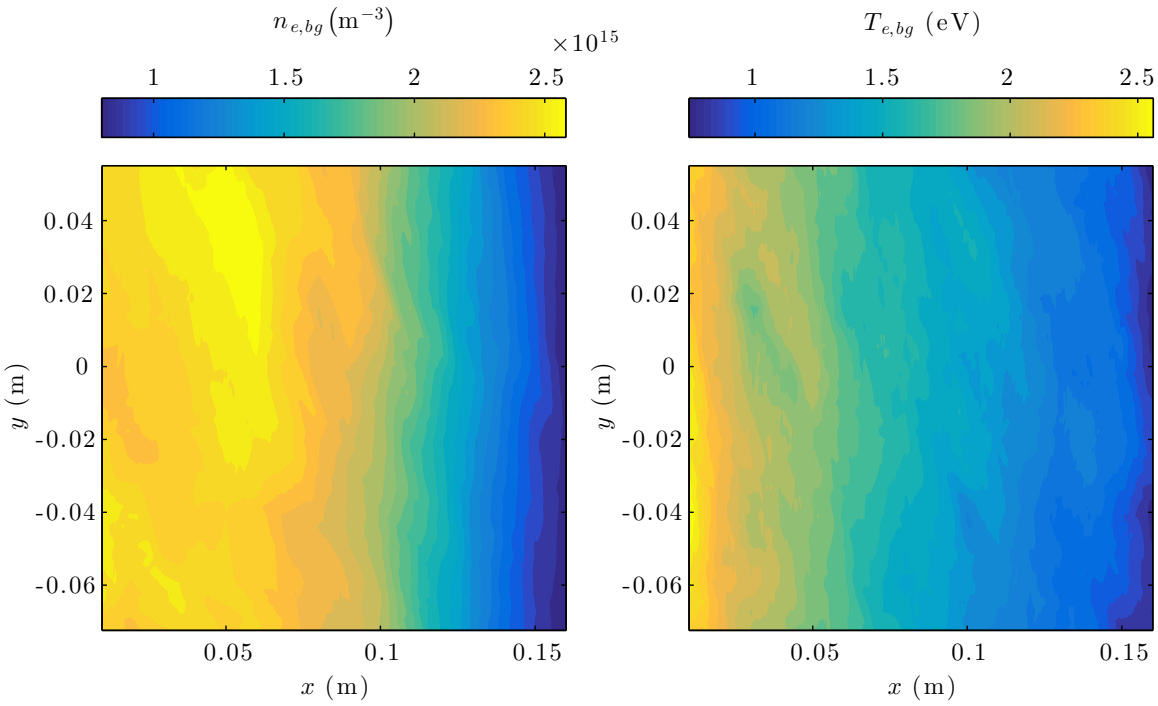

Figure 5.12: Time averaged experimental profiles of plasma density $n_{e,bg}$ and electron temperature, $T_{e,bg}$, in TORPEX, measured in poloidal plane located 3 cm away from the limiter. Data reproduced from Reference [248].

vertical direction, such that the signals measured by each of the reference probes had the same statistical properties. The measurements were repeated using different time lags between the detection of the filament and the application of the voltage on the swept probe, as well as for different radial positions of the swept probe (which was moved in between discharges). This allowed time-dependent profiles of plasma parameters in the perpendicular drift-plane of the conditionally averaged filament to be determined. In particular, the perturbation profiles were obtained by subtraction of the time averaged profiles shown in Figure 5.12. A more detailed explanation of the technique can be found in References [119] and [124].

Conditionally averaged filaments with three different peak density values were obtained by conditionally selecting filaments from different intervals of the probe signals. These intervals were $[2\sigma, 2.75\sigma]$, $[2.75\sigma, 3.5\sigma]$ and $[3.5\sigma, 4.25\sigma]$, where σ is the standard deviation of the reference signal. Hereafter, the conditionally averaged filaments corresponding to each of these intervals are referred to as Case 1, Case 2, and Case 3 respectively. The two dimensional profiles of the filaments' density perturbation, $n_{e,f}$, electron temperature perturbation $T_{e,f}$, and floating potential $\varphi_{fl,f}$ are plotted for each case at their detection time, $t = 0$, in Figure 5.13.

5.5.3 Other Simulation Codes

In addition to the STORM2D and STORM3D codes, three other fluid SOL simulation codes were used to simulate the conditionally averaged filaments from the TORPEX experiment. Since all the codes are reduced forms of the Braginskii equations [205], in the following discussion, only differences from the STORM3D and STORM2D models will be discussed.

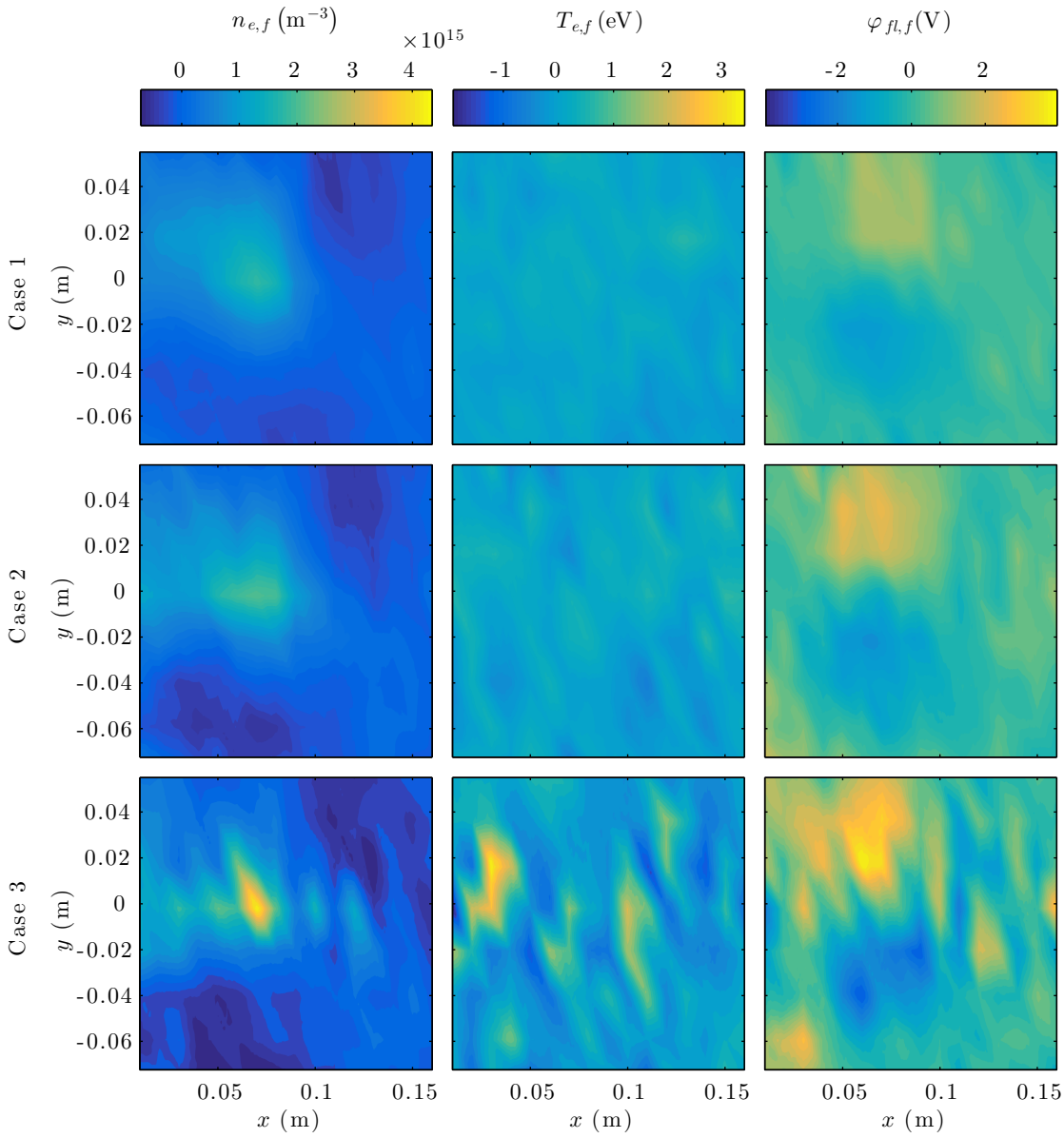

Figure 5.13: Experimental profiles of the TORPEX conditionally averaged filaments' density perturbations, $n_{e,f}$, electron temperature perturbations, $T_{e,f}$, and floating potential perturbations $\varphi_{fl,f}$, at their detection time $t = 0$. Data reproduced from Reference [248]

GBS

GBS (Global Braginskii Solver) [249] is a 3D code whose principle difference with respect to STORM3D is that it also evolves the electron temperature. Whilst it retains the influence of electron inertia in its parallel electron velocity equation, it neglects the effect in the parallel ion velocity equation. In each of these equations it also includes the effects of collisions with neutrals. In the present work, the evolution fields were split into equilibrium and perturbation components, with only the latter component evolved. Moreover, it includes arbitrary dissipative parameters in each evolution equation for numerical reasons.

TOKAM-3X

TOKAM-3X [243, 244] is another 3D code which neglects electron inertia completely, and does not make the infinite aspect ratio approximation in that it retains $\nabla \cdot \hat{\boldsymbol{b}}$ terms. It uses a linearised version of the sheath boundary conditions given by Equations (3.72) and (3.72), and like GBS, it also includes arbitrary dissipative parameters for numerical reasons.

HESEL

HESEL (Hot ion Edge-SOL ELectrostatic) [250] is a 2D code which evolves both electron and ion temperatures. Its model was reduced to two dimensions by approximating $u_{\parallel i}\nabla_\parallel \approx u_{\parallel e}\nabla_\parallel \approx c_s/\ell_\parallel$. For the parallel currents, it uses a sheath dissipation closure similar to that used in STORM2D, but different in that the closure term is averaged over the y direction. In effect, this negates the influence of parallel currents closing through the sheath and thus implicitly assumes that polarisation currents rather than sheath currents are the dominant path through which diamagnetic currents are closed. Its perpendicular dissipative terms seek to model the effect of electron and ion collisions with neutrals, in contrast to the STORM models, which are based upon electron-ion and ion-ion collisions. Finally, its curvature strength g is modelled to be half the value that is used in the other codes.

5.5.4 Simulation Initialisation

The filament simulations were initialised largely as described in Section 4.4. Whilst measurements of the parallel structure of the background or filament density perturbation were not available for the series of experiments from which the conditionally averaged filament data were obtained, it has been observed in previous TORPEX experiments that the background density profile is approximately flat except for a drop in the proximity of the limiter. Since the density profile produced by Equation (5.12) matches this behaviour, as shown in Figure 5.2, the density source in the STORM3D and TOKAM-3X simulations was prescribed to be of the form

$$S_n \propto \frac{\exp\left(10z/L_\parallel\right)}{L_\parallel\left(\exp(10)-1\right)}. \tag{5.27}$$

From Figure 5.12, the background profiles can be seen to exhibit only a very weak y dependence. These profiles were therefore approximated as

$$n_{e,bg} = 2.5\times10^{15} - 4.2\times10^{17}x^{2.9} \tag{5.28}$$

and

$$T_{e,bg} = 2.8\exp\left(-5.9x\right). \tag{5.29}$$

Table 5.2: TORPEX simulation parameters.

Input Parameters	Normalisation Parameters	Dimensionless Parameters
$T_e = 2.80$ eV	$\rho_s = 2.24 \times 10^{-3}$ m	$\hat{g} = 4.48 \times 10^{-3}$
$B = 0.076$ T	$c_s = 1.64 \times 10^{4}$ ms^{-1}	$\hat{\eta}_{\parallel} = 5.81 \times 10^{-7}$
$n_{e,0} = 2.5 \times 10^{15}$m^{-3}	$\Omega_i = 7.33 \times 10^{6}$ s^{-1}	$D_n = 2.32 \times 10^{-6}$
$R = 1.0$ m		$D_\Omega = 3.71 \times 10^{-5}$
$\ell_{\parallel} = 2\pi$ m		$\mu = 1823$
$m_i = 1.66 \times 10^{-27}$ kg		$L_{\parallel} = 1402$
$\ln \Lambda = 10$		
$q = 0$		

Here, $n_{e,bg}$, $T_{e,bg}$ and x are written in m^{-3}, eV and m respectively, and therefore Equation (5.28) cannot be used directly in Equation (5.27), which is dimensionless. Written in normalised form, Equation (5.28) is

$$n_{bg} = 1 - \left(1.91 \times 10^{-6}\right) x^{2.9}. \tag{5.30}$$

The input quantities used for normalisation and the resulting non-dimensional parameters are listed in Table 5.2. Returning the specification of the density source, S_n was therefore set to be

$$S_n = \left(1 - \left(1.91 \times 10^{-6}\right) x^{2.9}\right) \frac{\exp\left(10z/L_{\parallel}\right)}{L_{\parallel}\left(\exp(10) - 1\right)}. \tag{5.31}$$

It is noted that since the source has no y variation, this meant that a steady state equilibrium was obtained in which the $\boldsymbol{E} \times \boldsymbol{B}$ advection terms and curvature terms in the governing equations (Equations (3.66) to (3.69)) were zero. This equilibrium was two dimensional, in that is varied in both the parallel and x directions. Since the particle diffusion and viscosity parameters (given in Table 5.2) were small, the equilibrium produced can be approximated to be a series of independent parallel profiles, with one for each x position. Therefore from the analytical equilibrium density solution given by Equation (5.2), the equilibrium density solution produced at the target closely approximated the experimental background profile, as desired. For consistency between codes, the density equilibrium profile produced by STORM3D was used as the prescribed density background in the GBS simulations.

In the non-isothermal codes, GBS and HESEL, the background electron temperature was set to Equation (5.29). The background profile of φ in these codes was obtained by assuming zero background current and enforcing the sheath boundary conditions given by Equations (3.53) to (3.56), which resulted in a radially varying background electrostatic field, and hence a vertical $\boldsymbol{E} \times \boldsymbol{B}$ velocity. In addition, the background ion temperature in HESEL was assumed to be the same as the ambient temperature of the neutrals in TORPEX, and was therefore imposed uniformly to be $T_i = 0.025$ eV.

To allow the experimental filament perturbations to be initialised in the simulations, the experimental profiles of n_f, $T_{e,f}$ and $\varphi_{fl,f}$ at $t = 0$, shown in Figure 5.13, were fitted to the following analytic expressions which impose a monopolar structure in the poloidal plane for $n_{e,f}$ and $T_{e,f}$, and a dipolar structure for $\varphi_{fl,f}$:

$$n_{e,f} = n_{e,f,0} \exp\left(-\left(\frac{x - x_0}{\sigma_{n,x}}\right)^2 - \left(\frac{y}{\sigma_{n,y}}\right)^2\right), \tag{5.32}$$

Table 5.3: Parameters used to initialise the TORPEX filament profiles

Parameter		Case 1	Case 2	Case 3
$n_{e,f,0}$	$(\times 10^{15}\ \mathrm{m}^{-3})$	1.975 ± 0.135	2.335 ± 0.325	4.395 ± 0.855
$\sigma_{n,x}$	(cm)	2.20 ± 0.20	2.40 ± 0.30	1.65 ± 0.45
$\sigma_{n,y}$	(cm)	2.40 ± 0.20	2.10 ± 0.20	1.75 ± 0.25
$T_{e,f,0}$	(eV)	0.345 ± 0.065	0.96 ± 0.25	1.73 ± 0.28
$\sigma_{T,x}$	(cm)	1.05 ± 0.15	1.05 ± 0.25	0.80 ± 0.20
$\sigma_{T,y}$	(cm)	3.65 ± 1.05	1.45 ± 0.25	2.85 ± 0.95
φ_1	(V)	2.33 ± 0.17	4.60 ± 0.74	4.72 ± 0.405
$\sigma_{\varphi,x,1}$	(cm)	3.55 ± 0.25	3.25 ± 0.25	4.95 ± 0.35
y_1	(cm)	2.55 ± 0.25	2.60 ± 0.20	1.15 ± 0.35
$\sigma_{\varphi,y,1}$	(cm)	2.95 ± 0.05	3.10 ± 0.20	4.90 ± 0.60
φ_2	(V)	-1.54 ± 0.14	-2.35 ± 0.55	-6.155 ± 0.965
$\sigma_{\varphi,x,2}$	(cm)	3.10 ± 0.20	2.75 ± 0.35	2.95 ± 0.45
y_2	(cm)	-2.10 ± 0.40	-0.50 ± 0.80	-2.45 ± 0.15
$\sigma_{\varphi,y,2}$	(cm)	4.00 ± 0.30	4.75 ± 0.45	2.50 ± 0.30

$$T_{e,f} = T_{e,f,0} \exp\left(- \left(\frac{x - x_0}{\sigma_{T,x}} \right)^2 - \left(\frac{y}{\sigma_{T,y}} \right)^2 \right), \tag{5.33}$$

$$\begin{aligned} \varphi_{f,fl} = \varphi_1 \exp &\left(- \left(\frac{x - x_0}{\sigma_{\varphi,x,1}} \right)^2 - \left(\frac{y - y_1}{\sigma_{\varphi,y,1}} \right)^2 \right) \\ + \varphi_2 \exp &\left(- \left(\frac{x - x_0}{\sigma_{\varphi,x,2}} \right)^2 - \left(\frac{y - y_2}{\sigma_{\varphi,y,2}} \right)^2 \right). \end{aligned} \tag{5.34}$$

It is noted from Figure 5.13 that fitting a such Gaussian profile to the electron temperature perturbation is somewhat questionable. The value of x_0 was specified to be 0.07m, whilst the values of the remaining unknown parameters in Equations (5.32) to (5.34) were obtained through fitting procedures and are listed in Table 5.3 for each of the three filament cases. The filaments were initialised to these expressions assuming that the filament perturbation profiles were uniform along the parallel direction and then seeded on top of the equilibrium profiles to give the initial state of the system. Specifically, Ω was initialised to $\nabla_\perp^2 \varphi_{fl,f}$, whilst the $T_{e,f}$ profile was not used in the STORM2D, STORM3D or TOKAM-3X simulations as they are all isothermal, but was used within GBS and HESEL.

5.5.5 Observable Quantities

As ultimately filaments are of interest because of their contribution to cross-field transport, the radial and vertical positions and velocities of the filaments were used to compare between the experiment and simulations.

Since the experimental results were relatively noisy, the position of the filament was determined from the ion saturation current measurements of the single sided Langmuir probe, I_{sat}, as follows. The experimental current density associated with the filament was calculated as

$$j_{\mathrm{sat},f} = \frac{I_{\mathrm{sat}} - \breve{I}_{\mathrm{sat}}}{A_{\mathrm{probe}}} \tag{5.35}$$

where $\breve{I}_{\mathrm{sat}}$ denotes the median I_{sat} value in time, whilst A_{probe} is the projected area of the Langmuir probe. This quantity was then averaged in the perpendicular drift-plane over the

area that measurements were taken, A:

$$\langle j_{\mathrm{sat},f} \rangle_A = \frac{\iint_A j_{\mathrm{sat},f}\, dx\, dy}{\iint_A dx\, dy}. \tag{5.36}$$

A surface, $S_f(t)$, in the perpendicular drift plane was then defined which satisfied

$$\langle j_{\mathrm{sat},f} \rangle_{S_f} = 0.2 \langle j_{\mathrm{sat},f} \rangle_A \tag{5.37}$$

where

$$\langle j_{\mathrm{sat},f} \rangle_{S_f} = \frac{\iint_{S_f} j_{\mathrm{sat},f}\, dx\, dy}{\iint_{S_f} dx\, dy}. \tag{5.38}$$

The position of the filament in the drift plane was then identified as the geometrical centre of the surface $S_f(t)$:

$$x_c(t) = \iint_{S_f} x\, dx\, dy, \tag{5.39}$$

$$y_c(t) = \iint_{S_f} y\, dx\, dy\,. \tag{5.40}$$

By defining the x_c and y_c in this way, the observed position of the filament is dependent on integral values and is thus less sensitive to local fluctuations or noise. In the simulations, the same procedure was used to calculate x_c and y_c, except for the fact that the ion saturation current associated with the filament could be calculated explicitly from the evolution quantities as

$$j_{\mathrm{sat},f} = en_e \sqrt{\frac{T_e}{m_i}} - en_{e,bg} \sqrt{\frac{T_{e,bg}}{m_i}}. \tag{5.41}$$

The radial and vertical velocities, v_x and v_y, were calculated for both the experiment and the simulations by simply taking the derivatives with respect to time of x_c and y_c:

$$v_x = \frac{dx_c}{dt}, \tag{5.42}$$

$$v_y = \frac{dy_c}{dt}. \tag{5.43}$$

5.5.6 Sensitivity Study

Before directly comparing the simulation results with the experimental measurements, a study was carried out to determine the sensitivity of the simulation codes to the initial conditions and input parameters of the codes.

The sensitivity to the uncertainties of the initial conditions given in Table 5.3 was investigated by performing five simulations for each filament case. The first simulation, hereafter referred to as the standard simulation, was initialised with the central value of each of the parameters. Two simulations were initialised using the maximum and minimum values of the size of the filaments (i.e. of $\sigma_{n,x}$, $\sigma_{n,y}$, $\sigma_{T,x}$, $\sigma_{T,y}$, $\sigma_{\varphi,x,1}$, $\sigma_{\varphi,y,1}$, $\sigma_{\varphi,x,2}$ and $\sigma_{\varphi,y,2}$). A further two simulations were conducted using the values of φ_1 and φ_2 which gave the maximum and minimum values of the quantity $\varphi_1 - \varphi_2$. The maximum difference in the observables between the standard simulation and the other four simulations was then used as a measure of the uncertainty affecting the numerical results. Figure 5.14 plots the results of this study for the

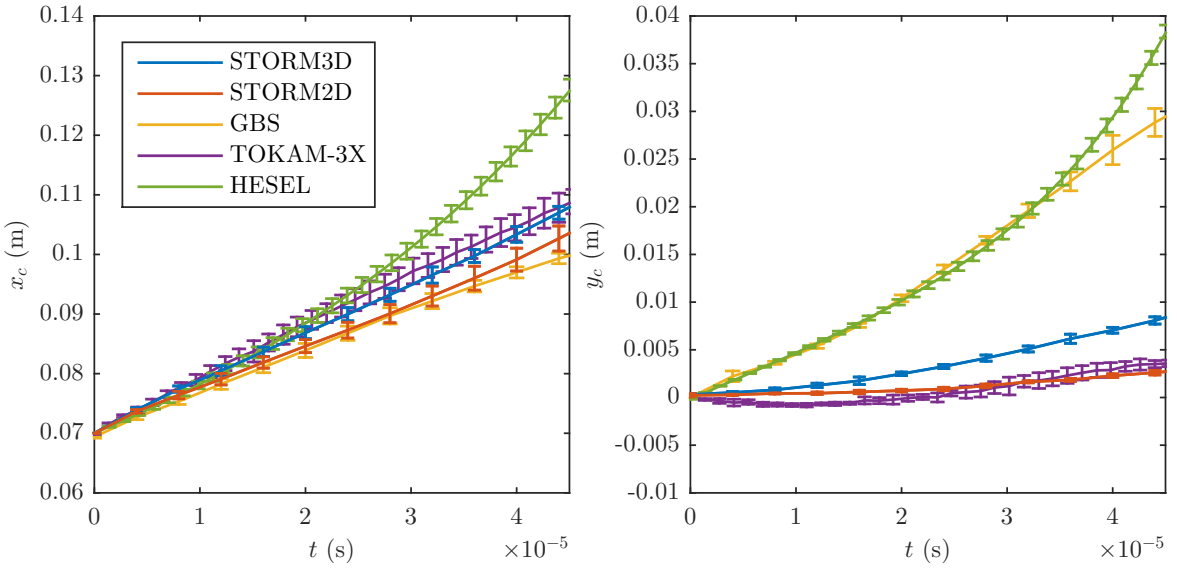

Figure 5.14: Radial (left, x_c) and vertical (right, y_c) positions of the TORPEX Case 1 filament as a function of time, t, as predicted by each simulation code. The solid lines correspond to the central values of each of the initialisation parameters in Table 5.3, whilst the error bars represent the sensitivity of the simulation results to the uncertainties of these parameters.

Case 1 filament, using x_c and y_c as the observable quantities. For each code, the standard simulation is plotted using a solid line, whilst the numerical uncertainty is plotted using error bars. It can be seen that the uncertainties are relatively small in that the overall trend displayed by each code is approximately the same within the extent of the error bars. Similar results were also obtained for the other two filament cases, and so it is concluded that the position of the filament is relatively insensitive to the uncertainties in the input parameters.

Next, the sensitivity of the isothermal codes to the input electron temperature T_e was investigated. A value of $T_e = 2.8$ eV has been selected as the default value for all the isothermal simulations presented in this validation exercise, which corresponds to the highest value of $T_{e,bg}$ in the domain. To test the dependence of the results on this choice, additional simulations were performed using STORM2D and STORM3D of the Case 1 filament using $T_e = 1.85$ eV. This corresponds approximately to the value of $T_{e,bg}$ at $x = 0.07$ cm, which is the centre of the filament in the x direction at $t = 0$. Figure 5.15 provides a comparison of the position of the filaments simulated with each code and T_e value. It is evident that for both STORM2D and STORM3D, a greater radial displacement is found using 2.8 eV than 1.85 eV, with the hotter filament having travelled approximately 15% further by the end of the simulation. A similar trend is shown for the vertical motion. It is therefore concluded that the simulations are relatively sensitive to the choice of T_e. The mechanism for this dependence is discussed and investigated in detail in Section 7.3.

Finally, sensitivity studies were carried out using GBS and TOKAM-3X to ensure that the arbitrary dissipative terms that they use for numerical stability did not significantly affect the simulation results, whilst the choice of the initial ion temperature in HESEL was found to have a negligible influence.

5.5.7 Results

The simulations were evolved to approximately $t = 50$ μs using each code because this was approximately the experimental filament correlation time for all three filament cases. Beginning

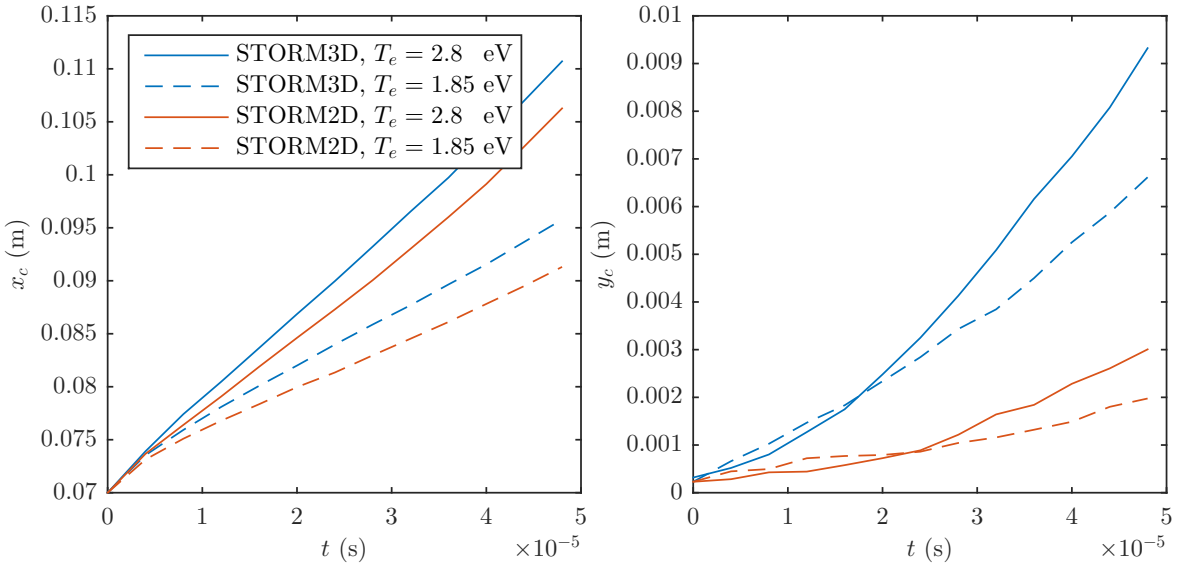

Figure 5.15: Equilibrium electron temperature sensitivity study results. The radial (left, x_c) and vertical (right, y_c) positions of the Case 1 filament are plotted as a function of time, t, as predicted by the STORM2D and STORM3D simulation codes using values of $T_e = 2.8$ eV and $T_e = 1.85$ eV.

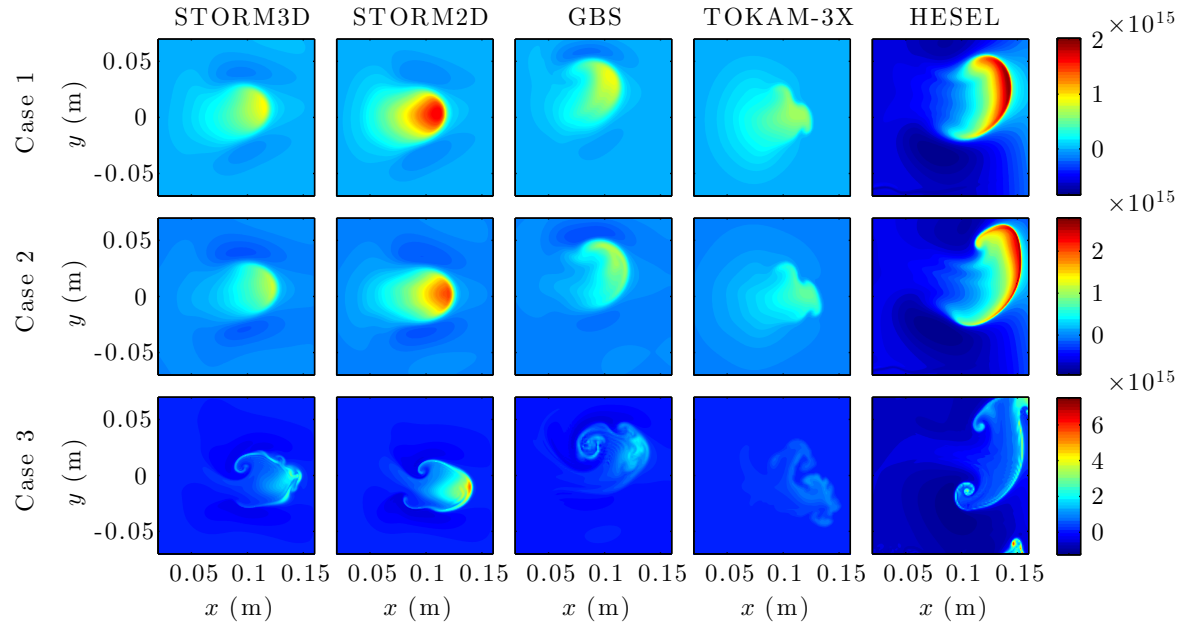

Figure 5.16: Cross-code comparison of the evolved density structure, $n_{e,f}$ (in m^{-3}) of TORPEX filaments. The profiles are shown at $t = 48$ μs, and are taken at the limiter drift-plane in the 3D codes.

first with a qualitative comparison of the evolved filament structures produced by each of the codes, Figures 5.16 and 5.17 display the perpendicular profiles of the density perturbation, $n_{e,f} = n_e - n_{e,bg}$, and the potential φ_f, associated with the filament perturbation for each of the three cases at $t = 48$ μs, from each of the simulation codes. Specifically, the profiles from each of the 3D codes are taken at the target. The following differences can be observed between the codes:

i The HESEL filaments exhibit a significantly different structure compared to all the other codes, in that the HESEL filaments' density profiles are more mushroomed and their potential fields are larger in both magnitude and size. These discrepancies are attributed to the fact that the HESEL sheath dissipation closure term for the parallel currents is averaged over the y direction. Since the potential is approximately an odd function in y with respect to the centre of the filament, this means that negligible dissipation of the electrostatic potential is present in HESEL.

ii The TOKAM-3X Case 1 and 2 filaments display slightly different dynamics to those from the STORM and GBS codes, in that filaments' density profiles are less coherent, and has more structure in the perpendicular plane, especially around the leading front. The cause of this discrepancy is not known.

iii The STORM2D filaments display larger peak density values than the 3D codes. This however, is consistent with the fact that a density drop in $n_{e,f}$ occurs near the target due to sheath losses and that the 3D codes' profiles are shown at the target, whilst STORM2D evolves quantities averaged along the parallel direction.

iv The STORM2D Case 3 filament remains significantly more coherent than any of the 3D codes, which is attributed to the presence of drift wave turbulence that develops in the 3D simulations, and which cannot be represented by the STORM2D model. This effect is apparent only for the Case 3 filament due to the larger density gradients in the initial filament.

v The STORM3D filament profiles are more round than those from GBS. Further tests have identified this is related to the plasma-neutral collisions which are modelled in GBS but not in STORM3D.

vi The GBS filaments each display an upward motion and are spinning counter-clockwise. This upward motion occurs due to the background vertical $\boldsymbol{E} \times \boldsymbol{B}$ velocity that is present due to the radial dependence of the electron temperature background, as discussed in Section 5.5.4.

A more quantitative comparison between each of the simulation codes and experiment is provided by Figures 5.18 and 5.19, which respectively plot the time evolution of v_x and v_y for each filament case. The grey shaded region surrounding the experimental data series represents the uncertainty due to the finite spatial resolution of the probes. The experimental measurements of the radial velocity for all three cases show the filament decelerating as time evolves. With the exception of HESEL, the codes each found a relatively constant radial velocity for Case 1 and deceleration in Case 2, although the deceleration is weaker than in the experiment and the initial velocity is not well represented. The radial velocities obtained in these codes for these cases are in reasonable agreement with the experiment, although they

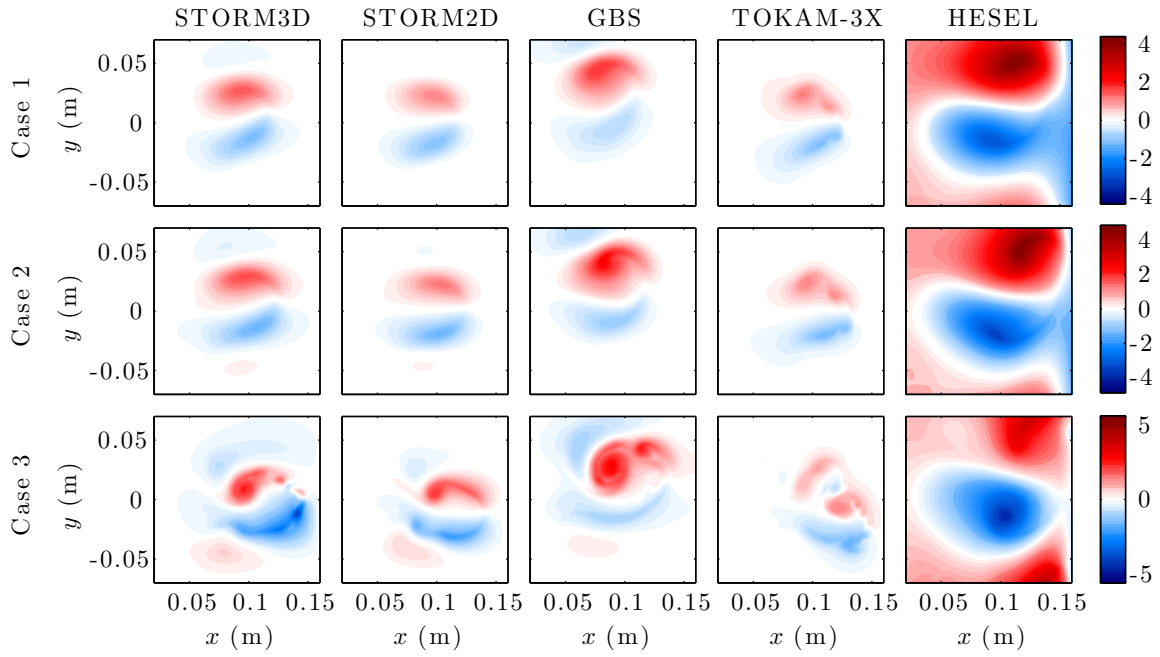

Figure 5.17: Cross-code comparison of the evolved electrostatic potential structure, φ_f, (in V) of TORPEX filaments. The profiles are shown at $t = 48$ μs, and are taken at the limiter drift-plane in the 3D codes.

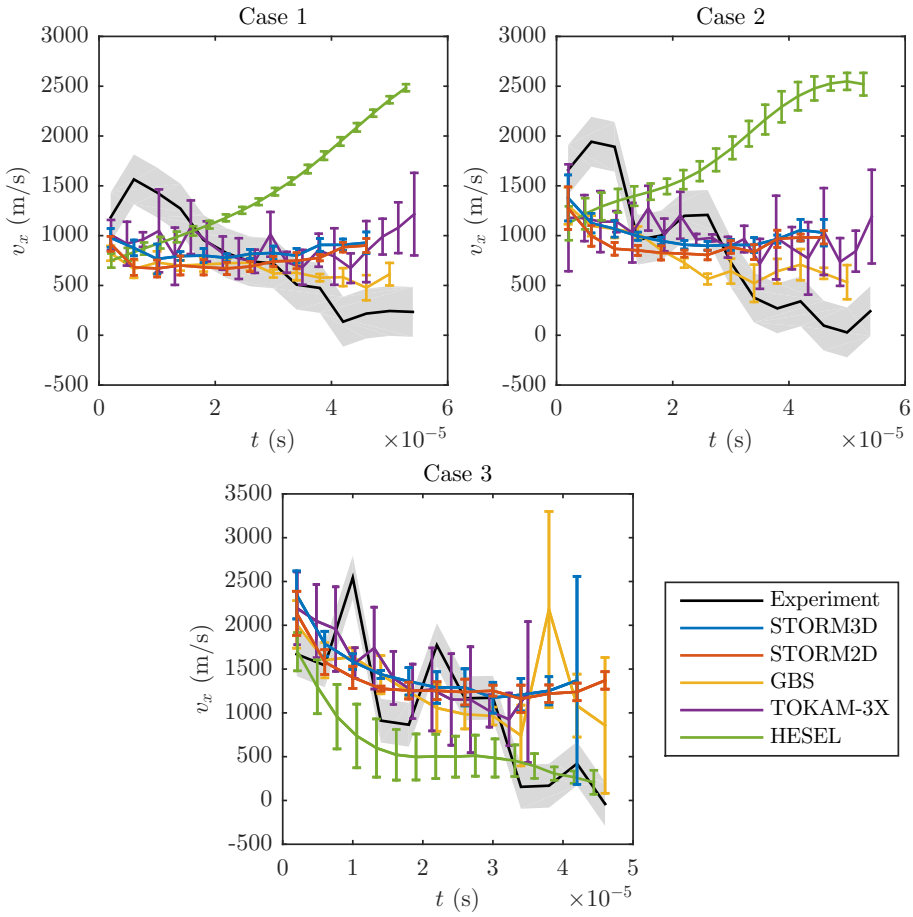

Figure 5.18: Comparison of the radial filament velocity, v_x, between experiment and the simulation codes for each TORPEX filament case.

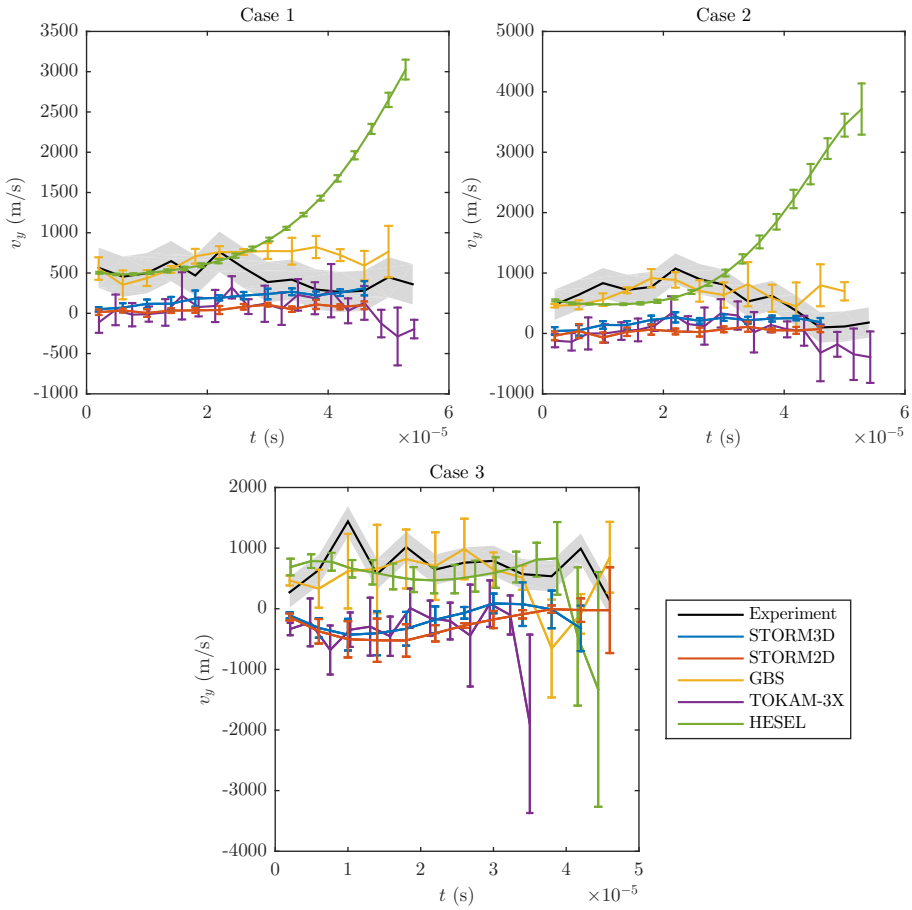

Figure 5.19: Comparison of the vertical filament velocity, v_y, between experiment and the simulation codes for each TORPEX filament case.

underestimate the radial velocity early in the simulation and overestimate the velocity towards the end. HESEL on the other hand displays a strong acceleration in each of these two cases, and clearly does not compare well to the experiment. This acceleration is again attributed to the HESEL sheath dissipation closure term, as discussed above. For Case 3, better agreement with the experiment is shown by all codes, including HESEL.

Concerning the vertical velocities, the best agreement between experiment and simulation is produced by GBS. HESEL displays good agreement in the first half of the Case 1 and Case 2 simulations, but then drastically over-estimates the velocity in the latter half. This better agreement between the non-isothermal codes and the experiment arises from the background vertical $\boldsymbol{E} \times \boldsymbol{B}$ velocity that is present due to the radial dependence of the electron temperature background, as discussed in Section 5.5.4.

The isothermal codes STORM2D, STORM3D and TOKAM-3X all show reasonable agreement amongst themselves in predicting negligible vertical motion for Cases 1 and 2, and a relatively small negative vertical velocity for much of Case 3. This negative velocity arose in these isothermal codes due to the initial condition on ϕ for Case 3, whereas in HESEL and GBS the positive background $\boldsymbol{E} \times \boldsymbol{B}$ velocity dominated.

The ion temperature dynamics present in HESEL were not found to significantly influence the results. Is it supposed that this may be due to the fact that in using a uniform $T_i = 0.025$ eV as an initial condition, $T_i \ll T_e$, and thus the cold ion approximation is valid.

Lastly, it is noted that no significant difference in the computational cost of performing the simulations was observed between STORM3D, GBS and TOKAM-3X.

5.6 Conclusions

This chapter has detailed three systematic verification exercises and one validation exercise which have been completed on STORM3D to ensure that its physical model has been implemented correctly in the code and furthermore that the model itself adequately represents the physics of SOL filaments.

Firstly, in Section 5.2 the equilibrium fields (onto which filaments are initialised in the subsequent chapters) have been verified against analytical results. The results did not converge at the theoretical order of accuracy for the numerical methods used due to the presence of infinite gradients at the sheath, which are inherent to the physics of the SOL. However, the simulations' equilibrium fields did still converge towards their analytic solutions and represented their key features well. Next, in Section 5.3, an analytical solution was derived to a shock tube-like problem, which was then used to carry out a more challenging verification of the code's representation of parallel dynamics. The most rigorous verification exercise of the three completed is presented in Section 5.4, where the Method of Manufactured Solutions was used to verify that every term and boundary condition of the STORM3D physical model has been implemented correctly in the simulation code and to the expected order of accuracy. The code was therefore demonstrated to be $\mathcal{O}(h^2)$ accurate unless first order upwinding is selected for an advection derivative term.

The validation exercise presented in Section 5.5 compared the motions of conditionally averaged filaments from the TORPEX experiment with seeded filament simulations completed using STORM2D and STORM3D, and also other SOL codes which each represented different physics. It was found that STORM3D was as good as any of the other SOL codes in that it provided a reasonable, although not perfect representation of the radial velocities of the filaments in the experiment, especially considering the experimental uncertainties. However, the non-isothermal code GBS was better at capturing the vertical motion of the filaments in the experiment than STORM3D, and so clearly the inclusion of electron temperature dynamics is a desirable future development.

By carrying out these verification and validation exercises, confidence has been gained that the STORM3D physical model has been successfully implemented in code without errors, and that the model itself captures the most important physics of radial filament motion to provide an adequate comparison with the physical reality of an experiment. This therefore justifies the use of STORM3D in subsequent chapters, where it is used to carry out detailed investigations of filamentary dynamics.

Chapter 6

3D Filament Dynamics and Comparison with 2D Models

6.1 Introduction

This chapter seeks to address two issues. Firstly, it will provide a thorough characterisation of the dynamics of filaments simulated using the STORM3D physics module, with particular emphasis on how the filament's initial geometry influences its motions. Secondly, comparisons will be made against STORM2D filament simulations using both the sheath dissipation and vorticity advection parallel closures to investigate which closure provides the best description of the 3D simulations.

6.1.1 Default Simulation Implementation

Unless specified otherwise, the results presented in this and the subsequent chapter were implemented as follows. The input parameters used are listed in Table 6.1 and are broadly relevant for the MAST tokamak. Each simulation was initialised by seeding filaments onto equilibria as described in Section 4.4, with the parameter α in Equation (4.27) specified such that $n_{eq}|_{z=0} = 1$ (in normalised units). The structure of the equilibrium fields used can be inferred from Figure 5.1. A default perpendicular domain of $L_x \times L_y = 15\hat{\delta}_\perp \times 10\hat{\delta}_\perp$ and a spatial mesh consisting of $N_x \times N_y \times N_z = 192 \times 128 \times 16$ was employed, where $\hat{\delta}_\perp$ is the initial perpendicular length scale of the filament perturbation according to Equation (4.28). Thus the perpendicular resolution of the simulations was scaled according to the initial perpendicular size of filament. Simulations have been performed at double this resolution to confirm that the results presented are sufficiently converged. Finally, the filaments were initialised using $x_0 = L_x/4$ and $y_0 = L_y/2$ in Equation (4.28), so that the filament had sufficient room to propagate radially to larger values of x.

6.2 Example Simulation

To begin, the dynamics of a filament initialised with $A = 2$, $L_f = L_\parallel$, $\hat{\delta}_\perp = 16$, and $\hat{\delta}_\parallel = 0$ are examined. The evolution of the filament's density, n_f, and potential, ϕ_f, at the mid-plane ($z = 0$) is shown in Figure 6.1. Here $n_f = n - n_{eq}$, $\phi_f = \phi - \phi_{eq}$ and as in all equivalent figures in the following two chapters, n_f is shown using filled contours, whilst ϕ_f is plotted using black contour lines, with dotted and dashed lines indicating positive and negative values respectively.

Table 6.1: Default parameters used for the simulations presented in this chapter. These parameters are broadly relevant to MAST.

Input Parameters	Normalisation Parameters	Dimensionless Parameters
$T_e = 40$ eV	$\rho_s = 1.82 \times 10^{-3}$ m	$\hat{g} = 2.43 \times 10^{-3}$
$T_i = 40$ eV	$c_s = 4.39 \times 10^{4}$ ms^{-1}	$\hat{\eta}_{\parallel} = 7.08 \times 10^{-6}$
$B = 0.5$ T	$\Omega_i = 2.41 \times 10^{7}$ s^{-1}	$D_n = 1.80 \times 10^{-3}$
$n_{e,0} = 8 \times 10^{18}$ m^{-3}	$D_{\text{Bohm}} = 7.98 \times 10^{1}$ m^{2}s^{-1}	$D_\Omega = 5.00 \times 10^{-2}$
$R = 1.5$ m		$\mu = 3646$
$\ell_{\parallel} = 10$ m		$L_{\parallel} = 5490$
$m_i = 3.32 \times 10^{-27}$ kg		
$\ln \Lambda = 13.28$		
$q = 7$		

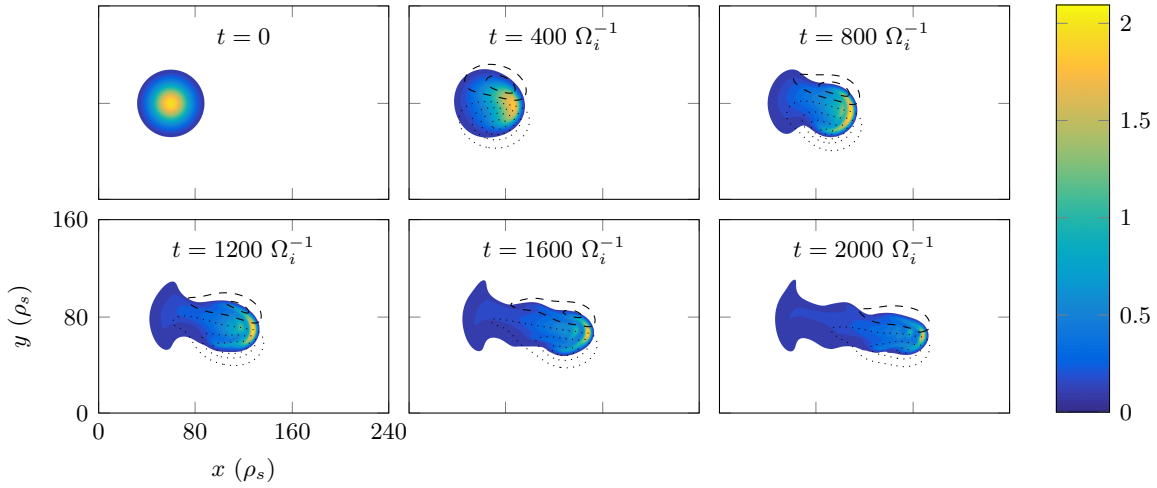

Figure 6.1: Evolution of a $A = 2$, $L_f = L_{\parallel}$, $\hat{\delta}_{\perp} = 16$, $\hat{\delta}_{\parallel} = 0$ filament's density, n_f, (filled contours) and potential, ϕ_f (contour lines) profiles at the mid-plane ($z = 0$). Values of n_f below 0.1 are not plotted. Dotted and dashed contour lines respectively indicate positive and negative values of ϕ_f.

The mid-plane evolution is representative of the entire filament as it remains highly field aligned throughout the simulation, as illustrated by the 3D visualisation of n_f at an example output time in Figure 6.2. Returning to Figure 6.1, it can be seen that as the simulation evolves, the filament develops a dipolar potential structure in the perpendicular plane, which through $\boldsymbol{E} \times \boldsymbol{B}$ advection correspond to a pair of counter-rotating vortices that transport the filament radially outwards. As the filament propagates, the filament's perpendicular structure is transformed from its initial Gaussian profile to have a steep density front at its leading edge and a more gentle decay in its trailing wake. It is noted also that the magnitude of the filament's positive potential lobe develops to become larger than that of its negative lobe and that the filament moves slightly in the negative y direction. The driving mechanism for this aspect of the filament's dynamics will be discussed later in Section 6.3.1.

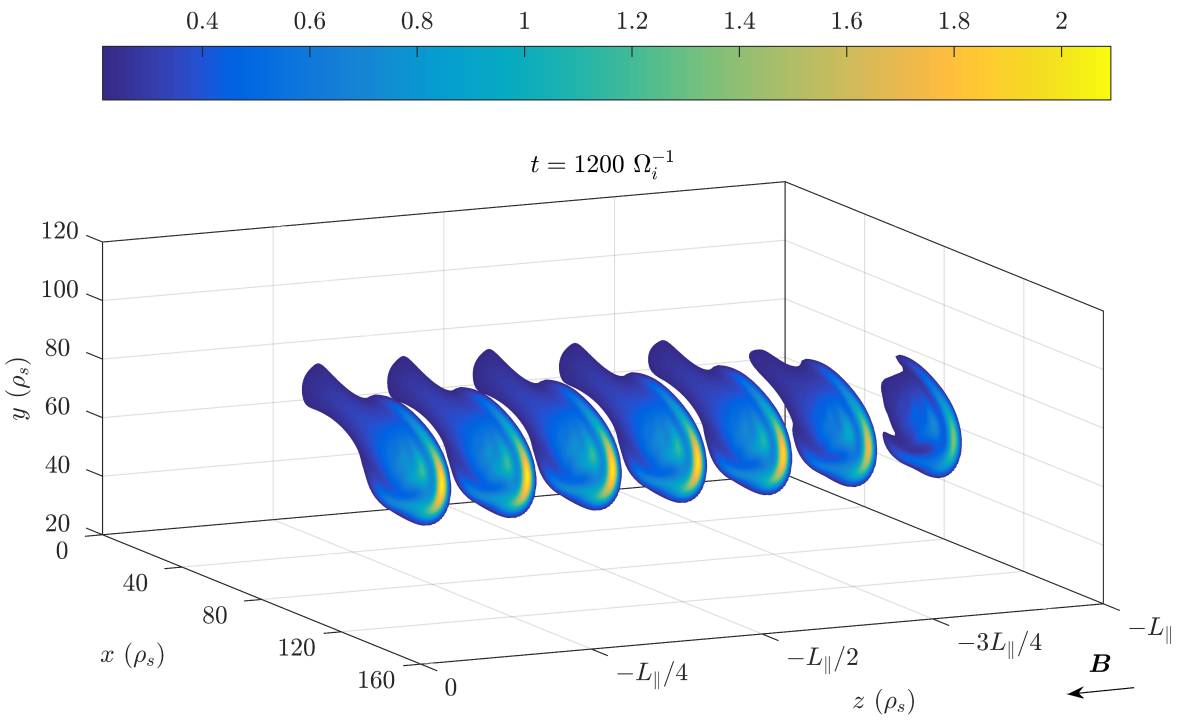

Figure 6.2: 3D visualisation of the $A = 2$, $L_f = L_\parallel$, $\hat{\delta}_\perp = 16$, $\hat{\delta}_\parallel = 0$ filament's density profile, n_f, at $t = 1200\Omega_i^{-1}$. Values of n_f below 0.2 are not plotted.

6.2.1 Quantifying Filaments' Motions

To quantify the motion of the filament, a number of different definitions for the filament's position, $\boldsymbol{x}_f = (x_f,\, y_f,\, z_f)$, are considered. The first is the Centre of Mass (CoM) of n_f, defined as

$$\boldsymbol{x}_f^{\mathrm{CoM}} = \frac{\int_0^{L_x}\int_0^{L_y}\int_0^{L_\parallel} \boldsymbol{x} n_f \,\mathrm{d}x\,\mathrm{d}y\,\mathrm{d}z}{\int_0^{L_x}\int_0^{L_y}\int_0^{L_\parallel} n_f \,\mathrm{d}x\,\mathrm{d}y\,\mathrm{d}z}, \tag{6.1}$$

where $\boldsymbol{x} = (x, y, z)$. It is noted that since the integral in the parallel direction is between 0 and $L_\parallel$, this allows z_f^{CoM} to take non zero values, and thus provides a measure of how far the filament has travelled towards the sheath. If instead the integral were between $-L_\parallel$ and $L_\parallel$, then $z_f^{\mathrm{CoM}} = 0$ by definition due to the symmetry of the system.

The second definition of the filament's position considered is the centre of mass of n_f above a certain threshold, γ:

$$\boldsymbol{x}_f^{\mathrm{CoM},\gamma} = \frac{\int_0^{L_x}\int_0^{L_y}\int_0^{L_\parallel} \boldsymbol{x} n_f^\gamma \,\mathrm{d}x\,\mathrm{d}y\,\mathrm{d}z}{\int_0^{L_x}\int_0^{L_y}\int_0^{L_\parallel} n_f^\gamma \,\mathrm{d}x\,\mathrm{d}y\,\mathrm{d}z}, \tag{6.2}$$

where

$$n_f^\gamma = \begin{cases} 0 & \text{if } n_f < \gamma \\ n_f & \text{if } n_f \geq \gamma \end{cases}. \tag{6.3}$$

The final definition considered is the location at which the filament's peak density occurs:

$$\boldsymbol{x}_f^{\max} = \arg\max\left(n_f\right). \tag{6.4}$$

It is noted that $\boldsymbol{x}_f^{\mathrm{CoM}}$ and $\boldsymbol{x}_f^{\max}$ are in fact specific cases of $\boldsymbol{x}_f^{\mathrm{CoM},\gamma}$, using $\gamma = -\infty$ and $\gamma = \max\left(n_f\right)$ respectively.

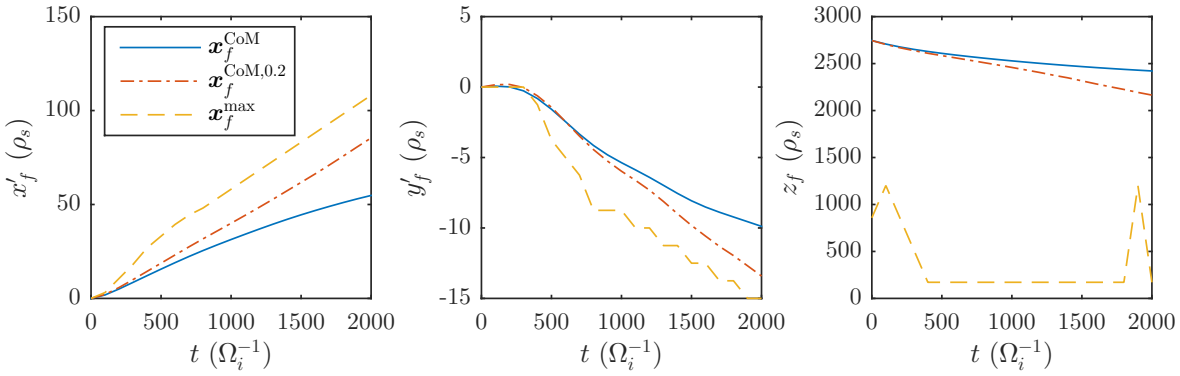

Figure 6.3: Evolution of the $A = 2$, $L_f = L_\parallel$, $\hat{\delta}_\perp = 16$ filament's perpendicular displacement, (x'_f, y'_f), and parallel position, z_f, using the definitions given by Equations (6.1) to (6.4)

Introducing the notation $x'_f = x_f - x_0$, and $y'_f = y_f - y_0$, the time evolution of the perpendicular displacement of the above filament from its original starting position and its position along the parallel direction is plotted in Figure 6.3, for each of the aforementioned definitions of $\boldsymbol{x}_f$. In particular a threshold of $\gamma = 0.2$ was used for $\boldsymbol{x}_f^{\mathrm{CoM},\gamma}$. Each definition produces a broadly similar trend for the perpendicular components, with the filament described to have moved significantly in the positive x direction and slightly downwards in y. Throughout the evolution, it can be seen that $x_f^{\mathrm{CoM}} \leq x_f^{\mathrm{CoM,0.2}} \leq x_f^{\mathrm{max}}$. The reason for this behaviour can be inferred from Figure 6.4, which plots both n_f and each definition of the filament's position at an example time of $t = 1700\ \Omega_i^{-1}$. It can be seen that $\boldsymbol{x}_f^{\mathrm{CoM}}$ lags somewhat behind the other two measures because the filament leaves a trailing wake of slightly enhanced density with respect to n_{eq}. This trailing wake is effectively ignored by $\boldsymbol{x}_f^{\mathrm{CoM,0.2}}$, which thus defines the filament's position to be at a larger value of x, and closer to where intuitively one may consider the filament's centre to be. Furthermore $\boldsymbol{x}_f^{\mathrm{max}}$ is always larger than the other two definitions because the peak value of density is invariably located on the filament's leading front. Returning to the parallel position in Figure 6.3, z_f^{max} shows disagreement with the other two definitions, remaining close to zero throughout. This is because the filament's density at the sheath is drained to the sheath, meaning that the peak density value always is found near to the mid-plane and therefore z_f^{max} is clearly not a good measure of the filament's position along the parallel direction.

Since filaments are primarily of interest because of their contribution to density transport, throughout the following analysis $\boldsymbol{x}_f^{\mathrm{CoM}}$ will used as the definition of $\boldsymbol{x}_f$ because it measures the average displacement of all of the initial density perturbation and also because it provides a better description of the filament's parallel position than $\boldsymbol{x}_f^{\mathrm{max}}$. It is noted however, that if comparisons were to be made with measurements in the perpendicular plane from light emission diagnostics in experiments, then $\boldsymbol{x}_f^{\mathrm{max}}$ may be an appropriate definition.

Measures of the filament's velocity, $\hat{\boldsymbol{v}}_f = (\hat{v}_{f,x}, \hat{v}_{f,y}, \hat{v}_{f,z})$, can be obtained by numerically calculating the time derivative of $\boldsymbol{x}_f$:

$$\hat{\boldsymbol{v}}_f = \frac{d\boldsymbol{x}_f}{dt}, \tag{6.5}$$

However, since this velocity can only be calculated as a post-processing routine using finite differences, the calculated velocity of the filament at a given time will not be an instantaneous velocity, but an average velocity filament between its two adjacent time outputs. Instead therefore the instantaneous perpendicular velocity components are approximated using the

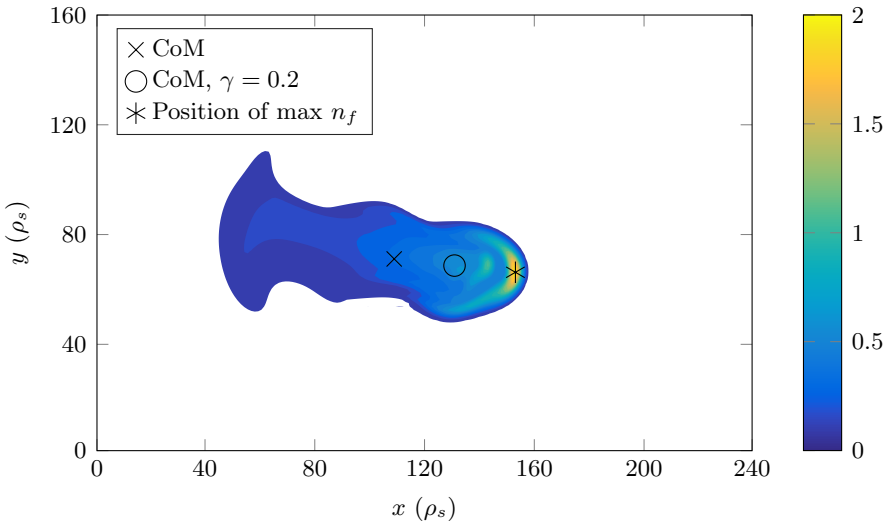

Figure 6.4: Demonstration of where each definition of the filament's position, given by Equations (6.1) to (6.4) locate the $A = 2$, $L_f = L_\parallel$, $\hat{\delta}_\perp = 16$ filament to be in the perpendicular plane at the example time $t = 1700\ \Omega_i^{-1}$, in relation to the filament's density profile, n_f, which is plotted using filled contours. Values of n_f below 0.1 are not plotted.

$\boldsymbol{E} \times \boldsymbol{B}$ velocity as follows:

$$\hat{v}_{f,x} = \frac{\int_0^{L_x}\int_0^{L_y}\int_0^{L_\parallel} n_f \frac{\partial \phi}{\partial y}\,\mathrm{d}x\,\mathrm{d}y\,\mathrm{d}z}{\int_0^{L_x}\int_0^{L_y}\int_0^{L_\parallel} n_f\,\mathrm{d}x\,\mathrm{d}y\,\mathrm{d}z}, \tag{6.6}$$

$$\hat{v}_{f,y} = \frac{\int_0^{L_x}\int_0^{L_y}\int_0^{L_\parallel} -n_f \frac{\partial \phi}{\partial x}\,\mathrm{d}x\,\mathrm{d}y\,\mathrm{d}z}{\int_0^{L_x}\int_0^{L_y}\int_0^{L_\parallel} n_f\,\mathrm{d}x\,\mathrm{d}y\,\mathrm{d}z}. \tag{6.7}$$

It is noted that these definitions neglect the lower order perpendicular velocities arising due to the diamagnetic velocity or through diffusive effects. The evolution of the example filament's perpendicular velocities calculated in this manner are plotted in Figure 6.5.

6.3 Effect of Filament Geometry

6.3.1 Parallel Extent, L_f

The influence of the parallel extent of a filament on its motions can be observed by comparing Figure 6.6, which plots the mid-plane dynamics of n_f and ϕ_f of a filament initialised as in the example simulation, but with $L_f = L_\parallel/2$ rather than $L_f = L_\parallel$. By cross comparison with Figure 6.1, it can be seen that when the filament does not extend all the way to the target (and hence parallel gradients are present), the potential field that develops is altered such that the positive lobe becomes significantly stronger and larger than the negative lobe. This effect has been observed in previous works [168, 192, 195, 197] and occurs due the presence of the term

$$\mu\left(\nabla_\parallel \phi - \nabla_\parallel \ln n\right)$$

in the parallel electron velocity equation, Equation (3.68). This term drives the filament's potential field to exhibit a *Boltzmann* response, in that it becomes aligned with $\ln n$. This

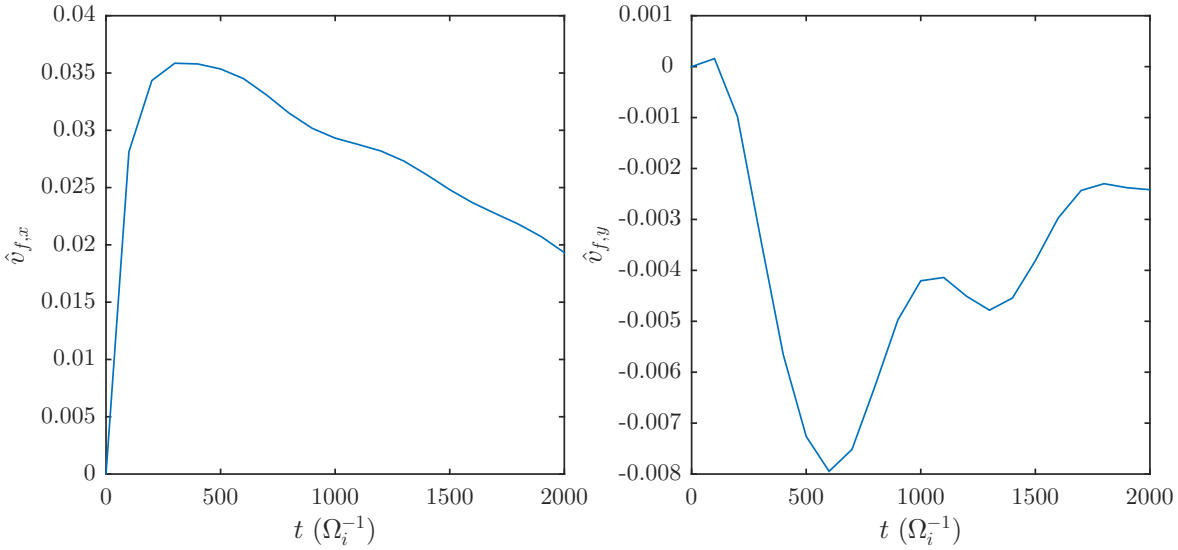

Figure 6.5: Evolution of the $A = 2$, $L_f = L_\parallel$, $\hat{\delta}_\perp = 16$ filament's perpendicular velocity components, $\hat{v}_{f,x}$, and $\hat{v}_{f,y}$.

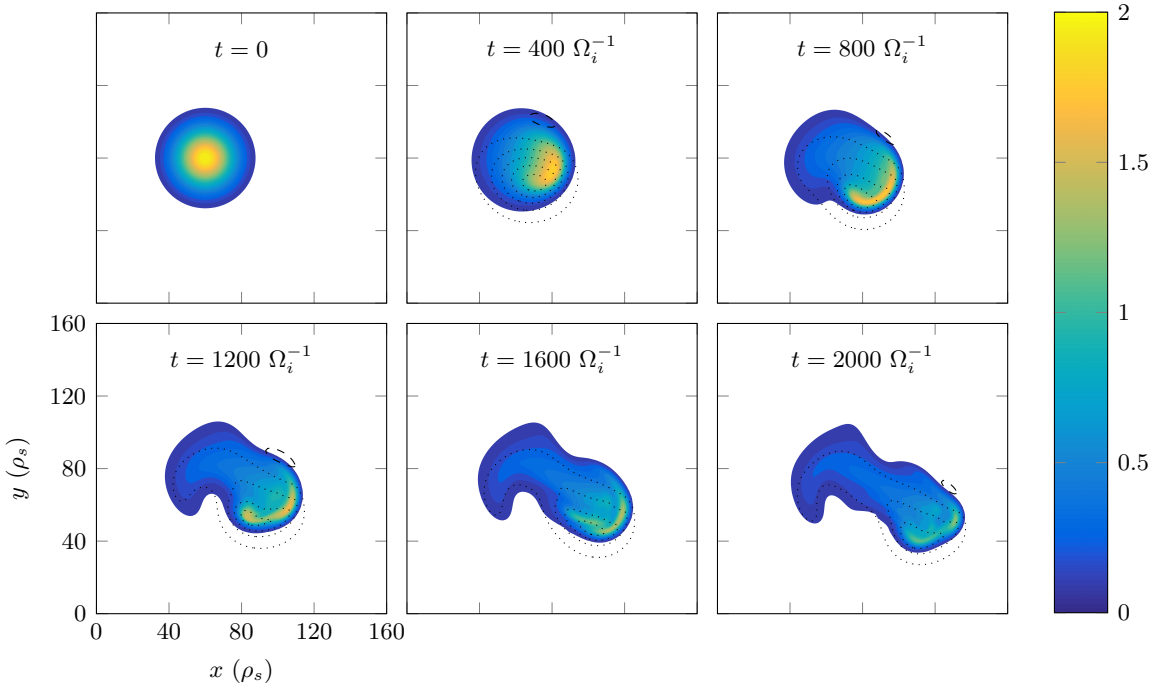

Figure 6.6: Evolution of the $A = 2$, $L_f = L_\parallel/2$, $\hat{\delta}_\perp = 16$, $\hat{\delta}_\parallel = 0$ filament's density (filled contours), n_f, and potential (contour lines), ϕ_f, profiles at the mid-plane ($z = 0$). Values of n_f below 0.1 are not plotted. Dotted and dashed contour lines respectively indicate positive and negative values of ϕ_f.

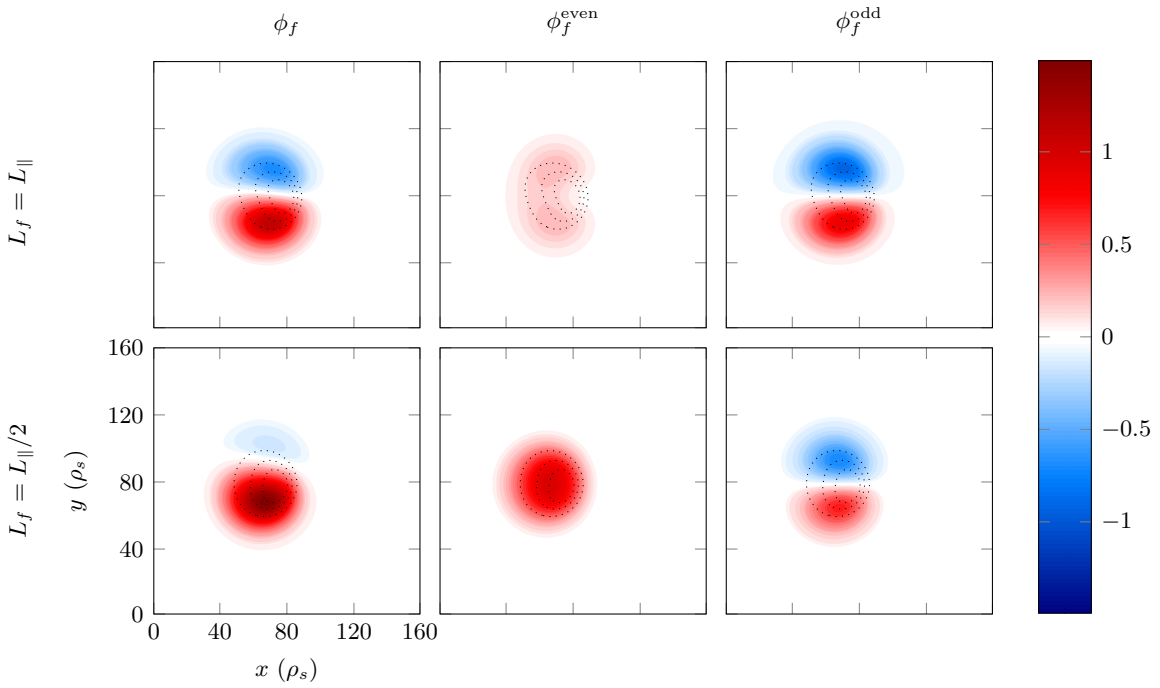

Figure 6.7: Decomposition of the potential field, ϕ_f, of $L_f = L_\parallel$ and $L_f = L_\parallel/2$ filaments into components with even (ϕ_f^{even}) and odd (ϕ_f^{odd}) parity in the bi-normal direction with respect to the centre of the filament. Both filaments were otherwise initialised with $A = 2$, $\hat{\delta}_\perp = 16$ and $\hat{\delta}_\parallel = 0$, and all fields are plotted at $z = 0$, $t = 300\ \Omega_i^{-1}$.

alignment can be demonstrated by isolating the components of ϕ_f which have even and odd parity in y with respect to the centre of the filament in the bi-normal direction, y_f. These components can be calculated for an arbitrary quantity, f, according to

$$f^{\text{even}} = \frac{f\left(y - y_f\right) + f\left(y_f - y\right)}{2}. \tag{6.8}$$

$$f^{\text{odd}} = \frac{f\left(y - y_f\right) - f\left(y_f - y\right)}{2}. \tag{6.9}$$

Figure 6.7 therefore plots ϕ_f and its constituent components, ϕ_f^{even} and ϕ_f^{odd}, for both the $L_f = L_\parallel$ and $L_f = L_\parallel/2$ filaments at $z = 0$ and $t = 300\ \Omega_i^{-1}$. The filament's density profile, n_f, which broadly has even parity is also plotted using black dotted contour lines for reference. It can be seen that the $L_f = L_\parallel/2$ filament has a much stronger ϕ_f^{even} component that is highly aligned to the density field and which when superposed with the ϕ_f^{odd} field, produces a ϕ_f whose positive lobe is stronger than its negative lobe. In contrast, the $L_f = L_\parallel$ filament has a much weaker ϕ_f^{even} component because only very weak parallel density gradients exist within the filament, and therefore $\phi_f \approx \phi_f^{\text{odd}}$. It is noted that it has been shown analytically that if ϕ_f^{even} is initialised to zero, as it is here, it can only grow within this model through the $\nabla_\parallel n$ term in Equation (3.68) [136, 196].

Returning to Figure 6.6, the broadly monopolar potential field corresponds to the filament spinning clockwise in the perpendicular plane through $\boldsymbol{E} \times \boldsymbol{B}$ motions, when viewed with the magnetic field directed out of the page. These *Boltzmann spinning* motions combine with the radial $\boldsymbol{E} \times \boldsymbol{B}$ velocity to produce a net displacement in the negative y direction. This can be observed in Figure 6.8, which compares the perpendicular displacements and velocities between the $L_f = L_\parallel$ and $L_f = L_\parallel/2$ filaments, in that the $L_f = L_\parallel/2$ filament exhibits a larger displacement in the negative y direction than the $L_f = L_\parallel$ case. Incidentally the reason

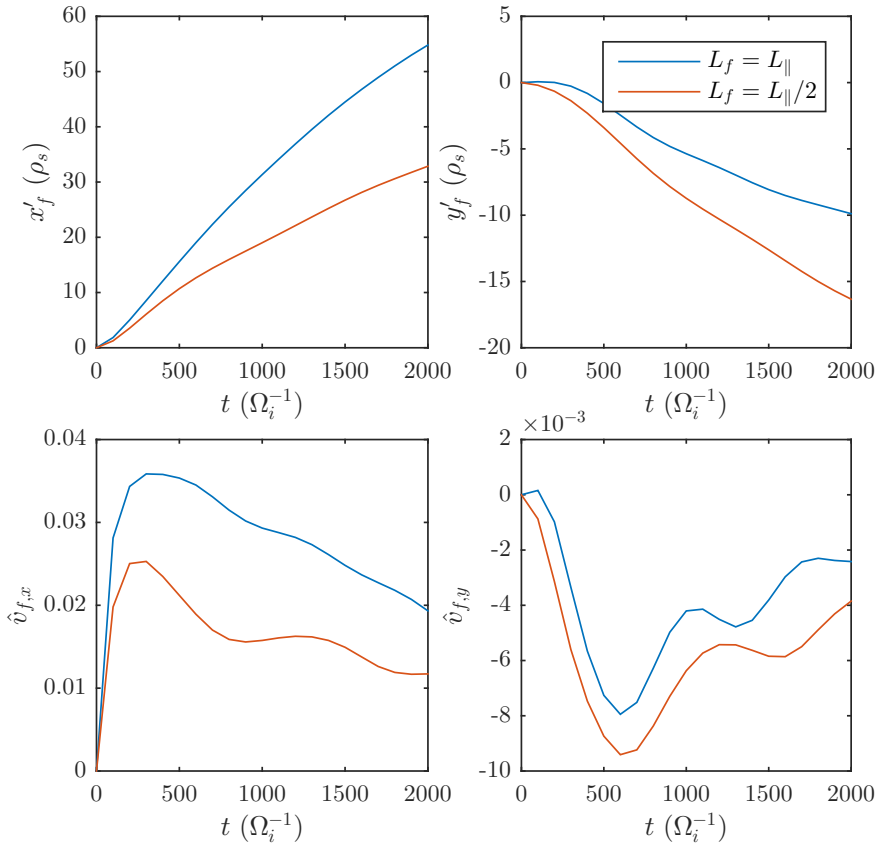

Figure 6.8: Comparison of the perpendicular displacements and velocities of filaments with $L_f = L_\parallel$ and $L_f = L_\parallel$. Both simulations were otherwise initialised with $A = 2$, $\hat{\delta}_\perp = 16$, and $\hat{\delta}_\parallel = 0$.

that the $L_f = L_\parallel$ filament exhibits a negative displacement at all, particularly in the later stages of the simulation, is that the draining of the filament's density to the sheath generates parallel gradients.

From Figure 6.8, it can also be seen that reducing the parallel extent of the filament reduces its radial velocity as the $L_f = L_\parallel/2$ filament moves more slowly in the radial direction. To explain this, it is first noted that the resistivity in the system is sufficiently small such that ϕ_f^{odd}, which is predominantly responsible for the radial velocity, is largely uniform along the field line. This potential is thus effectively determined by the parallel integral of the diamagnetic current drive throughout the domain. Since the $L_f = L_\parallel/2$ filament has approximately half the diamagnetic current drive that is present in the $L_f = L_\parallel$ case, it has a weaker ϕ_f^{odd} (as can be observed in Figure 6.7) which corresponds directly to a slower radial velocity.

6.3.2 Perpendicular size, $\hat{\delta}_\perp$

Theoretical Predictions

Before presenting simulations of filaments initialised with varying $\hat{\delta}_\perp$, it is useful to first derive the theoretical radial velocity scaling predictions from prior works [122, 160, 168], as comparisons will be made with these. Using the parameters given in Table 6.1, the resistivity of the plasma being simulated is small, in the sense that the resistance to currents travelling from the mid-plane to the sheath entrance is negligible compared to the resistance to currents

travelling through the sheath to the target,

$$\hat{\eta}_{\parallel} L_{\parallel} \ll \frac{1}{n_s}.$$

Here n_s denotes the normalised density at the sheath entrance, which is of order unity. In this low resistivity limit, the sheath dissipation closure (Equations (3.74) and (3.75)) is justified, and therefore the 3D model can be approximated by this closure (this is confirmed in Section 6.4). The sheath dissipation closure's vorticity equation will thus be used here to gain insight. Considering a filament of perpendicular length scale $\hat{\delta}$ that extends all the way to the target, and assuming that $\partial\Omega/\partial t = 0$, the magnitude of each of the terms in Equation (3.74) on the bottom half of the filament in the perpendicular plane can be be estimated as follows:

$$\frac{\partial \Omega}{\partial t} = -\left(\hat{\boldsymbol{b}} \times \nabla\phi\right) \cdot \nabla\Omega + \frac{\phi}{L_{\parallel}} - \frac{\hat{g}}{n}\frac{\partial n}{\partial y} + D_{\Omega}\nabla_{\perp}^2\Omega \tag{6.10}$$

$$\frac{\hat{g}}{\hat{\delta}} \sim \frac{\phi_{\text{peak}}^2}{\hat{\delta}^4} + \frac{\phi_{\text{peak}}}{L_{\parallel}} + \frac{D_{\Omega}\phi_{\text{peak}}}{\hat{\delta}^4}. \tag{6.11}$$

In Equation (6.11), ϕ_{peak} refers to the peak value of the positive potential lobe that is located on the bottom half of the filament. The $\hat{g}/\hat{\delta}$ term represents the diamagnetic current drive, whilst the three terms on the RHS respectively correspond to the polarisation current (inertial) term, the parallel sheath current term and the viscosity term.

From this expression, it can be seen that up to three different regimes will exist depending on the size of the filament, $\hat{\delta}$, the parallel connection length, $L_{\parallel}$, and the viscosity of the system, D_{Ω}. At the very smallest and largest filament sizes, the diamagnetic current will predominantly be balanced by the viscous and sheath current terms respectively. Assuming the viscosity to not be too large, there will also be a regime at intermediate sizes, where the polarisation current will instead dominate. These regimes will hereafter be referred to as the *viscous regime*, the *inertial regime*, and the *sheath current regime*. The approximate transition from the inertial regime to the sheath current regime will occur when the two respective terms are of equal magnitude, i.e. when $\phi = \hat{\delta}^4/L_{\parallel}$. By substituting this value of ϕ into Equation (6.11), and neglecting the viscous term, the filament size at which this transition occurs is estimated to be:

$$\hat{\delta}_* = \left(\frac{\hat{g}L_{\parallel}^2}{2}\right)^{1/5}. \tag{6.12}$$

It is noted from Reference [169] that $\hat{\delta}_*$ should also include an order unity correction to account for the magnitude of the filament's density perturbation, but since this can only be determined numerically via an amplitude scan, it has been neglected here. By applying an equivalent procedure, the filament size at which the transition from the viscous to the inertial regime occurs can also be approximated as:

$$\hat{\delta}_\dagger = \left(\frac{2D_{\Omega}^2}{\hat{g}}\right)^{1/3}. \tag{6.13}$$

It is noted however that if $\hat{\delta}_\dagger > \hat{\delta}_*$, or equivalently if

$$D_{\Omega} > \left(\frac{\hat{g}^4 L_{\parallel}^3}{2}\right)^{1/5},$$

then the inertial regime will not exist, and instead a transition from the viscous regime to the sheath current regime will occur at

$$\hat{\delta}_\triangle = \left(\frac{D_{\Omega}}{L_{\parallel}}\right)^{1/4} \tag{6.14}$$

An estimate of the value of ϕ_{peak}, and hence the radial velocity of the filament, $\hat{v}_{f,x} \sim \phi_{\text{peak}}/\hat{\delta}$, in each regime can be obtained by balancing the diamagnetic term with the respective dominant terms on the RHS in (6.11), yielding the following predictions for how the velocity of the filament will scale with its perpendicular size in each regime.

$$\hat{v}_{f,x} \sim \begin{cases} \hat{\delta}^2 & \text{for} \quad \hat{\delta} \ll \hat{\delta}_\dagger & \text{(Viscous regime)} \\ \hat{\delta}^{1/2} & \text{for} \quad \hat{\delta}_\dagger \ll \hat{\delta} \ll \hat{\delta}_* & \text{(Inertial regime)} \\ \hat{\delta}^{-2} & \text{for} \quad \hat{\delta} \gg \hat{\delta}_* & \text{(Sheath current regime)} \end{cases} . \tag{6.15}$$

In the above, it is implicitly assumed that $\hat{\delta}_\dagger < \hat{\delta}_*$. If instead, $\hat{\delta}_\dagger > \hat{\delta}_*$, the scaling predictions reduce to

$$\hat{v}_{f,x} \sim \begin{cases} \hat{\delta}^2 & \text{for} \quad \hat{\delta} \ll \hat{\delta}_\triangle & \text{(Viscous regime)} \\ \hat{\delta}^{-2} & \text{for} \quad \hat{\delta} \gg \hat{\delta}_\triangle & \text{(Sheath current regime)} \end{cases} . \tag{6.16}$$

It is noted that the viscous regime is absent from previous works, as unless the viscosity is very high, $\hat{\delta}_\dagger$ will typically be less than or of the order of the ion gyro-radius, and at such small scales, fluid models are not appropriate.

Simulations

To illustrate the different dynamics that are produced in the simulations depending on the perpendicular size of the filament, Figures 6.9 and 6.10 plot the mid-plane evolution of n_f and ϕ_f for filaments initialised as in the $\hat{\delta}_\perp = 16$ example simulation in Section 6.2 but with $\hat{\delta}_\perp = 5$ and $\hat{\delta}_\perp = 40$. Given that for the simulation parameters (listed in Table 6.1), $\hat{\delta}_* = 8.18$ and $\hat{\delta}_\dagger = 1.27$, these two filaments are predicted to lie in the inertial and sheath current limited regimes respectively.

It is clear from these figures that neither filament displays the coherent propagation that was produced by the $\hat{\delta}_\perp = 16$ filament, shown in Figure 6.1. The $\hat{\delta}_\perp = 5$ filament rapidly develops a potential field that extends in the perpendicular plane beyond the extent of the density perturbation. The associated counter rotating vortices therefore act to stretch the leading front of the filament, and cause it to form a mushroom-like structure through Rayleigh-Taylor-like motions. This, combined with collisional diffusion causes the filament to rapidly lose its coherence. In contrast, the $\hat{\delta}_\perp = 40$ filament develops a potential field during the early stages of its motion that lies almost entirely within the initial density perturbation. In this case the vortices cause the filament to expel a *finger* or *jet* of density, which then propagates radially outwards. Returning to the $\hat{\delta}_\perp = 16$ simulation, it is now clear that this filament was able to propagate relatively coherently because the spatial extent of its potential field was approximately the same as its density perturbation, meaning that neither mushrooming nor fingering motions occurred.

A quantitative comparison of the perpendicular displacements and velocities of these three filaments is provided in Figure 6.11. It can be seen that whilst the $\hat{\delta}_\perp = 5$ developed a faster radial velocity during the early stages of its motion than the other two filaments, this velocity dramatically reduced around $t = 300\ \Omega_i^{-1}$, which from Figure 6.9, can be seen to correspond to when filament developed a mushroom structure. The $\hat{\delta}_\perp = 16$ filament also reached a peak radial velocity in the early stages of the simulation, which then gradually decayed with time, but exhibits the greatest net radial displacement at the end of the simulation. Finally the $\hat{\delta}_\perp = 40$ filament's radial velocity was significantly less than that of the two smaller filaments throughout because effectively only its finger structure propagated, whilst the remainder of

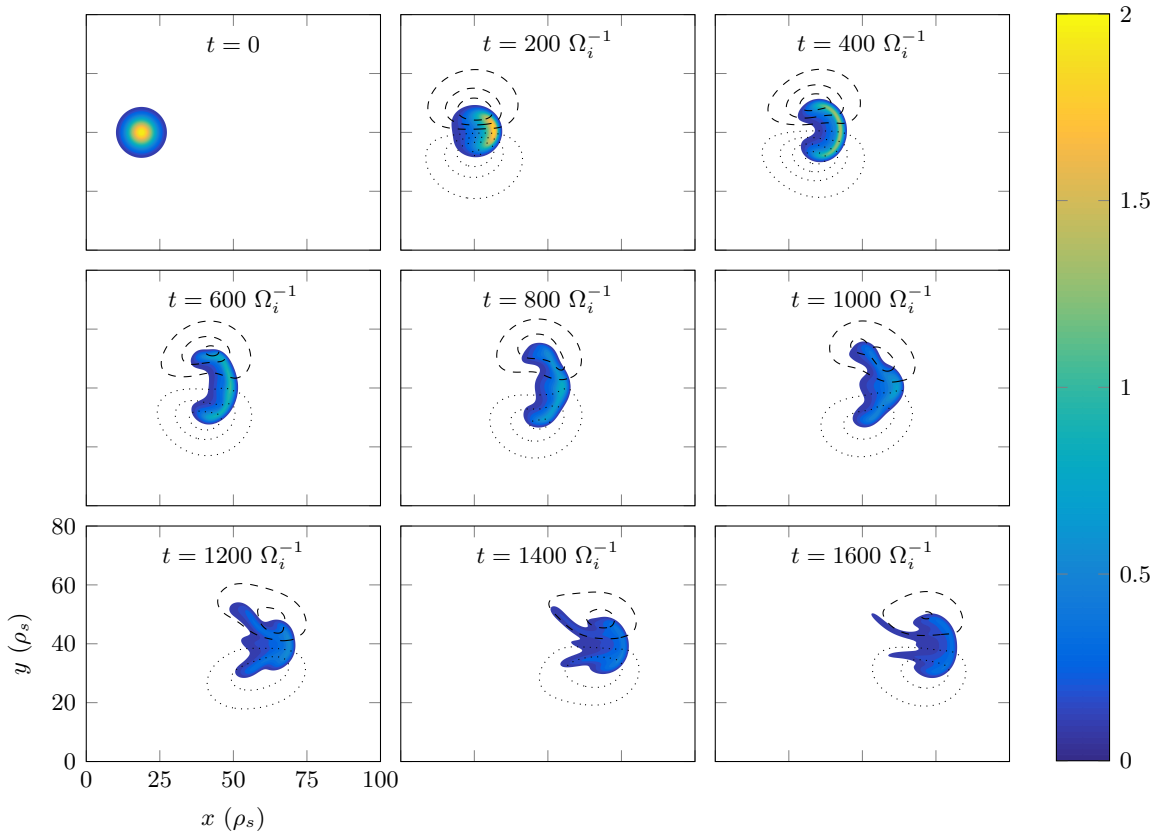

Figure 6.9: Evolution of a $A = 2$, $L_f = L_\parallel$, $\hat{\delta}_\perp = 5$, $\hat{\delta}_\parallel = 0$ filament's density (filled contours), n_f, and potential (contour lines), ϕ_f, profiles at the mid-plane ($z = 0$). Values of n_f below 0.1 are not plotted. Dotted and dashed contour lines respectively indicate positive and negative values of ϕ_f.

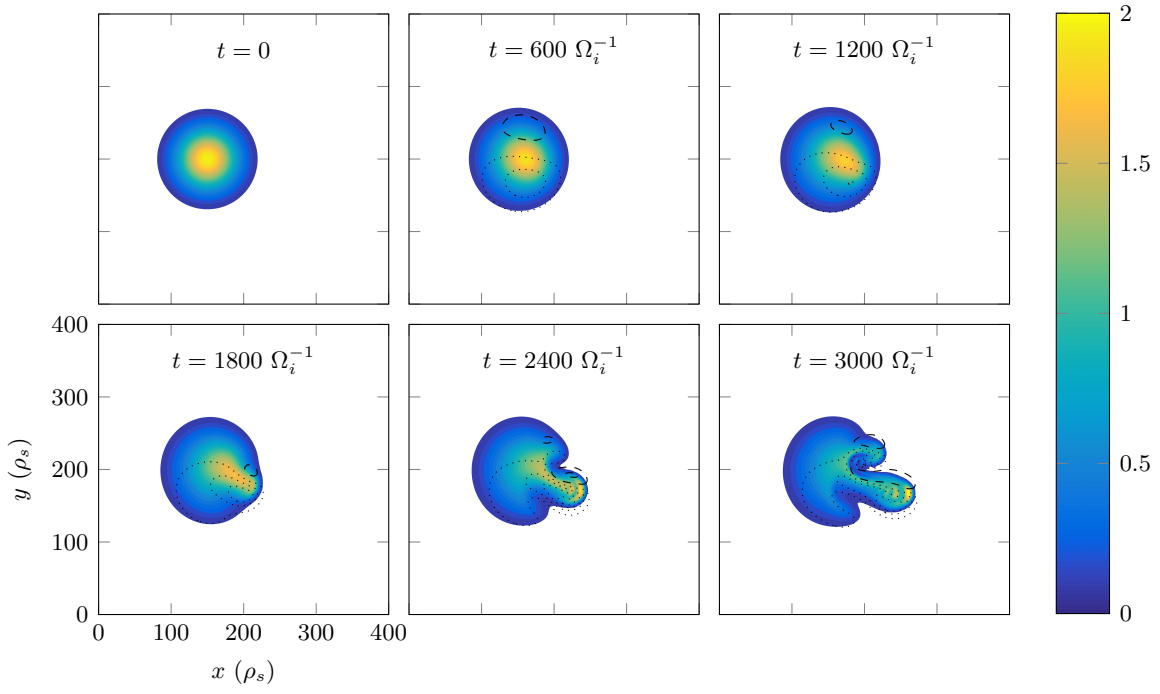

Figure 6.10: Evolution of a $A = 2$, $L_f = L_\parallel$, $\hat{\delta}_\perp = 40$, $\hat{\delta}_\parallel = 0$ filament's density (filled contours), n_f, and potential (contour lines), ϕ_f, profiles at the mid-plane ($z = 0$). Values of n_f below 0.1 are not plotted. Dotted and dashed contour lines respectively indicate positive and negative values of ϕ_f.

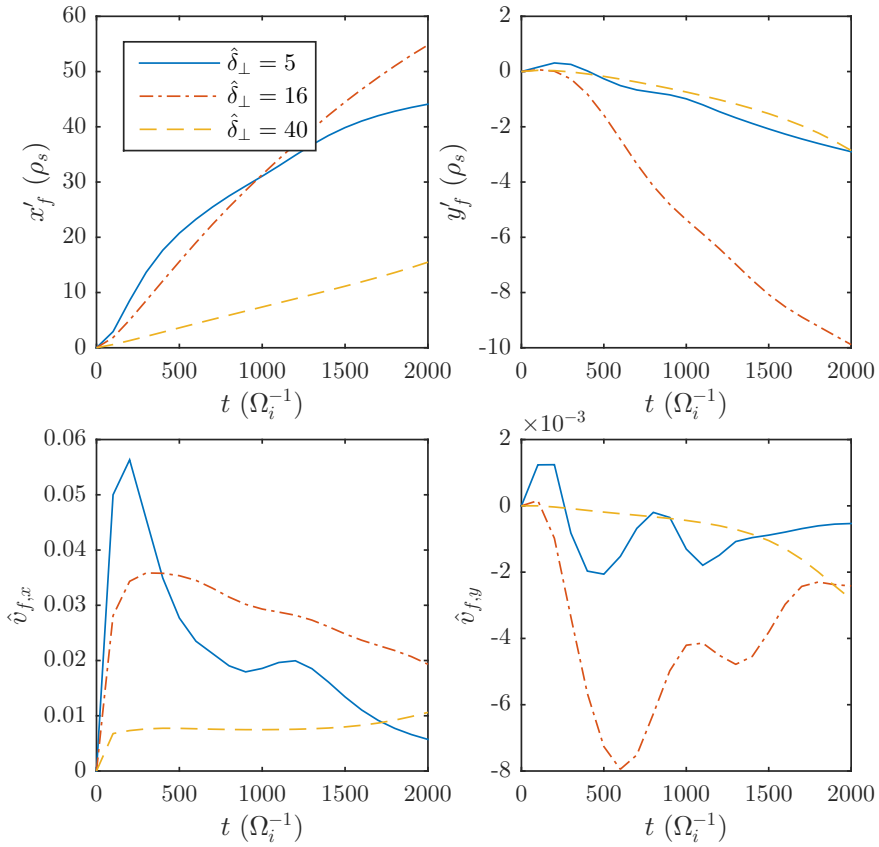

Figure 6.11: Comparison of the perpendicular displacements and velocities of filaments with $\hat{\delta}_\perp = 5$, 16 and 40. All simulations were otherwise initialised with $A = 2$, $L_f = L_\parallel$, and $\hat{\delta}_\parallel = 0$.

the initial filament was motionless. Furthermore this velocity remained relatively constant throughout the simulation because the finger structure's front maintained its coherence by being continually replenished by density travelling along the filament's column.

The contrasting current balances found in each of these three filaments, plus an additional $\hat{\delta}_\perp = 5$ simulation performed with zero viscosity and particle diffusion ($D_\Omega = 0$, $D_n = 0$) is shown in Figure 6.12. This figure plots for each filament the divergences of each of the current densities in the system, divided by density. These quantities correspond directly to the terms in the vorticity equation, Equation (3.66). The fields are plotted at $z = 0$ and at a time close to the peak velocity for each filament, and the dynamics shown are representative of the entire simulation. This figure shows that broadly, the current balance in each filament is as predicted by the scaling arguments discussed above. In the $\hat{\delta}_\perp = 40$ filament, which satisfies $\hat{\delta}_\perp > \hat{\delta}_*$, the compressible diamagnetic currents are almost entirely balanced by parallel currents. To demonstrate that these parallel currents form a closed circuit through the target, Figure 6.13, plots $J_\parallel$ in a $y - z$ plane through the middle of the filament again at a time close to the filament's peak velocity. An equivalent plot is shown for a $L_f = L_\parallel/2$ but otherwise identically initialised filament, to demonstrate that electrical connection to the target still occurs through the background plasma in this case, even if the filament perturbation itself does not reach the sheath.

Returning to Figure 6.12, parallel currents are almost negligible in the smaller $\hat{\delta}_\perp = 5$ filament, which satisfy $\hat{\delta}_\perp < \hat{\delta}_*$, and instead a combination of viscous currents and polarisation currents act to balance the diamagnetic currents, with the viscous currents playing a more dominant role. This is slightly surprising, since for this filament $\hat{\delta}_\perp > \hat{\delta}_\dagger$, and thus the above

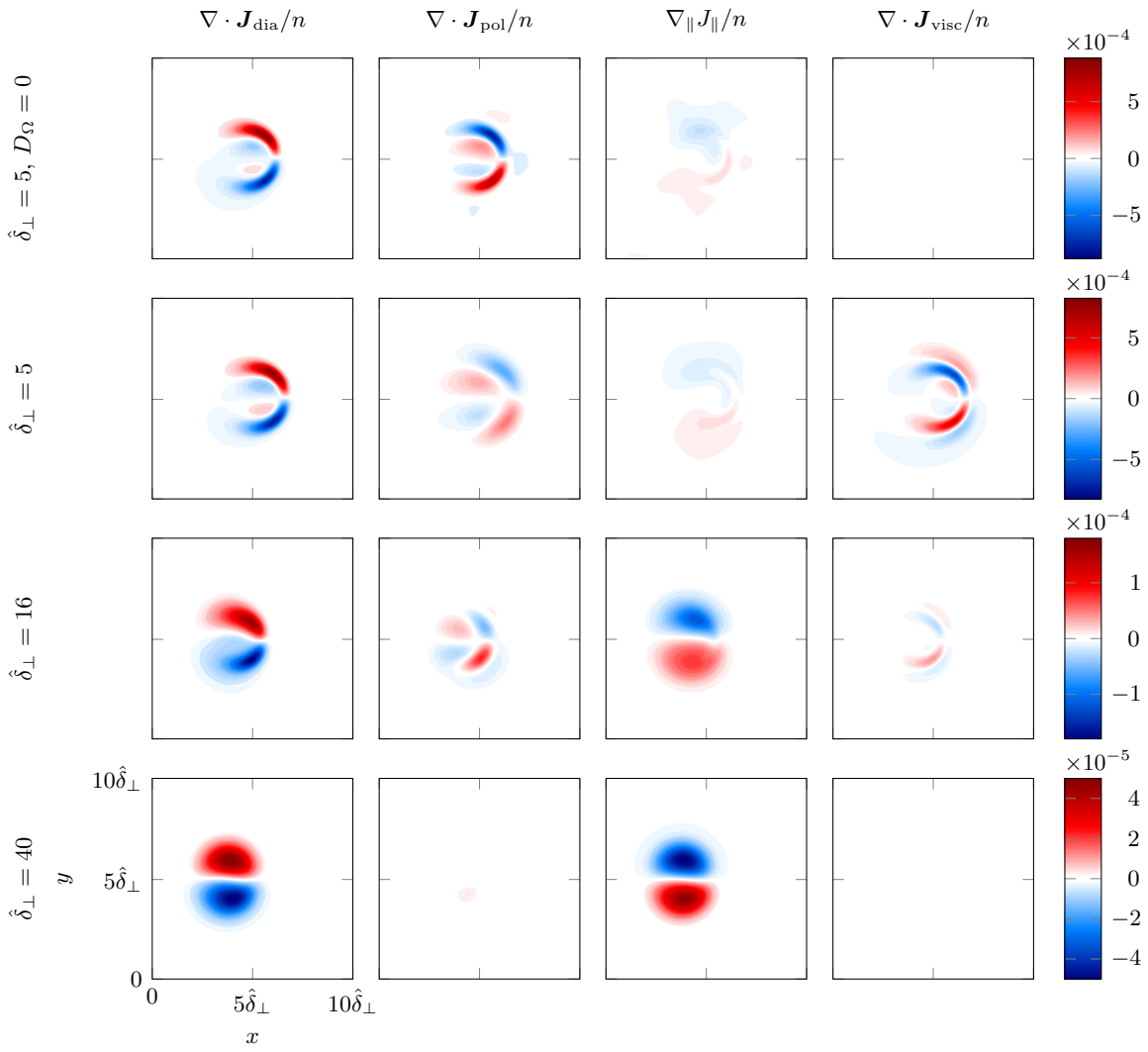

Figure 6.12: Comparison of the current balances found in $\hat{\delta}_{\perp} = 5$, 16, and 40 filaments. All quantities are plotted at the mid-plane ($z = 0$) and at a time close to the peak velocity of each filament and all filaments were otherwise initialised with $A = 2$, $L_f = L_{\parallel}$ and $\hat{\delta}_{\parallel} = 0$. The quantities are also plotted for a $\hat{\delta}_{\perp} = 5$ filament evolved with $D_{\Omega} = 0$ and $D_n = 0$.

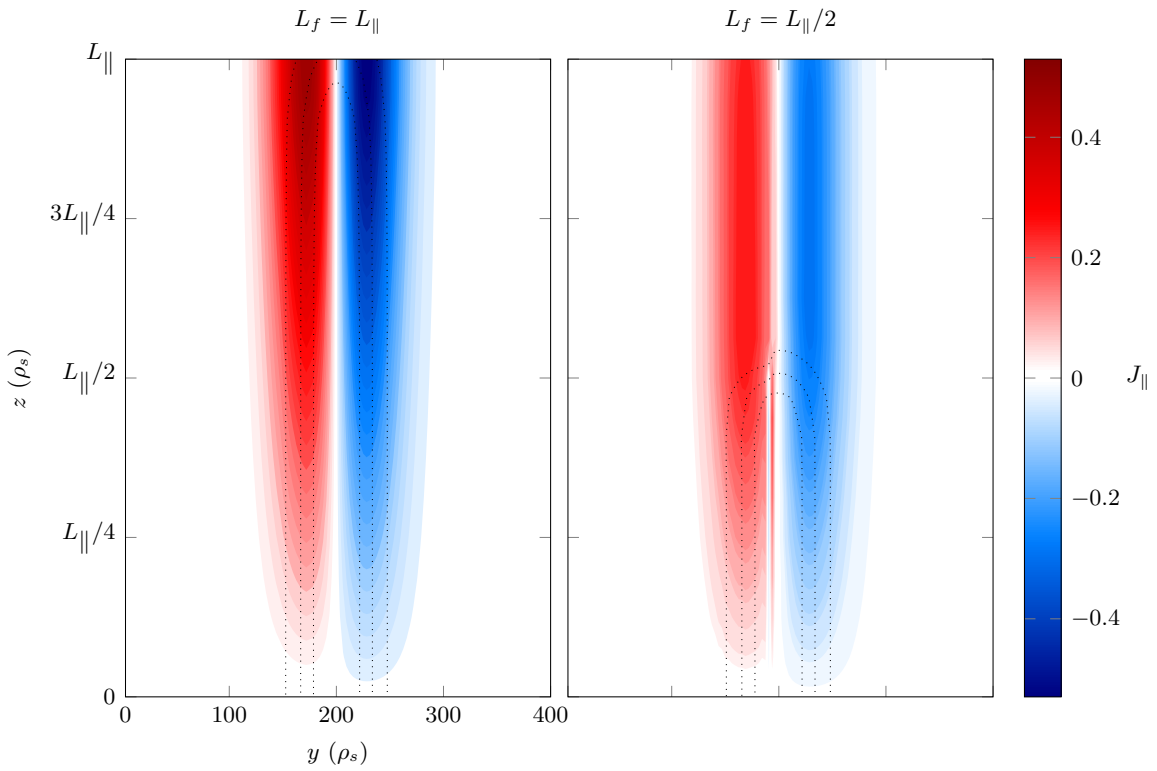

Figure 6.13: Structure of the parallel current density, $J_\parallel$, in the $y-z$ plane through the middle of $\hat{\delta}_\perp = 40$ filaments initialised with $L_f = L_\parallel$ (left) and $L_f = L_\parallel/2$ (right). Both filaments were otherwise initialised with $A = 2$, $\hat{\delta}_\parallel = 0$. Dotted contour lines of the filaments' density perturbation n_f are also plotted for reference.

scaling arguments predict the polarisation currents to be more important than viscous currents. It is emphasised however that firstly the theoretical predictions are only very rough estimates, and secondly for the simulation parameters, the regimes predictions become very congested at small $\hat{\delta}_\perp$, with little separation between 0, $\hat{\delta}_\dagger$ and $\hat{\delta}_*$. This means that the idealised viscous and inertial regimes do not truly exist and instead both effects play a role at small $\hat{\delta}_\perp$. Nevertheless, the $\hat{\delta}_\perp = 5, D_\Omega = 0$ filament case does show that in the absence of viscosity, the filament can be described as in the inertial regime, as the polarisation currents almost exclusively ensure current continuity. It is pertinent to note that both polarisation and parallel currents are important for the $\hat{\delta}_\perp = 16$ filament, which displays the most coherent propagation.

The mechanism for the observed difference in the relative spatial extent of a filament's potential field with respect to its density field, depending on $\hat{\delta}_\perp$, becomes apparent by Fourier transforming Equation (6.10) in the perpendicular plane to produce [159]

$$\frac{\partial \hat{\phi}_{\boldsymbol{k}}}{\partial t} = -\frac{1}{L_\parallel k_\perp^2}\hat{\phi}_{\boldsymbol{k}} + \frac{ik_y \hat{n}_k}{n_{bg} k_\perp^2} - D_\Omega k_\perp^2 \hat{\phi}_{\boldsymbol{k}}. \tag{6.17}$$

Here $\hat{f}_{\boldsymbol{k}}$ denotes the Fourier mode of a quantity f corresponding to a perpendicular wave vector $\boldsymbol{k} = (k_x, k_y)$, $k_\perp = |\boldsymbol{k}|$ and n_{bg} is the normalised value of the effective background number density. This equation shows that the sheath dissipation term, which is dominant for large $\hat{\delta}_\perp$ filaments, acts to preferentially damp large spatial length scales of potential. Therefore filaments with $\hat{\delta}_\perp > \hat{\delta}_*$ develop potential fields that are localised within the density profile of the filament, whilst those with $\hat{\delta}_\perp < \hat{\delta}_*$ develop potential fields extending beyond the filament's density.

Next, attention is turned to the functional dependence of the filament's radial velocity on

$\hat{\delta}_\perp$. To measure this, a characteristic radial velocity, $\hat{v}^\star_{f,x}$, is defined as the first maximum of $\hat{v}_{f,x}(t)$ that occurs in time. This is obtained more accurately from the discrete time outputs by using a cubic spline interpolation. The first maximum is selected in an attempt to avoid the influence of Boltzmann spinning motions, which can lead to a secondary, larger maximum in very small $\hat{\delta}_\perp$ filaments that possess parallel gradients. A series of extensive scans in $\hat{\delta}_\perp$ have been performed, with values ranging from 0.5 to 60. Four different datasets have been obtained, corresponding to filaments initialised with $L_f = L_\parallel$ or $L_f = L_\parallel/2$, with or without the dissipative parameters, D_Ω and D_n. The dependence of $\hat{v}^\star_{f,x}$ for each of these cases is shown in Figures 6.14, with the results plotted on both linear and log-log axes as the latter allow the scaling with $\hat{\delta}_\perp$ to be assessed clearly. For reference, the analytical velocity scaling predictions for the viscous, inertial and sheath current limited regimes are marked on the log-log axes, alongside the predicted transition boundaries between the regimes, $\hat{\delta}_*$ and $\hat{\delta}_\dagger$. A number of features are evident from these plots:

- All four cases produce peak characteristic velocities at a $\hat{\delta}_\perp$ close to, but always smaller than $\hat{\delta}_*$. It is noted however that this peak does not correspond to the most coherent filamentary motion or furthest radial distance travelled, which occurs for $\hat{\delta}_\perp$ slightly larger than $\hat{\delta}_*$ (See Figures 6.1, 6.9, 6.10 and 6.11.)
- All four cases produce characteristic radial velocities scaling like $\hat{v}^\star_{f,x} \propto \hat{\delta}_\perp^{-2}$ for $\hat{\delta}_\perp \gg \hat{\delta}_*$, as predicted for the sheath current limited regime.
- The $L_f = L_\parallel$ and non-zero dissipative parameters case produces velocities scaling like $\hat{v}^\star_{f,x} \propto \hat{\delta}_\perp^2$ for $\hat{\delta}_\perp \ll \hat{\delta}_\dagger$, in agreement with the viscous regime prediction.
- In the absence of viscosity and dissipation, the $L_\parallel$ filament velocities scale like $\hat{v}^\star_{f,x} \propto \hat{\delta}_\perp^{1/2}$ for $\hat{\delta}_\perp \ll \hat{\delta}_*$, in line with the inertial regime prediction.
- The $L_f = L_\parallel/2$ cases do not agree so well with the analytical predictions at small values of $\hat{\delta}_\perp$. This discrepancy is attributed to the Boltzmann spinning dynamics produced in these filaments, which depending on the size of the filament, can alter the peak velocity.
- Reducing the parallel extent of the filament reduces the radial velocity across all $\hat{\delta}_\perp$, although this reduction becomes negligible at larger $\hat{\delta}_\perp$.

In general therefore, the analytical scaling predictions are well reproduced by the simulations, particularly for the $L_f = L_\parallel$ cases. Perhaps more important than the exact $\hat{\delta}_\perp$ dependence of the radial velocities, is the fact that for all four cases, the radial velocity increases with $\hat{\delta}_\perp$ for $\hat{\delta}_\perp \ll \hat{\delta}_*$, whilst it decreases with $\hat{\delta}_\perp$ for $\hat{\delta}_\perp \gg \hat{\delta}_*$. This analysis has also been performed using an alternative definition of a characteristic radial velocity as the average radial velocity over a specified time period, and produced equivalent velocity scaling results.

Thus far, consideration has only been given to the effect of $\hat{\delta}_\perp$ on the perpendicular motions of the filaments. However, when $\hat{\delta}_\perp$ becomes very small, the parallel propagation is also affected. To illustrate this, a series of simulations have been performed with filaments initialised with $A = 2$, $L_f = L_\parallel/2$, $\hat{\delta}_\parallel = 0$ and values of $\hat{\delta}_\perp$ ranging from 1 to 5. In addition, to isolate the parallel dynamics, both the curvature drive and dissipative parameters were set to zero; $g = 0$, $D_n = 0$, $D_\Omega = 0$. The left hand plot of Figure 6.15 shows the evolution of the centre of mass of the filaments from each of these simulations, whilst the right hand plot shows example profiles of n_f along the centre of the filaments at $t = 80\ \Omega_i^{-1}$. It is clear that decreasing $\hat{\delta}_\perp$ leads to an increase in the parallel propagation of the filament for $\hat{\delta}_\perp \lesssim 5$. At values above this value, the propagation remains roughly constant.

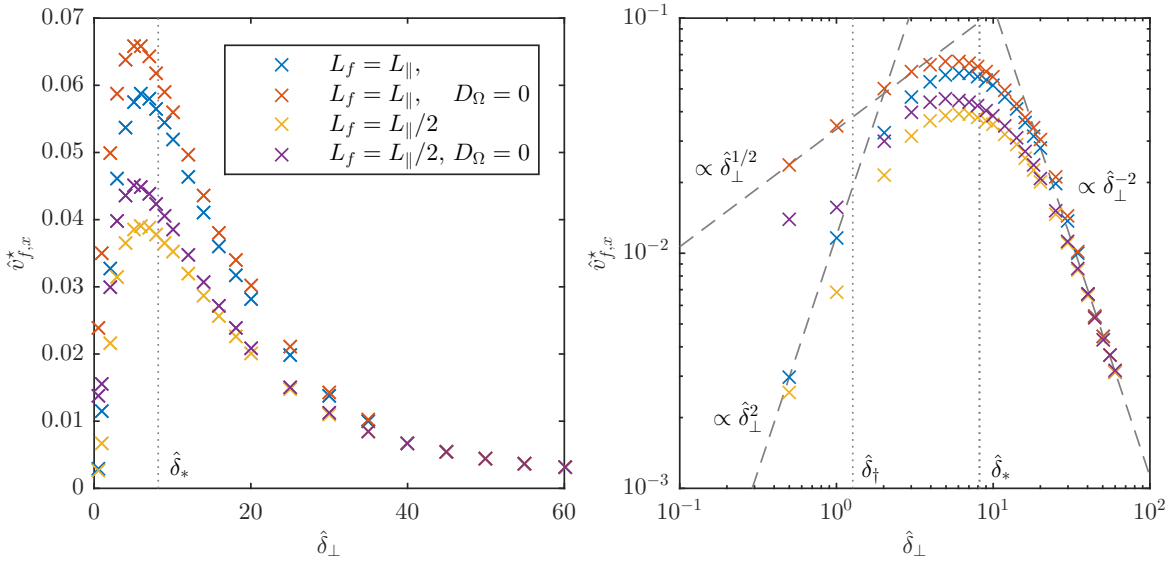

Figure 6.14: Dependence of the characteristic radial velocity, $\hat{v}^\star_{f,x}$, on the perpendicular size of the filament, $\hat{\delta}_\perp$, for filaments initialised with $L_f = L_\parallel$ or $L_f = L_\parallel/2$, with or without the dissipative parameters, D_Ω and D_n. The filaments were otherwise initialised using $A = 2$ and $\hat{\delta}_\parallel = 0$.

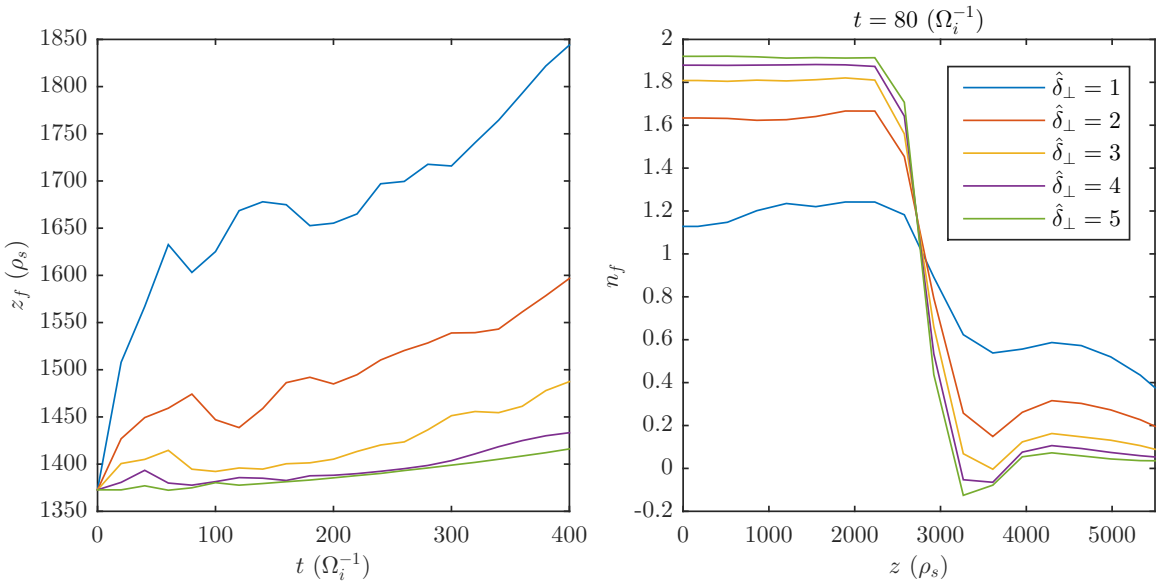

Figure 6.15: Demonstration of the influence of $\hat{\delta}_\perp$ on the parallel propagation of filaments. Left: Evolution of the parallel centre of mass coordinate, z_f, for filaments with varying $\hat{\delta}_\perp$. Right: Parallel profiles of the filament density, n_f, along the centre of the filament, $x = x_0$, $y = y_0$, at an example time $t = 80\ \Omega_i^{-1}$. All filaments were otherwise initialised with $A = 2$, $L_f = L_\parallel/2$ and $\hat{\delta}_\parallel = 0$, and were evolved using $g = 0$, $D_n = 0$ and $D_\Omega = 0$.

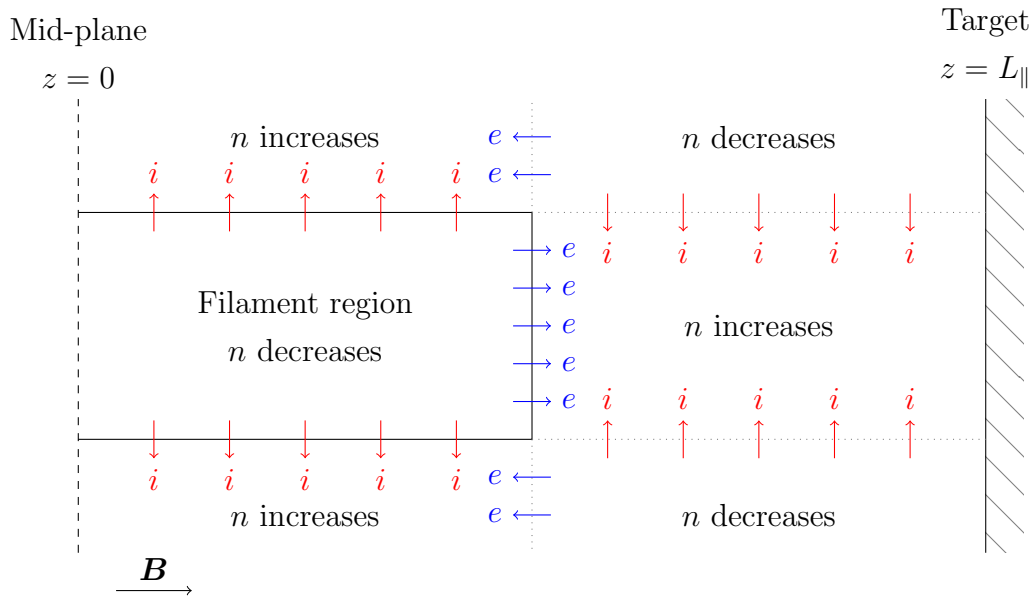

Figure 6.16: Schematic diagram of the mechanism that leads to enhanced parallel propagation at small $\hat{\delta}_\perp$. Here e and i denote electron and ion motions respectively.

The mechanism for this behaviour, shown schematically in Figure 6.16, is that as the filament size reduces, the gradients in the perpendicular direction increase, meaning that the ion polarisation currents are enhanced. These enhanced polarisation currents are then able to balance large parallel currents driven by the parallel density gradient of the filament front. These parallel currents effectively correspond to the motion of electrons only, as the ions' parallel velocity is approximately zero (because they are significantly heavier and therefore have a slower dynamical response). Therefore a situation develops in which the filament's electrons move along the parallel direction at a speed faster than the ion sound speed, and quasi-neutrality is ensured inside and downstream of the filaments by ions moving outwards and inwards in the perpendicular direction respectively through polarisation currents. Finally, to maintain current continuity throughout the entire domain, a return parallel current flows around the outside of the filament. This also corresponds to the density surrounding the filament in the perpendicular plane increasing slightly, similar to that caused by particle diffusion, as shown in Figure 6.17. Since $D_n = 0$, this spreading can be solely attributed to the above process*. For filaments above a certain perpendicular size, $\hat{\delta}_\perp \approx 5$, this mechanism no longer occurs because the polarisation currents are reduced and can no longer facilitate the parallel electron currents. Such filaments exhibit ambipolar propagation in the parallel direction, which thus occurs on the slower ion time-scale.

These results indicate that filaments with a smaller perpendicular size will reach the target quicker and also spread out in the perpendicular plane more quickly than larger filaments. These effects, combined with the facts that they contain less density and will be more affected by particle diffusion, imply that smaller filaments may have shorter lifetimes than larger filaments. It is however highlighted that these effects only become significant for very small values of $\hat{\delta}_\perp$, for which the fluid model used may no longer be appropriate as finite Larmor radius effects will be important.

*It is noted that this spreading is not an artefact of numerical diffusion because it does not occur in filaments that are uniform in the parallel direction.

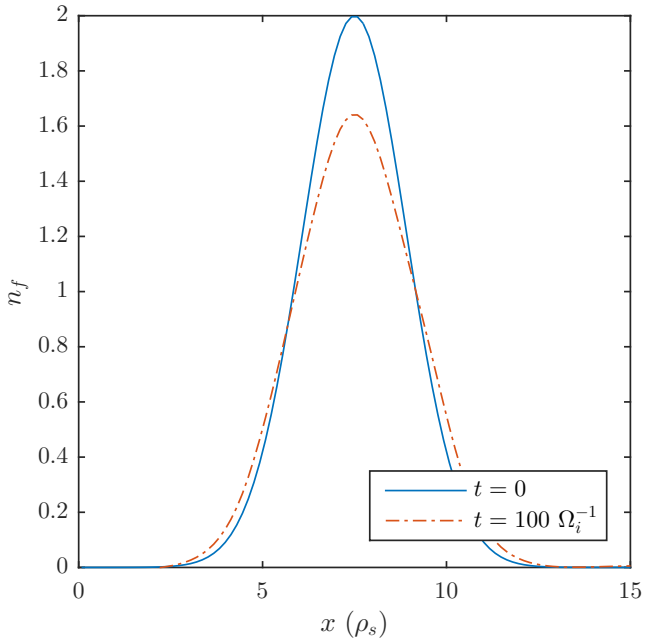

Figure 6.17: Demonstration of the enhanced perpendicular spreading of filaments that occurs at small $\hat{\delta}_\perp$. The profiles of the filament density, n_f, are plotted from a $\hat{\delta}_\perp = 2$, $A = 2$, $L_f = L_\parallel/2$, $\hat{\delta}_\parallel = 0$ filament, at $y = y_0$, $z = 0$. Both the initial profile ($t = 0$) and a later, evolved profile ($t = 100\ \Omega_i^{-1}$) are shown. The simulation was performed using $g = 0$, $D_n = 0$ and $D_\Omega = 0$, so the spreading in the perpendicular direction can be solely attributed to the mechanism shown in Figure 6.16.

6.3.3 Parallel density gradient, $\hat{\delta}_\parallel$

Next the effect of varying the gradient of the filament's density front is considered, which is controlled through the parameter $\hat{\delta}_\parallel$. A series of simulations have been performed using filaments initalised with $A = 2$, $L_f = L_\parallel$ and $\hat{\delta}_\parallel$ ranging from 0 to ∞. The parallel density profiles of the filaments simulated are plotted in Figure 6.18. From this figure it can be inferred that the integral value of n_f along the parallel direction is the same in each case. The $\hat{\delta}_\parallel$ scans were performed for two perpendicular filament sizes, $\hat{\delta}_\perp = 5$ and $\hat{\delta}_\perp = 16$. The evolution of the filament position and velocity for these two cases are plotted respectively in Figures 6.19 and 6.20 using the same colour scheme as in Figure 6.18. It can be seen that the radial motion of the $\hat{\delta}_\perp = 16$ case is invariant to $\hat{\delta}_\parallel$, but that a greater negative velocity in the y direction develops as $\hat{\delta}_\parallel$ decreases. This happens due to the enhanced Boltzmann spinning motions (described in Section 6.3.1) that develop in the presence of stronger parallel density gradients. In contrast, the radial motion of the $\hat{\delta}_\perp = 5$ filaments are affected by $\hat{\delta}_\parallel$, with larger $\hat{\delta}_\parallel$ filaments moving faster. This behaviour has also been attributed to the Boltzmann spinning motions, which are stronger for smaller $\hat{\delta}_\perp$ filaments, acting to reduce the radial velocity. Nevertheless, the effect that $\hat{\delta}_\parallel$ has on the radial motion in this case is very small; approximately a 10% reduction in the final x_f position between $\hat{\delta}_\parallel = \infty$ and $\hat{\delta}_\parallel = 0$. From these results therefore it can be inferred that for a given $\hat{\delta}_\perp$, the parallel integral value of n_f predominantly determines the filament's radial displacement and velocity, rather than $\delta_\parallel$.

6.3.4 Amplitude, A

The final property of the filaments' geometry to be investigated is the peak amplitude of the filament, A. To investigate the influence of this parameter, two additional simulations have been

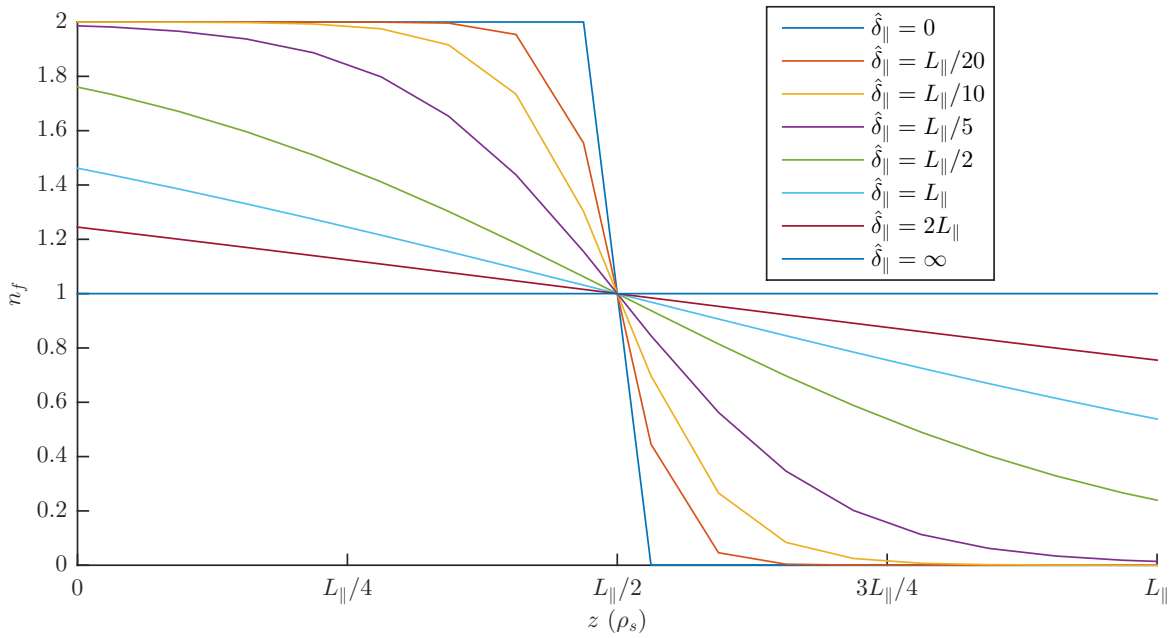

Figure 6.18: Filament density profiles, n_f, along the parallel direction for each of the values used in the $\hat{\delta}_\parallel$ scans. Profiles are taken at $t = 0$, $x = x_0$ and $y = y_0$.

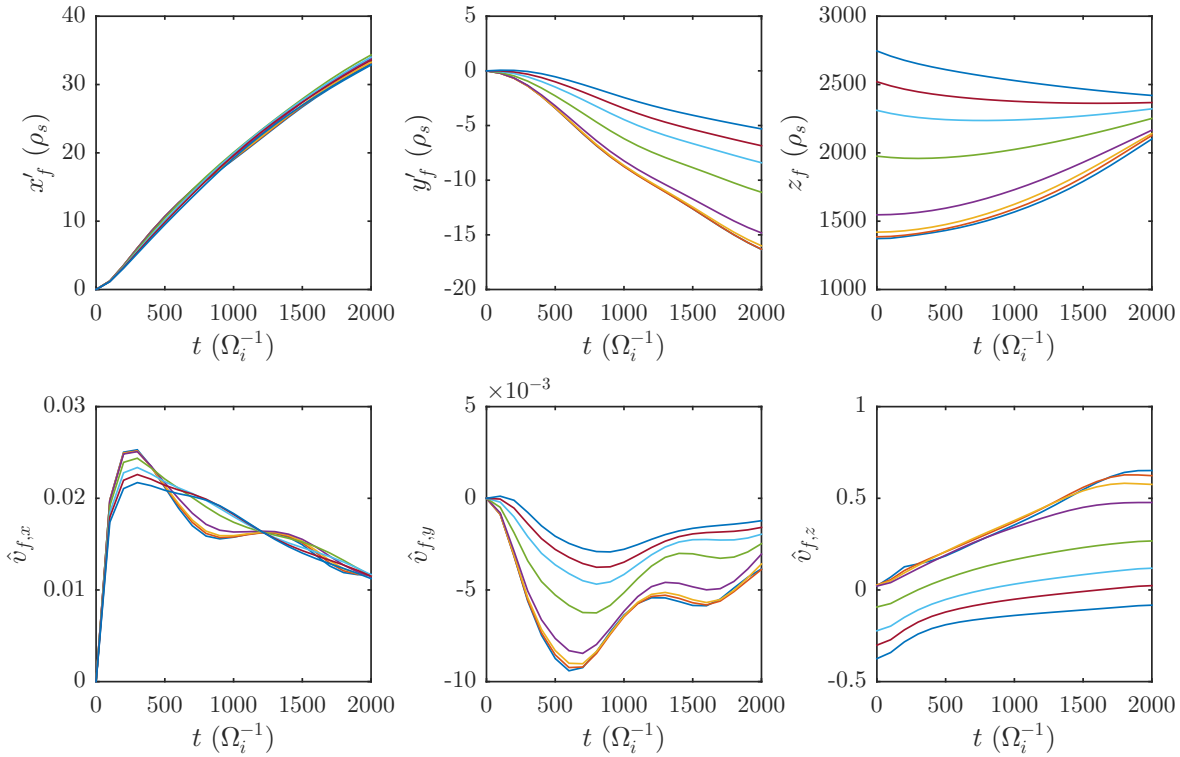

Figure 6.19: Evolution of the position and velocity of $\hat{\delta}_\perp = 16$, $A = 2$, $L_f = L_\parallel/2$ filaments with varying $\hat{\delta}_\parallel$. The colour scheme is the same as in Figure 6.18.

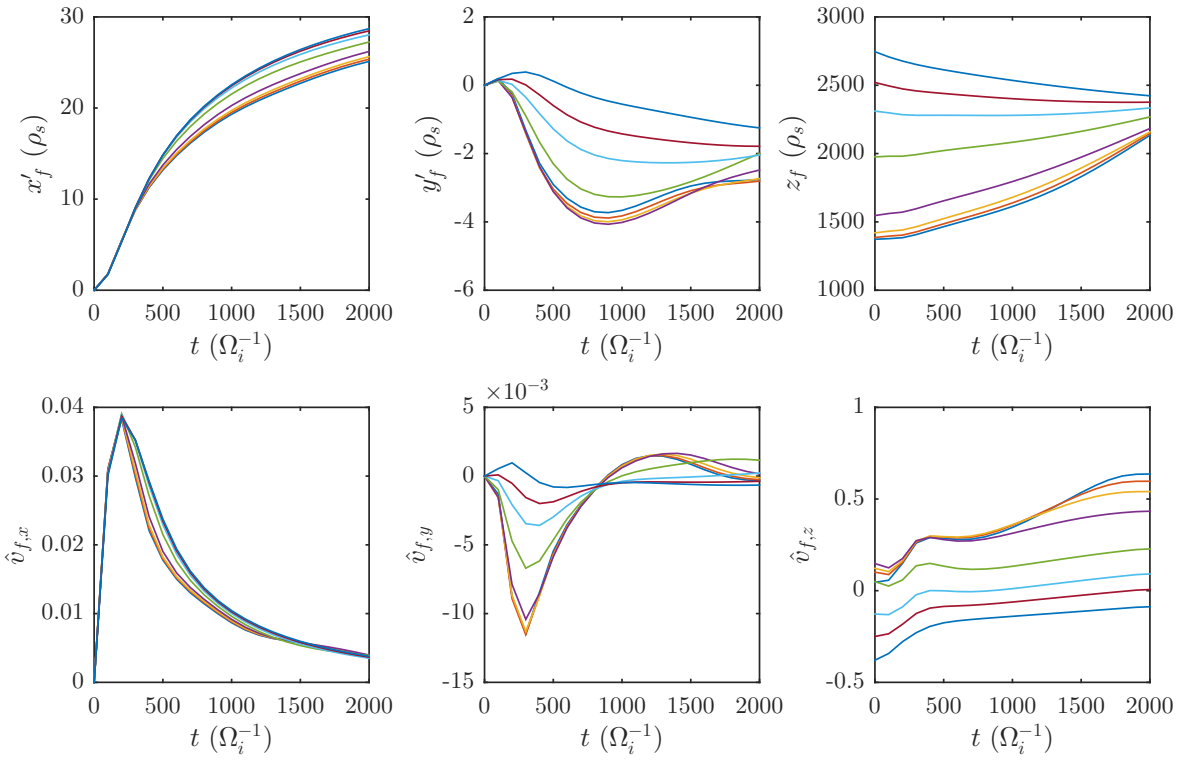

Figure 6.20: Evolution of the position and velocity of $\hat{\delta}_\perp = 5$, $A = 2$, $L_f = L_\parallel/2$ filaments with varying $\hat{\delta}_\parallel$. The colour scheme is the same as in Figure 6.18.

performed using the same filament parameters as in the example simulation ($A = 2$, $L_f = L_\parallel$, $\hat{\delta}_\perp = 16$ and $\hat{\delta}_\parallel = 0$) but with $A = 4$ and $A = 6$. To resolve the increased perpendicular gradients, the perpendicular resolution was doubled for these two higher amplitude simulations such that $N_x \times N_y \times N_z = 384 \times 256 \times 16$.

A comparison of all three cases is provided by both Figure 6.21, which shows the evolution of n_f and ϕ_f, and Figure 6.22, which plots the evolution of the filaments' perpendicular displacement and velocities. It can be seen that in the early stages ($t < 500\ \Omega_i^{-1}$), increasing the amplitude of the filament leads to faster radial velocities, as might be expected because the diamagnetic drive is enhanced. However, at around $t = 600\ \Omega_i^{-1}$, the $A = 6$ filament begins to exhibit perturbations in its density and potential structure along the leading front. As described in References [168] and [191], such perturbations are characteristic of the onset of unstable drift-waves. As the $A = 6$ filament evolves beyond this point, the drift-waves grow and develop into turbulent motions which act to tear the filament apart, destroying its coherence and spreading its density further in the bi-normal direction compared to the two smaller amplitude cases. From Figure 6.22, these drift wave dynamics can be seen to significantly reduce the filament's radial velocity, and by the end of simulation the $A = 4$ case exhibits a greater radial displacement. However it is emphasised that the $A = 6$ filament's net radial transport is not entirely halted by the development of drift-waves, as a number of smaller amplitude *child* filaments emerge from the turbulence which subsequently advect radially outwards themselves.

It is noted that whilst a comparison between radial velocities between filaments of different amplitudes is shown in Figure 6.22, the exact functional dependence or scaling of $\hat{v}_{f,x}$ with A has not been investigated because, as described in References [151] and [169], an incorrect scaling will be produced when the Boussinesq approximation is employed as it is here. Nevertheless,

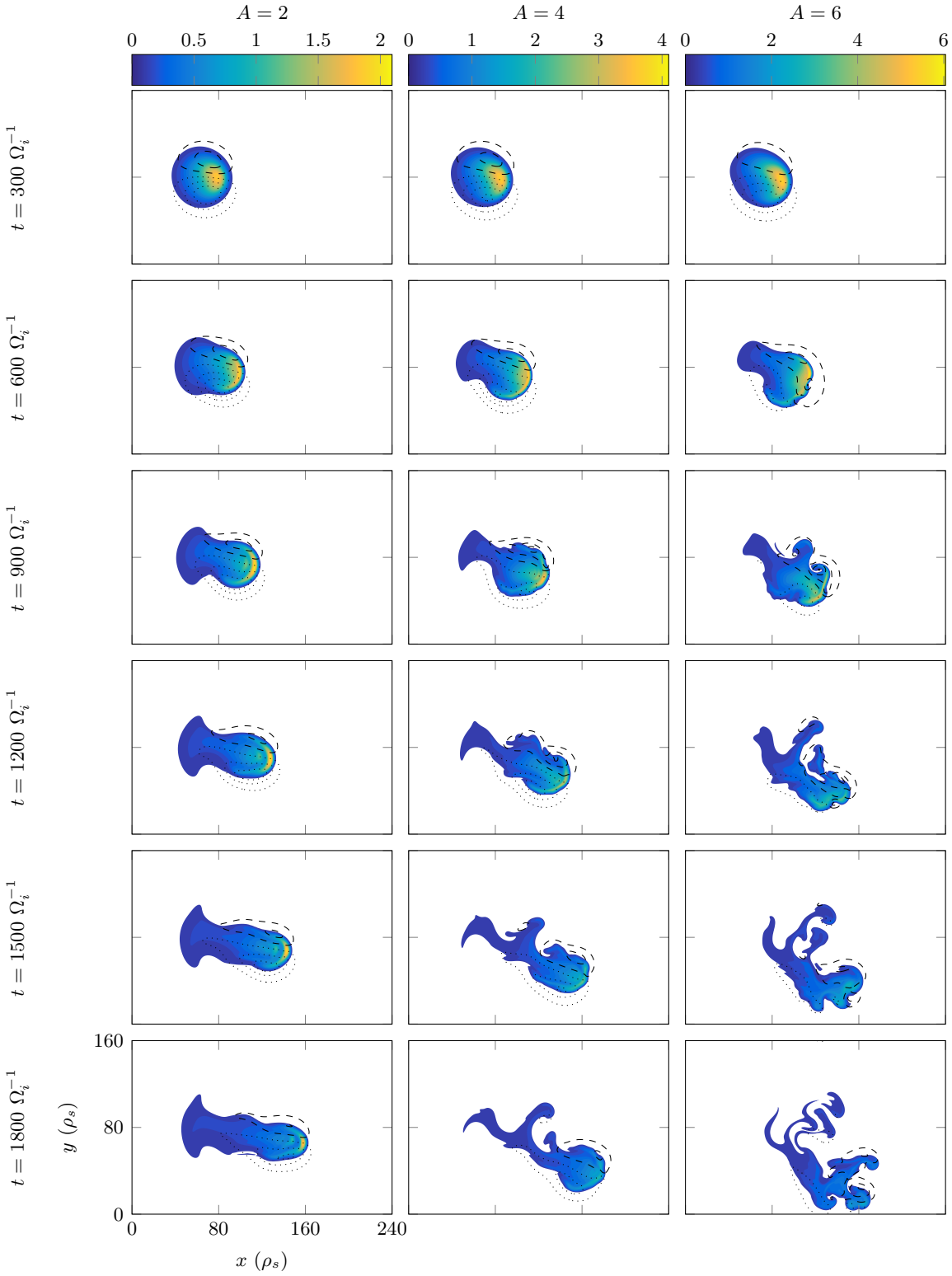

Figure 6.21: Comparison of the evolution of the filament's density, n_f, and potential, ϕ_f, between filaments initialised with amplitudes of $A = 2$, $A = 4$ and $A = 6$. All filaments were otherwise initialised with $\hat{\delta}_\perp = 16$, $L_f = L_\parallel$ and $\hat{\delta}_\parallel = 0$. Values of n_f below $A/20$ are not plotted. Dotted and dashed contour lines respectively indicate positive and negative values of ϕ_f.

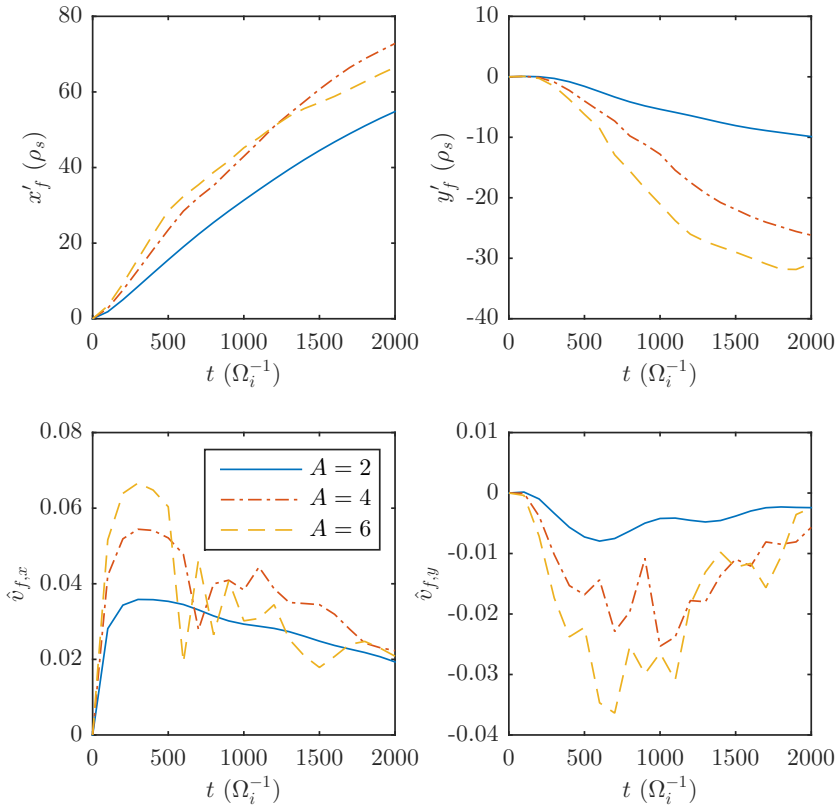

Figure 6.22: Evolution of the position and velocity of $\hat{\delta}_\perp = 16$, $L_f = L_\parallel/2$, $\hat{\delta}_\parallel = 16$ filaments with varying $\hat{\delta}_\parallel$.

it is expected that the result that increasing A leads to increased radial transport up until a critical point at which unstable drift-waves develop, will be unaffected by this simplification.

Figure 6.22 also displays the trend that higher amplitude filaments move faster (and hence further) in the bi-normal direction. This occurs because the higher amplitude filaments drive a larger even component of potential through the Boltzmann potential response described in Section 6.3.1. This therefore induces the filament to spin faster in the perpendicular plane, which combined with the faster radial velocities in the early stages of the simulations, acts to produce a faster bi-normal velocity.

6.4 Comparison with 2D Closures

In this section direct comparisons are made between 3D filament simulations and 2D simulations using the sheath dissipation and vorticity advection parallel closures described in Section 2.3.3.

To begin, the contrasting density and potential evolution of the example filament case ($A = 2$, $\hat{\delta}_\perp = 16$, $L_f = L_\parallel$, $\hat{\delta}_\parallel = 0$) using each model is shown in Figure 6.23, with the 3D fields taken at $z = 0$. It is recalled that the vorticity advection model seeks to represent the dynamics at this location but assumes $L_f = L_\parallel/2$, whilst the sheath dissipation model technically represents field line averaged quantities and assumes $L_f = L_\parallel$. From this plot, it is evident that the vorticity advection model produces drastically different dynamics compared to the other two models, in that its filament becomes strongly mushroomed. This occurs due to it developing a potential field that is much stronger and that extends further in the perpendicular plane those of the other two models. On the other hand, the sheath dissipation model produces broadly similar dynamics to the 3D model, particularly in terms of radial

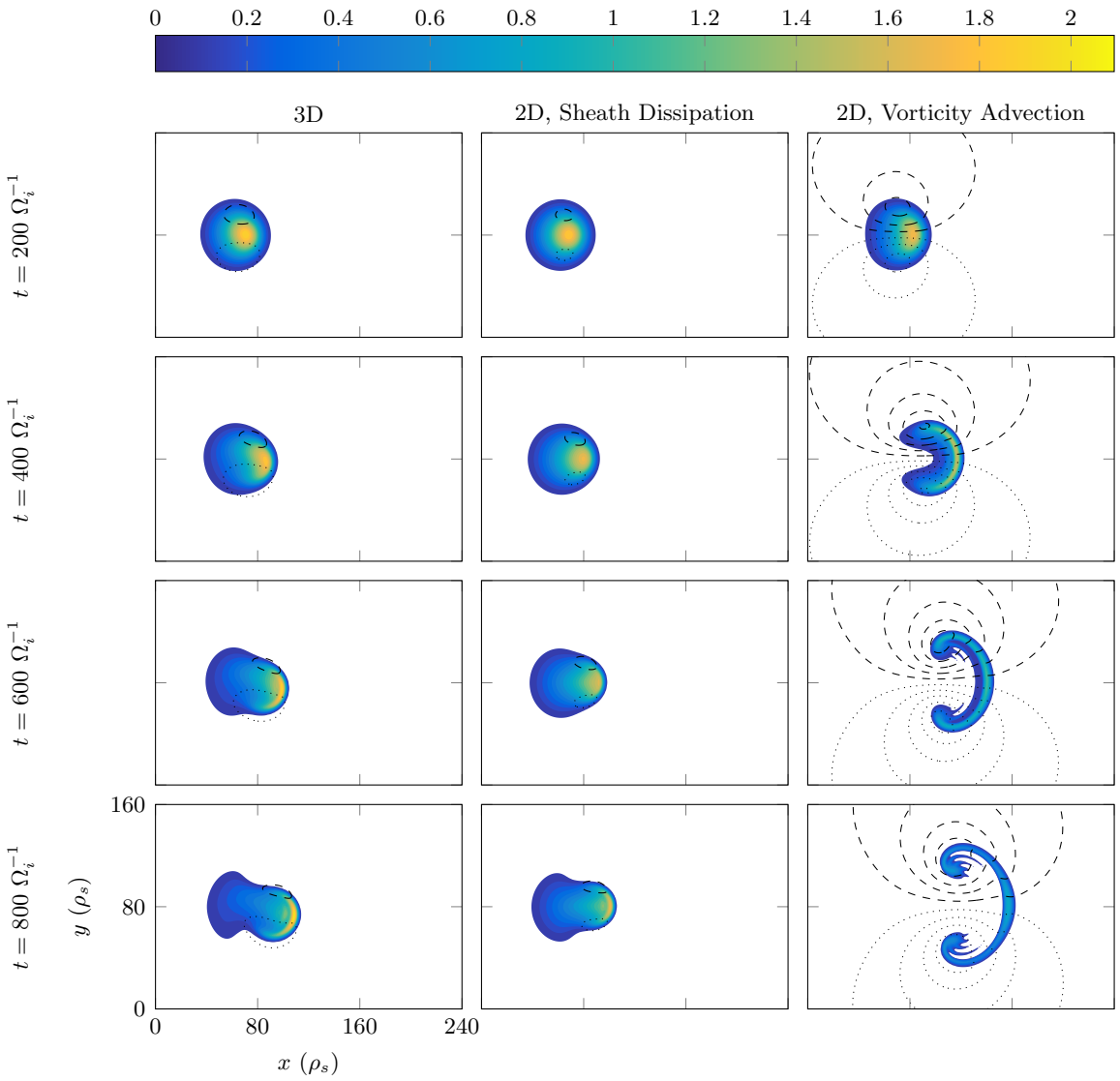

Figure 6.23: Comparison of the evolution of a $\hat{\delta}_\perp = 16$, $L_f = L_\parallel$, $A = 2$, $\hat{\delta}_\parallel = 0$ filament's density, n_f, and potential, ϕ_f, produced using the 3D model and the 2D sheath dissipation and vorticity advection models. The 3D simulation's plots are taken at the mid-plane ($z = 0$) which is where the vorticity advection model seeks to represent, whilst the sheath dissipation model technically represents field line averaged quantities. Values of n_f below 0.1 are not plotted. Dotted and dashed contour lines respectively indicate positive and negative values of ϕ_f.

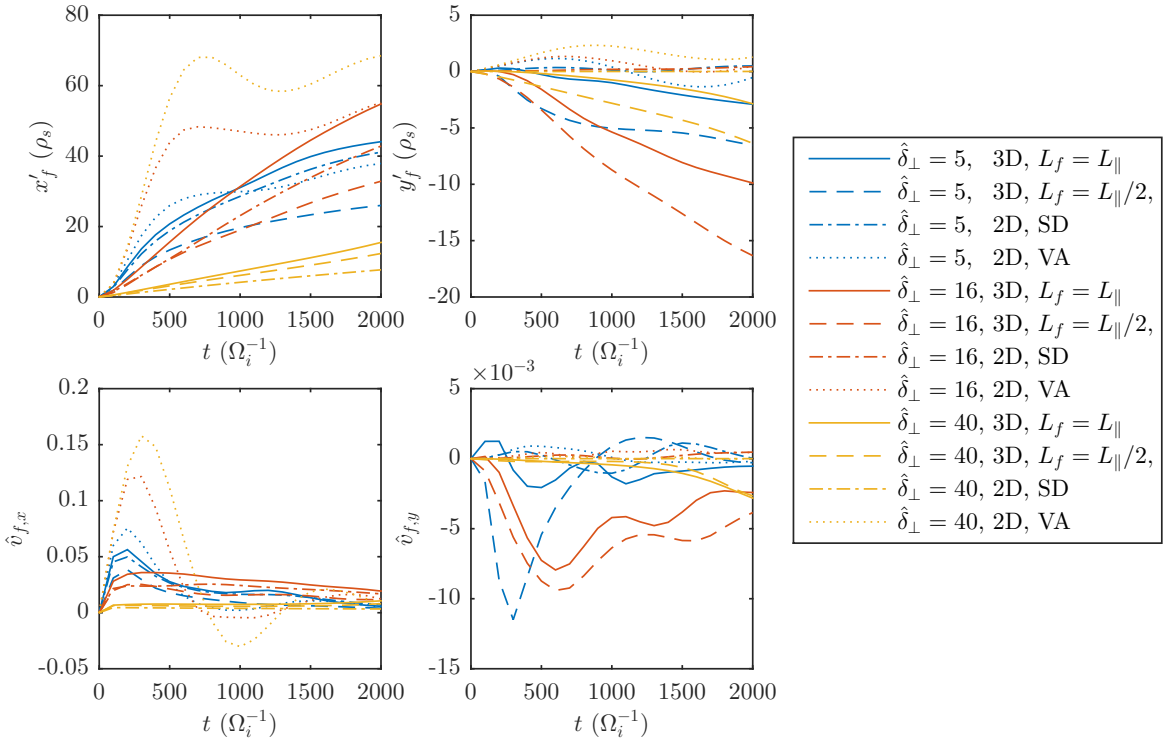

Figure 6.24: Comparison of the perpendicular displacements and velocities produced the 3D model and the 2D sheath dissipation (SD) and vorticity advection (VA) models for filaments initialised with $A = 2$, $L_f = L_\parallel$, $\hat{\delta}_\parallel = 0$ and varying $\hat{\delta}_\perp$.

displacement and overall structure. However, it does not reproduce the Boltzmann spinning motions and subsequent downwards displacement of the 3D simulation because there is no drive by which ϕ can become aligned with n (the same is true of the vorticity advection model). This $\hat{\delta}_\perp = 16$ comparison is representative of both smaller and larger $\hat{\delta}_\perp$. The vorticity advection model always produces strong mushrooming motions, even for $\hat{\delta}_\perp \gg \hat{\delta}_*$, where the 3D model and sheath dissipation models produce fingering motions. Furthermore, for $\hat{\delta}_\perp \ll \hat{\delta}_*$, where the 3D model and sheath dissipation models also produce mushrooming motions, the vorticity advection model mushrooms the filament more quickly and to a greater extent.

Quantitative comparisons of the perpendicular displacements and velocities produced by each model for various values of $\hat{\delta}_\perp$ are provided in Figure 6.24, with the 3D results shown for both $L_f = L_\parallel$ and $L_f = L_\parallel/2$. Regardless of the value of $\hat{\delta}_\perp$ or L_f, the vorticity advection closure produces a significantly larger radial displacement than the 3D model, with the discrepancy worse for larger $\hat{\delta}_\perp$. In contrast, the sheath dissipation model's radial displacements and velocities show good agreement for the 3D $L_f = L_\parallel$ case although they are consistently smaller across all $\hat{\delta}_\perp$. Whilst it does not provide quite such a satisfactory agreement for the $L_f = L_\parallel/2$ case, the agreement is still reasonable considering it is not strictly valid, and certainly it reproduces the 3D motions better than the vorticity advection closure. This in particular is a surprising result given that the vorticity advection closure was developed to better represent the dynamics of ballooned filaments, i.e. those that possess parallel density gradients. It is noted however that the agreement between the sheath dissipation closure and the 3D model becomes significantly reduced for sufficiently high amplitude filaments, as 2D models cannot represent the unstable drift wave dynamics that develop in the 3D simulations. This means that the sheath dissipation model leads to greater radial transport for such cases, as shown in Figure 6.25. Returning to Figure 6.24, neither 2D closure reproduces the downwards

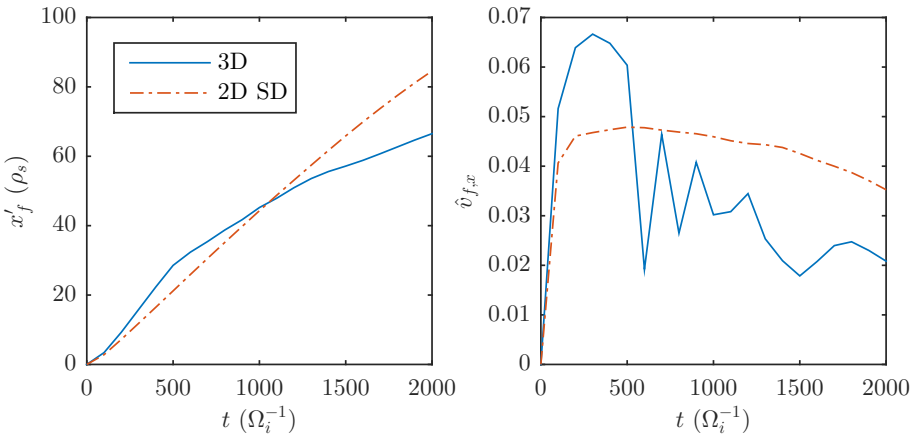

Figure 6.25: Comparison of the perpendicular displacements and velocities of a $A = 6$, $L_f = L_\parallel/2$, $\hat{\delta}_\parallel = 0$ filament using the 3D model and the 2D sheath dissipation (SD) model.

motion of the filament found using the 3D model for the reason discussed previously.

Perhaps the clearest demonstration that the vorticity advection closure produces drastically different results, particularly for $\hat{\delta}_\perp > \hat{\delta}_*$, is provided by Figure 6.26, which shows the $\hat{\delta}_\perp$ dependence of filaments' characteristic radial velocity, $\hat{v}^\star_{f,x}$, for each model. Whilst agreement is found between all three models for the very smallest $\hat{\delta}_\perp$, the vorticity advection produces a monotonically increasing $\hat{v}_f$ for all physically relevant $\hat{\delta}_\perp$, and does not exhibit the *roll over* from the inertial regime to the sheath current limited regime that occurs for the 3D and sheath dissipation models. This means that effectively that the vorticity advection closure only represents the viscous and inertial regimes, although there is some deviation from the inertial regime's $\hat{v}_{f,x} \propto \hat{\delta}_\perp^{-2}$ scaling at large $\hat{\delta}_\perp$ as the vorticity advection term $(-\Omega/2L_\parallel)$ becomes more important in Equation (3.78).

Additional simulations have been performed with the magnitude of this term increased, to determine whether a slight adjustment in the approximation $U\nabla_\parallel \approx 1/2L_\parallel$ would allow the vorticity advection model to better represent the 3D simulations. However it was found that the term had to be increased by approximately 3 orders of magnitude to bring the net radial velocities at large $\hat{\delta}_\perp$ down to the 3D model's values, and even then the filament's structure does not exhibit the fingering motions of the 3D simulations. This indicates that the functional form of the vorticity advection closure is unable to represent the 3D results.

This can be further understood by estimating each of the terms in the vorticity equation of the vorticity advection model, Equation (3.78), to scale like

$$\frac{\hat{g}}{\hat{\delta}_\perp} \sim \frac{\phi^2}{\hat{\delta}_\perp^4} + \frac{\phi}{2L_\parallel \hat{\delta}_\perp^2} + \frac{D_\Omega \phi}{\hat{\delta}_\perp^4}, \tag{6.18}$$

which at large $\hat{\delta}_\perp$ reduces to

$$\frac{\hat{g}}{\hat{\delta}_\perp} \sim \frac{\phi}{2L_\parallel \hat{\delta}_\perp^2}. \tag{6.19}$$

Therefore the radial velocity of large $\hat{\delta}_\perp$ filaments can be estimated to scale like $\phi/\hat{\delta}_\perp \sim 2\hat{g}L_\parallel$ and thus are expected to be invariant to $\hat{\delta}_\perp$, which is in contrast to the behaviour of the 3D model.

Ultimately, the reason why the vorticity advection closure produces such different dynamics to the 3D model is that it neglects parallel currents entirely. In the 3D simulations parallel currents closing through the target were observed to play an important role in all but the very

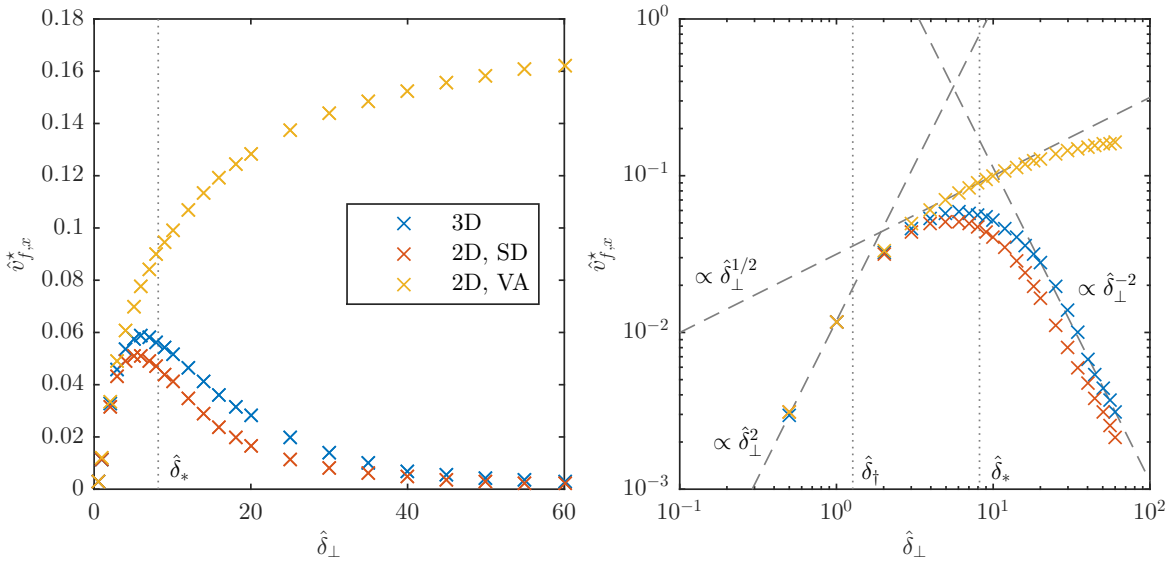

Figure 6.26: Comparison of the dependence of the characteristic radial velocity, $\hat{v}^{\star}_{f,x}$, on the perpendicular size of the filament, $\hat{\delta}_{\perp}$, between filaments simulated using the 3D model and the 2D Sheath Dissipation (SD) and Vorticity Advection (VA) closures. All simulations were filaments were initialised where appropriate with initialised with $L_f = L_{\parallel}$, $A = 2$ and $\hat{\delta}_{\parallel} = 0$.

smallest $\hat{\delta}_{\perp}$ filaments, in that they reduced the magnitude of the polarisation currents and hence the strength of the filament's potential field. As shown in Figure 6.13, this is true even for the $L_f = L_{\parallel}/2$ filaments that were physically disconnected from the target, as the currents were able to travel through the background plasma so that the filaments remained electrically connected to the target.

Whilst these results are fairly critical of the vorticity advection closure, it is emphasised that the 3D model used here is not likely to be universally valid, as physically relevant situations may exist where the divertor region may have a sufficiently increased resistivity to prevent parallel currents from closing through the sheath. This may occur due to increased particle densities and lower temperatures in the region that can occur in a conduction-limited divertor regime, or if the target temperature is sufficiently low, due to divertor detachment. The effect of increasing the resistivity of the plasma in the 3D model is thus investigated in detail in the following chapter. However, another effect neglected in the 3D model is that of magnetic shear, which will be particularly strong around the X-point region. This means that parallel currents may be able to close more easily in this location than through the target. The two region model [184] predicts radial velocities scaling like $\hat{v}_{f,x} \propto \hat{\delta}_{\perp}^{1/2}$ if such a current balance occurs (as in the inertial regime discussed in this chapter), but crucially also that the magnitude of the velocities to be reduced compared to a slab magnetic geometry case. Therefore although the $\hat{\delta}_{\perp}$ dependence of the vorticity advection closure would then be appropriate for this case, the radial transport would continue to be significantly overestimated across all filament sizes.

6.5 Conclusions

The first part of this chapter has presented a series of 3D isolated filament simulations performed using the STORM3D physics module and MAST relevant parameters to illustrate the effect of a filament's initial geometry on its subsequent motions.

The perpendicular size of the filament, $\hat{\delta}_\perp$, was demonstrated to have a strong influence. For filaments smaller than an approximate critical size, $\hat{\delta}_*$, the compressible diamagnetic currents are predominantly closed by a combination of viscous and polarisation currents, and the filaments develop a mushroom-like structure in the perpendicular plane as they evolve. In contrast, parallel currents closing through the target become dominant in balancing the diamagnetic currents in filaments much larger than $\hat{\delta}_*$, which do not move initially as a whole, but instead expel a finger-like structure. The most coherent motion, in which the filament largely retains its initial monopole density structure in the perpendicular plane as it evolves, is exhibited by filaments with intermediate sizes, slightly larger than $\hat{\delta}_*$, where both parallel currents and polarisation currents play an important role. Depending on which current path is dominant, the filament's radial velocity exhibits a different scaling with $\hat{\delta}_\perp$, in agreement with theoretical predictions. Specifically the radial velocity increases with $\hat{\delta}_\perp$ for $\hat{\delta}_\perp \ll \hat{\delta}_*$ but decreases with $\hat{\delta}_\perp$ for $\hat{\delta}_\perp \gg \hat{\delta}_*$. Finally, for very small $\hat{\delta}_\perp$ filaments, a mechanism has been identified by which polarisation currents and parallel currents balance each other to allow for enhanced parallel propagation of the filament towards the targets.

Reducing the parallel extent of the filament, L_f, such that the filaments no longer extend from target to target has two effects. Firstly it reduces the filament's radial velocity and hence displacement. Secondly the potential field exhibits a Boltzmann response to parallel density gradients, leading to the filament spinning in the perpendicular plane, which combined with the radial motions, makes the filament move also in the bi-normal direction. Whilst the first effect was found to be largely invariant to changes to the initial gradient of the filament's density front, $\hat{\delta}_\parallel$, the second effect was enhanced as the gradient increased, ($\hat{\delta}_\parallel \to 0$).

Increasing the starting peak amplitude of the filament, A, initially enhances its radial velocity, but eventually the gradients become sufficient that unstable drift-waves develop. The subsequent turbulent motions destroy the coherence of these high amplitude filaments and ultimately reduce its net radial displacement compared to lower amplitudes, where drift-waves are stabilised by viscosity and particle diffusion. Since the dissipative parameters used are believed to be physically justified, this indicates some filaments in MAST may exist which are stable to drift-waves.

Although the majority of these effects have been identified in previous filament studies, these simulations have been carried out using a more advanced physical model that includes parallel ion dynamics and evolves global fields, rather than evolving a filament perturbation on a fixed background. These results show therefore that these additions make little difference to the perpendicular dynamics of filaments, and justify prior approaches for filament studies. Nevertheless, the additions made in the STORM3D model compared to prior works are an important step forward towards 3D SOL turbulence simulations, where parallel ion dynamics will be required to allow for parallel draining of density to the targets to be represented, which is necessary in order to predict SOL profiles.

The second part of the chapter has compared the 3D results against 2D simulations employing either the sheath dissipation or vorticity advection parallel closures. The vorticity advection closure was found to not represent the 3D model's filament dynamics well, in that filaments of all $\hat{\delta}_\perp$ were observed to develop mushroom structures and produce radial velocities in the early stages far in excess of the 3D results. Furthermore, the radial velocity was found to increase monotonically with $\hat{\delta}_\perp$ for all filaments of a physically relevant size, which is again, in contrast to what was found in 3D. The sheath dissipation closure on the other hand provided a good comparison with the 3D model for smaller amplitude filaments. In particular

it reproduced the contrasting radial velocities and evolved structures of large and small $\hat{\delta}_\perp$ filaments found in 3D. For larger amplitude filaments, this comparison became less satisfactory as the 2D model could not represent the unstable drift wave dynamics that occur in the 3D simulations. In addition, neither 2D closure represented the Boltzmann spinning motions and subsequent displacement in the bi-normal direction that was observed in 3D.

The failure of the vorticity advection closure to replicate the 3D dynamics has been attributed to its assumption that parallel currents are negligible. It has been demonstrated that parallel currents closing through the sheath play an important role in the 3D simulations, even in cases where the filament perturbation does not extend to the target, as currents continue to flow through the background plasma. However, the 3D model is likely not to be universally valid, and there are a number of mechanisms by which the plasma's resistance to parallel currents may become increased, particularly in the divertor region. This motivates the following chapter, which investigates the effect of increasing the resistivity of the plasma.

Chapter 7

Effect of Plasma Resistivity

7.1 Introduction

In the previous chapter, it was demonstrated that parallel currents closing through the target played an important role in determining the dynamics of filaments simulated using the 3D model. In this chapter, the influence of plasma resistivity, $\eta_{\parallel}$, on filamentary dynamics is studied, as this quantity directly affects the extent to which these parallel currents can flow, and hence the behaviour of the filaments.

For explanatory purposes, it is first helpful to recall that resistivity is an intrinsic property of a medium which measures how strongly the medium opposes the flow of electric currents and is measured in SI units of Ohm-metres. Resistance on the other hand, is a property of a specific object that quantifies the difficulty of passing an electric current through it and is measured in units of Ohms. The resistance is dependent on both the resistivity and the geometry of the object. For example, the resistance of a simple wire can be calculated as $\eta\ell/A$, where ℓ is the length of the wire, A is its cross section, and η is the resistivity of the wire's material.

In plasma physics, it is convenient to quantify the flow of charge in terms of current densities (which have units of Amperes per square metre), instead of currents (which have units of Amperes), because a plasma is a continuous medium and because the resistivity of a plasma and the current densities which flow within it are not generally uniform (see Figure 6.13). Furthermore in the specific context of filament dynamics, the concept of resistance is not particularlyD meaningful, because it would be dependent on an arbitrarily chosen cross-section area. Instead, to quantify how difficult it is for a current density to travel along a specific path, one can integrate the resistivity along the path of interest. The resultant quantity, Γ, can be described as a *resistivity-length*, and has units of Ohm-metres^2. Using this definition, the basic electrostatic form of Ohm's law can be written as

$$\Delta\varphi = j\Gamma, \tag{7.1}$$

where j is the current density that flows between two points which have a potential difference of $\Delta\varphi$.

Applying this concept to filament dynamics, the total resistivity-length of the path by which parallel currents generated within a filament form a closed circuit through the target is given by $2(\Gamma_{\parallel} + \Gamma_{\text{sheath}})$. Here $\Gamma_{\parallel}$ is the resistivity-length of the path through the plasma from the filament to the sheath entrance and Γ_{sheath} is the resistivity-length of the path through

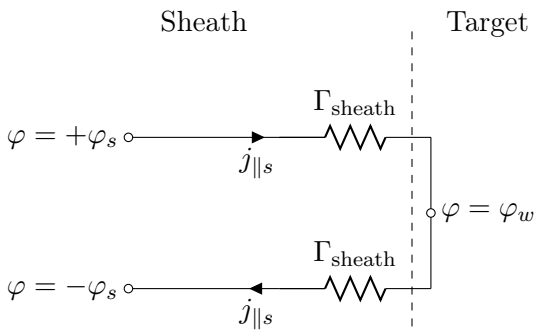

Figure 7.1: Schematic diagram of the current travelling through the sheath and target between two points at the sheath entrance with potentials of equal magnitude and opposite sign.

the sheath to the target. It is emphasised that in the simulation model, the target is assumed to have infinite conductivity (this can be inferred as it has a uniform potential).

Whilst strictly $\Gamma_\parallel$ is dependent on the position along the field line from which the path is defined, is it convenient to define a representative value for the entire filament for use throughout this chapter. It is recalled that the simulation model assumes a symmetric SOL, and hence enforces zero parallel current at $z = 0$. This means that the parallel currents driven in the region $z > 0$ close through the target at $z = \ell_\parallel$, whilst those driven in the region $z < 0$ close through the target at $z = -\ell_\parallel$. Considering only the positive z side of the domain, a representative value of $\Gamma_\parallel$ can be obtained by defining the current path to begin at the centre of mass position of the positive z half of the filament. For a filament that extends symmetrically from the mid-plane ($z = 0$) for a length of ℓ_f towards the targets and which has a steep parallel front, this centre of mass is approximately located at $\ell_f/2$ and so the representative value of $\Gamma_\parallel$ is given by

$$\Gamma_\parallel = \int_{\ell_f/2}^{\ell_\parallel} \eta_\parallel \, \mathrm{d}z \,. \tag{7.2}$$

This representative value thus corresponds to the path from $z = \ell_f/2$ to the sheath entrance.

The resistivity-length of the path through the sheath is harder to define exactly, but an approximate value can be obtained by considering the sheath boundary conditions given by Equations (3.58) to (3.61). By assuming the potential at the sheath entrance to be small, these boundary conditions can be linearised to estimate the current density entering the sheath to be

$$j_{\parallel s} = e n_{e,s} c_s \frac{e\varphi_s}{T_e}, \tag{7.3}$$

where the subscript s denotes the value of a field at the entrance to the sheath. Therefore two points at the sheath entrance which have a potential difference with equal magnitude but opposite sign correspond to the parallel current density at the first point travelling through the sheath, closing through the target and emerging at the second point. A schematic circuit diagram for this situation is provided in Figure 7.1. The potential difference between the two points at the sheath entrance is thus

$$2\varphi_s = j_{\parallel s} \frac{2T_e}{e^2 n_{e,s} c_s}. \tag{7.4}$$

By comparing this expression to Equation (7.1), the term $2T_e/e^2 n_{e,s} c_s$ can be understood to be the resistivity-length of the path through the sheath to the target and back again. Since this

path involves travelling through the sheath twice, the resistivity-length of travelling through the sheath just once is given by

$$\Gamma_{\text{sheath}} = \frac{T_e}{e^2 n_{e,s} c_s}. \tag{7.5}$$

It is noted that $\Gamma_{\text{sheath}} \propto T_e^{1/2}/n_{e,0}$, whilst $\Gamma_{\parallel} \propto T_e^{-3/2}$ because of its dependence on $\eta_{\parallel}$ and is invariant to $n_{e,0}$.

The normalised equivalents of $\Gamma_{\parallel}$ and Γ_{sheath} are obtained by dividing the dimensional quantities by $\rho_s B/e n_{e,0}$ to produce

$$\hat{\Gamma}_{\parallel} = \int_{L_f/2}^{L_{\parallel}} \hat{\eta}_{\parallel} \, \mathrm{d}z, \tag{7.6}$$

and

$$\hat{\Gamma}_{\text{sheath}} = \frac{1}{n_s}, \tag{7.7}$$

where z is itself normalised in Equation (7.6). It is highlighted that these normalised quantities display different dependencies on T_e and $n_{e,0}$ to their dimensional counterparts in that $\hat{\Gamma}_{\text{sheath}}$ is invariant to both T_e and $n_{e,0}$, whilst $\hat{\Gamma}_{\parallel} \propto n_{e,0} T_e^{-2}$. In addition to being a normalised resistivity-length, $\hat{\Gamma}_{\parallel}$ can be interpreted as a measure of the SOL electron collisionality, $\nu^* = \ell_{\parallel}/\lambda_e$, since $\hat{\Gamma}_{\parallel} \approx \nu^*/\sqrt{m_i/m_e}$.

By calculating $\hat{\Gamma}_{\text{sheath}}$ and $\hat{\Gamma}_{\parallel}$ for the parameters used in the previous chapter, it can be seen that it corresponds to a low resistivity case, in that $\hat{\Gamma}_{\parallel} \ll \hat{\Gamma}_{\text{sheath}}$. However, there exist a number of mechanisms by which $\hat{\Gamma}_{\parallel}$ may significantly increase, such that $\hat{\Gamma}_{\parallel}$ becomes comparable to or greater than $\hat{\Gamma}_{\text{sheath}}$, which in turn may lead to a suppression of parallel currents. One such mechanism is an increased parallel connection length, $\ell_{\parallel}$ [184], which can be achieved in a larger device or by use of a Super-X divertor [251]. Moreover, since $\hat{\Gamma}_{\parallel} \propto n_{e,0} T_e^{-2}$, enhanced densities and decreased temperatures within the SOL will also increase $\hat{\Gamma}_{\parallel}$. In a conduction-limited SOL [31], these effects can become very strong particularly in the divertor region, as colder temperatures and higher densities are found downstream at the target compared to upstream at the mid-plane. A similar mechanism has been observed in 3D turbulence simulations that used a realistic magnetic geometry [189]. In this work, the plasma was fuelled by neutral particle injection around the X-point, which led to a strong neutral cooling in the divertor. This enhanced the resistivity in the region and thus electrical disconnection of filaments from the sheath occurred. In addition to these effects, if the temperature at the target becomes sufficiently low ($T_e < 1$ eV), volume recombination becomes strong and divertor detachment will occur [31], meaning that a cloud of neutrals forms between the plasma and the target. If the ionisation fraction is sufficiently small, electron-neutral collisions become comparable to electron-ion collisions [252]. In such conditions, $\eta_{\parallel}$ must be redefined to include a component proportional to the ratio between neutral and electron densities [253] (see Section 7.2.1), which in turn will drastically increase $\hat{\Gamma}_{\parallel}$. In the limit of zero ionisation, the resistance of the neutral gas in front of the targets is effectively infinite.

The influence of parallel resistivity on the dynamics of filaments has previously been considered theoretically by Reference [184] using a two region model. The parameter Λ, defined in Equation (2.29), was used throughout this reference as a measure of the collisionality of the SOL and is approximately equal to $\hat{\Gamma}_{\parallel}$. In the absence of magnetic geometry effects that were also considered, the work predicts for $\hat{\Gamma}_{\text{sheath}} \gg \hat{\Gamma}_{\parallel}$ the existence of the inertial and sheath current regimes that were identified at small and large $\hat{\delta}_{\perp}$ in the previous chapter (although they are referred to as the *resistive ballooning* and *sheath connected interchange*

regimes respectively). For $\hat{\Gamma}_{\parallel} \geq \hat{\Gamma}_{\text{sheath}}$ on the other hand, the inertial regime is expected to continue for the smallest $\hat{\delta}_{\perp}$, as the regime does not involve parallel currents. For larger $\hat{\delta}_{\perp}$ filaments, what is described throughout this thesis as the *resistive sheath current* regime is predicted (Reference [184] uses the term *resistive X-point* regime). In this regime the diamagnetic currents are expected to be balanced by parallel currents closing through the target, but the parallel resistance of the plasma, rather than that of the sheath is expected to determine the filament's potential field. The radial velocity in this regime, which is directly determined by the potential, is predicted to scale like $\sim \hat{\Gamma}_{\parallel}\hat{\delta}_{\perp}^{-2}$. Furthermore, the reference predicts that the critical filament size at which filaments transition from the inertial regime, $\hat{\delta}_{*}$, increases with parallel resistivity as follows:

$$\hat{\delta}_{*} \sim \begin{cases} \hat{\delta}_{*0} & \text{for } \hat{\Gamma}_{\parallel} \ll \hat{\Gamma}_{\text{sheath}} \\ \hat{\delta}_{*0}\hat{\Gamma}_{\parallel}^{2/5} & \text{for } \hat{\Gamma}_{\parallel} \gg \hat{\Gamma}_{\text{sheath}} \end{cases}. \tag{7.8}$$

Here

$$\hat{\delta}_{*0} = \left(\frac{\hat{g}L_{\parallel}^{2}}{2}\right)^{1/5}, \tag{7.9}$$

is the value of $\hat{\delta}_{*}$ given in Equation (6.12). The estimate $\hat{\delta}_{*} \sim \hat{\delta}_{*0}$ thus corresponds to the transition between the inertial and sheath current regimes, whilst $\hat{\delta}_{*} \sim \hat{\delta}_{*0}\hat{\Gamma}_{\parallel}^{2/5}$ corresponds to the anticipated transition from the inertial regime to the resistive sheath current regime. A diagram identifying the extent of each of these regimes in the space of normalised collisionality and filament size is reproduced from Reference [184] in Figure 2.11. It is noted that this diagram includes an additional regime which arises when magnetic geometry effects are included within the two region model. By setting the parameter $\varepsilon_{x} = 1$, such effects are neglected and the regime disappears. The broad prediction that increasing the resistivity leads to faster radial filament velocities for larger filaments has been confirmed by simulations of isolated filaments [184] and saturated turbulence [155] conducted using the quasi-3D two region model equations.

In this chapter, the effect of resistivity on filament dynamics will be investigated using fully three-dimensional simulations. This can be viewed both as an extension of the work already conducted using the two region model, and also a validation exercise to determine whether the two region model sufficiently represents the full 3D dynamics. The investigation will consist of two parts. Firstly, the normalised resistivity, $\hat{\eta}_{\parallel}$ will be increased in isolation, to illustrate the influence that this parameter has. Since it is anticipated that the divertor region may have a particularly high resistivity, the effect of increasing this parameter in a region localised to the target will be studied first, and then compared against simulations in which the resistivity is increased uniformly throughout the domain. The second part of the investigation will directly vary the input parameters to the simulations upon which $\hat{\Gamma}_{\parallel}$ is dependent; namely $n_{e,0}$ and T_{e}. This will clarify the net effect that these parameters have on filamentary motion, as aspects of the simulations other than $\hat{\Gamma}_{\parallel}$ are also affected by these parameters, such as the strength of the diamagnetic current drive and the normalisation of lengths.

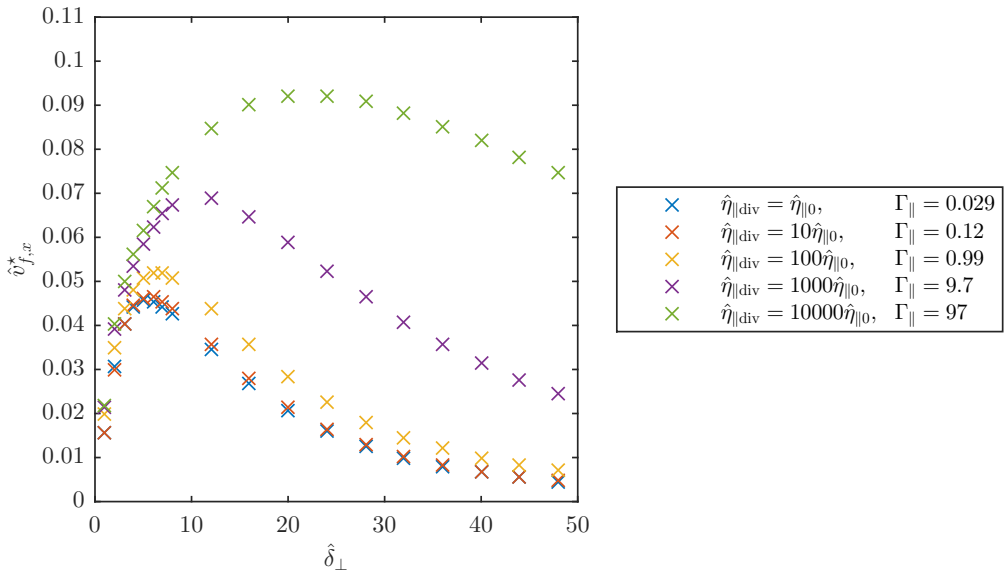

Figure 7.2: Dependence of a filament's characteristic radial velocity, $\hat{v}^{\star}_{f,x}$, on its initial perpendicular length scale, $\hat{\delta}_{\perp}$, for each of the values of $\hat{\eta}_{\parallel \mathrm{div}}$ used in the target-localised resistivity scan.

7.2 Enhanced Normalised Resistivity, $\hat{\eta}_{\parallel}$

7.2.1 Target Localised Resistivity

Simulation Implementation

The effect of an enhanced plasma resistivity in the divertor region is demonstrated in this section by presenting simulations in which $\hat{\eta}_{\parallel}$ has been increased from the default value, $\hat{\eta}_{\parallel 0}$, in the last 25% of the domain nearest the target, as follows

$$\hat{\eta}_{\parallel} \sim \begin{cases} \hat{\eta}_{\parallel 0} & \text{for } z \leq 3L_{\parallel}/4 \\ \hat{\eta}_{\parallel \mathrm{div}} & \text{for } z > 3L_{\parallel}/4 \end{cases}. \tag{7.10}$$

For this study, the majority of parameters used are the same as the MAST relevant set used in Chapter 6 (see Table 6.1) to allow for a direct comparison. In particular, $\hat{\eta}_{\parallel 0} = 7.08 \times 10^{-6}$, which is the value of $\hat{\eta}_{\parallel}$ used previously. The exceptions to this are the dissipative parameters, which are set to $D_n = 1.8 \times 10^{-5}$ and $D_{\Omega} = 5.0 \times 10^{-4}$. These are two orders of magnitude smaller than Chapter 6's default values and have been chosen to ensure that viscous currents play a negligible role and thus to essentially remove the viscous regime from the simulations.

A series of isolated filament simulations have been performed in which both $\hat{\delta}_{\perp}$ and $\hat{\eta}_{\parallel \mathrm{div}}$ have been systematically varied. The remaining filament initialisation parameters were held fixed at $A = 2$, $L_f = L_{\parallel}/2$ and $\hat{\delta}_{\parallel} = L_{\parallel}/10$. Values of $\hat{\eta}_{\parallel \mathrm{div}}$ were varied from $\hat{\eta}_{\parallel 0}$ (which will hereafter be referred to as the reference case) to $10000\hat{\eta}_{\parallel 0}$. These values correspond to values of $\hat{\Gamma}_{\parallel}$ ranging from 0.029 to 97 and span five orders of magnitude. Since the results presented in this section are taken before the filaments reach the target, the density at the sheath entrance remains largely constant at its equilibrium value, $n_s \approx 0.65$, and so $\hat{\Gamma}_{\mathrm{sheath}} \approx 1.53$ for all simulations. For reference $\hat{\Gamma}_{\parallel} \approx \hat{\Gamma}_{\mathrm{sheath}}$ at $\hat{\eta}_{\parallel \mathrm{div}} = 100\hat{\eta}_{\parallel 0}$.

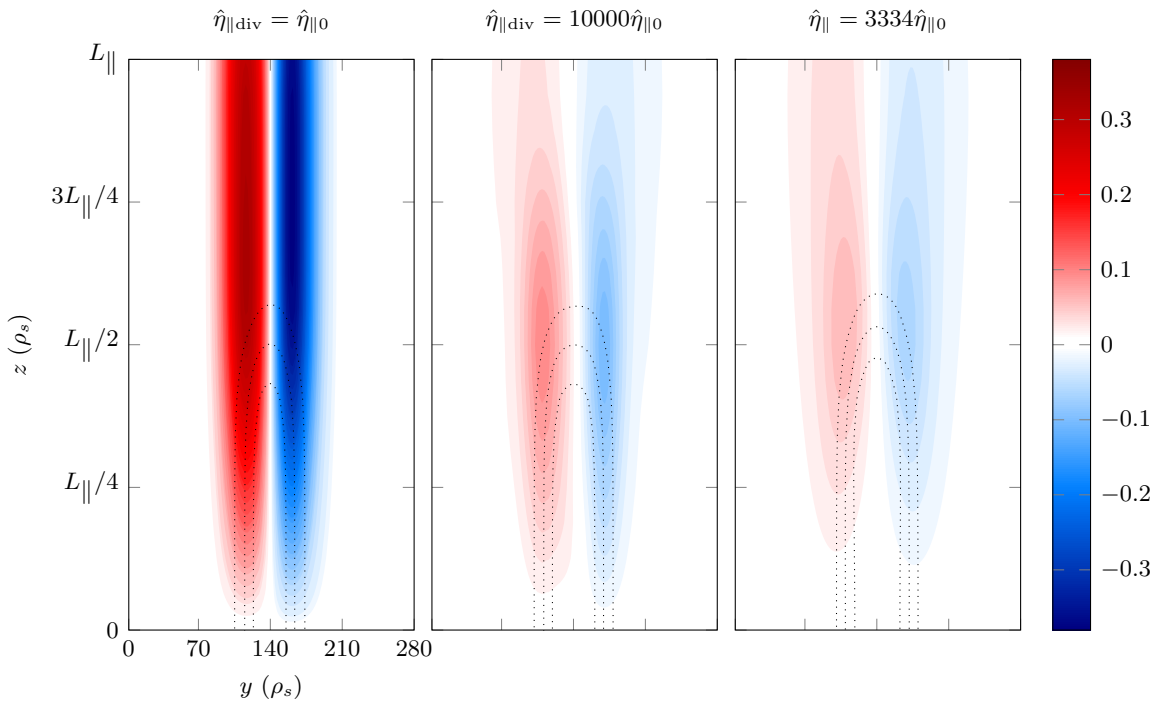

Figure 7.3: Structure of $J_\parallel$ in a $y-z$ plane through the middle of $A = 2$, $L_f = L_\parallel/2$, $\hat{\delta}_\perp = 28$, $\hat{\delta}_\parallel = L_\parallel/10$ filaments at $t = 250\ \Omega_i^{-1}$. The left, centre and right plots respectively correspond to the reference $\hat{\eta}_\parallel = \hat{\eta}_\parallel$ case, the target-localised enhanced resistivity $\hat{\eta}_{\parallel\text{div}} = 10000\hat{\eta}_{\parallel 0}$ case and the uniformly enhanced resistivity $\hat{\eta}_\parallel = 3334\hat{\eta}_{\parallel 0}$ case. Dotted contour lines of the filaments' density perturbation n_f are also plotted for reference.

Results

The dependence of $\hat{v}^\star_{f,x}$ on $\hat{\delta}_\perp$ for increasing values of $\hat{\eta}_{\parallel\text{div}}$ can be seen in Figure 7.2 and it is clear to see that increasing $\hat{\eta}_{\parallel\text{div}}$ leads to enhanced radial velocities across all $\hat{\delta}_\perp$, with the smallest $\hat{\delta}_\perp$ experiencing a relatively modest increase in $\hat{v}^\star_{f,x}$, compared to larger $\hat{\delta}_\perp$. This is to be expected because the smallest filaments are in the inertial regime for the reference case, meaning that parallel currents play a sub-dominant role in closing the diamagnetic currents. On the other hand, the largest filaments are in the sheath current regime in the reference case, meaning that parallel currents are dominant in maintaining current continuity and so increasing the resistivity has a greater influence on these filaments.

One of the mechanisms by which faster velocities are produced can be understood by observing that as $\hat{\eta}_{\parallel\text{div}}$ is increased, $\hat{v}^\star_{f,x}$ scales like $\hat{\delta}_\perp^{1/2}$ up until larger values of $\hat{\delta}_\perp$ and so the inertial regime is clearly extended or equivalently, $\hat{\delta}_*$ is increased. This occurs because increasing the resistivity suppresses the parallel currents and thus necessarily leads to an enhancement of the polarisation currents, given the same diamagnetic current source. The drastic reduction of $J_\parallel$ in a $\hat{\delta}_\perp = 28$ filament is evident upon comparison of the left and middle plots of Figure 7.3, which plot this quantity in a $y-z$ plane through the centre of the filament for the reference case $\hat{\eta}_{\parallel\text{div}} = \hat{\eta}_{\parallel 0}$ and $\hat{\eta}_{\parallel\text{div}} = 10000\hat{\eta}_{\parallel 0}$ simulations respectively.

To demonstrate that this suppression of $J_\parallel$ affects the current balance upstream, Figures 7.4 and 7.5 show the balance of currents at various positions along the field line for these two cases, by plotting the divergences of each of the various current densities in the system, divided by particle density. The viscous current density is not plotted as it is negligible. In the reference case, the compressible diamagnetic currents can be seen to be almost entirely

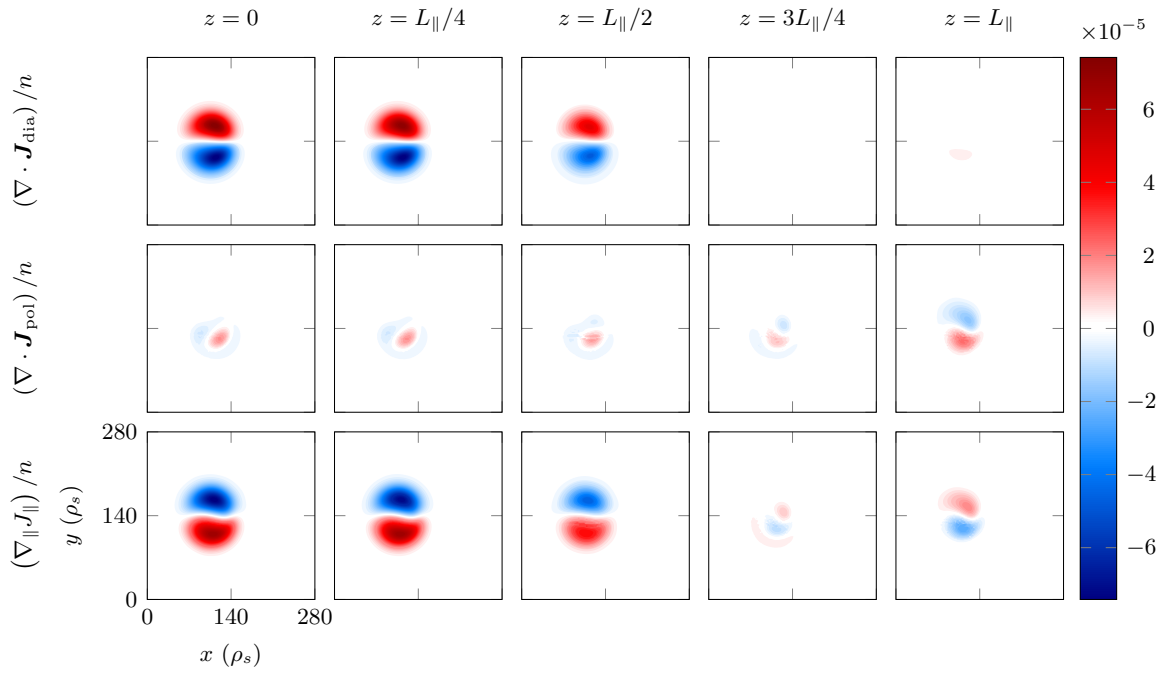

Figure 7.4: Example current balance found along the field line in a $\hat{\delta}_\perp = 28$, $L_f = L_\parallel/2$ filament in the reference case ($\hat{\eta}_{\parallel \mathrm{div}} = \hat{\eta}_{\parallel 0}$). The quantities are plotted at the time of the filament's peak radial velocity, $\hat{v}^\star_{f,x}$, and the filament was otherwise initialised using $A = 2$ and $\hat{\delta}_\parallel = L_\parallel/10$.

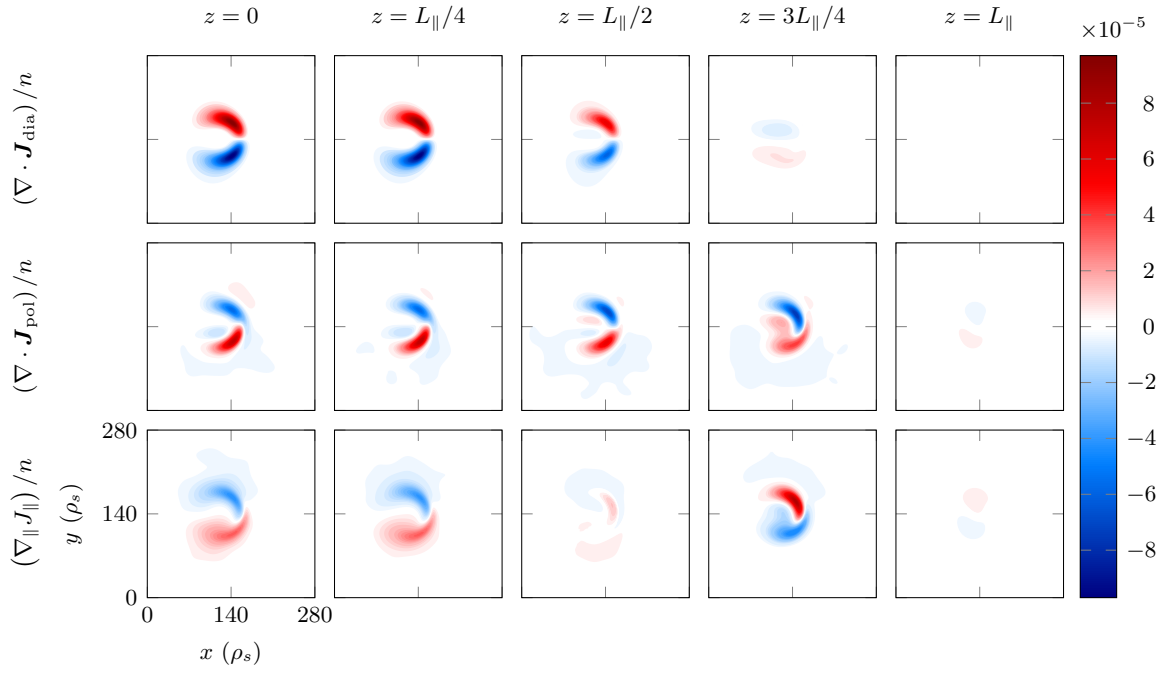

Figure 7.5: Example current balance found along the field line in a $\hat{\delta}_\perp = 28$, $L_f = L_\parallel/2$ filament in the target-localised enhanced resistivity $\hat{\eta}_{\parallel \mathrm{div}} = 10000\hat{\eta}_{\parallel 0}$ case. The quantities are plotted at the time of the filament's peak radial velocity, $\hat{v}^\star_{f,x}$, and the filament was otherwise initialised using $A = 2$ and $\hat{\delta}_\parallel = L_\parallel/10$.

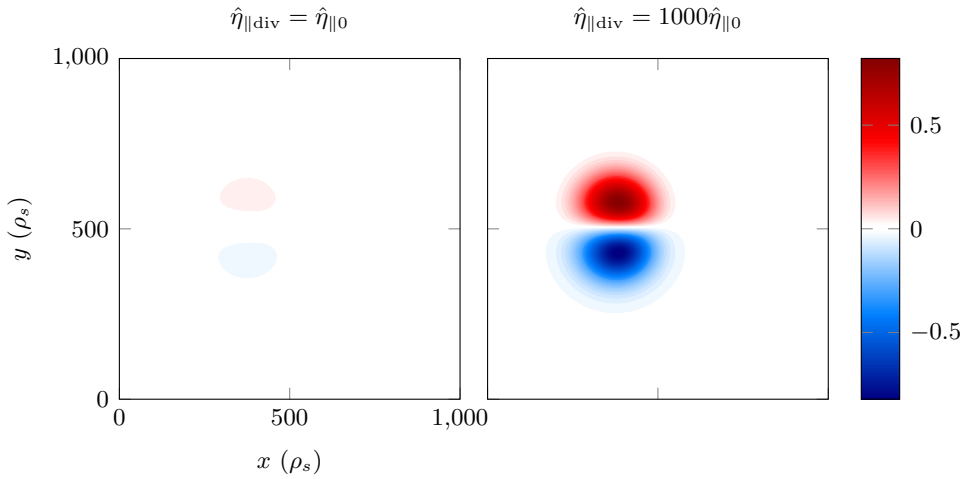

Figure 7.6: Comparison of the odd parity mid-plane to sheath potential difference, $\phi^{\mathrm{odd}}\big|_{z=L_{\parallel}} - \phi^{\mathrm{odd}}\big|_{z=0}$, in $\hat{\delta}_{\perp} = 100$ filaments between the reference $\hat{\eta}_{\parallel} = \hat{\eta}_{\parallel 0}$ case (left) and the enhanced target-localised resistivity $\hat{\eta}_{\parallel \mathrm{div}} = 1000\hat{\eta}_{\parallel 0}$ case (right). The filaments were otherwise initialised with $A = 2$, $L_f = L_{\parallel}/2$ and $\hat{\delta}_{\parallel} = L_{\parallel}/10$.

balanced by the parallel currents and polarisation currents are largely absent. In the enhanced resistivity case on the other hand, the suppression of parallel currents has necessitated an enhancement of the polarisation currents, which now take the dominant role in balancing the diamagnetic currents. However some parallel currents do continue to be driven in the region of the filament ($z < L_{\parallel}/2$) and form a closed circuit with the polarisation currents in the region between the filament front and the start of the enhanced resistivity region ($L_{\parallel}/2 < z < 3L_{\parallel}/4$). This allows the polarisation currents and thus ϕ and the filament's perpendicular velocity, to remain approximately constant all along the field line up until the enhanced resistivity region.

Through a different mechanism to the one described above, greater radial velocities are also produced at higher values of resistivity by the very largest $\hat{\delta}_{\perp}$ filaments, in which parallel currents closing at the target are still the main way in which the compressible diamagnetic currents are closed. These filaments attain greater velocities because the resistance of the plasma is sufficient to introduce a potential difference between the downstream at the sheath entrance and further upstream in the region of the filament density perturbation. Therefore for the same amount of current to flow into or out of the sheath, larger potentials are formed upstream at higher values of resistivity, which in turn correspond to faster radial velocities. Such filaments are described to be in the resistive sheath current regime.

To isolate the potential difference formed along the parallel direction at high values of resistivity, it is necessary to separate it from the potential difference that is produced by the Boltzmann potential response to the parallel density gradients in the filament discussed in Section 6.3.1. This can be achieved by isolating the component of ϕ^{odd} according to Equation (6.9). The right hand plot of Figure 7.6 thus plots the difference of ϕ^{odd} between the mid-plane and the sheath for a $\hat{\delta}_{\perp} = 100, \hat{\eta}_{\parallel} = 1000\hat{\eta}_{\parallel 0}$ filament at the time of its peak radial velocity. For comparison, the equivalent potential difference found in a filament of the same $\hat{\delta}_{\perp}$ using the reference case resistivity is illustrated in the left hand plot and is clearly negligible. In an experiment, this effect may manifest itself as larger potential fluctuations at the mid-plane than at the target, and could possibly be measured by comparison of the variance of potential measurements from probes in each location.

Despite different physical mechanisms being dominant in determining the radial velocity

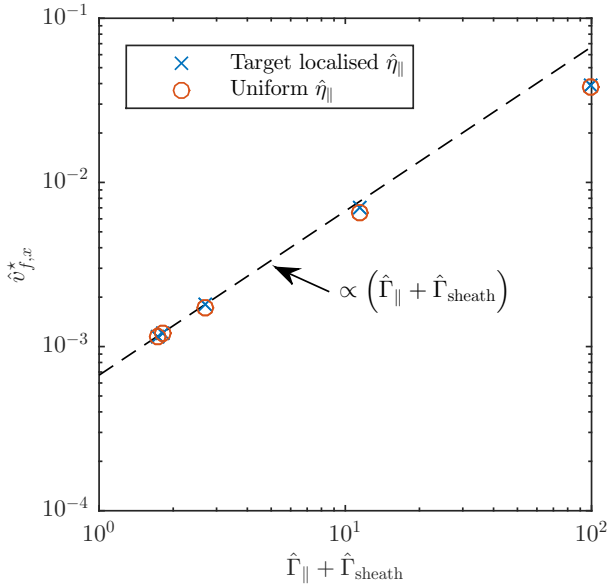

Figure 7.7: Dependence of the $\hat{\delta}_\perp = 100$ filaments' characteristic radial velocity, $\hat{v}^\star_{f,x}$, on $(\hat{\Gamma}_\parallel + \hat{\Gamma}_{\text{sheath}})$.

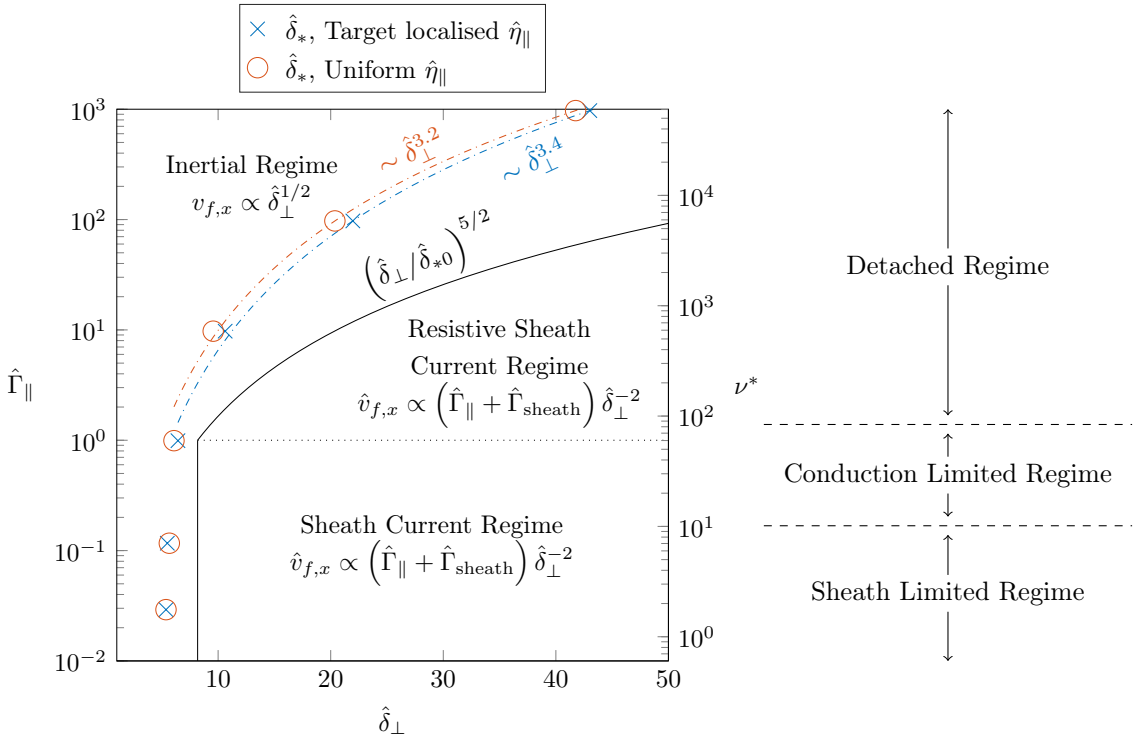

Figure 7.8: Diagram of the location of each filament regime in $\hat{\Gamma}_\parallel - \hat{\delta}_\perp$, or equivalently $\nu^* - \hat{\delta}_\perp$ space. The measured locations of the transition from the inertial regime, $\hat{\delta}_*$, for different values of $\hat{\Gamma}_\parallel$ are plotted using markers. Reference [184]'s analytical predictions for the locations of $\hat{\delta}_*$ and for the transition from the sheath current regime to the resistive sheath current regime are plotted using solid and dotted black lines respectively. On the right hand side, the approximate spans of different SOL operating regimes in terms of ν^* are provided for comparison.

of the filaments in the sheath current and resistive sheath current regimes (namely sheath resistivity and plasma resistivity respectively), the two regimes are unified in that the radial velocities produced across both regimes are proportional to $(\hat{\Gamma}_{\text{sheath}} + \hat{\Gamma}_{\parallel})\hat{\delta}_{\perp}^{-2}$, which is the total normalised resistivity-length of the path that parallel currents take to close through the target. This linear dependence is demonstrated in Figure 7.7 for $\hat{\delta}_{\perp} = 100$ filaments. The largest $(\hat{\Gamma}_{\text{sheath}} + \hat{\Gamma}_{\parallel})$ data point deviates from this scaling because polarisation currents are not negligible for this filament and thus it is not strictly in the resistive sheath current regime. The transition between the two regimes therefore occurs at the point at which $\hat{\Gamma}_{\parallel} \approx \hat{\Gamma}_{\text{sheath}}$, as this reflects the approximate point at which the sheath resistivity and plasma resistivity play an equal role in determining the filament's velocity. This is reflected in Figure 7.2, in that the filaments' radial velocities only noticeably deviate from their reference case values in the $\hat{\eta}_{\parallel\text{div}} = 100\hat{\eta}_{\parallel 0}$ data series, in which $\hat{\Gamma}_{\parallel} \approx \hat{\Gamma}_{\text{sheath}} \sim 1$. This transition point and the observed velocity scaling across the two regimes are consistent with the predictions of Reference [184].

Next, the perpendicular size at which filaments transition from the inertial regime to the sheath current or resistive sheath current regime, $\hat{\delta}_{*}$, is considered. In Section 6.3.2, this quantity was estimated analytically as the value of $\hat{\delta}_{\perp}$ at which the sheath current and polarisation current terms are equal in Equation (6.11), but this definition cannot be applied to simulation data. It is emphasised that in practice there is a relatively wide range of $\hat{\delta}_{\perp}$ over which both polarisation currents and parallel currents play a significant role, and that there is no distinct transition point. However, the $\hat{\delta}_{\perp}$ at which the maximum value of $\hat{v}_{f,x}^{\star}$ occurs does provide a reliable approximate location of this region. Therefore this definition is used throughout this chapter to quantitatively measure $\hat{\delta}_{*}$ from the simulations, with a cubic spline interpolation used to determine its value as accurately as possible.

The measured locations of $\hat{\delta}_{*}$ for each $\hat{\eta}_{\parallel\text{div}}$ simulated are plotted as blue crosses on the $\hat{\delta}_{\perp}$ - $\hat{\Gamma}_{\parallel}$ diagram in Figure 7.8 to show the location of the boundary of the inertial regime. For comparison, the analytical estimates for $\hat{\delta}_{*}$ from References [160] and [184], which are stated in Equation (7.8), are plotted using solid black lines, whilst a dotted black line shows the predicted location of the transition between the sheath current and resistive sheath current regimes. For $\hat{\Gamma}_{\parallel} \leq 1$, the simulations' $\hat{\delta}_{*}$ remains constant around $\hat{\delta}_{*0}$ and is insensitive to $\hat{\Gamma}_{\parallel}$ and thus good agreement is found with the analytical predictions. For $\hat{\Gamma}_{\parallel} > 1$, qualitative agreement is found with Reference [184]'s prediction in that $\hat{\delta}_{*}$ increases as $\hat{\Gamma}_{\parallel}$ rises. More quantitatively however, the observed power law dependence in this region, $\hat{\delta}_{*} \sim \hat{\Gamma}_{\parallel}^{1/3.4} \approx \hat{\Gamma}_{\parallel}^{0.3}$, obtained from the two highest $\hat{\Gamma}_{\parallel}$ data points and plotted using a blue dash-dot line, can be seen to have a weaker scaling than the $\hat{\delta}_{*} \sim \hat{\Gamma}_{\parallel}^{2/5}$ scaling predicted in Reference [184]. Using the relation $\nu^{*} \approx \hat{\Gamma}_{\parallel}\sqrt{m_i/m_e}$, the right hand vertical axis allows these results to also be interpreted in terms of the SOL collisionality. The approximate ν^{*} ranges of the SOL operating regimes described in Section 1.5.3 are indicated to the right of this plot and it can be seen that the transition from the sheath current regime to the resistive sheath current regime coincides with onset of detachment.

Estimate of $\hat{\eta}_{\parallel\text{div}}$ at Low Divertor Temperatures

In an attempt to relate the preceding results to experiments, this section provides an order of magnitude estimate of the electron temperature of the divertor region, T_e^{div}, that may be required to produce the values of $\hat{\eta}_{\parallel\text{div}}$ used in the preceding results. The definition of $\hat{\eta}_{\parallel}$ given in Chapter 3 is based upon electron-ion collisions, and is such that $\hat{\eta}_{\parallel} \propto T_e^{-3/2}$. However, at very low temperatures, collisions between electrons and neutrals may become important in the

Table 7.1: Estimated divertor temperature required to produce the values of $\hat{\eta}_{\parallel \mathrm{div}}$ used.

$\hat{\eta}_{\parallel \mathrm{div}}$	$\hat{\Gamma}_{\parallel}$	T_e^{div} required excluding neutral effects (eV)	T_e^{div} required including neutral effects (eV)
$\hat{\eta}_{\parallel 0}$	0.029	40	40
$10\hat{\eta}_{\parallel 0}$	0.12	8.6	8.6
$100\hat{\eta}_{\parallel 0}$	0.99	1.9	1.9
$1000\hat{\eta}_{\parallel 0}$	9.7	0.40	0.45
$10000\hat{\eta}_{\parallel 0}$	97	0.086	0.37
$100000\hat{\eta}_{\parallel 0}$	970	0.019	0.32

divertor region, and so more generally, the dimensional resistivity can be redefined as [253]:

$$\eta_{\parallel} = \frac{0.51 m_e \left(\nu_{ei} + \nu_{en}\right)}{n_e e^2}. \tag{7.11}$$

Here $\nu_{en} = n_n \langle \sigma v \rangle$ is the electron-neutral collision frequency, where n_n is the number density of neutral atoms, v is the velocity of an electron and σ is the cross section for collisions between electrons and neutrals (which is in principle a function of v). Furthermore $\langle \cdot \rangle$ denotes an average over all velocities in the (assumed) Maxwellian distribution function. Using this definition, the normalised resistivity, $\hat{\eta}_{\parallel} = \eta_{\parallel} / \left(B / \left(e n_{e,0}\right)\right)$, becomes

$$\hat{\eta}_{\parallel} = \hat{\eta}_{\parallel}^{ei} + \hat{\eta}_{\parallel}^{en}, \tag{7.12}$$

where $\hat{\eta}_{\parallel}^{ei}$ and $\hat{\eta}_{\parallel}^{en}$ are the normalised resistivity components due to electron-ion and electron-neutral collisions respectively. It is noted that elsewhere in this work, $\hat{\eta}_{\parallel} = \hat{\eta}_{\parallel}^{ei}$.

For this estimate, the densities of neutral deuterium atoms and electrons (or deuterium ions) at a given temperature were estimated using the Saha equation [254], alongside the assumption that $n_e + n_n = n_{e,0}$. It is noted that the Saha equation assumes the plasma and neutral gas to be in thermal equilibrium, which is not a valid assumption for edge plasmas. Moreover, its use implies an equilibrium between ionisation and recombination processes, which may not occur because recombination is a relatively slow process compared to the typical time scales of fluctuations in the divertor. Values of σ for elastic collisions between electrons and hydrogen atoms, obtained from Reference [255], were used. These calculations arguably provide a conservative estimate of the resistivity in the divertor region, as collisions with neutral particles other than deuterium that may be present due to sputtering or impurity seeding, have not been included. Furthermore, anomalous resistivity effects have also been neglected.

Figure 7.9 thus shows the estimated relative increase of the normalised resistivity in the divertor region, $\hat{\eta}_{\parallel \mathrm{div}}$, (and each of its constituent terms, $\hat{\eta}_{\parallel \mathrm{div}}^{ei}$ and $\hat{\eta}_{\parallel \mathrm{div}}^{en}$) compared to $\hat{\eta}_{\parallel 0}$ as T_e^{div} is decreased. For reference, the corresponding values of T_e^{div} estimated to produce the values of $\hat{\eta}_{\parallel \mathrm{div}}$, including and excluding neutral collisions, are given in Table 7.1. These calculations indicate that at temperatures below around 0.5 eV, electron collisions with neutrals may dominate over electron collisions with ions.

It is emphasised however, that these calculations are based upon a number of assumptions that may not be well justified in the SOL near the sheath, and so should only be used to give an order of magnitude indication of how the resistivity in the divertor region may depend on T_e. It is stressed that $\hat{\eta}_{\parallel}^{en}$ dominates at low temperatures because the ratio n_n/n_e becomes very large (> 1000) and so the plasma is estimated to be very weakly ionised. It is unclear

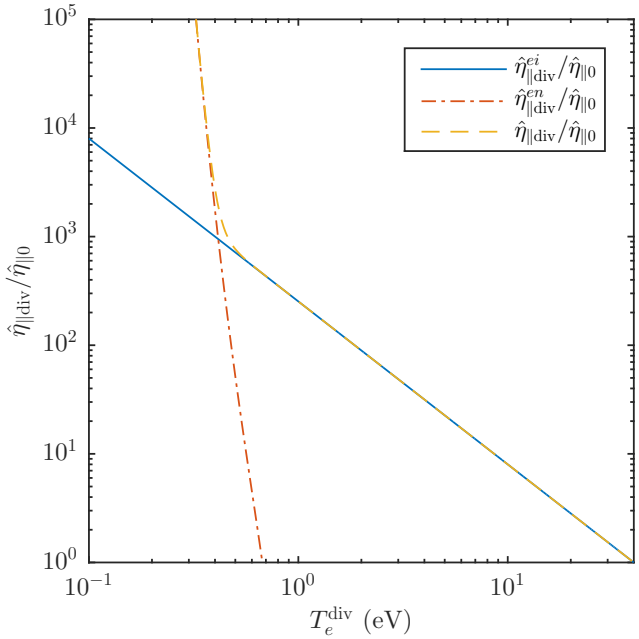

Figure 7.9: Estimate of relative magnitude of the normalised resistivity in the divertor region, $\hat{\eta}_{\parallel\mathrm{div}}$, (and each of its constituent terms, $\hat{\eta}^{ei}_{\parallel\mathrm{div}}$ and $\hat{\eta}^{en}_{\parallel\mathrm{div}}$) compared to $\hat{\eta}_{\parallel 0}$ as a function of temperature in the divertor, T_e^{div}.

whether such a weakly ionised plasma is achieved experimentally in the divertor region when detachment occurs. Furthermore, it is unlikely that such a weakly ionised plasma would extend in the parallel direction for 25% of the domain, which is the extent of the enhanced resistivity region in the simulations.

7.2.2 Uniform Resistivity

The effect of increasing the resistivity of the plasma uniformly along the field line, rather than just in the region nearest to the targets, has also been examined to compare and contrast against the results in the preceding section. To enable a direct comparison, simulations have been performed in which $\hat{\eta}_{\parallel}$ was increased from $\hat{\eta}_{\parallel 0}$ by factors such that the $\hat{\Gamma}_{\parallel}$ values are equal to those used in the target-localised resistivity simulations. For reference, these values are listed in Table 7.2. In addition, all filaments were initialised as in the previous section.

The dependence of $\hat{v}^{\star}_{f,x}$ on $\hat{\delta}_{\perp}$ for each value of $\hat{\eta}_{\parallel}$ used is shown in Figure 7.10. By cross comparison with Figure 7.2, it can be seen that identical trends are exhibited as in

Table 7.2: Values of the uniformly enhanced resistivity used in this section. These values correspond to same values of $\hat{\Gamma}_{\parallel}$ that were used in the target-localised resistivity case.

$\hat{\Gamma}_{\parallel}$	Target localised enhanced resistivity, $\hat{\eta}_{\parallel\mathrm{div}}$	Uniformly enhanced resistivity, $\hat{\eta}_{\parallel}$
0.029	$\hat{\eta}_{\parallel 0}$	$\hat{\eta}_{\parallel 0}$
0.12	$10\hat{\eta}_{\parallel 0}$	$4\hat{\eta}_{\parallel 0}$
0.99	$100\hat{\eta}_{\parallel 0}$	$34\hat{\eta}_{\parallel 0}$
9.7	$1000\hat{\eta}_{\parallel 0}$	$334\hat{\eta}_{\parallel 0}$
97	$10000\hat{\eta}_{\parallel 0}$	$3334\hat{\eta}_{\parallel 0}$
970	$100000\hat{\eta}_{\parallel 0}$	$33334\hat{\eta}_{\parallel 0}$

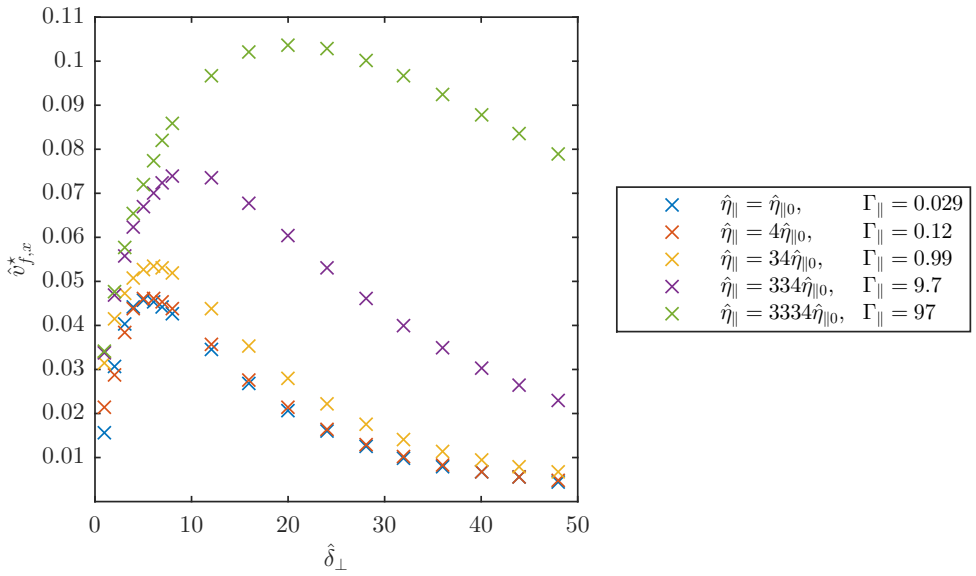

Figure 7.10: Dependence of a filament's characteristic radial velocity, $\hat{v}^{\star}_{f,x}$, on its initial perpendicular length scale, $\hat{\delta}_{\perp}$, for each of the values of $\hat{\eta}_{\parallel}$ used in the uniformly enhanced resistivity scan.

the target-localised resistivity case, although the uniformly increased resistivity does produce slightly faster radial velocities for the same value of $\hat{\Gamma}_{\parallel}$ in the inertial regime. For example, the $\hat{\eta}_{\parallel} = 3334\hat{\eta}_{\parallel 0}$ data series consistently attains higher radial velocities than the $\hat{\eta}_{\parallel \mathrm{div}} = 10000\hat{\eta}_{\parallel 0}$ data series in Figure 7.2 for $\hat{\delta}_{\perp} \lesssim 30$.

However, the actual balance of currents produced throughout the filament is subtly different between the two cases for the same value of $\hat{\Gamma}_{\parallel}$ (for high values of resistivity). This can be seen by cross comparison between Figure 7.11, which plots the divergence of current densities divided by n from the $\hat{\delta}_{\perp} = 28$, $\hat{\eta}_{\parallel} = 3334\hat{\eta}_{\parallel 0}$ filament, to Figure 7.5, which corresponds to a target-localised resistivity filament of the same $\hat{\delta}_{\perp}$ and $\hat{\Gamma}_{\parallel}$. Whilst in both cases the polarisation current path is dominant in closing the diamagnetic current drive, the parallel currents can be seen to play less of a role in the uniform resistivity case compared to the target-localised resistivity case.

This has two key effects, the first being that, as noted above, slightly faster radial velocities are produced in the inertial regime of the uniform resistivity case because the polarisation currents are necessarily more intense. The second effect is that the radial velocity exhibits a gradient along the parallel direction, in that the filament moves faster at $z = 0$ than it does at $z = L_{\parallel}/2$. This behaviour is demonstrated by the left hand plot of Figure 7.12, which plots n_f in a $x - z$ plane through the middle of the $\hat{\delta}_{\perp} = 12$, $\hat{\eta}_{\parallel} = 3334\hat{\eta}_{\parallel 0}$ filament at an example time $t = 250\ \Omega_i^{-1}$. For comparison the same quantity from the target-localised resistivity, $\hat{\eta}_{\parallel \mathrm{div}} = 10000\hat{\eta}_{\parallel 0}$, $\hat{\delta}_{\perp} = 12$ simulation is plotted in the right hand plot of the same figure. By introducing the drift-plane filament radial velocity,

$$\hat{v}^{\text{drift-plane}}_{f,x}(z) = \frac{\int_{-\infty}^{\infty}\int_{-\infty}^{\infty} n_f \dfrac{\partial \phi}{\partial y}\,\mathrm{d}x\,\mathrm{d}y}{\int_{-\infty}^{\infty}\int_{-\infty}^{\infty} n_f\,\mathrm{d}x\,\mathrm{d}y}, \tag{7.13}$$

the extent to which the radial velocity varies along the field line can be quantitatively assessed.

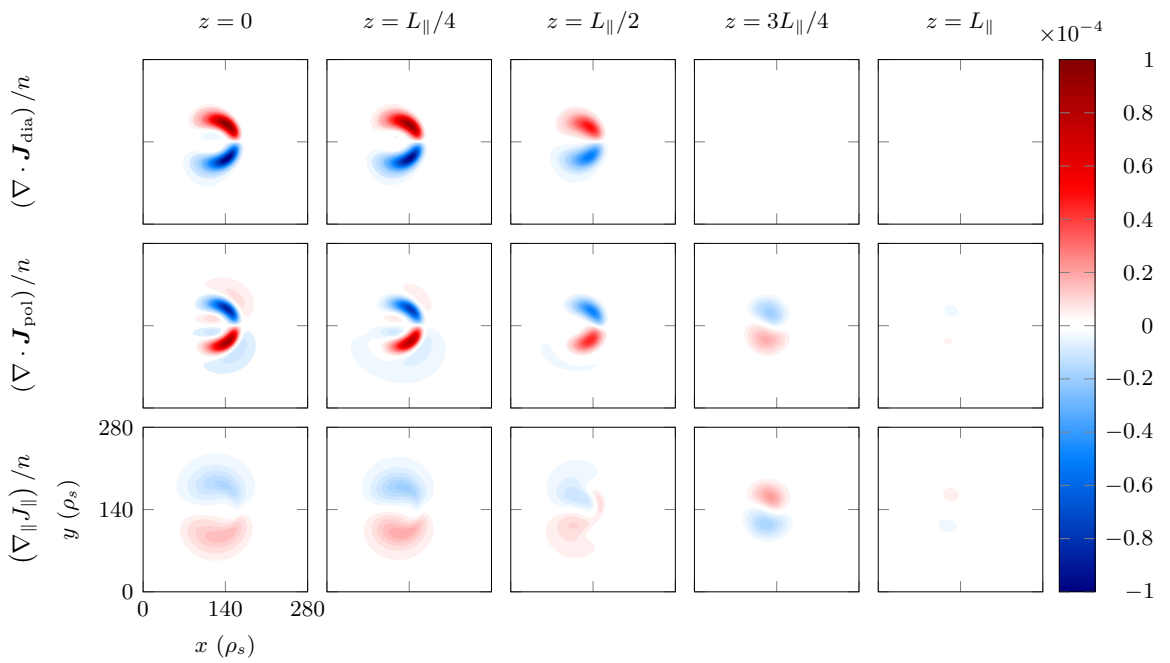

Figure 7.11: Example current balance found along the field line in a $\hat{\delta}_\perp = 28$, $L_f = L_\parallel/2$ filament in the uniformly enhanced resistivity $\hat{\eta}_\parallel = 3334\hat{\eta}_{\parallel 0}$ case. The quantities are plotted at the time of the filament's peak radial velocity, $\hat{v}_{f,x}$, and the filament was otherwise initialised using $A = 2$ and $\hat{\delta}_\parallel = L_\parallel/10$.

Figure 7.13 plots this quantity against time at various positions along the field line (in the region of density perturbation) for the $\hat{\delta}_\perp = 12$ simulations shown in Figure 7.12, as well as the reference case $\hat{\delta}_\perp = 12$ simulation. It can be seen that in the uniformly enhanced resistivity case, the radial velocity at $z = L_\parallel/2$ is approximately a third slower than that at $z = 0$ for most of the duration of simulation.

The gradient in the radial velocity along the field line occurs in the enhanced uniform resistivity case because the parallel currents, which are suppressed throughout the domain, are not able to balance the polarisation currents in the region $L_\parallel/2 < z < 3L_\parallel/4$, where the diamagnetic currents are reduced or negligible. The polarisation currents therefore can only develop to match the local diamagnetic current drive, meaning that they are not constant along z. Consequently ϕ and $\hat{v}_{f,x}^{\text{drift-plane}}$ develop larger values at $z = 0$ than at $z = L_\parallel/2$, where the density gradients are smaller. If the resistivity is high enough, ϕ is determined independently on each drift-plane and the dynamics of the filament are effectively decoupled along the field line. In contrast, in the enhanced target-localised resistivity case, the parallel currents are able to fulfil the role of balancing the polarisation currents in the region where the diamagnetic currents are absent, and so $\boldsymbol{J}_{\mathrm{pol}}$, ϕ and $\hat{v}_{f,x}$ are approximately constant from $z = 0$ to $z = 3L_\parallel/4$.

Regarding the behaviour of $\hat{\delta}_*$ under uniformly increased resistivity, a very similar trend was displayed to what was found using an enhanced target-localised resistivity. This can be observed in Figure 7.8, which plots using red circles the measured locations of $\hat{\delta}_*$ from this uniform resistivity series of simulations. The measured power law dependence, $\hat{\delta}_* \sim \hat{\Gamma}_\parallel^{1/3.2} \approx \hat{\Gamma}_\parallel^{0.3}$ in the region $\hat{\Gamma}_\parallel > 1$ is approximately the same as in the target-localised resistivity case and is again weaker than Reference [184]'s prediction.

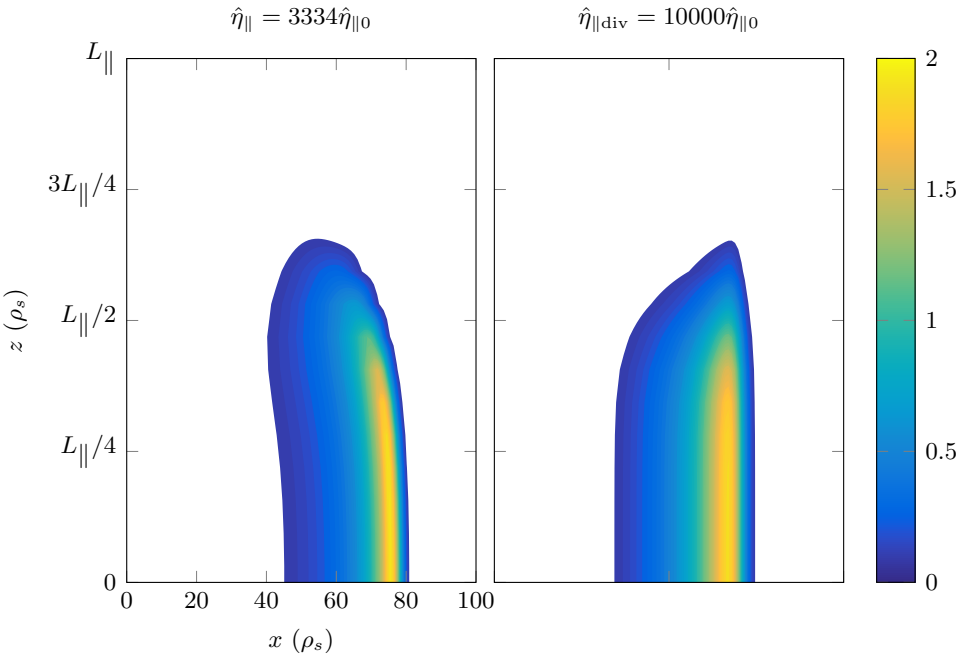

Figure 7.12: Comparison of the parallel structure of a filament density profile, n_f, between the enhanced target-localised resistivity $\hat{\eta}_{\parallel \mathrm{div}} = 10000\hat{\eta}_{\parallel 0}$ case and the uniformly enhanced resistivity $\hat{\eta}_\parallel = 3334\hat{\eta}_{\parallel 0}$ case. The data shown is from taken from $x - z$ planes through the middle of the filaments, at an example time $t = 250\ \Omega_i^{-1}$. Both filaments were initialised with $\hat{\delta}_\perp = 12$, $A = 2$, $L_f = L_\parallel/2$ and $\hat{\delta}_\parallel = L_\parallel/10$. Values of n_f below 0.1 are not plotted.

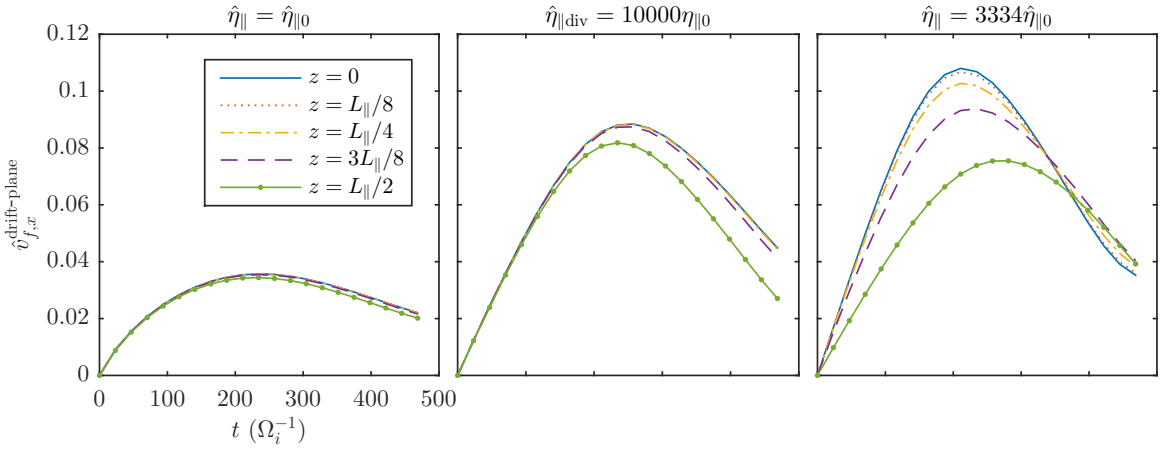

Figure 7.13: Drift plane radial velocity, $\hat{v}_{f,x}^{\text{drift-plane}}$, plotted against time at various positions along the field line, for $\hat{\delta}_\perp = 12$ filaments. The left, centre and right plots respectively correspond to the reference resistivity case, the enhanced target-localised resistivity $\hat{\eta}_{\parallel \mathrm{div}} = 10000\hat{\eta}_{\parallel 0}$ case and the uniformly enhanced resistivity $\hat{\eta}_\parallel = 3334\hat{\eta}_{\parallel 0}$ case. Different radial velocities can be observed at each position along the field line in the $\hat{\eta}_\parallel = 3334\hat{\eta}_{\parallel 0}$ case.

7.3 Effect of Input Parameters

In this section, the dependence of filaments' radial velocities on the reference plasma density, $n_{e,0}$, electron temperature, T_e, and magnetic field strength, B, is investigated. Since the latter two parameters affect the normalisation quantities ρ_s and c_s, some comparisons will be made in SI units. Therefore in this section a number of dimensional counterparts of previously defined normalised quantities are introduced and are identifiable by the absence of a hat. For example, $\delta_\perp$ and $v_{f,x}$ are the dimensional equivalents of $\hat{\delta}_\perp$ and $\hat{v}_{f,x}$.

7.3.1 Theoretical Predictions

Insight into the effect of these parameters can be gained through analytical estimates, which can then be used to compare against the simulation results. In Section 6.3.2, similar estimates were obtained using the sheath dissipations closure's vorticity equation, Equation (2.20). However, this closure inherently assumes $\Gamma_{\text{sheath}} \gg \Gamma_\parallel$ and therefore does not describe the dynamics of filaments when $\Gamma_{\text{sheath}} \ll \Gamma_\parallel$, which can occur depending on the input parameters. Here, both limits are modelled heuristically using the following 2D equation:

$$\frac{m_i}{B}\left(\frac{\partial}{\partial t} + \boldsymbol{v}_E \cdot \nabla\right)\frac{\nabla_\perp^2 \varphi}{B} = \frac{\varphi}{n_e \ell_\parallel \left(\Gamma_{\text{sheath}} + \Gamma_\parallel\right)} - \frac{eg}{n_e \Omega_i}\frac{\partial n_e}{\partial y}. \tag{7.14}$$

It is noted that by setting $\Gamma_\parallel = 0$ in the above expression, the standard sheath dissipation vorticity equation is recovered. In the following, two distinct cases will be considered corresponding to $\Gamma_{\text{sheath}} \gg \Gamma_\parallel$ and $\Gamma_{\text{sheath}} \ll \Gamma_\parallel$, as different predictions are obtained in each limit.

$\boldsymbol{\Gamma_{\text{sheath}} \gg \Gamma_\parallel}$

In this case, the resistance to parallel currents travelling from the filament to the sheath is negligible compared to the resistance to currents travelling through the sheath itself. Since $\Gamma_{\text{sheath}} \propto T_e^{1/2}/n_e$ and $\Gamma_\parallel \propto T_e^{-3/2}$, this situation occurs at low densities and at high temperatures, i.e. at low SOL collisionality. When this condition is satisfied, the magnitude of each term of Equation (7.14) in the region of a filament with perpendicular length scale $\delta_\perp$ can be estimated as

$$\frac{m_i \varphi^2}{B^3 \delta_\perp^4} \sim \frac{e^2 c_s \varphi}{\ell_\parallel T_e} - \frac{eg}{\Omega_i \delta_\perp}, \tag{7.15}$$

whilst $v_{f,x}$ can be approximated as

$$v_{f,x} \sim \frac{\varphi}{B\delta_\perp}. \tag{7.16}$$

In the inertial regime, where the polarisation current term predominantly balances the diamagnetic drive, $v_{f,x}$ can be estimated as

$$v_{f,x} \sim \sqrt{g\delta_\perp}, \tag{7.17}$$

$$v_{f,x} \sim \frac{T_e^{1/2}\delta_\perp^{1/2}}{R_c^{-1/2}}. \tag{7.18}$$

On the other hand, in the sheath current limited regime, where the diamagnetic drive term is balanced mainly by the sheath current term, $v_{f,x}$ can be estimated as

$$v_{f,x} \sim \frac{c_s g \ell_\parallel}{\Omega_i^2 \delta_\perp^2}, \tag{7.19}$$

$$v_{f,x} \sim \frac{T_e^{3/2}\ell_\parallel}{R_c B^2 \delta_\perp^2}. \tag{7.20}$$

In both these regimes, the velocity of a filament is predicted to increase with T_e. This arises due to the increased diamagnetic current drive, which is proportional to T_e, and also in the sheath current limited regime due to the effective resistivity-length of the sheath, Γ_{sheath}, which is proportional to $T_e^{1/2}$. Furthermore the radial velocity of a filament in the sheath current regime is expected to decrease with B, whilst it is anticipated that both regimes will be invariant to $n_{e,0}$.

The estimated critical $\delta_\perp$ at which filaments transition between the inertial and sheath current regimes, in dimensional units, is estimated to be

$$\delta_* = \delta_{*0}, \tag{7.21}$$

where

$$\delta_{*0} = \left(\frac{g\ell_\parallel^2 c_s^2}{2\Omega_i^4}\right)^{1/5}. \tag{7.22}$$

This means that δ_* is predicted to scale like

$$\delta_* \sim \frac{T_e^{2/5}\ell_\parallel^{2/5}}{R_c^{1/5}B^{4/5}}. \tag{7.23}$$

Therefore as T_e increases or as B decreases, the transition from the inertial regime to the sheath current regime is predicted to occur at larger $\delta_\perp$, providing another mechanism by which faster radial velocities may occur at hotter temperatures or at weaker magnetic fields.

$\boldsymbol{\Gamma_{\text{sheath}} \ll \Gamma_\parallel}$

In this case, the resistance to parallel currents travelling from the filament to the sheath is greater than the resistance to currents travelling through the sheath and the sheath current regime is effectively replaced with the resistive sheath current regime. This occurs at high densities and at low temperatures, i.e. at high SOL collisionality. In this limit, the magnitudes of each of the terms in Equation (7.14) can be estimated as

$$\frac{m_i\varphi^2}{B^3\delta_\perp^4} \sim \frac{e^2\varphi}{0.51\ell_\parallel^2 m_e\nu_{ei}} - \frac{eg}{\Omega_i\delta_\perp}. \tag{7.24}$$

The radial velocity scaling prediction for the inertial regime remains the same as in the $\Gamma_{\text{sheath}} \gg \Gamma_\parallel$ case, whilst the resistive sheath current regime scaling can be estimated as

$$v_{f,x} \sim \frac{0.51\nu_{ei}g\ell_\parallel^2}{\Omega_i^2\delta_\perp^2}\frac{m_e}{m_i}, \tag{7.25}$$

$$v_{f,x} \sim \frac{\ell_\parallel^2 n_{e,0}}{R_c T_e^{1/2} B^2\delta_\perp^2}. \tag{7.26}$$

The radial velocity is thus expected to decrease with temperature, which is the opposite trend to that which is predicted for the sheath current regime. Furthermore, a linear dependence on $n_{e,0}$ is anticipated, which arises because the polarisation and diamagnetic current terms in Equation (7.14) are proportional to $n_{e,0}$, whilst the parallel current term is not. As in the sheath current regime, the radial velocity is predicted to decrease with B.

The perpendicular size at which filaments transition between the inertial and resistive sheath current regime can be estimated to be

$$\delta_* = \delta_{*0}\left(\frac{\ell_\parallel\nu_{ei}m_e}{2c_s m_i}\right)^{2/5} \tag{7.27}$$

Table 7.3: Theoretical predictions for the scaling of $v_{f,x}$ and δ_* with input parameters.

	Inertial regime $v_{f,x}$ scaling	Sheath current regime/Resistive sheath current regime $v_{f,x}$ scaling	δ_* scaling
$\Gamma_{\text{sheath}} \gg \Gamma_{\parallel}$	$\sim \frac{T_e^{1/2}\delta_\perp^{1/2}}{R_c^{-1/2}}$	$\sim \frac{T_e^{3/2}\ell_\parallel}{R_c B^2 \delta_\perp^2}$	$\sim \frac{T_e^{2/5}\ell_\parallel^{2/5}}{R_c^{1/5}B^{4/5}}$
$\Gamma_{\text{sheath}} \ll \Gamma_{\parallel}$		$\sim \frac{\ell_\parallel^2 n_{e,0}}{R_c T_e^{1/2} B^2 \delta_\perp^2}$	$\sim \frac{\ell_\parallel^{4/5} n_{e,0}^{2/5}}{R_c^{1/5} T_e^{2/5} B^{4/5}}$

and therefore is predicted to scale like

$$\delta_* \sim \frac{\ell_\parallel^{4/5} n_{e,0}^{2/5}}{R_c^{1/5} T_e^{2/5} B^{4/5}}. \tag{7.28}$$

Equation (7.27) can be written in terms of normalised quantities as

$$\hat{\delta}_* = \hat{\delta}_{*0} \left(n \hat{\Gamma}_\parallel \right)^{2/5}, \tag{7.29}$$

which is identical to Reference [184]'s prediction, reproduced in Equation (7.8). It is highlighted that in this $\Gamma_{\text{sheath}} \ll \Gamma_{\parallel}$ case, δ_* is predicted to increase as T_e decreases, which is the opposite trend to that expected for $\Gamma_{\text{sheath}} \gg \Gamma_{\parallel}$. Moreover, δ_* is also expected to increase with $n_{e,0}$ for $\Gamma_{\text{sheath}} \ll \Gamma_{\parallel}$, whilst no dependence is anticipated for $\Gamma_{\text{sheath}} \gg \Gamma_{\parallel}$. In both cases, δ_* is predicted to decrease with B.

Summary of Scaling Predictions

A summary of the theoretical predictions for the scaling of $v_{f,x}$ and δ_* with input parameters is provided in Table 7.3. It is remarked that the B dependence of δ_* in both resistivity limits and of $v_{f,x}$ in both the sheath current and resistive sheath current regimes, indicates that slower radial filament velocities will occur at stronger magnetic fields. This is consistent with the Eich scaling prediction (obtained from using a regression analysis of existing experimental measurements) that the SOL heat flux width, λ_q, decreases with both the toroidal and the poloidal components of the magnetic field [34].

7.3.2 Results

To investigate the effect of the input parameters T_e, $n_{e,0}$ and B numerically, a series of filament simulations have been performed in which each of these parameters has been varied independently alongside $\delta_\perp$. In particular, the input parameters have been varied about the reference case given in Table 6.1 ($T_e = 40$ eV, $n_{e,0} = 8 \times 10^{18}$ m^{-3} and $B = 0.5$ T), with the Coulomb logarithm held fixed at $\ln \Lambda = 13.28$.

$n_{e,0}$ Scan

Since $n_{e,0}$ only affects $\hat{\eta}_\parallel$ in the normalised system of equations, the results presented in Section 7.2.2 in which $\hat{\eta}_\parallel$ was uniformly increased can be interpreted consistently as a scan in $n_{e,0}$. Nevertheless, additional simulations have been performed in which $n_{e,0}$ was increased by

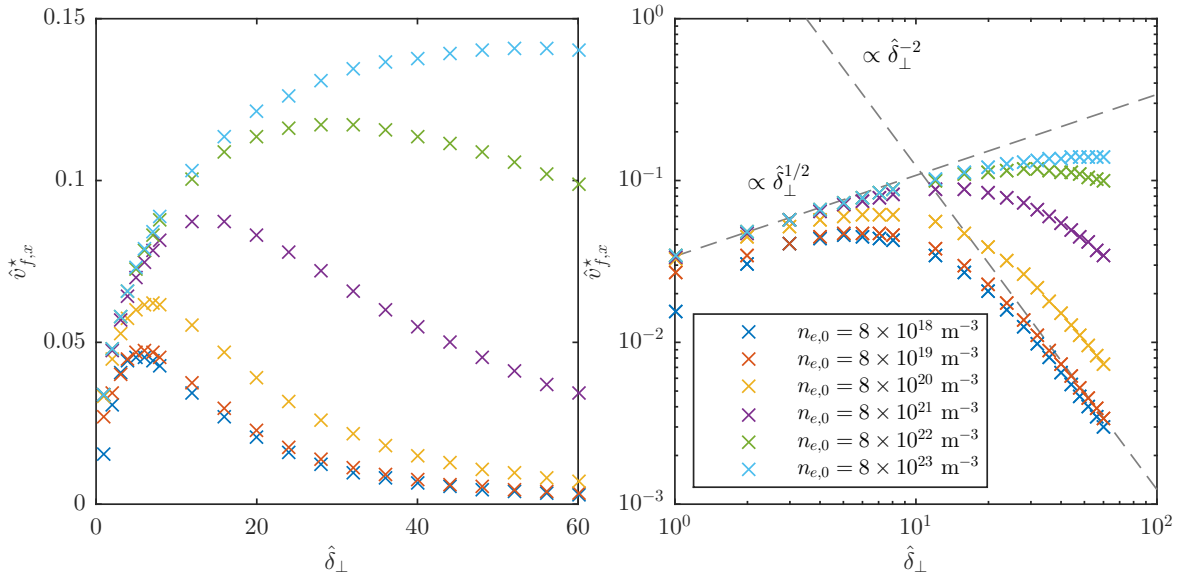

Figure 7.14: Dependence of a filament's normalised characteristic radial velocity, $\hat{v}^{\star}_{f,x}$, on its normalised perpendicular size, $\hat{\delta}_{\perp}$ for increasing values of the reference plasma density, $n_{e,0}$.

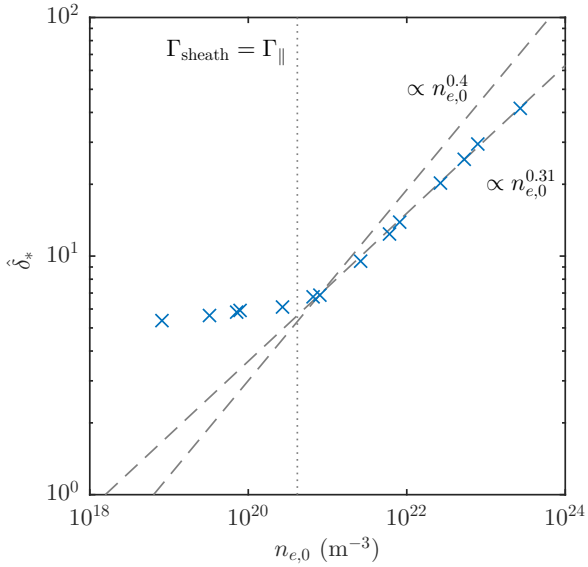

Figure 7.15: Dependence of the normalised filament size at which filaments transition from the inertial regime, $\hat{\delta}_{*}$, on the reference plasma density, $n_{e,0}$. A dotted line marks the value of $n_{e,0}$ at which $\Gamma_{\text{sheath}} \approx \Gamma_{\parallel}$, whilst the dashed lines mark the predicted scaling with $n_{e,0}$ of Equation (7.28) and the scaling obtained from the simulation results.

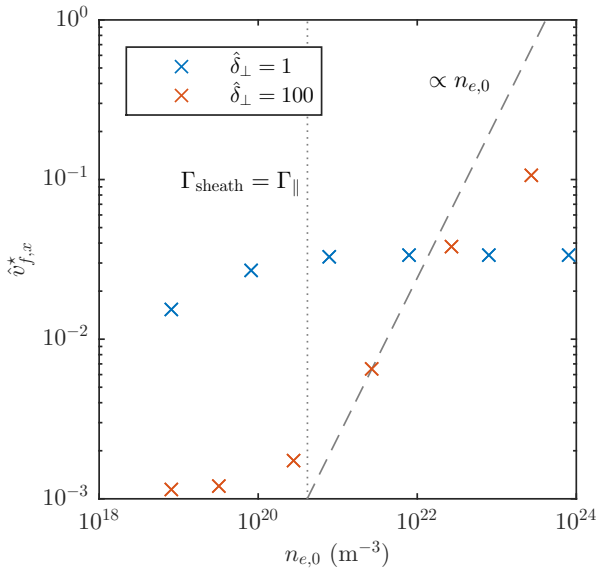

Figure 7.16: Dependence of the normalised characteristic radial velocity, $\hat{v}^{\star}_{f,x}$, on the reference plasma density, $n_{e,0}$, for filaments of perpendicular size $\hat{\delta}_\perp = 1$ and $\hat{\delta}_\perp = 100$. A dotted line marks the value of $n_{e,0}$ at which $\Gamma_{\text{sheath}} \approx \Gamma_\parallel$, whilst the $n_{e,0}$ scaling prediction of Equation (7.26) is plotted using a dashed line.

factors of ten from 8×10^{18} m^{-3} to 8×10^{23} m^{-3} *, with the filaments initialised as in Section 7.2 ($A = 2$, $L_f = L_\parallel/2$ and $\hat{\delta}_\parallel = L_\parallel/10$). For reference, $\Gamma_{\text{sheath}} \approx \Gamma_\parallel$ at $n_{e,0} \approx 4 \times 10^{20}$ m^{-3}.

The dependence of the normalised characteristic radial velocity, $\hat{v}^{\star}_{f,x}$, on $\hat{\delta}_\perp$ is plotted in Figure 7.14 for each value of $n_{e,0}$ simulated. As $n_{e,0}$ increases, the filaments' radial velocities scale like $\hat{\delta}_\perp^{1/2}$ up until larger values of $\hat{\delta}_\perp$, producing faster radial velocities. Physically, this enhancement in radial motion occurs because the polarisation and diamagnetic currents are proportional to $n_{e,0}$, and therefore the inertial regime is extended to larger filament sizes as $n_{e,0}$ increases. Figure 7.15 illustrates this effect, by plotting $\hat{\delta}_*$ (obtained from the simulation data as in Section 7.2) against $n_{e,0}$. For $n_{e,0} \lesssim 4 \times 10^{20}$ m^{-3}, where $\Gamma_{\text{sheath}} > \Gamma_\parallel$, $\hat{\delta}_*$ remains constant around $\hat{\delta}_{*0}$, whilst for $n_{e,0} \gtrsim 0.4 \times 10^{21}$ m^{-3}, where $\Gamma_{\text{sheath}} < \Gamma_\parallel$, $\hat{\delta}_*$ increases with $n_{e,0}$. Both of these trends are as expected, although for the latter a weaker scaling of $\delta_* \propto n_{e,0}^{0.31}$ is exhibited than the $\delta_* \propto n_{e,0}^{0.4}$ scaling predicted by Equation (7.28). It has been verified through an additional series of simulations using $L_f = L_\parallel$ that this discrepancy is not due to Boltzmann spinning motions.

The contrasting functional dependence of $\hat{v}_{f,x}$ on $n_{e,0}$, between filaments that satisfy $\hat{\delta}_\perp \ll \hat{\delta}_*$ and $\hat{\delta}_\perp \gg \hat{\delta}_*$, is illustrated in Figure 7.16. The small $\hat{\delta}_\perp = 1$ filament shows a slight increase in $\hat{v}_{f,x}$ as $n_{e,0}$ is increased until $n_{e,0} \approx 10^{20}$ m^{-3}. Albeit weak, this dependence is not predicted by Equation (7.18) and occurs at the lowest densities because whilst the compressible diamagnetic currents are predominantly balanced by polarisation currents, parallel currents closing through the sheath also play a small role. As the density increases, these parallel currents are suppressed and the filament becomes more strictly inertially limited. The velocity of this smaller filament then saturates at a constant value above $n_{e,0} \approx 10^{20}$ m^{-3}, as the parallel currents have been entirely suppressed.

The larger $\hat{\delta}_\perp = 100$ filament on the other hand, is in the sheath current limited regime at low densities, and thus its velocity shows little increase as $n_{e,0}$ increases until $n_{e,0} \approx 10^{20}$

*It is noted that $n_{e,0} > 10^{21}$ m^{-3} is unrealistic for both current and future devices.

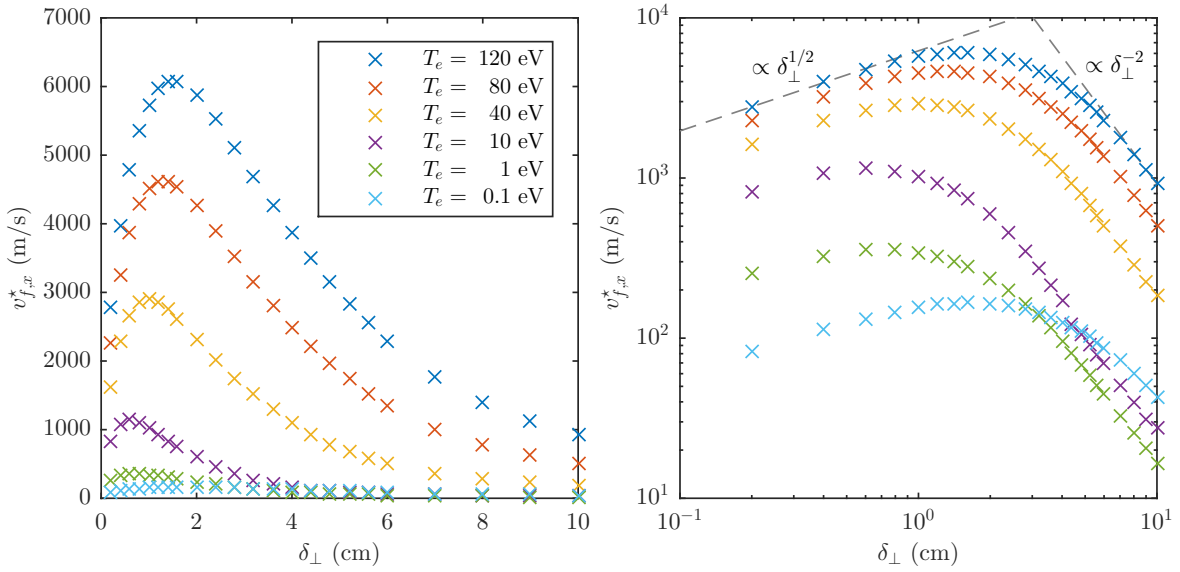

Figure 7.17: Dependence of a filament's characteristic radial velocity, $v^\star_{f,x}$, on its perpendicular size, $\delta_\perp$, for increasing values of electron temperature, T_e.

m^{-3}. At this point $\Gamma_\parallel \approx \Gamma_{\text{sheath}}$ and the filament transitions to the resistive sheath current regime. Therefore for densities $n_{e,0} > 10^{20}$ m^{-3}, its velocity scales broadly like $\hat{v}_{f,x} \propto n_{e,0}$, as predicted by Equation (7.26). The highest density data points drop away from this scaling because the resistivity in these cases is sufficiently large that polarisation currents begin to play a role and the filament is therefore not strictly in the resistive sheath current regime. It is noted that the $\hat{\delta} = 100$ filaments' radial velocities also exhibit a linear dependence on $\hat{\Gamma}_{\text{sheath}} + \hat{\Gamma}_\parallel$ for all but the largest values of $\hat{\Gamma}_\parallel$ (or equivalently, $n_{e,0}$), as shown in Figure 7.7.

T_e Scan

To investigate the effect of electron temperature, simulations have been performed using values of T_e ranging from 0.1 eV to 120 eV. For reference, $\Gamma_{\text{sheath}} \approx \Gamma_\parallel$ at $T_e = 5.5$ eV. In contrast to the simulations presented elsewhere in this chapter, the filaments were seeded without parallel density gradients to suppress Boltzmann spinning dynamics and allow for a more satisfactory comparison of the scaling of the filament's radial velocity with $\delta_\perp$ and T_e. Specifically, the filaments were initialised using $A = 2$, $L_f = L_\parallel$, and $\delta_\parallel = 0$.

Figure 7.17 plots the filament's characteristic radial velocity against its perpendicular size for each value of T_e simulated. Broadly speaking, decreasing T_e leads to slower radial velocities due to the reduced diamagnetic drive and sheath resistance. An exception to this is provided by the very coldest $T_e = 0.1$ eV data series, which has faster velocities than the $T_e = 1$ and $T_e = 10$ eV data series for $\delta_\perp \gtrsim 4$ cm. This occurs because the parallel resistivity of the plasma is sufficiently increased in the $T_e = 0.1$ eV case to increase δ_* and therefore extend the inertial regime. This effect is explicitly shown by Figure 7.18, which plots δ_* against T_e. A non-monotonic relationship between these two quantities is exhibited, which is in line with the theoretical predictions made in Section 7.3.1. For $T_e \gtrsim 5$ eV, where $\Gamma_{\text{sheath}} > \Gamma_\parallel$, δ_* increases with T_e, whilst for $T_e \lesssim 5$ eV, where $\Gamma_{\text{sheath}} < \Gamma_\parallel$, δ_* decreases with T_e. Furthermore, good agreement is found in each case with the specific T_e scaling predictions of Equations (7.23) and (7.28), which are plotted using dashed lines.

The exact dependence of the characteristic radial velocity on T_e is shown explicitly in Figure

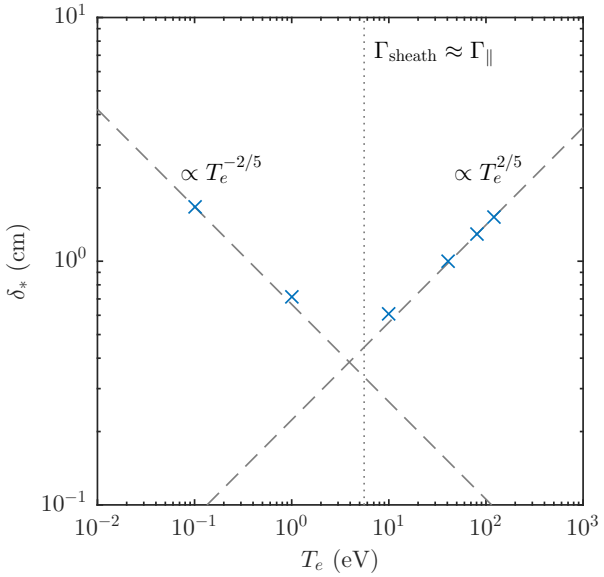

Figure 7.18: Dependence of the filament size at which filaments transition from the inertial regime, δ_*, on the electron temperature, T_e. A dotted line marks the value of T_e at which $\Gamma_{\text{sheath}} \approx \Gamma_{\parallel}$, whilst the T_e scaling predictions of Equations (7.23) and (7.28) are plotted using dashed lines.

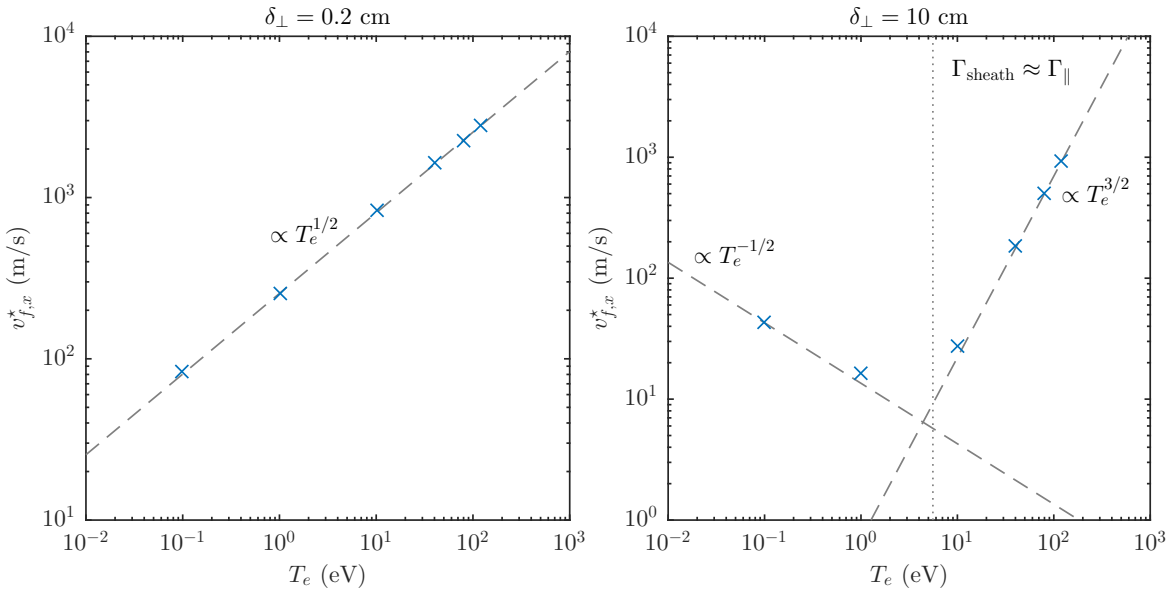

Figure 7.19: Dependence of the characteristic radial velocity, $v^\star_{f,x}$, on the input electron temperature, T_e, for filaments of perpendicular size $\delta_\perp = 0.2$ cm (left) and $\delta_\perp = 10$ cm (right). The scaling predictions of Equations (7.18), (7.20) and (7.26) are plotted for comparison using dashed lines. A dotted line marks the value of T_e at which $\Gamma_{\text{sheath}} \approx \Gamma_{\parallel}$ in the $\delta_\perp = 0.1$ m plot.

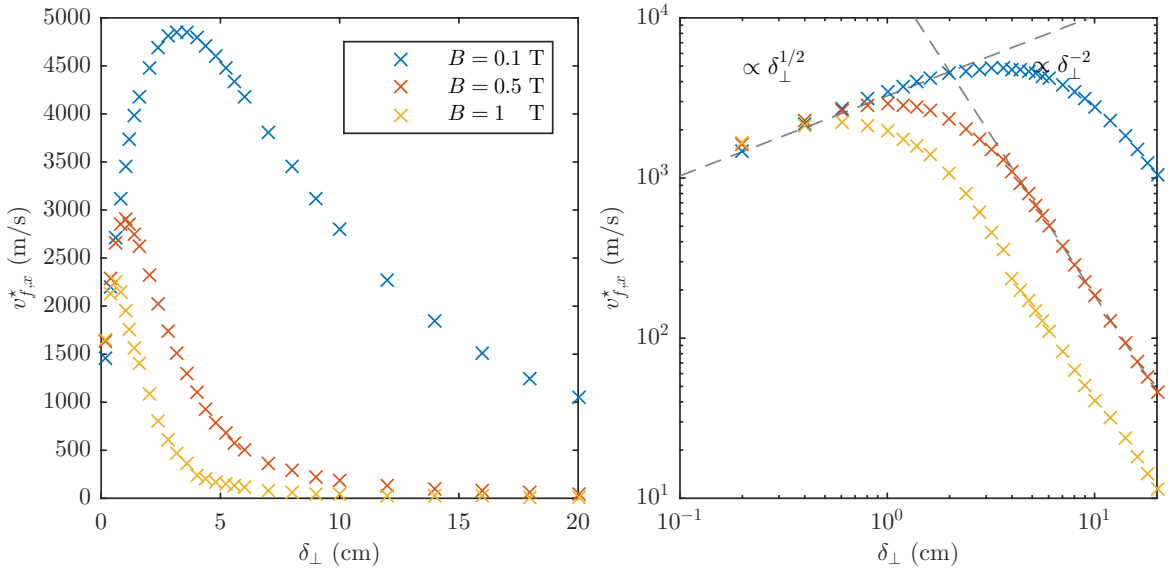

Figure 7.20: Dependence of a filament's characteristic radial velocity, $v^\star_{f,x}$, on its perpendicular size, $\delta_\perp$, for increasing values of magnetic field strength, B.

7.19, for filaments of size $\delta_\perp = 0.2$ cm and $\delta_\perp = 10$ cm, which satisfy $\delta_\perp \ll \delta_*$ and $\delta_\perp \gg \delta_*$ respectively. The former case shows excellent agreement with Equation (7.18), with $v^\star_{f,x}$ scaling like $\sim T_e^{1/2}$. The latter case is also in good agreement with the theoretical predictions of Equation (7.23) and (7.28), with $v^\star_{f,x}$ scaling like $\sim T_e^{-1/2}$ for $\Gamma_{\text{sheath}} \ll \Gamma_\parallel$ and like $\sim T_e^{3/2}$ for $\Gamma_{\text{sheath}} \gg \Gamma_\parallel$.

B Scan

To conclude the input parameters investigation, the effect of increasing the magnetic field strength, B, has been studied by performing scans of simulations at $B = 0.1$ T and $B = 1$ T, in addition to the reference $B = 0.5$ T case. As in the T_e scan simulations, the filaments were initialised with $L_f = L_\parallel$. It is noted that the magnetic field strength does not affect the plasma resistivity, so all simulations here satisfy $\Gamma_{\text{sheath}} \gg \Gamma_\parallel$. Nevertheless these results are presented here for completeness.

Figure 7.20 illustrates how the characteristic radial velocity of the filaments is affected by the magnetic field strength at different perpendicular filament sizes. In agreement with Equation (7.18), the smallest filaments in the inertial regime are invariant to B, but increasing B causes the transition to the sheath current limited regime to occur at smaller $\delta_\perp$. By plotting δ_* against B in Figure 7.21, it can be seen that this transition point scales like $\sim B^{-4/5}$, as predicted by Equation (7.23). To examine the dependence of filament velocities on B in sheath current regime, Figure 7.22 shows the dependence of $v^\star_{f,x}$ on B for the $\delta_\perp = 20$ cm filament. Whilst such a filament size is unrealistic (in experiments filaments typically have a perpendicular size of less than 5 cm), it is considered here because it is in the sheath current regime across all values of B. The velocity of this filament can be observed to scale like $\sim B^{-2}$, in line with Equation (7.20).

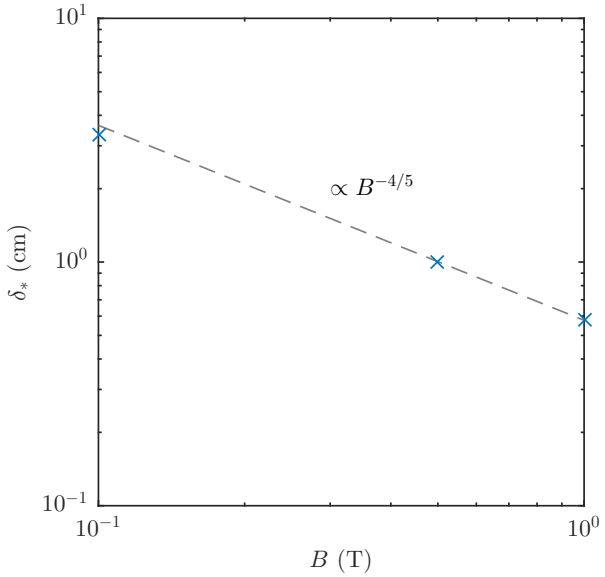

Figure 7.21: Dependence of the filament size at which filaments transition from the inertial regime, δ_*, on the magnetic field strength, B. The B dependence prediction of Equation (7.23) is plotted using a dashed line for comparison.

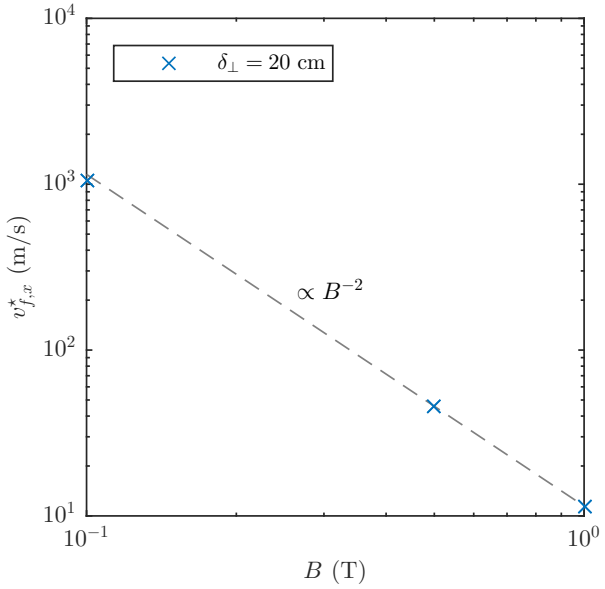

Figure 7.22: Dependence of the $\delta_\perp = 20$ cm filament's characteristic radial velocity, $v^\star_{f,x}$, on the magnetic field strength, B. The B scaling prediction of Equation (7.20) is plotted for comparison using a dashed line.

7.4 Conclusions

This chapter has investigated the effect of plasma resistivity on the dynamics of SOL filaments using STORM3D simulations. Motivated by the expectation of lower temperatures, high neutral densities and the possibility of detachment in the divertor region, the normalised resistivity, $\hat{\eta}_{\parallel}$, was first increased only in the last quarter of the domain nearest the targets. This led to a suppression of parallel currents, a corresponding enhancement of polarisation currents to maintain balance with the compressible diamagnetic currents, and the development of a potential difference along the field line. These intrinsically 3D effects meant that filaments attained faster radial velocities at higher values of resistivity. In particular, filaments with a large normalised perpendicular size, $\hat{\delta}_{\perp} = \delta_{\perp}/\rho_s$, experienced the greatest increase in radial velocity, because at low resistivity these filaments were sheath current limited, meaning that their diamagnetic currents were predominantly closed via parallel currents. In contrast, polarisation currents were dominant in ensuring current continuity for the smallest $\hat{\delta}_{\perp}$ filaments at low resistivity values and so these filaments only experienced a modest increase in their radial velocities at higher values.

More specifically, one mechanism by which greater radial velocities were produced at higher resistivity is that filaments that were in the *sheath current regime* transitioned into the *inertial regime* and so velocities scaled like $\hat{\delta}_{\perp}^{1/2}$ up until larger values of $\hat{\delta}_{\perp}$. The critical normalised size at which this transition occurs, $\hat{\delta}_{*}$, thus increased with resistivity and its dependence on the normalised resistivity-length of the path that parallel currents take from the filament to the sheath entrance, $\hat{\Gamma}_{\parallel}$, was measured to be approximately $\delta_{*} \propto \hat{\Gamma}_{\parallel}^{0.3}$, which is marginally weaker than that predicted by Reference [184]. Enhanced radial velocities were also observed in filaments that were sufficiently large ($\hat{\delta}_{\perp} \gg \hat{\delta}_{*}$), such that the parallel current path remained dominant over the polarisation current path even for high resistivity values. The mechanism for these *resistive sheath current regime* filaments was that the resistance of the plasma was sufficient to introduce a potential difference between downstream at the sheath entrance and further upstream in the region of the filament density perturbation, such that for the same amount of current to flow into the sheath, larger potentials were formed upstream at higher resistivity, corresponding to faster radial velocities.

However it is noted that quite drastic enhancements of the resistivity were required to see significant increases in the filament's radial velocity. For example, in the target-localised resistivity case, $\hat{\eta}_{\parallel}$ had to be increased by approximately three orders of magnitude relative to the reference MAST value to double the filament velocity across a large range of $\hat{\delta}_{\perp}$. It has been estimated that electron temperatures below 1 eV would be required to provide such an enhancement and the plasma in the divertor region would have to be very weakly ionised ($n_n/n_e > 1000$) to produce higher resistivity values still. Furthermore, the region in which the resistivity was enhanced spanned 25% of the parallel domain. It is unlikely that such a cold and weakly ionised plasma could extend so far upstream from the divertor region and thus the conditions described are extreme for experimental fusion devices.

For a theoretical comparison, investigations were next carried out in which $\hat{\eta}_{\parallel}$ was increased uniformly throughout the domain. The results were broadly the same as in the target-localised resistivity case, but some differences did arise. For the same value of $\hat{\Gamma}_{\parallel}$, marginally faster radial velocities were produced in the uniform resistivity case, as the parallel currents were more effectively suppressed. The biggest difference with respect to the target-localised resistivity simulations however was that the filaments' radial velocities exhibited gradients along the

field line, moving faster at the mid-plane than further downstream. This demonstrated that enhanced resistivity can decouple the dynamics of filaments along the parallel direction. Since $\hat{\eta}_{\parallel}$ is directly proportional to the reference plasma density, $n_{e,0}$, these uniformly enhanced resistivity results can be interpreted directly in terms of this quantity and therefore it can be concluded that increasing $n_{e,0}$ leads to faster radial filament velocities. It is noted that the dimensional plasma resistivity is invariant to $n_{e,0}$ and that this trend arises because both the polarisation and diamagnetic currents are directly proportional to the quantity.

Whilst $\hat{\eta}_{\parallel}$ is also proportional to $T_e^{-3/2}$, it is not possible to self consistently interpret the uniformly enhanced normalised resistivity scans in terms of a change of electron temperature. This is because T_e also affects the strength of the diamagnetic currents and the normalisation of lengths. Therefore in the final part of the chapter, a series of simulations were performed in which the electron temperature was varied self consistently and non-monotonic trends were observed. For the majority of the range of T_e considered, increasing T_e led to faster radial velocities, despite the reduced resistivity, because of enhancements to the diamagnetic drive and sheath resistance. The exception to this occurred at the lowest temperature simulated, $T_e = 0.1$ eV, which produced faster radial velocities than both the $T_e = 1$ eV and $T_e = 10$ eV cases for $\delta_{\perp} > 4$ cm. This occurred because the increase in resistivity sufficiently extended the inertial regime (by increasing δ_*) to overcome the aforementioned effects. Although these results generally indicate that faster filament radial velocities are produced at higher temperatures, it is emphasised that if the temperature of a filament were reduced in a region localised to the target (i.e, away from the bulk of the filament's density perturbation and hence diamagnetic drive), the increase in plasma resistivity in this region could dominate over the reduction in the sheath resistance to produce a faster velocity. It is this situation that the target-localised enhanced $\hat{\eta}_{\parallel}$ simulations sought to represent.

A clear limitation of these results is that whilst the low electron temperatures and high neutral densities have been used to justify the increased target-localised resistivity, the model used assumes isothermal electrons and neglects neutral physics. Moreover, the simulations have neglected the influence of enhanced magnetic shear around the X-point region, which could provide alternative current paths for the diamagnetic currents to be closed. Therefore, the inclusion of electron temperature dynamics, neutral physics and magnetic geometry effects to this model would be useful additions for future research, alongside more general improvements such as including hot ion effects and removing the Boussinesq assumption. Nevertheless, this chapter has demonstrated the physical mechanisms by which an enhanced collisionality in the divertor region may produce faster radial filament velocities, and provided an indication of how filamentary dynamics may be influenced by the SOL plasma density and electron temperature.

Chapter 8

Conclusions and Future Work

8.1 Conclusions

One of the biggest challenges to overcome to achieve a commercially viable fusion power-plant is controlling the excessive heat and particle fluxes to the divertor and first wall of the reactor to within sustainable limits. The fluxes to these plasma-facing components are largely determined by the width of the turbulent Scrape-Off Layer (SOL), which in turn is set by the competition between transport perpendicular and parallel to the magnetic field in the region. Experimental measurements suggest that cross-field transport of particles (and to a lesser extent, heat) in the SOL is predominantly due to the motion of coherent field-aligned filamentary structures, whose dynamics are determined by the currents that flow within them. Pressure gradients within these filaments drive diamagnetic currents, which due to the presence of magnetic curvature and gradients have a compressible component, and thus necessitate additional currents in the system to prevent charge accumulation. Amongst others, these can take the form of polarisation currents in the perpendicular plane, or parallel currents that yield a closed circuit via the divertor target or elsewhere along the field line. The former current path leads to the formation of an electrostatic potential with a dipole component in the perpendicular plane, which through $\boldsymbol{E} \times \boldsymbol{B}$ motions, corresponds to the filament moving radially outwards from the core plasma. This work has studied this propagation mechanism using three dimensional simulations of isolated filaments, which are amongst the first of their kind, to further theoretical understanding of SOL transport and thus facilitate future development of predictive models for SOL profiles in power-plant scale devices.

Verification and Validation

To enable this research, a new SOL simulation code called STORM3D has been written using the BOUT++ framework to implement an isothermal drift-reduced fluid model in a slab geometry. As part of the development process, a number of verification exercises have been performed, the most rigorous of which utilised the method of manufactured solutions to ensure that the model has been implemented correctly and that numerical errors converge at second order as desired. In addition, a validation exercise has been carried out to check that the model represents experimental observations. In this, STORM3D simulations of isolated filaments were compared against experimental measurements from the TORPEX device, and also against three other SOL codes which each included different physics. The performance of STORM3D was equal to that of any of the other codes in that it reproduced the experimental

filaments' radial velocities to within a factor of two. However, a non-isothermal code did more effectively capture the vertical motion of the filaments and so clearly the inclusion of electron temperature dynamics is a desirable future development. These verification and validation exercises have provided sufficient confidence in the STORM3D code and model to justify its use in the theoretical studies of filamentary dynamics presented in this thesis.

Effect of Filament Geometry

The first theoretical study investigated the influence of a filament's initial geometry on its subsequent motions using parameters relevant to MAST. In particular, the size of a filament in the perpendicular plane, $\delta_\perp$, was confirmed to have a strong influence. At low values of collisional dissipation, filaments much smaller than a critical size, δ_*, lie in an *inertial regime*, where the compressible diamagnetic currents are predominantly closed by polarisation currents and the filaments develop a mushroom-like structure in the perpendicular plane as they evolve. In contrast, filaments much larger than δ_* lie in a *sheath current limited regime*, in which parallel currents closing through the target become dominant and filaments expel a finger-like structure, rather than moving initially as a whole. The most coherent motion, in which the filament largely retains its initial monopole density structure in the perpendicular plane as it evolves, is exhibited by filaments with intermediate sizes, slightly larger than δ_*, where parallel and polarisation currents are of the same order. In agreement with theoretical expectations, the filament's radial velocity increases like $\sim \delta_\perp^{1/2}$ for $\delta_\perp \ll \delta_*$ but decreases like $\sim \delta_\perp^{-2}$ for $\delta_\perp \gg \delta_*$.

The introduction of parallel density gradients in a filament, such that it does not extend uniformly along magnetic field lines from target to target, was also studied, and was found to produce two key effects. Firstly, the filament's potential field exhibits a Boltzmann response to the parallel density gradients, which causes the filament to spin in the perpendicular plane and also move in the effective poloidal direction. Secondly, the filament's radial velocity is reduced, as the total diamagnetic current drive within the filament is decreased.

In addition, the influence of the initial peak amplitude of the filament was investigated. Whilst for small amplitudes ($\delta n/n_{bg} < 6$), increasing this parameter led to faster radial velocities, at higher amplitudes the perpendicular gradients become severe enough for unstable drift-waves to develop. The subsequent turbulent motions destroyed the filament's coherence and ultimately yielded a slower net velocity than that found at lower amplitudes, where drift-waves were stabilised by viscosity and particle diffusion. Since it is believed that the dissipative parameters used are physically justified, this suggests most filaments in MAST are not significantly fragmented by drift-waves, as observed experimentally.

Although the majority of these filament geometry effects have been identified in previous studies, the simulations in this work utilised a more advanced physical model that included parallel ion dynamics and evolved global fields, rather than evolving a filament perturbation on a fixed background. These results show therefore that these additions make little difference to the perpendicular dynamics of isolated filaments and justify prior approaches for filament studies. Nevertheless, the additions made in the STORM3D model are an important step towards 3D SOL turbulence simulations, where parallel ion dynamics will be required to produce physically realistic SOL profiles.

Comparisons between 3D and 2D Models

Direct comparisons have been made between STORM3D and two dimensional simulations utilising models for the parallel terms that are commonly found in the literature; the sheath dissipation and vorticity advection closures. The vorticity advection closure provided a poor representation of the 3D model's results, in that filaments of all $\delta_\perp$ were observed to develop mushroom structures and attained radial velocities in the early stages of their motion that were too fast. Furthermore, the radial velocity was found to increase monotonically with $\delta_\perp$ for all filaments of a physically relevant size, which is again in contrast to what was found in 3D. The sheath dissipation closure on the other hand compared quite favourably to the 3D model for small amplitude filaments. Specifically, it reproduced the $\delta_\perp$ dependence of the filament's radial velocity and evolved structure. However, since the sheath dissipation closure does not represent drift-wave dynamics (nor does the vorticity advection closure), this comparison was less satisfactory at higher amplitude filaments. In addition, neither 2D closure represented the Boltzmann spinning motions and subsequent displacement in the effective poloidal direction that was observed in 3D.

The poor performance of the vorticity advection closure is due to its assumption that parallel currents are negligible. Indeed, in the aforementioned STORM3D simulations, parallel currents closing through the sheath played an important role in reducing the extent to which polarisation currents were driven, even for filaments which did not extend to the target, as parallel currents could still pass through the background plasma. However, there are a number of mechanisms by which the resistivity of the plasma in an experiment may significantly increase beyond the reference MAST value used in these simulations. In particular, if the SOL is in a conduction limited or detached regime, the divertor region will have low temperatures and high neutral densities, which will enhance the resistivity in the region.

Effect of Plasma Resistivity

The effect of increasing the normalised resistivity in the last quarter of the domain nearest the targets, $\hat{\eta}_{\parallel\mathrm{div}}$, has been studied. Intuitively, it was found that increasing $\hat{\eta}_{\parallel\mathrm{div}}$ led to a suppression of parallel currents and a corresponding enhancement of polarization currents, so that the inertial regime extended to larger values of $\delta_\perp$. Thus faster radial velocities were produced at higher $\hat{\eta}_{\parallel\mathrm{div}}$, as the velocities scaled like $\sim \delta_\perp^{1/2}$ up until larger values of $\delta_\perp$. The dependence of the critical size at which the transition from the inertial regime occurred, δ_*, on the total resistance to parallel currents travelling through the plasma, $\Gamma_\parallel$, was measured to be $\delta_* \propto \Gamma_\parallel^{0.3}$, which is slightly weaker than that predicted theoretically by Reference [184].

Faster radial velocities at higher $\hat{\eta}_{\parallel\mathrm{div}}$ were also found for filaments that were sufficiently large ($\delta_\perp \gg \delta_*$), such that parallel currents remained dominant over the polarisation currents even at high $\hat{\eta}_{\parallel\mathrm{div}}$. For these *resistive sheath current regime* filaments, the increase in velocity occurred because the resistance of the plasma was sufficient to introduce a potential difference between downstream at the sheath entrance and further upstream in the region of the filament density perturbation, so that for the same amount of current to flow into the sheath, larger potentials were formed upstream at higher resistivity, corresponding to faster radial velocities.

For a theoretical comparison, investigations were also carried out in which the normalised resistivity, $\hat{\eta}_\parallel$, was increased uniformly throughout the domain. Whilst broadly similar results were produced as in the target-localised enhanced resistivity study, the filaments' radial velocities did exhibit gradients along the parallel direction at high $\hat{\eta}_\parallel$, meaning that the

filaments moved faster at the mid-plane than further downstream towards the target. This demonstrated that enhanced resistivity can decouple the dynamics of the filaments along the parallel direction.

However, a clear limitation of these resistivity studies is that severe enhancements of $\hat{\eta}_{\parallel}$ were required to yield significant increases in the filament's radial velocity. For example the target-localised $\hat{\eta}_{\parallel}$ was increased by approximately three orders of magnitude relative to the reference MAST value in a region spanning 25% of the parallel domain to produce approximately a factor two increase in the filament velocity across a wide range of $\delta_{\perp}$. It has been estimated that electron temperatures below 1 eV would be required to provide such an enhancement and the plasma in the divertor region would have to be very weakly ionised ($n_n/n_e > 1000$) to produce higher resistivity values still. It is unlikely that such a cold and weakly ionised plasma could extend so far upstream from the divertor region and thus the conditions described are extreme for experimental fusion devices.

Effect of Input Parameters

A final series of simulations studied the influence of the reference plasma density, $n_{e,0}$, electron temperature, T_e, and magnetic field strength, B, on the filament's radial velocity. Since $\hat{\eta}_{\parallel} \propto n_{e,0}$, the uniformly enhanced resistivity simulations can be interpreted directly in terms of $n_{e,0}$ and therefore it can be concluded that increasing this quantity leads to faster radial filament velocities. It is emphasised however that the dimensional plasma resistivity, $\eta_{\parallel}$, is in fact invariant to $n_{e,0}$ and that this trend arises because both the polarisation and diamagnetic currents are directly proportional to the quantity. Similarly, the magnetic field strength does not affect the dimensional resistivity of the plasma, but δ_* does increase as B reduces. Therefore faster radial velocities were also found at lower B, as the inertial regime was again extended to larger $\delta_{\perp}$.

The influence of T_e is more complicated than that of the other two input parameters investigated, in that non-monotonic trends were observed. Generally, increasing T_e led to faster radial velocities, because this enhanced both the diamagnetic currents and the resistance of the sheath. However, at very low temperatures ($T_e < 1$ eV) reducing the temperature produced faster radial velocities for $\delta_{\perp} > 3$ cm. This occurred because $\hat{\eta}_{\parallel} \propto T_e^{-3/2}$ and the enhancement in resistivity sufficiently extended the inertial regime (by increasing δ_*) to overcome the aforementioned effects. Although these results generally indicate that faster filament radial velocities are produced at higher temperatures, it is emphasised that if the temperature of a filament were reduced in a region localised to the target (i.e, away from the bulk of the filament's density perturbation and hence diamagnetic drive), the increase in plasma resistivity in this region could dominate over the reduction in the sheath resistance to produce a faster velocity. It is this situation that the target-localised enhanced $\hat{\eta}_{\parallel}$ simulations sought to represent.

Contribution to the Fusion Research Program

This research outlined in this thesis has made a number of important contributions to the overall fusion research program. A powerful and versatile 3D SOL simulation code has been developed, which will allow future studies into SOL physics to be carried out relatively easily and with minimal further development. This code has been used to provide a comprehensive characterisation of 3D filamentary dynamics, which will aid future understanding of how SOL

profiles are determined. In particular, it has been suggested in the literature that electrical disconnection of filaments from the target is a possible mechanism by which broader SOL profiles are produced at high values of SOL collisionality [80]. Whilst such a disconnection has been demonstrated, it is unlikely that the extreme conditions required to produce this phenomenon are found in experiments. Lastly, the effect of key input parameters on filaments' radial velocities has been established, which will aid comparison of experimental measurements between different machines and allows for extrapolation to future devices such as ITER.

8.2 Future Work

There are a number of limitations of the work presented in this thesis. Firstly, cold ions have been assumed and the Boussinesq assumption has been employed, despite both of these simplifications being poorly justified in the SOL. Furthermore, low electron temperatures and high neutral densities in the divertor have been used as justification for using enhanced resistivity values near to the target, but the physical model assumes isothermal electron temperatures and neglects neutral physics entirely. Moreover, magnetic geometry effects are entirely absent in the current version of STORM3D, which is significant because enhanced polarisation currents due to the magnetic shear around the X-point region could allow parallel currents to form a closed circuit there, rather than at the target. Finally, electromagnetic effects have also been neglected.

Whilst this list of simplifications is quite long, it is emphasised that these neglected effects are not expected to significantly change the dynamics of filaments and hence invalidate the results presented in this thesis. For example, it was shown in the TORPEX comparison exercise that whilst a filament's poloidal displacement is affected if electron temperature dynamics are included, its radial velocity was changed by less than a factor of two. A similar order of magnitude change in the radial velocity has been found when the Boussinesq approximation was removed in recent 2D filament simulations [256].

Nevertheless, each of these limitations does provide an opportunity to expand and improve the physical model of STORM3D. With the exception of the cold ion assumption, it should be relatively easy to address each issue due to the flexibility of the BOUT++ framework. Indeed, electron temperature dynamics have already been included in the latest version of STORM3D and studies have been carried out to illustrate how this addition affects filamentary dynamics [131, 199]. With respect to utilising more complicated magnetic geometries, it may be enlightening to first simulate filaments using a sheared slab, before employing a realistic tokamak magnetic geometry, as this will allow the influence of magnetic shear to be isolated from other effects that would also be included in a realistic geometry, such as a varying curvature strength.

Aside from improvements to the model, a valuable contribution to the understanding of SOL transport could be made by using the STORM3D code to simulate multiple filaments at once, to investigate how a filament's dynamics can be affected by nearby filaments. In particular it would allow an assessment of how separated filaments have to be from one another for isolated filament simulations to be justified. Following this, simulations of saturated SOL turbulence should be carried out. Such turbulence can be generated by introducing a radial gradient in background density and temperature profiles, which could in turn be achieved through the structure of the particle and energy sources. Whilst such turbulence simulations would be significantly more computationally expensive than seeded filament simulations, they

should be considered the ultimate application of a SOL code such as STORM3D, as they would allow average SOL profiles to be calculated.

Appendices

Appendix A

Equilibrium Solution

This Appendix provides a derivation of the equilibrium solution to the evolution equations of the model, Equations (3.66) to (3.69), which are reproduced below for convenience.

$$\frac{\partial \Omega}{\partial t} = -\left(\hat{\boldsymbol{b}} \times \nabla\phi\right) \cdot \nabla\Omega - U\nabla_{\parallel}\Omega + \frac{1}{n}\nabla_{\parallel}J_{\parallel} - \frac{\hat{g}}{n}\frac{\partial n}{\partial y} + D_{\Omega}\nabla_{\perp}^{2}\Omega, \tag{A.1}$$

$$\frac{\partial n}{\partial t} = -\left(\hat{\boldsymbol{b}} \times \nabla\phi\right) \cdot \nabla n - \nabla_{\parallel}\left(nV\right) + n\hat{g}\frac{\partial \phi}{\partial y} - \hat{g}\frac{\partial n}{\partial y} + D_{n}\nabla_{\perp}^{2}n + S_{n}, \tag{A.2}$$

$$\frac{dV}{dt} = -\left(\hat{\boldsymbol{b}} \times \nabla\phi\right) \cdot \nabla V - V\nabla_{\parallel}V + \mu\left(\nabla_{\parallel}\phi - \frac{1}{n}\nabla_{\parallel}n + \hat{\eta}_{\parallel}J_{\parallel}\right) - \frac{S_{n}V}{n}, \tag{A.3}$$

$$\frac{\partial U}{\partial t} = -\left(\hat{\boldsymbol{b}} \times \nabla\phi\right) \cdot \nabla U - U\nabla_{\parallel}U - \nabla_{\parallel}\phi - \frac{\hat{\eta}_{\parallel}}{\mu}J_{\parallel} - \frac{S_{n}U}{n}. \tag{A.4}$$

The case for which $S_n = S_n(z)$ is considered, which means that all fields must be uniform in the perpendicular direction. Accompanying this condition with the assumption of steady state equilibrium fields reduce Equations (A.1) to (A.4) to

$$0 = \frac{1}{n}\nabla_{\parallel}J_{\parallel}, \tag{A.5}$$

$$0 = -\nabla_{\parallel}\left(nV\right) + S_{n}, \tag{A.6}$$

$$0 = -V\nabla_{\parallel}V + \mu\left(\nabla_{\parallel}\phi - \frac{1}{n}\nabla_{\parallel}n + \hat{\eta}_{\parallel}J_{\parallel}\right) - \frac{S_{n}V}{n}, \tag{A.7}$$

$$0 = -U\nabla_{\parallel}U - \nabla_{\parallel}\phi - \frac{\nu_{\parallel}}{\mu}J_{\parallel} - \frac{S_{n}U}{n}. \tag{A.8}$$

A solution to Equations (A.5) to (A.8) is sought on the simulation domain, that is $0 \geq y \geq L_{\parallel}$, which satisfies the stagnation point boundary conditions at $y = 0$:

$$U|_{z=0} = 0, \tag{A.9a}$$

$$V|_{z=0} = 0. \tag{A.9b}$$

The boundary conditions at $z = L_{\parallel}$ are examined in detail later in this derivation. By integrating Equation (A.5) along the parallel direction and imposing Equation (A.9), the result $J_{\parallel} = 0$ is obtained. Assuming a non-zero density throughout the domain, this necessitates

$$U = V. \tag{A.10}$$

Combining Equations (A.7) and (A.8) to remove the $\nabla_{\parallel}\phi$ terms yields

$$\left(1 + \frac{1}{\mu}\right)\left(n\nabla_{\parallel}U + S_{n}U\right) = -\nabla_{\parallel}n. \tag{A.11}$$

Another expression for $\nabla_\parallel n$ is obtained by rewriting Equation (A.6):

$$\nabla_\parallel n = \frac{S_n - n\nabla_\parallel U}{U}. \tag{A.12}$$

Moreover, integrating Equation (A.6) along the parallel direction allows n to be expressed as:

$$n = \frac{S_n'}{U}, \tag{A.13}$$

where

$$S_n' = \int_0^z S_n\left(z'\right) \mathrm{d}z'. \tag{A.14}$$

Equations (A.12) and (A.13) can thus be used to write Equation (A.11) in terms of only S_n and U:

$$\left(1 + \frac{1}{\mu}\right)\left(S_n'\nabla_\parallel U + S_n U\right) + \frac{S_n}{U} - \frac{S_n'\nabla_\parallel U}{U^2} = 0. \tag{A.15}$$

By noting that

$$\nabla_\parallel\left(S_n' U\right) = S_n'\nabla_\parallel U + S_n U$$

and that

$$\nabla_\parallel\left(\frac{S_n'}{U}\right) = \frac{S_n}{U} - \frac{S_n'\nabla_\parallel U}{U^2},$$

Equation (A.15) can be written as

$$\nabla_\parallel\left[\left(\left(1 + \frac{1}{\mu}\right)U + \frac{1}{U}\right)S_n'\right] = 0. \tag{A.16}$$

Equation (A.16) can then be easily integrated to produce

$$\left(\left(1 + \frac{1}{\mu}\right)U + \frac{1}{U}\right)S_n' = C \tag{A.17}$$

where C is a constant that can be determined by application of boundary conditions. However, the boundary condition given by Equation (A.9) cannot be used to determine C, since both U and S_n' are zero at the boundary, and the quantity S_n'/U cannot be evaluated. Therefore the boundary condition on U at the entrance to the sheath, $z = L_\parallel$, must be used instead. Letting this boundary condition be given by

$$U\big|_{z=L_\parallel} = U_s, \tag{A.18}$$

and applying this condition to Equation (A.17) yields

$$\left(\left(1 + \frac{1}{\mu}\right)U + \frac{1}{U}\right) = \alpha\left(\left(1 + \frac{1}{\mu}\right)U_s + \frac{1}{U_s}\right) \tag{A.19}$$

where

$$\alpha = \frac{\displaystyle\int_0^{L_\parallel} S_n\left(z'\right)\mathrm{d}z'}{\displaystyle\int_0^z S_n\left(z'\right)\mathrm{d}z'}. \tag{A.20}$$

Solving Equation (A.19) for U gives

$$U = \frac{\alpha\left(\left(1 + \frac{1}{\mu}\right)U_s + \frac{1}{U_s}\right) \pm \sqrt{\alpha^2\left(\left(1 + \frac{1}{\mu}\right)U_s + \frac{1}{U_s}\right)^2 - 4\left(1 + \frac{1}{\mu}\right)}}{2\left(1 + \frac{1}{\mu}\right)}. \tag{A.21}$$

This solution has two branches, corresponding to whether the positive or negative square root is selected. The appropriate branch can be selected by ensuring it is consistent with the boundary conditions. Given that $\alpha \to \infty$ as $z \to 0$, taking the same limit of Equation (A.21) produces

$$\lim_{z\to 0} U = \lim_{\alpha\to\infty} \frac{\alpha\left(\left(1+\frac{1}{\mu}\right)U_s + \frac{1}{U_s}\right) \pm \sqrt{\alpha^2\left(\left(1+\frac{1}{\mu}\right)U_s + \frac{1}{U_s}\right)^2 - 4\left(1+\frac{1}{\mu}\right)}}{2\left(1+\frac{1}{\mu}\right)}$$

$$\lim_{z\to 0} U = \lim_{\alpha\to\infty} \frac{\alpha\left(\left(1+\frac{1}{\mu}\right)U_s + \frac{1}{U_s}\right)(1\pm 1)}{2\left(1+\frac{1}{\mu}\right)}. \tag{A.22}$$

Therefore, as only the negative root is consistent with the stagnation point boundary condition on U at $z = 0$ given by Equation (A.9a), the final solution for U is given by:

$$U = \frac{\alpha\left(\left(1+\frac{1}{\mu}\right)U_s + \frac{1}{U_s}\right) - \sqrt{\alpha^2\left(\left(1+\frac{1}{\mu}\right)U_s + \frac{1}{U_s}\right)^2 - 4\left(1+\frac{1}{\mu}\right)}}{2\left(1+\frac{1}{\mu}\right)}. \tag{A.23}$$

By checking that this solution also satisfies the boundary condition at the sheath boundary given by Equation (A.18), an important condition on range the values that U_s can take is found. At this location ($z = L_\parallel$), $\alpha = 1$ and so Equation (A.23) reduces to

$$U|_{z=L_\parallel} = \frac{\left(\left(1+\frac{1}{\mu}\right)U_s + \frac{1}{U_s}\right) - \sqrt{\left(1+\frac{1}{\mu}\right)^2 {U_s}^2 - 2\left(1+\frac{1}{\mu}\right) + \frac{1}{{U_s}^2}}}{2\left(1+\frac{1}{\mu}\right)}. \tag{A.24}$$

In simplifying the square root in Equation (A.24), it is important to ensure that the square root term remains positive to be consistent with the earlier selection of the negative branch of the solution. In isolation, the square root can be simplified to

$$\sqrt{\left(1+\frac{1}{\mu}\right)^2 {U_s}^2 - 2\left(1+\frac{1}{\mu}\right) + \frac{1}{{U_s}^2}} = \pm\left(\left(1+\frac{1}{\mu}\right)U_s - \frac{1}{U_s}\right). \tag{A.25}$$

Whether the positive or negative root of Equation (A.25) actually corresponds to a positive quantity is dependent on the value of U_s. It is trivial to show that the solution to

$$\left(1+\frac{1}{\mu}\right)U_s - \frac{1}{U_s} = 0$$

is

$$U_s = \pm\frac{1}{\sqrt{1+1/\mu}},$$

and considering only positive values of U_s (as negative values would correspond to an inflow, rather than an outflow, of plasma at the sheath edge), that

$$\left(1+\frac{1}{\mu}\right)U_s - \frac{1}{U_s} \le 0 \quad \text{for} \quad 0 < U_s \le \frac{1}{\sqrt{1+1/\mu}},$$
$$\left(1+\frac{1}{\mu}\right)U_s - \frac{1}{U_s} \ge 0 \quad \text{for} \quad U_s \ge \frac{1}{\sqrt{1+1/\mu}}.$$

Considering first the case $U_s \geq 1/\sqrt{1+1/\mu}$, Equation (A.24) can be simplified as follows.

$$U|_{z=L_\parallel} = \frac{\left(\left(1+\frac{1}{\mu}\right)U_s + \frac{1}{U_s}\right) - \left(\left(1+\frac{1}{\mu}\right)U_s - \frac{1}{U_s}\right)}{2\left(1+\frac{1}{\mu}\right)}$$

$$U|_{z=L_\parallel} = \frac{1}{U_s\left(1+1/\mu\right)}$$

This means that for the case $U_s \geq 1/\sqrt{1+1/\mu}$, the solution can only satisfy the boundary condition imposed at the sheath only if in fact

$$U_s = \frac{1}{\sqrt{1+1/\mu}}. \tag{A.27}$$

Therefore the solution cannot satisfy the boundary conditions imposed at the sheath if $U_s > 1/\sqrt{1+1/\mu}$. For the case $U_s \leq 1/\sqrt{1+1/\mu}$ on the other hand, Equation (A.24) reduces to be consistent with the sheath boundary condition, as demonstrated below.

$$U|_{z=L_\parallel} = \frac{\left(\left(1+\frac{1}{\mu}\right)U_s + \frac{1}{U_s}\right) - \left(\frac{1}{U_s} - \left(1+\frac{1}{\mu}\right)U_s\right)}{2\left(1+\frac{1}{\mu}\right)},$$

$$U|_{z=L_\parallel} = U_s.$$

This analysis shows that a solution only exists for $U_s \leq 1/\sqrt{1+1/\mu}$. Moreover, whilst this derivation has specified U_s to be the value of U at the entrance to the sheath, the result can be generalised to show $U \leq 1/\sqrt{1+1/\mu}$ anywhere in the domain, by replacing $L_\parallel$ with z in Equation (A.18) and the subsequent workings. Alternatively this more general result can be obtained by rearranging Equation (A.15) as

$$\nabla_\parallel U = \frac{S_n}{n}\left(\frac{1+\left(1+1/\mu\right)U^2}{1-\left(1+1/\mu\right)U^2}\right). \tag{A.28}$$

Since when $U = 1/\sqrt{1+1/\mu}$ the denominator of the fraction inside the bracket equals zero, this expression states that $\nabla_\parallel U \to \infty$ as $U \to 1/\sqrt{1+1/\mu}$ and therefore that assuming $S_n \geq 0$, physical solutions cannot occur if $U > 1/\sqrt{1+1/\mu}$.

Recalling that U is the parallel ion velocity normalised to the sound speed of the plasma neglecting electron inertia, $c_s = \sqrt{T_e/m_i}$, this condition therefore states that

$$u_{\parallel i} \leq \sqrt{\frac{T_e}{m_i + m_e}} \tag{A.29}$$

in a steady state system that is uniform in the perpendicular direction if $S_n \geq 0$. The quantity $\sqrt{T_e/\left(m_i+m_e\right)}$ is the sound speed of the plasma, corrected to account for the inertia of the electrons. This specific condition is incompatible with the standard sheath boundary condition that states that $U_s \geq 1$ or equivalently that $u_\parallel \geq c_s$ [31, 158]. This discrepancy arises because the aspects of the derivation of this Bohm boundary condition neglect the influence of electron inertia in the sheath, whilst the governing equations of the plasma model retain the effect. Whilst no exact relation has been derived, it has been demonstrated that inclusion of electron inertia will act to reduce the minimum speed that the ions must have at the entrance to the sheath from c_s [220]. Therefore the STORM module utilises the adjusted boundary condition

$$U|_{z=L_\parallel} \geq 1/\sqrt{1+1/\mu}. \tag{A.30}$$

The $\geq$ relation is retained here to allow for possibility of supersonic flows in systems in which any of the conditions on Equation (A.29) are relaxed (i.e. non steady state, variation in perpendicular direction, $S_n < 0$) [221]. To be consistent with this change from the standard definition, the corresponding boundary condition on V is also altered to be

$$V|_{z=L_\parallel} = \frac{1}{\sqrt{1+1/\mu}} \exp\left(-\phi|_{z=L_\parallel}\right). \tag{A.31}$$

In practical terms, this assumed correction to the boundary conditions makes little difference to the results of the code except at very high resolutions, because the effective error introduced by not using the electron inertia corrected boundary conditions is negligible compared to the discretisation errors present. Moreover, the code has been tested to ensure it does robustly produce effectively the same results with the standard boundary conditions.

Using these boundary conditions, Equation (A.23) simplifies to

$$U = \frac{\alpha - \sqrt{\alpha^2 - 1}}{\sqrt{1+1/\mu}}. \tag{A.32}$$

Substituting Equation (A.32) into Equation (A.13), gives an expression for n in terms of only S_n:

$$n = \frac{S_n' \sqrt{1+1/\mu}}{\alpha - \sqrt{\alpha^2 - 1}}. \tag{A.33}$$

All that remains to complete the solution is to obtain an expression for ϕ. Subtracting Equation (A.3) from (A.4) and recalling that $U = V$, yields

$$\nabla_\parallel \phi = \frac{\mu}{1+\mu} \nabla_\parallel \ln n.$$

Integrating this expression along the parallel direction and determining the constant of integration using the values of n and ϕ at the sheath entrance ($z = L_\parallel$) produces

$$\phi = \frac{\mu}{1+\mu} \ln\left(\frac{n}{n|_{z=L_\parallel}}\right) + \phi|_{z=L_\parallel} \tag{A.34}$$

Given that $U = V$ in this equilibrium solution, $\phi|_{z=L_\parallel}$ can be determined from Equations (A.30) and (A.31) to be zero. From Equation (A.33), the value of n at the sheath entrance is

$$n|_{z=L_\parallel} = \sqrt{1+\frac{1}{\mu}} \int_0^{L_\parallel} S_n\left(z'\right) \mathrm{d}z'. \tag{A.35}$$

Therefore, Equation (A.34) becomes

$$\phi = -\frac{\mu}{1+\mu} \ln\left(\alpha^2 - \alpha\sqrt{\alpha^2 - 1}\right). \tag{A.36}$$

In summary, the analytical equilibrium solution is given by

$$\Omega_{eq} = 0, \tag{A.37}$$

$$n_{eq} = \frac{\sqrt{1+\frac{1}{\mu}} \int_0^z S_n\left(z'\right) \mathrm{d}z'}{\alpha - \sqrt{\alpha^2 - 1}}, \tag{A.38}$$

$$U_{eq} = V_{eq} = \frac{\alpha - \sqrt{\alpha^2 - 1}}{\sqrt{1+1/\mu}}, \tag{A.39}$$

$$\phi_{eq} = -\frac{\mu}{1+\mu} \ln\left(\alpha^2 - \alpha\sqrt{\alpha^2 - 1.}\right), \tag{A.40}$$

where the subscript *eq* denotes the equilibrium of the quantity and

$$\alpha = \frac{\int_0^{L_\parallel} S_n\left(z'\right) \mathrm{d}z'}{\int_0^{z} S_n\left(z'\right) \mathrm{d}z'}. \tag{A.41}$$

Appendix B

Shock Tube Problem

In this appendix analytical solutions for well studied problems in fluid dynamics will be derived for the Storm3D plasma fluid model, following the derivations given for a neutral fluid in Reference [242]. In particular, solutions are derived for expansion waves and shock waves produced by moving a piston in the end of a long tube. These solutions are then combined to provide a solution to the shock tube problem, which is commonly used for testing and verification of neutral fluid dynamics codes.

B.1 Method of Characteristics

By assuming variation only in the parallel direction, the perpendicular terms in Equations (3.66) to (3.69) can be dropped to produce

$$\frac{1}{n}\nabla_{\parallel} J_{\parallel} = 0, \tag{B.1}$$

$$\frac{\partial n}{\partial t} + \nabla_{\parallel}\left(nV\right) = S_n, \tag{B.2}$$

$$\frac{dV}{dt} + V\nabla_{\parallel} V - \mu\left(\nabla_{\parallel}\phi - \frac{1}{n}\nabla_{\parallel} n + \hat{\eta}_{\parallel} J_{\parallel}\right) + \frac{S_n V}{n} = 0, \tag{B.3}$$

$$\frac{\partial U}{\partial t} + U\nabla_{\parallel} U + \nabla_{\parallel}\phi + \hat{\eta}_{\parallel} J_{\parallel} + \frac{S_n U}{n} = 0. \tag{B.4}$$

As in the analytical equilibrium solution derived in Section A, integrating Equation (B.1) along the parallel direction and imposing the stagnation point boundary conditions given by Equation (A.9) gives $J_{\parallel} = 0$. Again assuming non-zero densities throughout, this necessitates $U = V$. This allows Equations (B.3) and (B.4) to be combined to eliminate the $\nabla_{\parallel}\phi$ terms as follows

$$\frac{\partial U}{\partial t} + U\nabla_{\parallel} U + \frac{1}{\left(1 + 1/\mu\right) n}\nabla_{\parallel} n + \frac{S_n U}{n} = 0. \tag{B.5}$$

B.1.1 Characteristic Form

The system of equations comprising of Equations (B.2) and (B.5) can be written using the Einstein summation convention as

$$\frac{\partial u_i}{\partial t} + \alpha_{ij}\frac{\partial u_j}{\partial z} + \beta_i = 0, \tag{B.6}$$

where

$$\boldsymbol{u} = \begin{pmatrix} n \\ U \end{pmatrix}, \quad \boldsymbol{\alpha} = \begin{pmatrix} U & n \\ 1/\left(n + n/\mu\right) & U \end{pmatrix}, \quad \boldsymbol{\beta} = \begin{pmatrix} -S_n \\ S_n U/n \end{pmatrix}. \tag{B.7}$$

It is desirable find a linear combination of Equations (B.2) and (B.5), of the form written below,

$$l_i \frac{\partial u_i}{\partial t} + l_i \alpha_{ij} \frac{\partial u_j}{\partial z} + l_i \beta_i = 0, \tag{B.8}$$

such that the combination takes the *characteristic form*

$$l_i \frac{du_i}{dt} + l_i \beta_i = 0. \tag{B.9}$$

Here the total derivative is given by

$$\frac{d}{dt} = \frac{\partial}{\partial t} + c \frac{\partial}{\partial z}. \tag{B.10}$$

where $c = dz/dt$. This is achieved provided that

$$l_i \alpha_{ij} \frac{\partial u_j}{\partial z} = l_i c \frac{\partial u_i}{\partial z}. \tag{B.11}$$

Writing the right hand side of this equation as $l_j c \partial u_j / \partial z$, we have the refined requirement that

$$l_i \alpha_{ij} = l_j c. \tag{B.12}$$

This is an eigenvalue problem and in order for there to be a non trivial solution (i.e. $\boldsymbol{l} \neq 0$), c must satisfy

$$|\boldsymbol{\alpha} - c\boldsymbol{I}| = 0, \tag{B.13}$$

where $\boldsymbol{I}$ is the identity matrix. The eigenvalues are therefore given by

$$c_\pm = U \pm a \tag{B.14}$$

where $a = 1/\sqrt{1 + 1/\mu}$ is the speed of sound in this system of normalised equations. The corresponding eigenvectors are

$$\boldsymbol{l}_\pm = \begin{pmatrix} a \\ \pm n \end{pmatrix}, \quad \text{for } c_\pm = U \pm a. \tag{B.15}$$

The resulting characteristic equations are thus given by

$$a \frac{dn}{dt} \pm n \frac{dU}{dt} - S_n (a \pm U) = 0 \quad \text{on } c_\pm = \frac{dz}{dt} = U \pm a. \tag{B.16}$$

B.1.2 Riemann Variables and Invariants

Next, it is required to write the characteristic equations in the further simplified form

$$\frac{dr_\pm}{dt} + f_\pm (x, t, \boldsymbol{u}) = 0 \tag{B.17}$$

Equation (B.16) can be written in the form above when

$$\lambda a \frac{dn}{dt} \pm \lambda n \frac{dU}{dt} = \frac{dr_\pm}{dt} \tag{B.18}$$

An integration factor λ has been included here to aid the subsequent derivation. Writing, $r_\pm = P_\pm (n) + Q_\pm (U)$, the preceding equation becomes

$$\lambda a \frac{dn}{dt} \pm \lambda n \frac{dU}{dt} = \frac{dP_\pm}{dn} \frac{dn}{dt} + \frac{dQ_\pm}{dU} \frac{dU}{dt}, \tag{B.19}$$

which implies that

$$\frac{dP_\pm}{dn} = \lambda a \tag{B.20}$$

$$\frac{dQ_\pm}{dU} = \pm\lambda n \tag{B.21}$$

Letting $\lambda = 1/n$, Equations (B.20) and (B.21) can be integrated (neglecting constants of integration) to give $P_\pm = a \ln n$ and $Q_\pm = \pm U$, so that

$$r_\pm = a \ln n \pm U. \tag{B.22}$$

Equation (B.16) can thus be written as

$$\frac{dr_\pm}{dt} - \frac{S_n}{n}(a \pm U) = 0 \quad \text{on } c_\pm = \frac{dz}{dt} = U \pm a, \tag{B.23}$$

which is the form of Equation (B.17), with $f_\pm = -S_n (a \pm U)/n$. The quantities r_+ and r_- are in general known as *Riemann variables*. Equation (B.23) can then be integrated along characteristic lines which satisfy c_+ and c_-. The original system of partial differential equations, Equations (B.2) and (B.5), has been reduced to two independent ordinary differential equations, that can be integrated easily along their corresponding characteristic lines c. In the specific case that $S_n = 0$, the integration becomes trivial as the Riemann variables remain constant on their respective characteristic lines. Thus the Riemann variables can be described as Riemann invariants for $S_n = 0$.

B.2 Expansion Wave Produced by a Piston

Consider the case of the expansion wave produced in a plasma by a piston moving at the end of a long tube. The influence of plasma-surface interactions, such as the formation of the sheath, are neglected so that Bohm boundary conditions are not included; in effect the plasma is modelled as a neutral gas. In addition, $S_n = 0$ is assumed. At $t = 0$, the piston is located at $z = 0$, and the plasma is at rest and uniform, with $n = n_0$ and $U = 0$ for $z \leq 0$. For $t > 0$, the piston moves with a constant velocity of v_P, with boundary condition on U at the piston face is that the plasma moves at the velocity of the piston, $U = v_P$.

This situation is represented schematically on a $z - t$ diagram in Figure B.1. An example line from the family of lines C_+, which satisfy $= dz/dt = U + a$, is plotted using a dashed line. Assuming that $U \geq 0$ everywhere in the plasma, it can be deduced that every member of this family will intercept the z axis in the uniform region, $z < 0$. Since $S_n = 0$, the quantity $a \ln n + U$ is a Riemann invariant along each C_+ line and so is equal to a constant. This constant can be assessed from the boundary conditions at the z axis, $U = 0, n = n_0$. Therefore the relation

$$a \ln n + U = a \ln n_0 \tag{B.24}$$

holds throughout the entire domain. Also shown in the diagram is the family of lines C_-, which each satisfy $dz/dt = U - a$. These lines have been split into three sub-families. Those which intercept the z axis are labelled C_-^z and are drawn in red, those which intercept the piston are labelled as C_-^P and are drawn in blue, whilst those which intercept the origin are labelled C_-^F and are drawn in green. Along each C_- line, the Riemann invariant $U - a \ln n$ remains constant. For the C_-^z family this constant can again be determined using the z axis boundary conditions so that the relation

$$a \ln n - U = a \ln n_0 \tag{B.25}$$

holds. Combining this with (B.24) yields $U = 0$ and $n = n_0$ along each C_-^z line. The characteristic line which marks the boundary of the C_-^z region is therefore given by $z = -at$, as this intersects the origin. Considering next the C_-^P family, the relationship

$$a \ln n - U = D \tag{B.26}$$

exists, where D is some undetermined constant. By subtracting Equation (B.26) from (B.24) U, and therefore n can be determined to remain constant along each C_+^P line. Using the piston boundary condition and Equation (B.24), $U = v_P$ and $n = n_0 \exp(-v_P/a)$ inside the C_-^P region. The boundary of this region is given by $z = (v_P - a)\, t$. All that remains is to determine the solution in the region containing the C_-^F family of lines, $-at < z < (v_P - a)\, t$. This C_-^F family consists of a centred fan of characteristics meeting at the origin, given by the expression

$$z = (U - a)\, t, \qquad 0 < U < v_P. \tag{B.27}$$

Each member of the fan corresponds to taking a different value of U between 0 and v_P at the origin. Since the condition that U and n remain constant along C_+ lines also holds here, the solution for U in this region can be obtained by rearranging Equation (B.27) to give

$$U = a + \frac{z}{t}. \tag{B.28}$$

Then using Equation (B.24), the solution to n in this region is

$$n = n_0 \exp\left(-\frac{z}{at} - 1\right) \tag{B.29}$$

The full solution is thus

$$U = \begin{cases} 0 & \dfrac{z}{at} \le -1 \\ a + \dfrac{z}{t} & -1 \le \dfrac{z}{at} \le \dfrac{v_P}{a} - 1 \\ v_P & \dfrac{v_P}{a} - 1 \le \dfrac{z}{at} \le \dfrac{v_P}{a} \end{cases} \tag{B.30a}$$

$$n = \begin{cases} n_0 & \dfrac{z}{at} \le -1 \\ n_0 \exp\left(-\dfrac{z}{at} - 1\right) & -1 \le \dfrac{z}{at} \le \dfrac{v_P}{a} - 1 \\ n_0 \exp\left(-\dfrac{v_P}{a}\right) & \dfrac{v_P}{a} - 1 \le \dfrac{z}{at} \le \dfrac{v_P}{a} \end{cases} \tag{B.30b}$$

The fan region can be understood to be an expansion fan, in which the density decreases from n_0 to $n_0 \exp(-v_P/a)$.

B.3 Shock Wave Relations

Equation (B.31) is a prototypic conservation equation written in integral form

$$\frac{\partial}{\partial t} \int_{x_2}^{x_1} \rho \, dx + [q]_{x_2}^{x_1} + \int_{x_2}^{x_1} h \, dx = 0. \tag{B.31}$$

Here $\rho(x,t)$ is the density of some quantity, $q(x,t)$ is the flux per unit time of the quantity, and $h(x,t)$ is a source (or sink) of the quantity. Assuming h remains continuous, a discontinuity or shock can be sustained in ρ and q if the relationship

$$q_1 - q_2 = v_{shock}\,(\rho_2 - \rho_1) \tag{B.32}$$

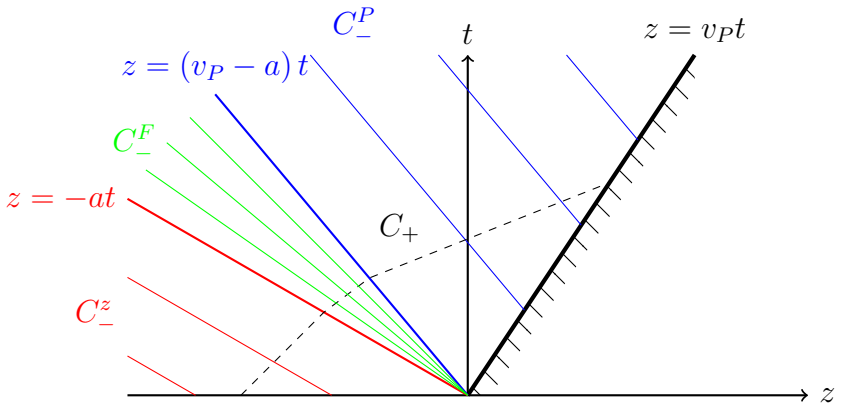

Figure B.1: Schematic diagram of different families of characteristic lines satisfying Equation (B.14) for a 1D expansion wave produced by a moving piston.

is satisfied [242]. Here the subscripts 1 and 2 denote the values of the quantities just ahead and behind of the shock itself. Equations (B.2) and (B.5) in the form of Equation (B.31) are

$$\frac{\partial}{\partial t}\int_{z_2}^{z_1} n\, dz + [nU]_{z_2}^{z_1} + \int_{z_2}^{z_1} S_n\, dz = 0, \tag{B.33}$$

$$\frac{\partial}{\partial t}\int_{z_2}^{z_1} nU\, dz + \left[nU^2 + a^2 n\right]_{z_2}^{z_1} = 0. \tag{B.34}$$

Therefore the following shock relations apply:

$$n_1 U_1 - n_2 U_2 = v_{shock}\,(n_2 - n_1)\,, \tag{B.35}$$

$$n_1 U_1^2 + n_1 - n_2 U_2^2 - n_2 = v_{shock}\,(n_2 U_2 - n_1 U_1)\,. \tag{B.36}$$

Letting $\mathcal{V} = v_{shock} - U$, these relations become

$$n_2 \mathcal{V}_2 = n_1 \mathcal{V}_1, \tag{B.37}$$

$$a^2 n_2 + n_2 \mathcal{V}_2^2 = a^2 n_1 + n_1 \mathcal{V}_1^2. \tag{B.38}$$

Defining $M = \mathcal{V}_1/a$ to be the Mach number of the shock relative to the flow ahead, and after some manipulation of Equations (B.37) and (B.38), the following relations can be obtained which are more convenient to use

$$\frac{U_2 - U_1}{a} = \frac{M^2 - 1}{M}, \tag{B.39}$$

$$\frac{n_2}{n_1} = M^2 \tag{B.40}$$

$$\frac{U_2 - U_1}{a} = \sqrt{\frac{n_2}{n_1}} - \sqrt{\frac{n_1}{n_2}}. \tag{B.41}$$

B.4 Shock Wave Produced by a Piston

Consider again the plasma flow produced by a piston moving at the end of a long tube. This time the plasma is located in the region $z > 0$ at $t = 0$, and it again begins uniform and at rest; $n = n_0$, $U = 0$. The piston, located at $x = 0$ at $t = 0$ is again suddenly moved at constant velocity v_P, so that this time, the plasma is compressed, rather than expanded. Again, the boundary condition on U at the piston is $U = v_P$. This situation is schematically drawn on a $z - t$ diagram in Figure B.2. It is assumed that this situation leads to a shock, travelling at

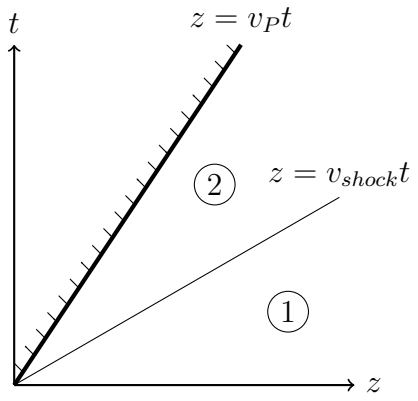

Figure B.2: Schematic diagram of the distinct regions in (z, t) space that exist for a 1D planar shock wave produced by a piston moving at constant velocity.

velocity v_{shock} in the plasma. Ahead of the shock is labelled region 1, and behind the shock is labelled region 2.

It is important to note that whilst the Riemann invariants given by Equation (B.22) do remain constant on their appropriate characteristic lines within each region, they will each exhibit a discontinuity across the shock. This means that a complete solution cannot be obtained using only equivalent arguments regarding families of characteristic lines that were used for the expansion wave case. These arguments however can be used to determine that U and n remain constant in each region. From the boundary conditions along the z axis, it is determined that $n_1 = n_0$ and that $U_1 = 0$, whilst the piston boundary condition yields $U_2 = v_P$. The shock relations given by Equations (B.40) and (B.41) then can be reduced to

$$v_{shock} = a\sqrt{\frac{n_2}{n_1}} \tag{B.42}$$

and

$$\frac{v_P}{a} = \sqrt{\frac{n_2}{n_1}} - \sqrt{\frac{n_1}{n_2}}. \tag{B.43}$$

After some manipulation of Equations (B.42) and (B.43), the following explicit expressions for v_{shock} and n_2 as a function of the known variables v_P and n_1 can be obtained:

$$v_{shock} = \frac{v_P + \sqrt{v_P^2 + 4a^2}}{2}, \tag{B.44}$$

$$n_2 = n_1 \frac{v_P^2 + 2a^2 + v_p\sqrt{v_P^2 + 4a^2}}{2}. \tag{B.45}$$

In obtaining these relations, the positive square root was selected when solving the quadratic that arises by enforcing that the shock moves in the positive z direction, $v_{shock} > 0$. The overall solution is therefore

$$U = \begin{cases} v_P & \dfrac{v_P}{a} \leq \dfrac{z}{at} \leq \sqrt{\dfrac{n_2}{n_1}} \\ 0 & \sqrt{\dfrac{n_2}{n_1}} \leq \dfrac{z}{at} \end{cases} \tag{B.46a}$$

$$n = \begin{cases} n_2 & \dfrac{v_P}{a} \leq \dfrac{z}{at} \leq \sqrt{\dfrac{n_2}{n_1}} \\ n_1 & \sqrt{\dfrac{n_2}{n_1}} \leq \dfrac{z}{at} \end{cases} \tag{B.46b}$$

where n_2 is given by Equation (B.45).

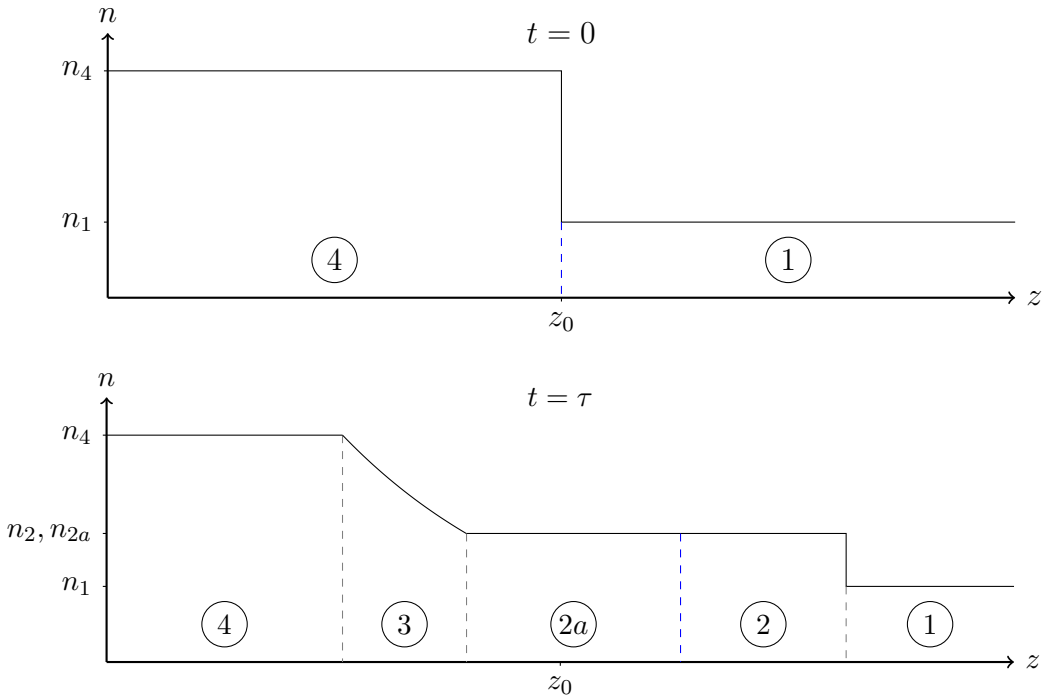

Figure B.3: Schematic diagrams of the density profile of the analytical solution to the shock tube problem, with distinct regions labelled. Top: The initial density profile, showing two distinct regions. Bottom: The density profile at a later time $t = \tau$.

B.5 Shock Tube Problem Solution

Next, the shock tube problem is examined. A shock tube is long tube in which there is a thin diaphragm separating two gases which are uniform and at rest. One of the gases is pumped up to a higher pressure, and then the diaphragm is burst. This produces both a shock wave and an expansion wave moving in opposite directions down the tube. Assuming that the viscous effects of the side walls are negligible, an analytical solution can be obtained relatively easily and therefore this problem is commonly used for verification of fluid dynamics codes. From a SOL plasma perspective, this situation can be considered to be equivalent to the parallel propagation of an idealised filament perturbation (consisting of a top hat function in the parallel direction) that suddenly appears on top of a uniform SOL background, in the absence of perpendicular dynamics.

The top plot of Figure B.3 schematically shows the shock tube set up at $t = 0$, just as the diaphragm is burst. The interface between two uniform plasma regions is located at $z = z_0$, where the diaphragm was present. This interface is plotted using a dashed blue line. To the left of the interface is region 4, where the density level is $n = n_4$, whilst to the right is region 1, where the density level is $n = n_1$. In both regions the plasma is at rest.

The state of the plasma at a later time, $t = \tau$, is shown in the bottom plot of the same figure. The interface between the two plasmas, has moved in the positive z direction, producing a shock moving into the low density side, and an expansion wave moving into the high density side. The values of U on either side of the interface must be the same as the velocity of the interface itself, and so the interface is like a solid wall as far as the flow on either side is concerned. The interface can therefore be treated as an effective piston moving at a constant velocity v_p, which is to be determined. The shock tube can thus be considered to be a combination of the piston expansion wave and shock wave problems considered previously.

On the expansion wave side, the solution is given by Equation (B.30) with $n_0 = n_4$, and thus there are 3 distinct regions. Firstly, next to the interface is a new uniform region, labelled region $2a$, which has velocity $U = v_P$ and density $n = n_{2a}$, where

$$n_{2a} = n_4 \exp\left(-\frac{v_P}{a}\right). \tag{B.47}$$

Next, there is an expansion wave region, called region 3 in which the density rises from n_{2a} to n_4. Finally, Region 4 contains the undisturbed plasma with density $n = n_4$.

On the shock wave side, the solution is given by Equation (B.46). Two uniform regions are produced, between which a shock wave exists moving at a velocity v_{shock} given by Equation (B.44). Immediately to the right of the interface is region 2, which has density $n = n_2$, where n_2 is given by Equation (B.45) and velocity $U = v_p$, whilst to right of the shock is region 1 containing the undisturbed plasma with $n = n_1$.

In order to completely solve this problem, the values of n_{2a}, n_2 and v_P must be determined. First, since the interface itself has no mass, it cannot sustain a net force, and so the pressure on either side must be equal. In this isothermal plasma model therefore the density on each side must be equal, $n_{2a} = n_2$ (It is noted in a non-isothermal model, discontinuities will exist in the density and the temperature fields at the interface). To obtain the exact value of n_2, Equation (B.47) can be rearranged to isolate the quantity v_P/a. This can then be combined with Equation (B.43) to give

$$\ln n_4 - \ln n_2 = \sqrt{\frac{n_2}{n_1}} - \sqrt{\frac{n_1}{n_2}}. \tag{B.48}$$

This is an implicit expression for n_2 in terms of the known values n_1 and n_4, which can be solved numerically to give n_2. The value of v_P, whilst relatively unimportant, can then be determined from Equation (B.43). Thus by combining Equations (B.30) and (B.46) appropriately, the overall shock tube solution in terms of the values n_1, n_2 and n_4, which are all now known is

$$U = \begin{cases} 0 & \dfrac{z-z_0}{at} \le -1 \\ a + \dfrac{z-z_0}{t} & -1 \le \dfrac{z-z_0}{at} \le \sqrt{\dfrac{n_2}{n_1}} - \sqrt{\dfrac{n_1}{n_2}} - 1 \\ a\sqrt{\dfrac{n_2}{n_1}} - a\sqrt{\dfrac{n_1}{n_2}} & \sqrt{\dfrac{n_2}{n_1}} - \sqrt{\dfrac{n_1}{n_2}} - 1 \le \dfrac{z-z_0}{at} \le \sqrt{\dfrac{n_2}{n_1}} \\ 0 & \sqrt{\dfrac{n_2}{n_1}} \le \dfrac{z-z_0}{at} \end{cases}, \tag{B.49a}$$

$$n = \begin{cases} n_4 & \dfrac{z-z_0}{at} \le -1 \\ n_4 \exp\left(-\dfrac{z-z_0}{at} - 1\right) & -1 \le \dfrac{z-z_0}{at} \le \sqrt{\dfrac{n_2}{n_1}} - \sqrt{\dfrac{n_1}{n_2}} - 1 \\ n_2 & \sqrt{\dfrac{n_2}{n_1}} - \sqrt{\dfrac{n_1}{n_2}} - 1 \le \dfrac{z-z_0}{at} \le \sqrt{\dfrac{n_2}{n_1}} \\ n_1 & \sqrt{\dfrac{n_2}{n_1}} \le \dfrac{z-z_0}{at} \end{cases}. \tag{B.49b}$$

Appendix C

MMS in BOUT++

This appendix provides a brief description of how to use the MMS testing features that have been implemented in BOUT++.

C.1 Activating MMS Testing Mode

In order to enable MMS testing to be carried out as routinely as possible and to minimise the possibility of introducing additional errors through an incorrect implementation of the method itself, BOUT++ has a MMS testing mode which automates as much of the method as possible. This mode can be activated through the BOUT.inp input file by setting the 'mms' flag in the solver settings:

```
[solver]
...
mms = true
```

When MMS testing is activated, BOUT++ initialises each evolving variable to its manufactured solution at $t = 0$, and modifies the time derivatives before they are passed to the time integration code by adding the additional source terms. Moreover, at every output time step, the difference between the evolved fields and the manufactured solution is calculated at each output time step and saved to file. In order to do all this, the source and manufactured solution for each variable must be specified in the BOUT.inp file under a section with the name of the variable, as in the example below for the variable n.

```
[n]
solution = ...
source   = ...
```

It is very easy to make a mistake either in the calculation of the source terms or in inputting the expressions into the input file. Therefore it is recommended to use a symbolic package such as Mathematica or Sympy to produce the expressions which can then be copied and pasted directly into the input file. A library has been written for the Sympy to translate the expressions for the PDES used within the physics module so that they can used directly with the package and can be found at BOUT-dev/tools/pylib/boutdata/mms. Example python scripts utilising this library can be found alongside the MMS examples in BOUT-dev/examples/MMS.

C.2 Specifying Boundary Conditions

Manufactured solutions can (and, to test all aspects of the code, should) vary in space and time at the boundaries and the boundary conditions must reflect this. The boundary conditions in BOUT++ have therefore been developed to allow for the value (Dirichlet) or gradient (Neumann) of a field at a boundary to be set to that of an analytical function of time and space. The choice of boundary condition and the analytical function must again be specified in the BOUT.inp file under a section with the name of the variable. For example, the following code sets a variety of Dirichlet and Neumann boundary conditions on x and y boundaries respectively of the variable `n` :

```
[n]
solution = ...
source   = ...
ddx = ...
ddy = ...

bndry_xin   = dirichlet_o4(n:solution)
bndry_xout  = neumann_o2(n:ddx)
bndry_yup   = dirichlet_o3(n:solution)
bndry_ydown = neumann_o2(n:ddy)
```

The suffix `_o2` denotes the order accuracy the boundary condition is implemented to. So for example, `dirichlet_o3` is a Dirichlet boundary condition implemented to third order accuracy in space. Confusingly `neumann_o2` actually has an an $\mathcal{O}(h^3)$ error. Implementations are available up to fourth order (`_o4`).

There also exist implementations of 'free' boundary conditions; `free_o2`, `free_o3` and `free_o4`, which aim to impose no constraint on the solution at the boundary by extrapolation into the boundary points. No additional arguments are necessary when specifying these boundary conditions in the input file.

C.3 Convergence of Boundary Conditions

Where the boundary points are used by the gradient operators, they are divided through by h or h^2 for first and second derivatives respectively. This means that it is necessary to set the boundary condition to a higher order than what is desired for the global convergence of the code. For example, if global $\mathcal{O}(h^2)$ convergence is desired, and only first derivatives are used, then $\mathcal{O}(h^3)$ boundary conditions are necessary. It has been observed that when second derivatives are used, then third order remains sufficient to achieve global $\mathcal{O}(h^2)$ convergence. This has been attributed to the fact that second order derivatives are dissipative in nature, and therefore any errors that develop at the boundary as a result of the boundary conditions will be damped away. This is fortunate, as fourth order boundary conditions have been observed to produce numerical instabilities and so it is advised not to use them. It is emphasised here that `neumann_o2` confusingly has a $\mathcal{O}(h^3)$ error and so can be used to obtain global $\mathcal{O}(h^2)$ convergence.

Instabilities have also been encountered using the `dirichlet_o3` boundary condition on un-staggered grids under some specific circumstances. If such instabilities are encountered, `dirichlet_o2` must be used at the expense of global convergence. Such instabilities were not encountered using the Storm3D physics module.

Nomenclature

A peak density amplitude of initialised filament with respect to the background/equilibrium plasma

A_{probe} projected area of a Langmuir probe

$\boldsymbol{B}$ magnetic field

B_0 magnetic field strength at R_0

B_θ poloidal magnetic field strength

D particle diffusivity (see Equation (3.50))

D_{Bohm} Bohm diffusion coefficient ($\rho_s^2\Omega_i$)

D_Ω normalised ion kinematic viscosity ($\nu_i/\rho_s^2\Omega_i$)

D_{eff} effective diffusion coefficient

D_n normalised particle diffusivity ($D/\rho_s^2\Omega_i$)

$\boldsymbol{E}$ electric field

$\boldsymbol{E}_{\text{pol}}$ poloidal electric field

$\boldsymbol{F}_{ei}$ effective frictional force between electrons and ions (see Equation (3.17))

I_s Langmuir probe ion saturation current

I_{sat} Langmuir probe ion saturation current

$\breve{I}_{\text{sat}}$ median value of I_{sat}

$\boldsymbol{J}_{\text{dia}}$ normalised diamagnetic current density ($\boldsymbol{j}_{\text{dia}}/(n_{e,0}ec_s)$)

$\boldsymbol{J}_{\text{pol}}$ normalised polarisation current density ($\boldsymbol{j}_{\text{pol}}/(n_{e,0}ec_s)$)

$\boldsymbol{J}_{\text{visc}}$ normalised viscous current density ($\boldsymbol{j}_{\text{visc}}/(n_{e,0}ec_s)$)

$J_\parallel$ normalised parallel current density ($j_\parallel/(n_{e,0}ec_s)$)

K kurtosis (see Equation (2.3))

L_f normalised approximate parallel length that filaments extend from the mid-plane towards the targets (ℓ_f/ρ_s, see Equation (4.28))

L_x normalised length of domain in x direction

L_y normalised length of domain in y direction

$L_\parallel$ normalised mid-plane to sheath parallel connection length ($\ell_\parallel/\rho_s$)

N_x number of grid points in the x direction

N_y number of grid points in the y direction

N_z number of grid points in the z direction

P convergence order of a numerical method

P_{fusion} fusion power produced by the plasma

P_{heating} external heating power put into the plasma

Q fusion energy gain factor ($P_{\text{fusion}}/P_{\text{heating}}$)

R major radius

R_0 reference major radius location

$\mathcal{R}$ reaction rate per unit volume (see Equation (1.1))

S skewness (see Equation (2.2))

S_n normalised particle source ($s_n/(n_{e,0}\Omega_i)$)

T_e electron temperature

$T_{e,bg}$ background electron temperature

$T_{e,f}$ filament electron temperature profile

T_e^{div} electron temperature of the divertor region

T_i ion temperature

U normalised parallel ion velocity ($v_{\parallel i}/c_s$)

U^M Manufactured solution for U for use in the method of manufactured solutions

U_{eq} normalised parallel ion velocity

V normalised parallel electron velocity ($v_{\parallel e}/c_s$)

V^M Manufactured solution for V for use in the method of manufactured solutions

V_{eq} normalised parallel electron velocity

$\bar{X}$ mean value of the variable X

Z vertical coordinate in a toroidal coordinate system

Z_i ion charge state

$\hat{\boldsymbol{b}}$ $\boldsymbol{B}/B$

c_s cold ion sound speed ($\sqrt{T_e/m_e}$)

e elementary charge

g magnetic curvature strength ($2c_s/R_0$)

$\hat{g}$ normalised magnetic curvature strength ($2\rho_s/R_0$)

h mesh spacing

$\boldsymbol{j}$ current density

$\boldsymbol{j}_{\text{dia}}$ diamagnetic current density ($-en_e\boldsymbol{v}_D$)

$\boldsymbol{j}_{\text{pol}}$ polarisation current density ($en_e\boldsymbol{v}_{Pi}$)

$j_{\text{sat},f}$ ion saturation current density associated with a filament (see Equations (5.35) and (5.41))

$\boldsymbol{j}_{\text{visc}}$ viscous current density ($en_e\boldsymbol{v}_{\pi i}$)

$j_{\parallel}$ parallel current density ($en_e(v_{\parallel i} - v_{\parallel e})$)

$j_{\parallel s}$ parallel current density at the entrance to the sheath

$\boldsymbol{k}$ perpendicular wave number ((k_x, k_y))

k_x wave number in the x direction

k_x wave number in the x direction

$\ln\Lambda$ Coulomb logarithm

$l_{\parallel}$ characteristic parallel length scale of a plasma

$l_{\perp}$ characteristic perpendicular length scale of a plasma

ℓ_f approximate parallel length that filaments extend from the mid-plane towards the targets (see Equation (4.28))

$\ell_{\parallel}$ parallel SOL connection length (typically mid-plane to target)

m_e electron mass

m_i ion mass

n normalised electron number density ($n_e/n_{e,0}$)

n^M Manufactured solution for n for use in the method of manufactured solutions

n_{bg} normalised background electron number density

n_e electron number density

$n_{e,bg}$ background electron number density

$n_{e,eq}$ equilibrium electron number density

$n_{e,f}$ filament number density ($n_e - n_{e,eq}$)

$n_{e,s}$ electron number density at the entrance to the sheath

$n_{e,0}$ reference SOL electron number density

n_{eq} normalised equilibrium number density ($n_{e,eq}/n_{e,0}$)

n_f normalised filament number density ($n - n_{eq}$)

n_i ion number density

$\hat{n}_k$ Fourier mode of n corresponding to the perpendicular wave number $\boldsymbol{k}$

n_n neutral particle number density

n_s normalised electron number density at the entrance to the sheath

p plasma pressure ($n_i T_i + n_e T_e$)

p_e electron pressure ($n_i T_i$)

p_i ion pressure ($n_i T_i$)

q safety factor (rB_Φ/RB_θ)

q_{95} value of q at the flux surface that contains 95% of the toroidal magnetic flux

q_s charge of a particle species s

r minor radius

s_n particle source

t time

$\boldsymbol{v}$ particle velocity

v particle collision velocity

$\hat{v}$ radial filament velocity normalised to v_* (v_r/v_*)

v_* estimate of the radial filament velocity of a filament with $\delta_\perp = \delta_{*0}$ in the low collisionality limit, $\Gamma_{\text{sheath}} \gg \Gamma_\parallel$ (see Equation (2.24))

$\boldsymbol{v}_D$ electron diamagnetic fluid velocity (see Equation (3.26))

$\boldsymbol{v}_E$ $\boldsymbol{E} \times \boldsymbol{B}$ fluid velocity (see Equation (3.25))

$\boldsymbol{v}_F$ perpendicular fluid velocity owing to collisions between electrons and ions (see Equation (3.31))

$\boldsymbol{v}_{Pe}$ electron polarisation fluid velocity (see Equation (3.27))

$\boldsymbol{v}_{Pi}$ ion polarisation fluid velocity (see Equation (3.28))

$\boldsymbol{v}_{Se}$ perpendicular electron fluid velocity owing to particle sources/sinks (see Equation (3.32))

$\boldsymbol{v}_{Si}$ perpendicular electron fluid velocity owing to particle sources/sinks (see Equation (3.33))

$\boldsymbol{v}_e$ electron fluid velocity

$\hat{\boldsymbol{v}}_f$ filament velocity ($d\boldsymbol{x}_f/dt$)

$\hat{v}_{f,x}$ radial filament velocity (See Equation (6.6))

$\hat{v}_{f,x}^{\text{drift-plane}}$ drift-plane radial filament velocity (see Equation (7.13))

$\hat{v}_{f,x}^{\star}$ characteristic radial filament velocity, defined as the first maximum of $\hat{v}_{f,x}$ that occurs in time

$\hat{v}_{f,y}$ binormal filament velocity (See Equation (6.7))

$\boldsymbol{v}_i$ ion fluid velocity

$\boldsymbol{v}_{\pi e}$ perpendicular electron fluid velocity owing to viscous forces (see Equation (3.29))

$\boldsymbol{v}_{\pi i}$ perpendicular ion fluid velocity owing to viscous forces (see Equation (3.30))

$\boldsymbol{v}_r$ radial filament velocity vector

v_r radial filament velocity, equivalent to $v_{f,x}$

$\boldsymbol{v}_s$ velocity of a particle species s

$v_{th,e}$ ion thermal velocity ($\sqrt{T_i/m_i}$)

$v_{th,i}$ ion thermal velocity ($\sqrt{T_i/m_i}$)

v_x filament velocity in the x direction, as defined for the TORPEX validation exercise in Section 5.5 (dx_c/dt)

v_y filament velocity in the y direction, as defined for the TORPEX validation exercise in Section 5.5 (dx_c/dt)

$v_{\parallel e}$ parallel electron velocity

$v_{\parallel i}$ parallel ion velocity

$\boldsymbol{v}_{\perp e}$ perpendicular electron fluid velocity

$\boldsymbol{v}_{\perp i}$ perpendicular ion fluid velocity

$\boldsymbol{x}$ (x, y, z)

x effective radial coordinate

x_0 initial position of filament in x

x_c filament position in x, as defined for the TORPEX validation exercise in Section 5.5 (see Equation (5.39))

$\boldsymbol{x}_f$ filament position ((x_f, y_f, z_f))

x_f filament position in x

$\boldsymbol{x}_f^{\text{CoM}}$ filament position defined as the centre of mass of n_f (see Equation (6.1))

$\boldsymbol{x}_f^{\text{CoM},\gamma}$ filament position defined as the centre of mass of n_f above a threshold γ (see Equation (6.2))

$\boldsymbol{x}_f^{\max}$ filament position defined as the location at which the maximum value of n_f occurs ($\arg\max(n_f)$)

y bi-normal coordinate

y_0 initial position of filament in y

y_c filament position in y, as defined for the TORPEX validation exercise in Section 5.5 (see Equation (5.40))

y_f filament position in y

z coordinate parallel to the magnetic field

z_f filament position in z

Γ_{sheath} effective resistivity length of the path through the sheath to the target ($T_e/e^2 n_{e,s} c_s$)

$\hat{\Gamma}_{\text{sheath}}$ normalised effective resistivity length of the path through the sheath to the target ($1/n_s$)

$\Gamma_{\parallel}$ resistivity-length of the path that parallel currents take from the filament to the sheath entrance (see Equation (7.2))

$\hat{\Gamma}_{\parallel}$ normalised resistivity-length of the path that parallel currents take from the filament to the sheath entrance (see Equation (7.6))

Γ_{pol} resistivity length of the polarisation current path

Ω normalised vorticity (ω/Ω_i)

Ω^M Manufactured solution for Ω for use in the method of manufactured solutions

Ω_e electron gyro-frequency (eB/m_e)

Ω_{eq} normalised equilibrium vorticity

Ω_i ion gyro-frequency (eB/m_i)

$\hat{\Omega}_{k_y}$ Fourier mode of ϕ corresponding to the wave number k_y

Φ azimuthal coordinate in a toroidal coordinate system

β plasma beta ($8\pi T_e/B^2$)

$\hat{\delta}$ perpendicular filament size normalised to δ_{*0} ($\delta_\perp/\delta_*$)

δ_e $\rho_e/l_\perp$

δ_i $\rho_i/l_\perp$

δ_* $\delta_\perp$ at which filaments transition from the inertial regime to either the sheath current or resistive sheath current regime

δ_{*0} estimated value of $\delta_\perp$ at which filaments transition from the inertial regime to the sheath current regime ($(g\ell_\parallel^2/2\rho_s c_s^2)^{1/5}$)

$\hat{\delta}_{*0}$ estimated value of $\hat{\delta}_\perp$ at which filaments transition from the inertial regime to the sheath current regime ($(gL_\parallel^2/2)^{1/5}$)

$\hat{\delta}_\dagger$ estimated value of $\hat{\delta}_\perp$ at which filaments transition from the viscous regime to the inertial regime ($(2D_\Omega^2/\hat{g})^{1/3}$)

$\hat{\delta}_\triangle$ estimated value of $\hat{\delta}_\perp$ at which filaments transition from the viscous regime to the sheath current regime ($(D_\Omega/L_\parallel)^{1/4}$)

$\delta_\parallel$ parallel length scale of filament front in the parallel direction (see Equation (4.28))

$\hat{\delta}_\parallel$ normalised parallel length scale of filament front in the parallel direction ($\delta_\parallel/\rho_s$, see Equation (4.28))

$\delta_\perp$ perpendicular size of a filament

$\hat{\delta}_\perp$ normalised perpendicular size of a filament ($\delta_\perp/\rho_s$)

ε_0 permittivity of free space

ϵ simulation error

ϵ_{max} maximum simulation error (see Equation (5.7))

ϵ_{rms} root means square simulation error (see Equation (5.6))

$\eta_\parallel$ parallel plasma resistivity ($1/\sigma_\parallel$)

$\hat{\eta}_\parallel$ normalised parallel plasma resistivity ($en_{e,0}\eta_\parallel/B$)

$\hat{\eta}_\parallel^{ei}$ normalised parallel plasma resistivity due to electron-ion collisions (see Equations (7.11) and (7.12))

$\hat{\eta}_\parallel^{en}$ normalised parallel plasma resistivity due to electron-neutral collisions (see Equations (7.11) and (7.12))

$\eta_{\parallel 0}$ reference case parallel plasma resistivity used in Chapter 7

$\hat{\eta}_{\parallel 0}$ normalised reference case parallel plasma resistivity used in Chapter 7 ($en_{e,0}\eta_{\parallel 0}/B$)

$\eta_{\parallel \mathrm{div}}$ parallel plasma resistivity in the last 25% of the domain nearest to the target

$\hat{\eta}_{\parallel \mathrm{div}}$ normalised parallel plasma resistivity in the last 25% of the domain nearest to the target ($en_{e,0}\eta_{\parallel \mathrm{div}}/B$)

$\boldsymbol{\kappa}$ magnetic curvature ($(\hat{\boldsymbol{b}}\cdot\nabla)\hat{\boldsymbol{b}}$)

λ_e electron mean free path ($v_{th,e}/\nu_{ei}$)

λ_i ion mean free path ($v_{th,i}/\nu_{ii}$)

λ_n SOL density width

λ_q SOL heat flux width

μ mass ratio (m_i/m_e)

μ_0 magnetic permeability in a classical vacuum

ν^* SOL collisionality ($\ell_\parallel/\lambda_e$)

ν_{ei} electron-ion collision frequency (see Equation (3.10))

ν_{en} electron-neutral collision frequency ($n_n \langle\sigma v\rangle$)

ν_i ion cross-field kinematic viscosity (see Equation (3.51))

ν_{ii} ion-ion collision frequency (see Equation (3.11))

$\nu_\parallel$ normalised electron-ion collisionality ($0.51\nu_{ei}/\Omega_i$)

ω vorticity ($\nabla_\perp^2\varphi/B$)

ω_c characteristic inverse time-scale of a plasma

ϕ normalised electrostatic potential ($e\varphi/T_e$)

ϕ^M Manufactured solution for ϕ for use in the method of manufactured solutions

ϕ_{eq} normalised equilibrium electrostatic potential

ϕ_f normalised filament potential profile ($\phi - \phi_{eq}$)

ϕ_f^{even} component of ϕ_f which has even parity in the y direction with respect to the centre of the filament (see Equation (6.8))

ϕ_f^{odd} component of ϕ_f which has odd parity in the y direction with respect to the centre of the filament (see Equation (6.9))

$\hat{\phi}_k$ Fourier mode of ϕ corresponding to the perpendicular wave number $\boldsymbol{k}$

$\hat{\phi}_{k_y}$ Fourier mode of ϕ corresponding to the wave number k_y

ϕ_w normalised electrostatic potential of the wall of a limiter or divertor ($e\varphi_w/T_e$)

φ electrostatic potential

φ_{fl} floating electrostatic potential

$\varphi_{fl,f}$ filament floating electrostatic potential

φ_s electrostatic potential of the entrance to the sheath

φ_w electrostatic potential of the wall of a limiter or divertor

$\boldsymbol{\pi}_e$ electron viscous stress tensor

$\boldsymbol{\pi}_i$ ion viscous stress tensor

ρ_e electron Larmor radius ($v_{th,e}/\Omega_e$)

ρ_i ion Larmor radius ($v_{th,i}/\Omega_i$)

ρ_s combined species Larmor radius (c_s/Ω_i)

σ collision cross-section

σ_X standard deviation of the variable X

$\sigma_{\parallel}$ parallel plasma conductivity (see Equation (3.18))

$\sigma_{\perp}$ perpendicular plasma conductivity ($0.51\sigma_{\parallel}$)

τ_E energy confinement time

Bibliography

[1] U.S. Energy Information Administration. *International Energy Outlook 2016*. Tech. rep. DOE/EIA-0484(2016). 2016. URL: http://www.eia.gov/forecasts/ieo/.

[2] British Petroleum. *BP Energy Outlook - 2016 edition*. Tech. rep. 2016. URL: http://www.bp.com/en/global/corporate/energy-economics/energy-outlook-2035/energy-outlook-downloads.html.

[3] World Health Organization. *Ambient (outdoor) air quality and health*. 2014. URL: http://www.who.int/mediacentre/factsheets/fs313/en/ (visited on 11/07/2016).

[4] World Health Organization. *Household air pollution and health*. 2014. URL: http://www.who.int/mediacentre/factsheets/fs292/en/ (visited on 11/07/2016).

[5] J. Cook, N. Oreskes, P. T. Doran et al. 'Consensus on consensus: a synthesis of consensus estimates on human-caused global warming'. *Environmental Research Letters* **11**.4 (2016), p. 048002. DOI: 10.1088/1748-9326/11/4/048002.

[6] British Petroleum. *BP Statistical Review of World Energy June 2015*. Tech. rep. 2015. URL: http://www.bp.com/content/dam/bp/pdf/energy-economics/statistical-review-2015/bp-statistical-review-of-world-energy-2015-full-report.pdf.

[7] International Energy Agency. *Resources to Reserves 2013*. 2013. ISBN: 978-92-64-08354-7. URL: http://www.iea.org/publications/freepublications/publication/resources-to-reserves-2013.html.

[8] International Energy Agency. *World Energy Outlook 2013*. 2013. ISBN: 9789264201309. URL: http://www.iea.org/publications/freepublications/publication/world-energy-outlook-2013.html.

[9] H. Chen, T. N. Cong, W. Yang et al. 'Progress in electrical energy storage system: A critical review'. *Progress in Natural Science* **19**.3 (2009), pp. 291–312. DOI: 10.1016/j.pnsc.2008.07.014.

[10] International Energy Agency. *Key World Energy Statistics 2015*. Tech. rep. 2015. URL: http://www.iea.org/publications/freepublications/publication/key-world-energy-statistics-2015.html.

[11] D. J. C. MacKay. *Sustainable Energy — without the hot air*. Cambridge: UIT, 2009. ISBN: 0954452933. URL: https://www.withouthotair.com/download.html.

[12] J. D. Huba. *NRL Plasma Formulary*. Naval Research Laboratory. Washington, DC, 2011. URL: http://www.nrl.navy.mil/ppd/sites/www.nrl.navy.mil.ppd/files/pdfs/NRL_FORMULARY_16.pdf.

[13] W. J. Garland, ed. *The Essential CANDU*. University Network of Excellence in Nuclear Engineering (UNENE), 2014. ISBN: 0-9730040. URL: http://www.nuceng.ca/candu/.

[14] J. Ongena and G. Van Oost. *Energy for Future Centuries – Will Fusion be an Inexhaustible, Safe and Clean Energy Source?* Tech. rep. EFDA–JET–RE(00)01. 2001. URL: http://www.euro-fusionscipub.org/wp-content/uploads/2014/11/EFDR00001.pdf.

[15] R. Clausius. 'XVI. On a mechanical theorem applicable to heat'. *The London, Edinburgh, and Dublin Philosophical Magazine and Journal of Science* **40**.265 (1870), pp. 122–127. DOI: 10.1080/14786447008640370.

[16] L. E. J. Brouwer. 'Über Abbildung von Mannigfaltigkeiten'. German. *Mathematische Annalen* **71**.1 (1911), pp. 97–115. DOI: 10.1007/BF01456931.

[17] M. Wakatani. *Stellarator and Heliotron Devices*. International series of monographs on physics. Oxford University Press, 1998. ISBN: 9780195078312.

[18] J. Wesson. *Tokamaks*. Oxford University Press, 2011. ISBN: 0199592233.

[19] M. Yoshikawa. 'The JT-60 project and its present status'. *Nuclear Fusion* **25**.9 (1985), pp. 1081–1085. DOI: 10.1088/0029-5515/25/9/014.

[20] K. Tobita and JT-60 Team. 'Latest plasma performance and experiments on JT-60U'. *Plasma Physics and Controlled Fusion* **41**.3A (1999), A333–A343. DOI: 10.1088/0741-3335/41/3A/027.

[21] J. Wesson. *The Science of JET*. JET Reports, 2000. URL: http://www.euro-fusionscipub.org/wp-content/uploads/2014/11/JETR99013.pdf.

[22] M. Keilhacker, A. Gibson, C. Gormezano et al. 'High fusion performance from deuterium-tritium plasmas in JET'. *Nuclear Fusion* **39**.2 (1999), pp. 209–234. DOI: 10.1088/0029-5515/39/2/306.

[23] ITER Physics Basis Editors, ITER Physics Expert Group Chairs and Co-Chairs and ITER Joint Central Team and Physics Integration Unit. 'ITER Physics Basis - Chapter 1: Overview and Summary'. *Nuclear Fusion* **39**.12 (1999), pp. 2137–2638. DOI: 10.1088/0029-5515/39/12/301.

[24] M. Shimada, D. J. Campbell, M. Fujiwara et al. 'Chapter 1: Overview and summary'. *Nuclear Fusion* **47**.6 (2007), S1–S17. DOI: 10.1088/0029-5515/47/6/S01.

[25] ITER. *Frequently Asked Questions*. URL: http://www.iter.org/faq (visited on 11/07/2016).

[26] ITER. *What Will ITER do?* URL: http://www.iter.org/sci/Goals (visited on 11/07/2016).

[27] EFDA. *Fusion Electricity: A roadmap to the realisation of fusion energy*. Tech. rep. JG12.356. 2012. URL: https://www.euro-fusion.org/wpcms/wp-content/uploads/2013/01/JG12.356-web.pdf.

[28] F. Wagner. 'A quarter-century of H-mode studies'. *Plasma Physics and Controlled Fusion* **49**.12B (2007), B1–B33. DOI: 10.1088/0741-3335/49/12B/S01.

[29] F. Wagner, G. Fussmann, T. Grave et al. 'Development of an Edge Transport Barrier at the H-Mode Transition of ASDEX'. *Physical Review Letters* **53**.15 (1984), pp. 1453–1456. DOI: 10.1103/PhysRevLett.53.1453.

[30] M. Keilhacker. 'H-mode confinement in tokamaks'. *Plasma Physics and Controlled Fusion* **29**.10A (1987), pp. 1401–1413. DOI: 10.1088/0741-3335/29/10A/320.

[31] P. C. Stangeby. *The Plasma Boundary of Magnetic Fusion Devices*. CRC Press, 2000. ISBN: 9780750305594.

[32] W. Fundamenski. *Power Exhaust in Fusion Plasmas*. Cambridge University Press, 2010. ISBN: 0521851718.

[33] G. F Matthews. 'Plasma detachment from divertor targets and limiters'. *Journal of Nuclear Materials* **220-222** (1995), pp. 104–116. DOI: 10.1016/0022-3115(94)00450-1.

[34] T. Eich, A. W. Leonard, R. A. Pitts et al. 'Scaling of the tokamak near the scrape-off layer H-mode power width and implications for ITER'. *Nuclear Fusion* **53**.9 (2013), pp. 093031–8. DOI: 10.1088/0029-5515/53/9/093031.

[35] J. A. Goetz, B. LaBombard and B. L. Lipschultz. 'High confinement dissipative divertor operation on Alcator C-Mod'. *Physics of Plasmas* **6**.5 (1999), p. 1899. DOI: 10.1063/1.873447.

[36] A. Loarte, B. L. Lipschultz, A. S. Kukushkin et al. 'Chapter 4: Power and particle control'. *Nuclear Fusion* **47**.6 (2007), S203–S263. DOI: 10.1088/0029-5515/47/6/S04.

[37] J. Roth, E. Tsitrone, T. Loarer et al. 'Tritium inventory in ITER plasma-facing materials and tritium removal procedures'. *Plasma Physics and Controlled Fusion* **50**.10 (2008), p. 103001. DOI: 10.1088/0741-3335/50/10/103001.

[38] M. V. Umansky, S. I. Krasheninnikov, B. LaBombard et al. 'Comments on particle and energy balance in the edge plasma of Alcator C-Mod'. *Physics of Plasmas* **5**.9 (1998), pp. 3373–5. DOI: 10.1063/1.873051.

[39] B. LaBombard, M. V. Umansky, R. L. Boivin et al. 'Cross-field plasma transport and main-chamber recycling in diverted plasmas on Alcator C-Mod'. *Nuclear Fusion* **40**.12 (2000), pp. 2041–2060. DOI: 10.1088/0029-5515/40/12/308.

[40] J. A. Boedo, D. L. Rudakov, R. A. Moyer et al. 'Transport by intermittency in the boundary of the DIII-D tokamak'. *Physics of Plasmas* **10**.5 (2003), p. 1670. DOI: 10.1063/1.1563259.

[41] B. LaBombard, R. L. Boivin, M. Greenwald et al. 'Particle transport in the scrape-off layer and its relationship to discharge density limit in Alcator C-Mod'. *Physics of Plasmas* **8**.5 (2001), pp. 2107–12. DOI: 10.1063/1.1352596.

[42] S. J. Zweben, J. A. Boedo, O. Grulke et al. 'Edge turbulence measurements in toroidal fusion devices'. *Plasma Physics and Controlled Fusion* **49**.7 (2007), S1–S23. DOI: 10.1088/0741-3335/49/7/S01.

[43] G. Y. Antar, S. I. Krasheninnikov, P. Devynck et al. 'Experimental Evidence of Intermittent Convection in the Edge of Magnetic Confinement Devices'. *Physical Review Letters* **87**.6 (2001), p. 065001. DOI: 10.1103/PhysRevLett.87.065001.

[44] G. Y. Antar, G. F. Counsell, Y. Yu et al. 'Universality of intermittent convective transport in the scrape-off layer of magnetically confined devices'. *Physics of Plasmas* **10**.2 (2003), p. 419. DOI: 10.1063/1.1536166.

[45] D. A. D'Ippolito, J. R. Myra and S. J. Zweben. 'Convective transport by intermittent blob-filaments: Comparison of theory and experiment'. *Physics of Plasmas* **18**.6 (2011), p. 060501. DOI: 10.1063/1.3594609.

[46] N. Ben Ayed, A. Kirk, B. D. Dudson et al. 'Inter-ELM filaments and turbulent transport in the Mega-Amp Spherical Tokamak'. *Plasma Physics and Controlled Fusion* **51**.3 (2009), p. 035016. DOI: 10.1088/0741-3335/51/3/035016.

[47] S. I. Krasheninnikov, D. A. D'Ippolito and J. R. Myra. 'Recent theoretical progress in understanding coherent structures in edge and SOL turbulence'. *Journal of Plasma Physics* **74**.05 (2008), pp. 679–717. DOI: 10.1017/S0022377807006940.

[48] O. E. Garcia. 'Blob Transport in the Plasma Edge: a Review'. *Plasma and Fusion Research* **4** (2009), pp. 019–019. DOI: 10.1585/pfr.4.019.

[49] J. L. Terry, S. J. Zweben, K. Hallatschek et al. 'Observations of the turbulence in the scrape-off-layer of Alcator C-Mod and comparisons with simulation'. *Physics of Plasmas* **10**.5 (2003), p. 1739. DOI: 10.1063/1.1564090.

[50] G. S. Kirnev, V. P. Budaev, S. A. Grashin et al. 'Comparison of plasma turbulence in the low- and high-field Scrape-Off Layers in the T-10 tokamak'. *Nuclear Fusion* **45**.6 (2005), pp. 459–467. DOI: 10.1088/0029-5515/45/6/007.

[51] D. H. J. Goodall. 'High speed cine film studies of plasma behaviour and plasma surface interactions in tokamaks'. *Journal of Nuclear Materials* **111-112** (1982), pp. 11–22. DOI: 10.1016/0022-3115(82)90174-X.

[52] S. J. Zweben. 'Search for coherent structure within tokamak plasma turbulence'. *Physics of Fluids* **28**.3 (1985), p. 974. DOI: 10.1063/1.865069.

[53] S. I. Krasheninnikov. 'Physical mechanisms in divertors and their impact on the core'. *Czechoslovak Journal of Physics* **48**.S2 (1998), pp. 97–112. DOI: 10.1007/s10582-998-0027-7.

[54] R. J. Maqueda, D. P. Stotler and S. J. Zweben. 'Intermittency in the scrape-off layer of the National Spherical Torus Experiment during H-mode confinement'. *Journal of Nuclear Materials* **415**.1 (2011), S459–S462. DOI: 10.1016/j.jnucmat.2010.11.002.

[55] S. I. Krasheninnikov. 'On scrape off layer plasma transport'. *Physics Letters A* **283**.5-6 (2001), pp. 368–370. DOI: 10.1016/S0375-9601(01)00252-3.

[56] D. A. D'Ippolito, J. R. Myra and S. I. Krasheninnikov. 'Cross-field blob transport in tokamak scrape-off-layer plasmas'. *Physics of Plasmas* **9**.1 (2002), p. 222. DOI: 10.1063/1.1426394.

[57] S. I. Krasheninnikov, S. A. Galkin, A. Y. Pigarov et al. 'Blobby cross-field plasma transport in tokamak edge'. *19th IAEA Fusion Energy Conference*. International Atomic Energy Agency. Vienna, 2003. URL: http://www-pub.iaea.org/MTCD/publications/PDF/csp_019c/pdf/th4_1.pdf.

[58] J. A. Boedo, D. L. Rudakov, R. A. Moyer et al. 'Transport by intermittent convection in the boundary of the DIII-D tokamak'. *Physics of Plasmas* **8**.11 (2001), pp. 4826–9. DOI: 10.1063/1.1406940.

[59] Y. H. Xu, S. Jachmich, R. R. Weynants et al. 'On the properties of turbulence intermittency in the boundary of the TEXTOR tokamak'. *Plasma Physics and Controlled Fusion* **47**.10 (2005), pp. 1841–1855. DOI: 10.1088/0741-3335/47/10/014.

[60] J. Cheng, L. W. Yan, W. Y. Hong et al. 'Statistical characterization of blob turbulence across the separatrix in HL-2A tokamak'. *Plasma Physics and Controlled Fusion* **52**.5 (2010), pp. 055003–21. DOI: 10.1088/0741-3335/52/5/055003.

[61] G. Y. Antar, G. F. Counsell and J. W. Ahn. 'On the scaling of avaloids and turbulence with the average density approaching the density limit'. *Physics of Plasmas* **12**.8 (2005), p. 082503. DOI: 10.1063/1.1953592.

[62] D. L. Rudakov, J. A. Boedo, R. A. Moyer et al. 'Fluctuation-driven transport in the DIII-D boundary'. **44**.6 (2002), pp. 717–731. DOI: 10.1088/0741-3335/44/6/308.

[63] J. A. Boedo, D. L. Rudakov, R. J. Colchin et al. 'Intermittent convection in the boundary of DIII-D'. *Journal of Nuclear Materials* **313-316** (2003), pp. 813–819. DOI: 10.1016/S0022-3115(02)01443-5.

[64] D. L. Rudakov, J. A. Boedo, R. A. Moyer et al. 'Far SOL transport and main wall plasma interaction in DIII-D'. *Nuclear Fusion* **45**.12 (2005), pp. 1589–1599. DOI: 10.1088/0029-5515/45/12/014.

[65] M. Greenwald. 'Density limits in toroidal plasmas'. *Plasma Physics and Controlled Fusion* **44**.8 (2002), R27–R53. DOI: 10.1088/0741-3335/44/8/201.

[66] B. LaBombard, J. W. Hughes, D. Mossessian et al. 'Evidence for electromagnetic fluid drift turbulence controlling the edge plasma state in the Alcator C-Mod tokamak'. *Nuclear Fusion* **45**.12 (2005), pp. 1658–1675. DOI: 10.1088/0029-5515/45/12/022.

[67] J. R. Myra, J. A. Boedo, B. Coppi et al. 'Blob transport models, experiments, and the accretion theory of spontaneous rotation'. *Fusion Energy 2006 Proceedings of the 21st IAEA Conference held in Chengdu, China, 16–21 October 2006*. IAEA. Vienna, 2007. URL: http://www-naweb.iaea.org/napc/physics/FEC/FEC2006/papers/th_p6-21.pdf.

[68] J. R. Myra, D. A. Russell and D. A. D'Ippolito. 'Transport of perpendicular edge momentum by drift-interchange turbulence and blobs'. *Physics of Plasmas* **15**.3 (2008), p. 032304. DOI: 10.1063/1.2889419.

[69] H. Zohm. 'Edge localized modes (ELMs)'. *Plasma Physics and Controlled Fusion* **38**.2 (1996), pp. 105–128. DOI: 10.1088/0741-3335/38/2/001.

[70] A. Kirk, N. Ben Ayed, G. F. Counsell et al. 'Filament structures at the plasma edge on MAST'. *Plasma Physics and Controlled Fusion* **48**.12B (2006), B433–B441. DOI: 10.1088/0741-3335/48/12B/S41.

[71] P. Migliucci, V. Naulin and JET EFDA contributors. 'Magnetic signature of current carrying edge localized modes filaments on the Joint European Torus tokamak'. *Physics of Plasmas* **17**.7 (2010), p. 072507. DOI: 10.1063/1.3436608.

[72] C. Silva, B. Gonçalves, C. Hidalgo et al. 'Fluctuation measurements using a five-pin triple probe in the Joint European Torus boundary plasma'. *Review of Scientific Instruments* **75**.10 (2004), pp. 4314–4316. DOI: 10.1063/1.1787578.

[73] B. Gonçalves, C. Hidalgo, C. Silva et al. 'Statistical description of the radial structure of turbulence in the JET plasma boundary region'. *Journal of Nuclear Materials* **337-339** (2005), pp. 376–380. DOI: 10.1016/j.jnucmat.2004.09.062.

[74] C. Silva, B. Gonçalves, C. Hidalgo et al. 'Intermittent transport in the JET far-SOL'. *Journal of Nuclear Materials* **390-391**.C (2009), pp. 355–358. DOI: 10.1016/j.jnucmat.2009.01.068.

[75] G. S. Xu, V. Naulin, W. Fundamenski et al. 'Blob/hole formation and zonal-flow generation in the edge plasma of the JET tokamak'. *Nuclear Fusion* **49**.9 (2009), pp. 092002–8. DOI: 10.1088/0029-5515/49/9/092002.

[76] G. S. Xu, V. Naulin, W. Fundamenski et al. 'Intermittent convective transport carried by propagating electromagnetic filamentary structures in nonuniformly magnetized plasma'. *Physics of Plasmas* **17**.2 (2010), p. 022501. DOI: 10.1063/1.3302535.

[77] R. A. Moyer, J. W. Cuthbertson, T. E. Evans et al. 'The role of turbulent transport in DIII-D edge and divertor plasmas'. *Journal of Nuclear Materials* **241-243** (1997), pp. 633–638. DOI: 10.1016/S0022-3115(97)80113-4.

[78] G. Y. Antar, M. Tsalas, E. Wolfrum et al. 'Turbulence during H- and L-mode plasmas in the scrape-off layer of the ASDEX Upgrade tokamak'. *Plasma Physics and Controlled Fusion* **50**.9 (2008), pp. 095012–8. DOI: 10.1088/0741-3335/50/9/095012.

[79] B. Nold, G. D. Conway, T. Happel et al. 'Generation of blobs and holes in the edge of the ASDEX Upgrade tokamak'. *Plasma Physics and Controlled Fusion* **52**.6 (2010), pp. 065005–13. DOI: 10.1088/0741-3335/52/6/065005.

[80] D. Carralero, G. Birkenmeier, H. W. Müller et al. 'An experimental investigation of the high density transition of the scrape-off layer transport in ASDEX Upgrade'. *Nuclear Fusion* **54**.12 (2014), pp. 123005–17. DOI: 10.1088/0029-5515/54/12/123005.

[81] D. Carralero, P. Manz, L. Aho-Mantila et al. 'Experimental Validation of a Filament Transport Model in Turbulent Magnetized Plasmas'. *Physical Review Letters* **115**.21 (2015), pp. 215002–5. DOI: 10.1103/PhysRevLett.115.215002.

[82] R. J. Maqueda, G. A. Wurden, S. J. Zweben et al. 'Edge turbulence measurements in NSTX by gas puff imaging'. *Review of Scientific Instruments* **72**.1 (2001), pp. 931–4. DOI: 10.1063/1.1321009.

[83] R. J. Maqueda, G. A. Wurden, D. P. Stotler et al. 'Gas puff imaging of edge turbulence (invited)'. *Review of Scientific Instruments* **74**.3 (2003), pp. 2020–7. DOI: 10.1063/1.1535249.

[84] S. J. Zweben, R. J. Maqueda, D. P. Stotler et al. 'High-speed imaging of edge turbulence in NSTX'. *Nuclear Fusion* **44**.1 (2004), pp. 134–153. DOI: 10.1088/0029-5515/44/1/016.

[85] J. R. Myra, D. A. D'Ippolito, D. P. Stotler et al. 'Blob birth and transport in the tokamak edge plasma: Analysis of imaging data'. *Physics of Plasmas* **13**.9 (2006), p. 092509. DOI: 10.1063/1.2355668.

[86] M. Agostini, S. J. Zweben, R. Cavazzana et al. 'Study of statistical properties of edge turbulence in the National Spherical Torus Experiment with the gas puff imaging diagnostic'. *Physics of Plasmas* **14**.10 (2007), p. 102305. DOI: 10.1063/1.2776912.

[87] R. J. Maqueda, D. P. Stotler and The NSTX Team. 'Intermittent divertor filaments in the National Spherical Torus Experiment and their relation to midplane blobs'. *Nuclear Fusion* **50**.7 (2010), p. 075002. DOI: 10.1088/0029-5515/50/7/075002.

[88] B. D. Dudson. 'Edge Turbulence in the Mega-amp Spherical Tokamak'. PhD thesis. 2007. URL: http://ethos.bl.uk/OrderDetails.do?uin=uk.bl.ethos.489432.

[89] B. D. Dudson, N. Ben Ayed, A. Kirk et al. 'Experiments and simulation of edge turbulence and filaments in MAST'. *Plasma Physics and Controlled Fusion* **50**.12 (2008), p. 124012. DOI: 10.1088/0741-3335/50/12/124012.

[90] G. Y. Antar, G. F. Counsell, J. W. Ahn et al. 'The poloidal distribution of turbulent fluctuations in the Mega-Ampère Spherical Tokamak'. *Physics of Plasmas* **12**.3 (2005), p. 032506. DOI: 10.1063/1.1861894.

[91] B. Hnat, B. D. Dudson, R. O. Dendy et al. 'Characterization of edge turbulence in relation to edge magnetic field configuration in Ohmic L-mode plasmas in the Mega Amp Spherical Tokamak'. *Nuclear Fusion* **48**.8 (2008), p. 085009. DOI: 10.1088/0029-5515/48/8/085009.

[92] J. P. Graves, J. Horacek, R. A. Pitts et al. 'Self-similar density turbulence in the TCV tokamak scrape-off layer'. *Plasma Physics and Controlled Fusion* **47**.3 (2005), pp. L1–L9. DOI: 10.1088/0741-3335/47/3/L01.

[93] O. E. Garcia, J. Horacek, R. A. Pitts et al. 'Interchange turbulence in the TCV scrape-off layer'. *Plasma Physics and Controlled Fusion* **48**.1 (2006), pp. L1–L10. DOI: 10.1088/0741-3335/48/1/L01.

[94] O. E. Garcia, J. Horacek, R. A. Pitts et al. 'Fluctuations and transport in the TCV scrape-off layer'. *Nuclear Fusion* **47**.7 (2007), pp. 667–676. DOI: 10.1088/0029-5515/47/7/017.

[95] O. E. Garcia, R. A. Pitts, J. Horacek et al. 'Turbulent transport in the TCV SOL'. *Journal of Nuclear Materials* **363-365** (2007), pp. 575–580. DOI: 10.1016/j.jnucmat.2006.12.063.

[96] O. E. Garcia, R. A. Pitts, J. Horacek et al. 'Collisionality dependent transport in TCV SOL plasmas'. *Plasma Physics and Controlled Fusion* **49**.12B (2007), B47–B57. DOI: 10.1088/0741-3335/49/12B/S03.

[97] S. J. Zweben, D. P. Stotler, J. L. Terry et al. 'Edge turbulence imaging in the Alcator C-Mod tokamak'. *Physics of Plasmas* **9**.5 (2002), p. 1981. DOI: 10.1063/1.1445179.

[98] J. L. Terry, N. P. Basse, I. Cziegler et al. 'Transport phenomena in the edge of Alcator C-Mod plasmas'. *Nuclear Fusion* **45**.11 (2005), pp. 1321–1327. DOI: 10.1088/0029-5515/45/11/013.

[99] O. Grulke, J. L. Terry, B. LaBombard et al. 'Radially propagating fluctuation structures in the scrape-off layer of Alcator C-Mod'. *Physics of Plasmas* **13**.1 (2006), p. 012306. DOI: 10.1063/1.2164991.

[100] J. L. Terry, B. LaBombard, B. L. Lipschultz et al. 'The scrape-off layer in Alcator C-mod: Transport, turbulence, and flows'. *Fusion Science and Technology* **51** (2007), pp. 342–356. URL: http://www.ans.org/pubs/journals/fst/a_1426.

[101] J. L. Terry, S. J. Zweben, M. V. Umansky et al. 'Spatial structure of scrape-off-layer filaments near the midplane and X-point regions of Alcator-C-Mod'. *Journal of Nuclear Materials* **390-391** (2009), pp. 339–342. DOI: 10.1016/j.jnucmat.2009.01.152.

[102] R. Kube, O. E. Garcia, B. LaBombard et al. 'Blob sizes and velocities in the Alcator C-Mod scrape-off layer'. *Journal of Nuclear Materials* **438**.S (2013), S505–S508. DOI: 10.1016/j.jnucmat.2013.01.104.

[103] K. Tanaka, C. Michael, A. L. Sanin et al. 'Experimental study of particle transport and density fluctuations in LHD'. *Nuclear Fusion* **46**.1 (2005), pp. 110–122. DOI: 10.1088/0029-5515/46/1/013.

[104] N. Ohno, S. Masuzaki, H. Miyoshi et al. 'Analysis on Relation Between Magnetic Structure and Bursty Fluctuation in SOL/Divertor Plasmas of LHD'. *Contributions to Plasma Physics* **46**.7-9 (2006), pp. 692–697. DOI: 10.1002/ctpp.200610065.

[105] J. M. Dewhurst, B. Hnat, N. Ohno et al. 'Statistical properties of edge plasma turbulence in the Large Helical Device'. *Plasma Physics and Controlled Fusion* **50**.9 (2008), pp. 095013–16. DOI: 10.1088/0741-3335/50/9/095013.

[106] O. Grulke, T. Klinger, M. Endler et al. 'Analysis of large-scale fluctuation structures in the scrape-off layer of the Wendelstein 7-AS stellarator'. *Physics of Plasmas* **8**.12 (2001), pp. 5171–11. DOI: 10.1063/1.1418021.

[107] N. P. Basse, S. Zoletnik, P. K. Michelsen et al. 'Study of intermittent small-scale turbulence in Wendelstein 7-AS plasmas during controlled confinement transitions'. *Physics of Plasmas* **12**.1 (2005), pp. 012507–12. DOI: 10.1063/1.1818142.

[108] M. Spolaore, V. Antoni, R. Cavazzana et al. 'Effects of E×B velocity shear on electrostatic structures'. *Physics of Plasmas* **9**.10 (2002), pp. 4110–5. DOI: 10.1063/1.1506310.

[109] M. Spolaore, N. Vianello, M. Agostini et al. 'Direct Measurement of Current Filament Structures in a Magnetic-Confinement Fusion Device'. *Physical Review Letters* **102**.16 (2009), pp. 165001–4. DOI: 10.1103/PhysRevLett.102.165001.

[110] M. Spolaore, N. Vianello, M. Agostini et al. 'Magnetic and electrostatic structures measured in the edge region of the RFX-mod experiment'. *Journal of Nuclear Materials* **390-391**.C (2009), pp. 448–451. DOI: 10.1016/j.jnucmat.2009.01.132.

[111] M. Agostini, P. Scarin, R. Cavazzana et al. 'Edge turbulence characterization in RFX-mod with optical diagnostics'. *Plasma Physics and Controlled Fusion* **51**.10 (2009), pp. 105003–17. DOI: 10.1088/0741-3335/51/10/105003.

[112] T. A. Carter. 'Intermittent turbulence and turbulent structures in a linear magnetized plasma'. *Physics of Plasmas* **13**.1 (2006), pp. 010701–5. DOI: 10.1063/1.2158929.

[113] T. Windisch, O. Grulke and T. Klinger. 'Radial propagation of structures in drift wave turbulence'. *Physics of Plasmas* **13**.12 (2006), pp. 122303–8. DOI: 10.1063/1.2400845.

[114] S. H. Müller, A. Diallo, A. Fasoli et al. 'Probabilistic analysis of turbulent structures from two-dimensional plasma imaging'. *Physics of Plasmas* **13**.10 (2006), pp. 100701–5. DOI: 10.1063/1.2351960.

[115] S. H. Müller, A. Diallo, A. Fasoli et al. 'Plasma blobs in a basic toroidal experiment: Origin, dynamics, and induced transport'. *Physics of Plasmas* **14**.11 (2007), pp. 110704–5. DOI: 10.1063/1.2813193.

[116] B. Labit, A. Diallo, A. Fasoli et al. 'Statistical properties of electrostatic turbulence in toroidal magnetized plasmas'. *Plasma Physics and Controlled Fusion* **49**.12B (2007), B281–B290. DOI: 10.1088/0741-3335/49/12B/S26.

[117] M. Podesta, A. Fasoli, B. Labit et al. 'Cross-Field Transport by Instabilities and Blobs in a Magnetized Toroidal Plasma'. *Physical Review Letters* **101**.4 (2008), pp. 045001–4. DOI: 10.1103/PhysRevLett.101.045001.

[118] I. Furno, B. Labit, M. Podesta et al. 'Experimental Observation of the Blob-Generation Mechanism from Interchange Waves in a Plasma'. *Physical Review Letters* **100**.5 (2008), pp. 055004–4. DOI: 10.1103/PhysRevLett.100.055004.

[119] I. Furno, B. Labit, A. Fasoli et al. 'Mechanism for blob generation in the TORPEX toroidal plasma'. *Physics of Plasmas* **15**.5 (2008), pp. 055903–8. DOI: 10.1063/1.2870082.

[120] S. H. Müller, C. Theiler, A. Fasoli et al. 'Studies of blob formation, propagation and transport mechanisms in basic experimental plasmas (TORPEX and CSDX)'. *Plasma Physics and Controlled Fusion* **51**.5 (2009), pp. 055020–16. DOI: 10.1088/0741-3335/51/5/055020.

[121] C. Theiler, A. Diallo, A. Fasoli et al. 'The role of the density gradient on intermittent cross-field transport events in a simple magnetized toroidal plasma'. *Physics of Plasmas* **15**.4 (2008), pp. 042303–11. DOI: 10.1063/1.2901188.

[122] C. Theiler, I. Furno, P. Ricci et al. 'Cross-Field Motion of Plasma Blobs in an Open Magnetic Field Line Configuration'. *Physical Review Letters* **103**.6 (2009), p. 065001. DOI: 10.1103/PhysRevLett.103.065001.

[123] I. Furno, C. Theiler, D. Lançon et al. 'Blob current structures in TORPEX plasmas: experimental measurements and numerical simulations'. *Plasma Physics and Controlled Fusion* **53**.12 (2011), p. 124016. DOI: 10.1088/0741-3335/53/12/124016.

[124] C. Theiler, I. Furno, A. Fasoli et al. 'Blob motion and control in simple magnetized plasmas'. *Physics of Plasmas* **18**.5 (2011), pp. 055901–8. DOI: 10.1063/1.3562944.

[125] M. Endler. 'Turbulent SOL transport in stellarators and tokamaks'. *Journal of Nuclear Materials* **266-269** (1999), pp. 84–90. DOI: 10.1016/S0022-3115(98)00659-X.

[126] F. Sattin, M. Agostini, P. Scarin et al. 'On the statistics of edge fluctuations: comparative study between various fusion devices'. *Plasma Physics and Controlled Fusion* **51**.5 (2009), pp. 055013–12. DOI: 10.1088/0741-3335/51/5/055013.

[127] F. Sattin, M. Agostini, R. Cavazzana et al. 'About the parabolic relation existing between the skewness and the kurtosis in time series of experimental data'. *Physica Scripta* **79**.4 (2009), pp. 045006–5. DOI: 10.1088/0031-8949/79/04/045006.

[128] F. Militello, P. Tamain, W. Fundamenski et al. 'Experimental and numerical characterization of the turbulence in the scrape-off layer of MAST'. *Plasma Physics and Controlled Fusion* **55**.2 (2013), p. 025005. DOI: 10.1088/0741-3335/55/2/025005.

[129] N. Katz, J. Egedal, W. Fox et al. 'Experiments on the Propagation of Plasma Filaments'. *Physical Review Letters* **101**.1 (2008), p. 015003. DOI: 10.1103/PhysRevLett.101.015003.

[130] J. R. Harrison, G. M. Fishpool, A. J. Thornton et al. 'The appearance and propagation of filaments in the private flux region in Mega Amp Spherical Tokamak'. *Physics of Plasmas* **22**.9 (2015), pp. 092508–10. DOI: 10.1063/1.4929924.

[131] F. Militello, N. R. Walkden, T. Farley et al. 'Multi-code analysis of scrape-off layer filament dynamics in MAST'. *Plasma Physics and Controlled Fusion* **58**.10 (2016), p. 105002. DOI: 10.1088/0741-3335/58/10/105002.

[132] D. Farina, R. Pozzoli and D. D. Ryutov. 'Effect of the magnetic field geometry on the flute-like perturbations near the divertor X point'. *Nuclear Fusion* **33**.9 (1993), pp. 1315–1317. DOI: 10.1088/0029-5515/33/9/I06.

[133] S. Elmore, S. Y. Allan, A. Kirk et al. 'Upstream and divertor ion temperature measurements on MAST by retarding field energy analyser'. *Plasma Physics and Controlled Fusion* **54**.6 (2012), pp. 065001–12. DOI: 10.1088/0741-3335/54/6/065001.

[134] M. Kočan, F. P. Gennrich, A. Kendl et al. 'Ion temperature fluctuations in the ASDEX Upgrade scrape-off layer'. *Plasma Physics and Controlled Fusion* **54**.8 (2012), pp. 085009–12. DOI: 10.1088/0741-3335/54/8/085009.

[135] S. Y. Allan, S. Elmore, G. Fishpool et al. 'Ion temperature measurements of L-mode filaments in MAST by retarding field energy analyser'. *Plasma Physics and Controlled Fusion* **58**.4 (2016), pp. 1–11. DOI: 10.1088/0741-3335/58/4/045014.

[136] N. R. Walkden. 'Properties of Intermittent Transport in the Mega Ampere Spherical Tokamak'. PhD thesis. 2014. URL: http://etheses.whiterose.ac.uk/id/eprint/8674.

[137] A. Kirk, A. J. Thornton, J. R. Harrison et al. 'L-mode filament characteristics on MAST as a function of plasma current measured using visible imaging'. *Plasma Physics and Controlled Fusion* **58**.8 (2016), p. 085008. DOI: 10.1088/0741-3335/58/8/085008.

[138] R. H. Cohen and D. D. Ryutov. 'Dynamics of an Isolated Blob in the Presence of the X-Point'. *Contributions to Plasma Physics* **46**.7-9 (2006), pp. 678–684. DOI: 10.1002/ctpp.200610063.

[139] S. I. Krasheninnikov, A. I. Smolyakov and T. K. Soboleva. 'On anomalous cross-field edge plasma convection in fusion devices'. *Physics of Plasmas* **12**.7 (2005), pp. 072502–6. DOI: 10.1063/1.1940061.

[140] S. I. Krasheninnikov, A. I. Smolyakov and G. Yu. 'Transport of meso-scale structures in tokamak edge plasmas'. *Czechoslovak Journal of Physics* **55**.3 (2005), pp. 307–316. DOI: 10.1007/s10582-005-0043-9.

[141] D. D. Ryutov. 'The dynamics of an isolated plasma filament at the edge of a toroidal device'. *Physics of Plasmas* **13**.12 (2006), pp. 122307–10. DOI: 10.1063/1.2403092.

[142] S. I. Krasheninnikov and A. I. Smolyakov. 'On neutral wind and blob motion in linear devices'. *Physics of Plasmas* **10**.7 (2003), pp. 3020–3. DOI: 10.1063/1.1579692.

[143] P. B. Parks. 'Electric field and current distribution near the ablation cloud of a pellet injected into a tokamak'. *Nuclear Fusion* **32**.12 (1992), pp. 2137–2145. DOI: 10.1088/0029-5515/32/12/I05.

[144] M. N. Rosenbluth and C. L. Longmire. 'Stability of plasmas confined by magnetic fields'. *Annals of Physics* **1**.2 (1957), pp. 120–140. DOI: 10.1016/0003-4916(57)90055-6.

[145] R. D. Hazeltine and J. D. Meiss. *Plasma Confinement*. Courier Dover Publications, 2003. ISBN: 9780486432427.

[146] F. L. Hinton and C. W. Horton. 'Amplitude Limitation of a Collisional Drift Wave Instability'. *Physics of Fluids* **14**.1 (1971), pp. 116–9. DOI: 10.1063/1.1693260.

[147] E. V. Belova. 'Nonlinear gyroviscous force in a collisionless plasma'. *Physics of Plasmas* **8**.9 (2001), pp. 3936–10. DOI: 10.1063/1.1389093.

[148] J. J. Ramos. 'General expression of the gyroviscous force'. *Physics of Plasmas* **12**.11 (2005), pp. 112301–8. DOI: 10.1063/1.2114747.

[149] G. Q. Yu, S. I. Krasheninnikov and P. N. Guzdar. 'Two-dimensional modelling of blob dynamics in tokamak edge plasmas'. *Physics of Plasmas* **13**.4 (2006), p. 042508. DOI: 10.1063/1.2193087.

[150] J. R. Angus and M. V. Umansky. 'Modeling of large amplitude plasma blobs in three-dimensions'. *Physics of Plasmas* **21**.1 (2014), p. 012514. DOI: 10.1063/1.4863503.

[151] J. R. Angus and S. I. Krasheninnikov. 'Inviscid evolution of large amplitude filaments in a uniform gravity field'. *Physics of Plasmas* **21**.11 (2014), pp. 112504–9. DOI: 10.1063/1.4901237.

[152] M. Wiesenberger, J. Madsen and A. Kendl. 'Radial convection of finite ion temperature, high amplitude plasma blobs'. *Physics of Plasmas* **21**.9 (2014), pp. 092301–12. DOI: 10.1063/1.4894220.

[153] S. I. Krasheninnikov, D. D. Ryutov and G. Yu. 'Large plasma pressure perturbations and radial convective transport in a tokamak'. *Journal of Plasma and Fusion Research* **6** (2004), pp. 139–143. URL: http://www.jspf.or.jp/Journal/JPFR/itc13/jpfr2004_06-139.pdf.

[154] D. D. Ryutov and R. H. Cohen. 'Instability Driven by Sheath Boundary Conditions and Limited to Divertor Legs'. *Contributions to Plasma Physics* **44**.13 (2004), pp. 168–175. DOI: 10.1002/ctpp.200410023.

[155] D. A. Russell, J. R. Myra and D. A. D'Ippolito. 'Collisionality and magnetic geometry effects on tokamak edge turbulent transport. II. Many-blob turbulence in the two-region model'. *Physics of Plasmas* **14**.10 (2007), p. 102307. DOI: 10.1063/1.2780137.

[156] N. Bisai, A. Das, S. Deshpande et al. 'Edge and scrape-off layer tokamak plasma turbulence simulation using two-field fluid model'. *Physics of Plasmas* **12**.7 (2005), p. 072520. DOI: 10.1063/1.1942427.

[157] P. Ghendrih, Y. Sarazin, G. Attuel et al. 'Theoretical analysis of the influence of external biasing on long range turbulent transport in the scrape-off layer'. *Nuclear Fusion* **43**.10 (2003), pp. 1013–1022. DOI: 10.1088/0029-5515/43/10/001.

[158] R. Fitzpatrick. *Plasma Physics: An Introduction*. CRC Press, 2014. ISBN: 1466594268.

[159] O. E. Garcia, N. H. Bian and W. Fundamenski. 'Radial interchange motions of plasma filaments'. *Physics of Plasmas* **13**.8 (2006), p. 082309. DOI: 10.1063/1.2336422.

[160] G. Q. Yu and S. I. Krasheninnikov. 'Dynamics of blobs in scrape-off-layer/shadow regions of tokamaks and linear devices'. *Physics of Plasmas* **10**.11 (2003), p. 4413. DOI: 10.1063/1.1616937.

[161] G. Q. Yu and S. I. Krasheninnikov. 'Stability of plasma blobs in tokamak scrape off layer'. *European Conference Abstracts* **27A** (2003). URL: http://crpppc42.epfl.ch/StPetersburg/PDFS/P3_171.pdf.

[162] N. H. Bian, S. Benkadda, J. V. Paulsen et al. 'Blobs and front propagation in the scrape-off layer of magnetic confinement devices'. *Physics of Plasmas* **10**.3 (2003), p. 671. DOI: 10.1063/1.1541021.

[163] D. A. D'Ippolito, J. R. Myra, S. I. Krasheninnikov et al. 'Blob Transport in the Tokamak Scrape-off-Layer'. *Contributions to Plasma Physics* **44**.1-3 (2004), pp. 205–216. DOI: 10.1002/ctpp.200410030.

[164] D. A. D'Ippolito, J. R. Myra, D. A. Russell et al. 'Rotational stability of plasma blobs'. *Physics of Plasmas* **11**.10 (2004), p. 4603. DOI: 10.1063/1.1785791.

[165] J. R. Myra, D. A. D'Ippolito, S. I. Krasheninnikov et al. 'Convective transport in the scrape-off-layer by nonthermalized spinning blobs'. *Physics of Plasmas* **11**.9 (2004), pp. 4267–4274. DOI: 10.1063/1.1774168.

[166] A. Y. Aydemir. 'Convective transport in the scrape-off layer of tokamaks'. *Physics of Plasmas* **12**.6 (2005), pp. 062503–12. DOI: 10.1063/1.1927539.

[167] R. Kube and O. E. Garcia. 'Velocity scaling for filament motion in scrape-off layer plasmas'. *Physics of Plasmas* **18**.10 (2011), p. 102314. DOI: 10.1063/1.3647553.

[168] J. R. Angus, S. I. Krasheninnikov and M. V. Umansky. 'Effects of parallel electron dynamics on plasma blob transport'. *Physics of Plasmas* **19**.8 (2012), p. 082312. DOI: 10.1063/1.4747619.

[169] J. T. Omotani, F. Militello, L. Easy et al. 'The effects of shape and amplitude on the velocity of scrape-off layer filaments'. *Plasma Physics and Controlled Fusion* **58**.1 (2015), p. 014030. DOI: 10.1088/0741-3335/58/1/014030.

[170] D. A. Russell, J. R. Myra and D. A. D'Ippolito. 'Saturation mechanisms for edge turbulence'. *Physics of Plasmas* **16**.12 (2009), p. 122304. DOI: 10.1063/1.3270051.

[171] D. A. Russell, J. R. Myra, D. A. D'Ippolito et al. 'Comparison of scrape-off layer turbulence simulations with experiments using a synthetic gas puff imaging diagnostic'. *Physics of Plasmas* **18**.2 (2011), p. 022306. DOI: 10.1063/1.3553024.

[172] J. R. Myra, D. A. Russell, D. A. D'Ippolito et al. 'Reduced model simulations of the scrape-off-layer heat-flux width and comparison with experiment'. *Physics of Plasmas* **18**.1 (2011), p. 012305. DOI: 10.1063/1.3526676.

[173] J. R. Myra, D. A. Russell, D. A. D'Ippolito et al. 'Turbulent transport and the scrape-off-layer width'. *Journal of Nuclear Materials* **415**.1 (2011), S605–S608. DOI: 10.1016/j.jnucmat.2010.10.030.

[174] J. R. Myra, D. A. Russell and D. A. D'Ippolito. 'Diffusive–convective transition for scrape-off layer transport and the heat-flux width'. *Plasma Physics and Controlled Fusion* **54**.5 (2012), p. 055008. DOI: 10.1088/0741-3335/54/5/055008.

[175] D. A. Russell, D. A. D'Ippolito, J. R. Myra et al. 'Numerical investigation of edge plasma phenomena in an enhanced D-alpha discharge at Alcator C-Mod: Parallel heat flux and quasi-coherent edge oscillations'. *Physics of Plasmas* **19**.8 (2012), p. 082311. DOI: 10.1063/1.4747503.

[176] J. R. Myra, W. M. Davis, D. A. D'Ippolito et al. 'Edge sheared flows and the dynamics of blob-filaments'. *Nuclear Fusion* **53**.7 (2013), p. 073013. DOI: 10.1088/0029-5515/53/7/073013.

[177] W. Fundamenski, O. E. Garcia, V. Naulin et al. 'Dissipative processes in interchange driven scrape-off layer turbulence'. *Nuclear Fusion* **47**.5 (2007), pp. 417–433. DOI: 10.1088/0029-5515/47/5/006.

[178] O. E. Garcia, V. Naulin, A. H. Nielsen et al. 'Turbulence and intermittent transport at the boundary of magnetized plasmas'. *Physics of Plasmas* **12**.6 (2005), p. 062309. DOI: 10.1063/1.1925617.

[179] O. E. Garcia, V. Naulin, A. H. Nielsen et al. 'Computations of Intermittent Transport in Scrape-Off Layer Plasmas'. *Physical Review Letters* **92**.16 (2004), p. 165003. DOI: 10.1103/PhysRevLett.92.165003.

[180] F. Militello, W. Fundamenski, V. Naulin et al. 'Simulations of edge and scrape off layer turbulence in mega ampere spherical tokamak plasmas'. *Plasma Physics and Controlled Fusion* **54**.9 (2012), p. 095011. DOI: 10.1088/0741-3335/54/9/095011.

[181] F. Militello, V. Naulin and A. H. Nielsen. 'Numerical scalings of the decay lengths in the scrape-off layer'. *Plasma Physics and Controlled Fusion* **55**.7 (2013), p. 074010. DOI: 10.1088/0741-3335/55/7/074010.

[182] F. Militello, W. Fundamenski, V. Naulin et al. 'Numerical investigation of Scrape Off Layer anomalous particle transport for MAST parameters'. *Journal of Nuclear Materials* **438** (2013), pp. 1–6. DOI: 10.1016/j.jnucmat.2013.01.110.

[183] J. R. Myra and D. A. D'Ippolito. 'Edge instability regimes with applications to blob transport and the quasicoherent mode'. *Physics of Plasmas* **12**.9 (2005), p. 092511. DOI: 10.1063/1.2048847.

[184] J. R. Myra, D. A. Russell and D. A. D'Ippolito. 'Collisionality and magnetic geometry effects on tokamak edge turbulent transport. I. A two-region model with application to blobs'. *Physics of Plasmas* **13**.11 (2006), p. 112502. DOI: 10.1063/1.2364858.

[185] D. Jovanović, U. de Angelis, R. Fedele et al. 'Effects of dust particles on the dynamics of blobs in the scrape off layer'. *Physics of Plasmas* (2007). DOI: 10.1063/1.2767617.

[186] D. Jovanović, P. K. Shukla and F. Pegoraro. 'Effects of the parallel electron dynamics and finite ion temperature on the plasma blob propagation in the scrape-off layer'. *Physics of Plasmas* **15**.11 (2008), p. 112305. DOI: 10.1063/1.3008050.

[187] O. E. Garcia, N. H. Bian, V. Naulin et al. 'Mechanism and scaling for convection of isolated structures in nonuniformly magnetized plasmas'. *Physics of Plasmas* **12**.9 (2005), p. 090701. DOI: 10.1063/1.2044487.

[188] X. Q. Xu, M. V. Umansky and B. D. Dudson. 'Boundary plasma turbulence simulations for tokamaks'. *Communications in Computational Physics* **4**.5 (2008), pp. 949–979. DOI: 10.4208/cicp.2008.v4.949.

[189] D. A. Russell, D. A. D'Ippolito, J. R. Myra et al. 'Blob Dynamics in 3D BOUT Simulations of Tokamak Edge Turbulence'. *Physical Review Letters* **93**.26 (2004), p. 265001. DOI: 10.1103/PhysRevLett.93.265001.

[190] R. H. Cohen, B. LaBombard, D. D. Ryutov et al. 'Theory and fluid simulations of boundary-plasma fluctuations'. *Nuclear Fusion* **47**.7 (2007), pp. 612–625. DOI: 10.1088/0029-5515/47/7/012.

[191] J. R. Angus, M. V. Umansky and S. I. Krasheninnikov. 'Effect of Drift Waves on Plasma Blob Dynamics'. *Physical Review Letters* **108**.21 (2012), p. 215002. DOI: 10.1103/PhysRevLett.108.215002.

[192] J. R. Angus, M. V. Umansky and S. I. Krasheninnikov. '3D Blob Modelling with BOUT++'. *Contributions to Plasma Physics* **52**.5-6 (2012), pp. 348–352. DOI: 10.1002/ctpp.201210015.

[193] B. D. Dudson, M. V. Umansky, X. Q. Xu et al. 'BOUT++: A framework for parallel plasma fluid simulations'. *Computer Physics Communications* **180**.9 (2009), pp. 1467–1480. DOI: 10.1016/j.cpc.2009.03.008.

[194] B. D. Dudson, A. Allen, G. Breyiannis et al. 'BOUT++: Recent and current developments'. *Journal of Plasma Physics* **81**.1 (2015), p. 365810104. DOI: 10.1017/S0022377814000816.

[195] N. R. Walkden, B. D. Dudson and G. Fishpool. 'Characterization of 3D filament dynamics in a MAST SOL flux tube geometry'. *Plasma Physics and Controlled Fusion* **55**.10 (2013), p. 105005. DOI: 10.1088/0741-3335/55/10/105005.

[196] N. R. Walkden, B. D. Dudson, L. Easy et al. 'Numerical investigation of isolated filament motion in a realistic tokamak geometry'. *Nuclear Fusion* **55**.11 (2015), p. 113022. DOI: 10.1088/0029-5515/55/11/113022.

[197] F. D. Halpern, A. Cardellini, P. Ricci et al. 'Three-dimensional simulations of blob dynamics in a simple magnetized torus'. *Physics of Plasmas* **21** (2014), p. 022305. DOI: 10.1063/1.4864324.

[198] W. Lee, M. V. Umansky, J. R. Angus et al. 'Electromagnetic effects on dynamics of high-beta filamentary structures'. *Physics of Plasmas* **22**.1 (2015), p. 012505. DOI: 10.1063/1.4905639.

[199] N. R. Walkden, L. Easy, F. Militello et al. 'Dynamics of 3D isolated thermal filaments'. *Plasma Physics and Controlled Fusion* **58**.11 (2016), p. 115010. DOI: 10.1088/0741-3335/58/11/115010.

[200] J. Morales, B. Frei, F. Halpern et al. *The impact of the Boussinesq approximation on plasma turbulence in the scrape-off layer*. Tech. rep. WP14ER-PR(16) 15739. EUROFUSION. URL: http://www.euro-fusionscipub.org/wp-content/uploads/WP14ERCP16_15739_submitted.pdf.

[201] J. Madsen, O. E. Garcia, J. Stærk Larsen et al. 'The influence of finite Larmor radius effects on the radial interchange motions of plasma filaments'. *Physics of Plasmas* **18**.11 (2011), pp. 112504–16. DOI: 10.1063/1.3658033.

[202] N. Bisai and P. Kaw. 'Role of ion temperature on scrape-off layer plasma turbulence'. *Physics of Plasmas* **20**.4 (2013), p. 042509. DOI: 10.1063/1.4801737.

[203] P. Manz, D. Carralero, G. Birkenmeier et al. 'Filament velocity scaling laws for warm ions'. *Physics of Plasmas* **20**.10 (2013), pp. 102307–9. DOI: 10.1063/1.4824799.

[204] P. Manz, G. Birkenmeier, D. Carralero et al. 'The influence of finite ion temperature on plasma blob dynamics'. *Plasma Physics and Controlled Fusion* **57**.1 (2014), pp. 014012–7. DOI: 10.1088/0741-3335/57/1/014012.

[205] S. I. Braginskii. 'Transport processes in a plasma'. *Reviews of Plasma Physics* **1** (1965), p. 205.

[206] H. Hasegawa and S. Ishiguro. 'Particle Simulation of Plasma Blob Dynamics: Preliminary Results'. *Plasma and Fusion Research* **7**.0 (2012), pp. 2401060–2401060. DOI: 10.1585/pfr.7.2401060.

[207] T. T. Ribeiro and B. D. Scott. 'Gyrofluid turbulence studies of the effect of the poloidal position of an axisymmetric Debye sheath'. *Plasma Physics and Controlled Fusion* **50**.5 (2008), p. 055007. DOI: 10.1088/0741-3335/50/5/055007.

[208] T. T. Ribeiro and B. D. Scott. 'Tokamak turbulence computations on closed and open magnetic flux surfaces'. *Plasma Physics and Controlled Fusion* **47**.10 (2005), pp. 1657–1679. DOI: 10.1088/0741-3335/47/10/005.

[209] B. L. Lipschultz, B. LaBombard, C. S. Pitcher et al. 'Investigation of the origin of neutrals in the main chamber of Alcator C-Mod'. *Plasma Physics and Controlled Fusion* **44**.6 (2002), pp. 733–748. DOI: 10.1088/0741-3335/44/6/309.

[210] B. L. Lipschultz, D. G. Whyte and B. LaBombard. 'Comparison of particle transport in the scrape-off layer plasmas of Alcator C-Mod and DIII-D'. *Plasma Physics and Controlled Fusion* **47**.10 (2005), pp. 1559–1578. DOI: 10.1088/0741-3335/47/10/001.

[211] D. G. Whyte, B. L. Lipschultz, P. C. Stangeby et al. 'The magnitude of plasma flux to the main-wall in the DIII-D tokamak'. *Plasma Physics and Controlled Fusion* **47**.10 (2005), pp. 1579–1607. DOI: 10.1088/0741-3335/47/10/002.

[212] A. Y. Pigarov, S. I. Krasheninnikov, T. D. Rognlien et al. 'Tokamak edge plasma simulation including anomalous cross-field convective transport'. *Physics of Plasmas* **9**.4 (2002), p. 1287. DOI: 10.1063/1.1459059.

[213] P. C. Stangeby. 'Modeling plasma contact with the main vessel walls of a divertor tokamak'. *Physics of Plasmas* **9**.8 (2002), p. 3489. DOI: 10.1063/1.1493207.

[214] R. Schneider, X. Bonnin, K. Borrass et al. 'Plasma Edge Physics with B2-Eirene'. *Contributions to Plasma Physics* **46**.1-2 (2006), pp. 3–191. DOI: 10.1002/ctpp.200610001.

[215] V. Naulin. 'Turbulent transport and the plasma edge'. *Journal of Nuclear Materials* **363-365** (2007), pp. 24–31. DOI: 10.1016/j.jnucmat.2006.12.058.

[216] R. O. Dendy. *Plasma Physics: An Introductory Course*. Cambridge University Press, 1995. ISBN: 9780521484527.

[217] A. N. Simakov and P. J. Catto. 'Drift-ordered fluid equations for field-aligned modes in low-β collisional plasma with equilibrium pressure pedestals'. *Physics of Plasmas* **10**.12 (2003), pp. 4744–15. DOI: 10.1063/1.1623492.

[218] A. N. Simakov and P. J. Catto. 'Erratum: "Drift-ordered fluid equations for field-aligned modes in low-β collisional plasma with equilibrium pressure pedestals" [Phys. Plasmas 10, 4744 (2003)]'. *Physics of Plasmas* **11**.5 (2004), pp. 2326–2. DOI: 10.1063/1.1703527.

[219] J. Madsen, V. Naulin, A. H. Nielsen et al. 'Collisional transport across the magnetic field in drift-fluid models'. *Physics of Plasmas* **23**.3 (2016), pp. 032306–15. DOI: 10.1063/1.4943199.

[220] U. Deka and C. B. Dwivedi. 'Effect of electron inertial delay on Debye sheath formation'. *Brazilian Journal of Physics* (2010), pp. 333–339. DOI: 10.1590/S0103-97332010000300014.

[221] P. Ghendrih, K. Bodi and H. Bufferand. 'Transition to supersonic flows in the edge plasma'. *Plasma Physics and Controlled Fusion* (2011). DOI: 10.1088/0741-3335/53/5/054019.

[222] E. Buckingham. 'On Physically Similar Systems; Illustrations of the Use of Dimensional Equations'. *Physical Review* **4**.4 (1914), pp. 345–376. DOI: 10.1103/PhysRev.4.345.

[223] B. D. Dudson. *BOUT++ Developers' Manual*.

[224] B. D. Dudson and BOUT++ Contributors. *BOUT++ Users Manual*. URL: http://www-users.york.ac.uk/%7Ebd512//bout/user_manual.pdf.

[225] S. Hamdi, W. Schiesser and G. Griffiths. 'Method of lines'. *Scholarpedia* **2**.7 (2007), p. 2859. DOI: 10.4249/scholarpedia.2859.

[226] R. Courant, K. Friedrichs and H. Lewy. 'Über die partiellen Differenzengleichungen der mathematischen Physik'. German. *Mathematische Annalen* **100**.1 (1928), pp. 32–74. DOI: 10.1007/BF01448839.

[227] D. A. Knoll and D. E. Keyes. 'Jacobian-free Newton–Krylov methods: a survey of approaches and applications'. *Journal of Computational Physics* **193**.2 (2004), pp. 357–397. DOI: 10.1016/j.jcp.2003.08.010.

[228] G. E. Karniadakis, M. Israeli and S. A. Orszag. 'High-order splitting methods for the incompressible Navier-Stokes equations'. *Journal of Computational Physics* **97**.2 (1991), pp. 414–443. DOI: 10.1016/0021-9991(91)90007-8.

[229] W. H. Press. *Numerical Recipes 3rd Edition*. The Art of Scientific Computing. Cambridge University Press, 2007. ISBN: 0521880688.

[230] S. Gottlieb, C. W. Shu and E. Tadmor. 'Strong stability-preserving high-order time discretization methods'. *SIAM review* **43**.1 (2001), p. 89. DOI: 10.1137/S003614450036757X.

[231] G. D. Byrne and A. C. Hindmarsh. 'PVODE, an ODE solver for parallel computers'. *International Journal of High Performance Computing Applications* **13**.4 (1999), pp. 354–365. DOI: 10.1177/109434209901300405.

[232] P. N. Brown and A. C. Hindmarsh. 'Reduced storage matrix methods in stiff ODE systems'. *Applied Mathematics and Computation* **31** (1989), pp. 40–91. DOI: 10.1016/0096-3003(89)90110-0.

[233] A. C. Hindmarsh, P. N. Brown, K. E. Grant et al. 'SUNDIALS: Suite of Nonlinear and Differential/Algebraic Equation Solvers'. *ACM Transactions on Mathematical Software* **31**.3 (2005), pp. 363–396. DOI: 10.1145/1089014.1089020.

[234] S. Balay, S. Abhyankar, M. Adams et al. *PETSc Users Manual*. Tech. rep. ANL-95/11 Rev 3.7. Argonne National Laboratory, 2016. URL: http://www.mcs.anl.gov/petsc/petsc-current/docs/manual.pdf.

[235] A. Arakawa. 'Computational design for long-term numerical integration of the equations of fluid motion: Two-dimensional incompressible flow. Part I'. *Journal of Computational Physics* **1**.1 (1966), pp. 119–143. DOI: 10.1016/0021-9991(66)90015-5.

[236] L. H. Thomas. *Elliptic Problems in Linear Differential Equations over a Network; Watson Science Computer Laboratory Report*. Columbia University: New York, 1949.

[237] D. Coppersmith and S. Winograd. 'Matrix multiplication via arithmetic progressions'. *Journal of Symbolic Computation* **9**.3 (1990), pp. 251–280. DOI: 10.1016/S0747-7171(08)80013-2.

[238] W. L. Briggs, V. E. Henson and S. F. McCormick. *A Multigrid Tutorial: Second Edition*. Society for Industrial and Applied Mathematics (SIAM), 2000. ISBN: 9780898714623.

[239] D. Braess. *Finite Elements*. Third Edition. Cambridge University Press, 2007. ISBN: 9780511618635. DOI: 10.1017/CBO9780511618635.

[240] K. Salari and P. Knupp. *Code verification by the method of manufactured solutions*. Tech. rep. SAND2000 - 1444. Albuquerque: Sandia National Laboratories, 2000.

[241] F. Riva, P. Ricci, F. D. Halpern et al. 'Verification methodology for plasma simulations and application to a scrape-off layer turbulence code'. *Physics of Plasmas* **21**.6 (2014), p. 062301. DOI: 10.1063/1.4879778.

[242] G. B. Whitham. *Linear and Nonlinear Waves*. John Wiley & Sons, 2011. ISBN: 1118031202.

[243] P. Tamain, P. Ghendrih, E. Tsitrone et al. 'TOKAM-3D: A 3D fluid code for transport and turbulence in the edge plasma of Tokamaks'. *Journal of Computational Physics* **229**.2 (2010), pp. 361–378. DOI: 10.1016/j.jcp.2009.09.031.

[244] P. Tamain, H. Bufferand, G. Ciraolo et al. '3D Properties of Edge Turbulent Transport in Full-Torus Simulations and their Impact on Poloidal Asymmetries'. *Contributions to Plasma Physics* **54**.4-6 (2014), pp. 555–559. DOI: 10.1002/ctpp.201410017.

[245] E. Havlíčková, W. Fundamenski, V. Naulin et al. 'Steady-state and time-dependent modelling of parallel transport in the scrape-off layer'. *Plasma Physics and Controlled Fusion* **53**.6 (2011), p. 065004. DOI: 10.1088/0741-3335/53/6/065004.

[246] H. K. Versteeg and W. Malalasekera. *An Introduction to Computational Fluid Dynamics*. The Finite Volume Method. Pearson Education, 2007. ISBN: 9780131274983.

[247] B. D. Dudson, J. Madsen, J. T. Omotani et al. 'Verification of BOUT++ by the method of manufactured solutions'. *Physics of Plasmas* **23**.6 (2016), pp. 062303–13. DOI: 10.1063/1.4953429.

[248] F. Riva, C. Colin, J. Denis et al. 'Blob dynamics in the TORPEX experiment: a multi-code validation'. *Plasma Physics and Controlled Fusion* **58**.4 (2016), pp. 1–16. DOI: 10.1088/0741-3335/58/4/044005.

[249] P. Ricci, F. D. Halpern, S. Jolliet et al. 'Simulation of plasma turbulence in scrape-off layer conditions: the GBS code, simulation results and code validation'. *Plasma Physics and Controlled Fusion* **54**.12 (2012), p. 124047. DOI: 10.1088/0741-3335/54/12/124047.

[250] A. H. Nielsen, G. S. Xu, J. Madsen et al. 'Simulation of transition dynamics to high confinement in fusion plasmas'. *Physics Letters A* **379**.47-48 (2015), pp. 3097–3101. DOI: 10.1016/j.physleta.2015.10.004.

[251] I. Katramados, G. Fishpool, M. Fursdon et al. 'MAST upgrade closed pumped divertor design and analysis'. *Fusion Engineering and Design* **86**.9-11 (2011), pp. 1595–1598. DOI: 10.1016/j.fusengdes.2011.02.060.

[252] R. J. Goldston and P. H. Rutherford. *Introduction to Plasma Physics*. CRC Press, 1995. ISBN: 9781439822074.

[253] U. S. Inan and M. Gołkowski. *Principles of Plasma Physics for Engineers and Scientists*. Cambridge University Press, 2010. ISBN: 1139492241.

[254] F. F. Chen. *Introduction to Plasma Physics and Controlled Fusion: Volume 1: Plasma Physics*. Springer US, 2013. ISBN: 9781475755954.

[255] R. Janev. *Atomic and Molecular Processes in Fusion Edge Plasmas*. Springer US, 2013. ISBN: 9781475793192.

[256] F. Militello. Private communication. 2016.